
Investigating the contribution of substrate
collecting antenna to the proton/lactate cotransport
(in PfFNT and MCT1)

Dissertation

In fulfilment of the requirements for the degree of Doctorate
of the Faculty of Mathematical and Natural Sciences
at Kiel University

submitted by
Nathan Epalle

Romans-sur-Isère, 2023

First examiner: Prof. Dr. Eric Beitz

Second examiner: Prof. Dr. Axel Scheidig

Date of the oral examination: 05.09.2023

“It's better to light a candle than curse the darkness [...]” - Constable Carrot

Terry Pratchett, *Men At Arms* (Discworld #15)

CONTENT

CONTENT	I
Abbreviations.....	VII
ABSTRACT	1
ZUSAMMENFASSUNG	2
1. INTRODUCTION	3
1.1. Glycolysis produces lactate and proton.....	3
1.2. <i>Plasmodium falciparum</i> FNT	7
1.2.1. Malaria.....	7
1.2.2. <i>Plasmodium</i> lifecycle	7
1.2.3. <i>Plasmodium</i> glycolytic pathway.....	8
1.2.4. PfFNT structure and transport mechanism.....	9
1.2.5. Therapeutic target.....	11
1.3. Human MCT1.....	13
1.3.1. The MCT family.....	13
1.3.2. MCT lactate transport in human cells.....	14
1.3.3. Structure and mechanism of <i>MCT1</i>	15
1.3.4. Partner proteins.....	17
1.4. Proton antenna	18
1.5. Aims of this work.....	20
2. MATERIAL	21
2.1. Protein coding sequences	21
2.2. Plasmids.....	22
2.2.1. pDR196 derivatives for expression in yeast.....	22
2.2.2. IPTG inducible plasmid for expression in <i>E. coli</i>	25
2.2.3. pIVEX 2.3w and derivatives for cell-free protein production.....	25
2.2.4. pcDNA 3.1 derivatives for human cells protein production.....	27
2.3. DNA oligonucleotides.....	29
2.3.1. Sequencing.....	29
2.3.2. Annealing.....	29
2.3.3. Mutagenesis	30
2.3.4. PCR.....	30

2.4. Molecular biology, enzymes and buffers	31
2.4.1. Restriction enzymes.....	31
2.4.2. Restriction enzymes buffers	31
2.4.3. Other enzymes	32
2.5. Organisms and strains	33
2.6. Antibodies	33
2.7. Chemicals list and provider.....	34
2.8. Culture media	37
2.8.1. Bacteria cultures	37
2.8.2. Yeast cultures	37
2.8.3. HEK293T cells media and buffers	38
2.9. Buffers and solutions.....	40
2.9.1. Molecular Biology	40
2.9.2. Cell-free expression system.....	41
2.9.2.1. <i>Buffers and stocks</i>	41
2.9.2.2. <i>Amino acids stocks</i>	42
2.9.2.3 <i>Bacterial extracts</i>	43
2.9.3. SDS-PAGE	43
2.9.4. Western blot.....	43
2.9.5. Radiolabeled substrate transport assay	44
2.9.6 Protoplasts solutions	44
2.9.7 Protein purifications	45
2.9.8. Liposomes buffers	45
2.10. Commercial kits.....	46
2.11. Consumables	47
2.12. Equipment.....	48
2.13. Software.....	51
2.13.1. Laboratory software.....	51
2.13.2 Online software.....	51
3. METHODS	53
3.1. Molecular biology	53
3.1.1. Restriction enzyme digestion.....	53
3.1.2. Polymerase Chain Reaction (PCR).....	53
3.1.3. Site-directed mutagenesis.....	55

3.1.4. DNA extraction from agarose gels	56
3.1.5. Introduction of DNA fragments into plasmids	56
3.1.6. Dephosphorylation of linear DNA	57
3.1.7. DNA ligation	57
3.1.8. <i>E. coli</i> transformation	58
3.1.9. <i>E. coli</i> plasmid extraction	58
3.1.9.1. DNA Minipreps and Maxipreps.....	58
3.1.9.2. Determining DNA concentrations	59
3.1.9.3. Ethanol precipitation of plasmid DNA.....	59
3.2. Methods for protein identification.....	59
3.2.1. Bradford protein quantification assay.....	59
3.2.2. BCA	60
3.2.3. TCA precipitation	61
3.2.4. SDS-PAGE	61
3.2.4.1. Coomassie staining.....	62
3.2.4.2. Western Blot	63
3.2.4.3. Ponceau Red staining	64
3.2.4.4. Observing the in-gel fluorescence	64
3.3. Methods for protein purification	65
3.3.1. Immobilized metallic anion chromatography.....	65
3.3.2. Streptavidin-purification.....	66
3.3.3. Ion Exchange chromatography	66
3.4. Production of proteins in <i>E. coli</i>	67
3.4.1. Culture conditions and induction.....	67
3.4.2. Cell lysis	67
3.4.2.1. Sonication:.....	67
3.4.2.2. French Press lysis.....	68
3.5. Protein production in yeast	69
3.5.1. Yeast transformation.....	69
3.5.2. Yeast culture cultures	69
3.5.3. Yeast glycerol stocks	70
3.5.4. Extraction of the microsomal fraction from <i>S. cerevisiae</i>	70
3.5.5. Intracellular yeast pH determination	71
3.5.6. Preparation of yeasts protoplasts	71
3.6. Radiolabeled substrate transport assay in yeasts.....	72

3.6.1. Uptake of radiolabeled substrate	72
3.6.1.1. Uptake assay.....	72
3.6.1.2 Calculating the intracellular substrate concentrations	73
3.6.1.3. Substrate uptake curves	75
3.6.2. Substrate efflux.....	75
3.6.3. IC ₅₀ measures.....	76
3.6.4. pH dependency of transport.....	76
3.7. Cell-free production of proteins.....	77
3.8. Protein production in human embryonic kidney cells.....	79
3.8.1. HEK 293 T-REx cell cultures conditions	79
3.8.2. Determination of HEK 293 T-REx cell culture density	80
3.8.3. Preparation of plasmids for HEK 293 T-REx production	80
3.8.4. HEK 293 T-REx cells transformation	81
3.8.5. Screening for genomic integration and protein expression	81
3.8.6. Storage of HEK 293 T-REx cells	82
3.8.7. HEK cells membrane protein extraction	82
3.9. Protein reconstitution in proteoliposomes	83
3.9.1. Lipid preparation	83
3.9.2. (Proteo)Liposome preparation	84
3.9.3. Extrusion.....	84
3.9.4. Pyranine loaded liposomes preparation	85
3.9.5. Stopped-flow measurement of substrate transport	86
3.9.5.1 Measurement of light scattering	87
3.9.5.2. Measures of fluorescence	87
3.9.6. Sucrose gradient-density centrifugation	88
4. RESULTS.....	89
4.1. Producing functional PffNT for structure determination.....	89
4.1.1. Membrane scaffold protein production and purification	89
4.1.2. Cell-free production of PffNT	93
4.1.3. Reconstitution of PffNT in proteoliposomes.....	96
4.1.4. Producing PffNT in human embryonic kidney cells.	104
4.1.4.1. Testing and validating the HEK 293 T-REx selection process.....	104
4.1.4.2. Establishing stable HEK 293 T-REx TM cell lines.....	108
4.2. Investigating potential proton antenna in PffNT	112
4.2.1. The PffNT C-terminus could be acting as a proton collecting antenna.....	112

4.2.2. Point mutations of The Tyr285 and Glu289	118
4.2.3. Deletion of the PfFNT C-terminal.....	120
4.3. Effects of proton antenna on the MCT1 transport	128
4.3.1. Effects of the MCT1 chaperones (BSG and EMB)	128
4.3.1.1. Intracellular pH of BSG-MCT1 expressing yeasts	128
4.3.1.2. pH-rate dependency of BSG-MCT1 transport.....	130
4.3.1.3. Expression of EMB-MCT1 fusion constructs.....	133
4.3.2 Investigating the role of carbonic anhydrase IV in MCT1 transport.....	135
4.3.2.1. Expression of carbonic anhydrase as a fusion protein.....	136
4.3.2.2. Yeast expressed Basigin - MCT1 and soluble CAIV.....	141
4.4. Investigating the influence of terminal tags on transporters functionality.....	160
4.4.1. Verifying the effect of terminal tags on MCT1 transport.....	160
4.4.2. Investigating the potential effect of the terminal tags on PfFNT transport.....	163
5. DISCUSSION	168
5.1. Contributing to the determination of PfFNT structures	168
5.1.1. Formation of PfFNT nanodiscs	168
5.1.2. Cell-free expression of PfFNT	168
5.1.2.1. Production of N-term Strep II tagged PfFNT.....	168
5.1.2.2. Production of C-term His-tagged PfFNT.....	170
5.1.3. PfFNT reconstitution in proteoliposomes.....	171
5.1.4. HEK cells expression.....	172
5.1.4.1. Expression and extraction of PfFNT mutants.....	172
5.1.4.2. Pertinence of the Metformin/AZD3965 selection	173
5.1.4.3. Antibodies non-specific interactions.	173
5.2. Investigating the PfFNT C-terminus	175
5.2.1. The role of Tyr285 and Glu289	175
5.2.2. Explaining the previous observations of termini deletion affecting capacity	175
5.2.3. C-terminal deletion increases transport capacity, but only in acidic pH	176
5.3. MCT1 proton antennas.....	178
5.3.1. Effects of the Basigin chaperone on transport.....	178
5.3.1.1. Intracellular pH of Basigin -MCT1 expressing yeasts.....	178
5.3.1.2. pH transport rate dependency of the Basigin – MCT1 fusion constructs.....	179
5.3.2. Effects of the Embigin chaperone on transport	180
5.3.3. Carbonic anhydrase	181
5.3.3.1. CAIV – Basigin - MCT1 fusion constructs	181

5.3.3.2. <i>Expression and purification of soluble CAIV</i>	181
5.4. Effects of terminal tags	182
5.4.1. His ₁₀ deletion appeared to increase MCT1 transport capacity	183
5.4.2. Effects of the terminal tags on PfFNT transport.....	184
5.4.2.1. <i>Alterations of the expression levels</i>	184
5.4.2.2. <i>Effect of the tags on transport.</i>	185
5.4.2.3. <i>PfFNT pH-rate dependency</i>	186
5.4.3. Pertinence of the radiolabeled substrate efflux assay	191
References	193
SUPPLEMENTARY MATERIALS	209
Supp. 1: DNA and protein sequences	209
Supp. 2: Plasmids maps	216
Supp. 3: Lamda DNA/PstI Marker	221
Supp. 4: preqGOLD Marker III (VWR).....	221
Supp. 5: Cell-free expression system: reaction chambers	222
Eidesstattliche Erklärung	XIII
Curriculum Vitae	XV
Acknowledgements	XVI

Abbreviations

%	percent
Δ	deletion
°C	Celcius
μCi	microCurie, 10 ⁻⁶ Ci
μg	micrograms, 10 ⁻⁶ g
μL	Microliters, 10 ⁻⁶ L
μm	Micrometers, 10 ⁻⁶ m
μM	micromol, 10 ⁻⁶ M, micromole per Liter
¹⁴ C	Carbone isotope
3'	3'-hydroxyl end of DNA
4ME 16:0 PC	1,2-diphytanoyl-sn-glycero-3-phosphocholine
5'	5'-phosphate end of DNA
A	Absorbance (spectroscopy)
A	Ampere
A	Alanine (Ala), amino acid
A, a	Adenine (nucleotide)
Å	Ångström, 10 ⁻¹⁰ m
AA	Amino acids (mix)
Acetyl-CoA	Acetyl coenzyme A
AcP	Acetyl phosphate
ADP	Adenosine diphosphate
Ady2	Yeast endogenous Acetate transporter
Amp	Ampicillin
AmpR	<i>E. coli</i> Ampicillin resistance protein
ApoA-1	human Apolipoprotein AI
APS	Ammonium persulfate
AQP	Aquaporin(s)
AQP9	human Aquaporin 9
Arg	Arginine (R), amino acid
Asn	Asparagine (N), amino acid
Asp	Aspartate, Aspartic acid (D), amino acid
ATP	Adenosine triphosphate
Atto488	Green-fluorescent dye, γ-(6-Aminoethyl)-adenosine-5'-triphosphate
AZD3965	<i>MCT1</i> inhibitor
BCA	Bicinchoninic acid
BH267. <i>meta</i>	4,4,5,5,5-Pentafluoro-3-hydroxy-1-(3-pyridyl)pent-2-en-1-one
BH296	4,4,5,5,5-Pentafluoro-3-hydroxy-1-(4-methoxyphenyl)pent-2-en 1-on
BL21 (DE3)	<i>E. coli</i> genotype
BLAST	Basic Local Alignment Search Tool
bp	Base pair (DNA length)
Brij 78	Polyoxyethylene (23) lauryl ether
BSA	Bovine Serum Albumin
BSG	human Basigin (CD147, EMMPRIN)

C, c	Cytosine (nucleotide)
CA	human carbonic anhydrase
CAIV	human Carbonic anhydrase 4
CAVA	human Carbonic anhydrase 5 isoform A
CD147	human Basigin (BSG, EMMPRIN)
CFDA-SE	5'(6')-carboxyfluorescein-diacetatesuccinimidyl-ester
cfu	Colony forming unit
CHS	Cholesterylhemisuccinate
Ci	Curie (measure of radioactivity)
cm	centimeters, 10 ⁻² m
cm ²	centimeters square, 10 ⁻² m ²
cpm	counts per minutes
C-term	carboxyl protein extremity
CTP	Cysteine triphosphate
D	dextrogyre
D	Aspartate, Aspartic acid (Asp), amino acid
Da	Dalton (Protein mass, 1 Da=1.66 ⁻²⁴ g)
dATP	Deoxyadenosine triphosphate
dCTP	Deoxycytidine triphosphate
ddH ₂ O	Doubly distilled water
DDM	Dodecyl-β-D-Maltoside
dGTP	Deoxyguanosine triphosphate
DH5α	<i>E. coli</i> genotype
DMEM	Dulbecco's Modified Eagle Media
DMSO	Dimethyl sulfoxide
DNA	Desoxyribonucleic acid
dNTP	Deoxy Nucleotide
DTT	Dithiothreitol
dTTP	Deoxythymidine triphosphate
DY647	red-fluorescent dye, DyLight 647 phosphoramidite
E	Glutamate, Glutamic acid (Glu), amino acid
E289Q	Glutamate 289 to glutamine mutant
<i>E. coli</i>	<i>Escherichia coli</i> (<i>Ec</i>)
<i>Ec</i>	<i>Escherichia coli</i> (<i>E. coli</i>)
ECL	Electrochemiluminescence
EDTA	Ethylenediaminetetraacetic acid
<i>e.g.</i>	<i>exempli gratia</i> , "for example"
EM	Electron microscopy
EMB	human Embigin (GP70)
EMMPRIN	human Basigin (BSG, CD147)
<i>et al.</i>	<i>et alii</i> . Latin: "and [the] others"
F	Phenylalanine (Phe), amino acid
F. Xa	Factor Xa
FBS	Fetal Bovin Serum
fL	femtoliters, 10 ⁻¹⁵ L

FNT	Formate Nitrite transporter
FocA	Formate channel
FT	Flow through
G	Glycine (Gly), amino acid
G, g	Guanidine (nucleotide)
g	grams (mass)
g	gravity (centrifugational strength)
G107S	Glycine 107 to Serine mutant
G21E	Glycine 21 to Glutamate mutant
GFP	Green Fluorescent protein
Gln	Glutamine(Q), amino acid
Glu	Glutamate, Glutamic acid (E)
GLUT1	human Glucose transporter 1
Gly	Glycine (G), amino acid
GP70	human Embigin (EMB)
GPI	Glycosylphosphatidylinositol or glycosphosphatidylinositol
GTP	Guanosine triphosphate
h	Hour, 60 min
H	Histidine (His), amino acid
H ⁺	Proton
H ₂ O	water
HABA	2-(4'-hydroxy-benzeneazo)benzoic acid
HA-tag	Hemagglutinin tag
HBSS	Hank's balanced salt solution
HCl	Hydrochloric acid
H-E	Buffer HEPES EDTA
HEK293T-REx	Human embryonic kidney cells (HEK)
HEPES	4-(2-hydroxyethyl)-1-piperazineethanesulfonic acid
His	Histidine (H), amino acid
His ₁₀	10×Histidines tag
His ₆	6×Histidines tag
His-tag	Histidine tag
<i>MCT</i>	human Monocarboxylate transporter
HRP	horseradish peroxidase
HT	human Hexokinase
I	Isoleucine (Ile), amino acid
<i>i.e.</i>	<i>id est</i> , "which is"
IB	Inclusion bodies
IC ₅₀	half-maximal inhibitory concentration
IEX	Ion Exchange Chromatography
Ig	Immunoglobulin-like (domain)
Ile	Isoleucine (I), amino acid
IMAC	Immobilized metal affinity chromatography
IPTG	Isopropyl β-D-1-thiogalactopyranoside
J	Joules

Jen1	Yeast endogenous Monocarboxylate transmembrane transporter
K	Lysin (Lys), amino acid
K38M	Lysine 38 to Methionine mutant
KAc	Potassium acetate
Kan	Kanamycin
KanR	<i>Bacillus subtilis</i> Kanamycin resistance protein
kDa	kiloDalton, 10^3 Da
kJ	kiloJoules, 10^3 J
KOH	Potassium hydroxide
L	Liter, 0.001 m^3
L	Leucine (Leu), amino acid
L	levogyre
Lac ⁻	Lactate anion
LacH	Lactic acid
LB	Lysogeny Broth (also called Luria-Bertani media)
LDH	Lactate dehydrogenase
Leu	Leucine (L), amino acid
Lys	Lysin (K), amino acid
M	Methionine (Met), amino acid
m	meters
M	mole per liter
MCS	Multiple cloning sites
MCT	Monocarboxylate transporter
MES	2-(N-morpholino)ethanesulfonic acid
Met	Methionine (M)
mg	milligrams, 10^{-3} g
min	minute, 60 s
mL	milliliters 10^{-3} L
mM	millimol, 10^{-3} M, millimole per liter
MMV007839	2-hydroxy-7-methoxy-2-(perfluoroethyl)chroman-4-one
MMV	Medicines for Malaria Venture
MOPS	3-(N-morpholino)propanesulfonic acid
MPC	Mitochondrial Pyruvate Carrier
ms	milliseconds (10^{-3} s)
MSP	Membrane Scaffold Protein
mV	millivolt 10^{-3} V
MWCO	Molecular Weight Cut-Off
myc	c-myc tag
N	Asparagine (Asn), amino acid
NAD ⁺	Nicotinamide Adenine Dinucleotide (oxidized)
NADH	Nicotinamide Adenine Dinucleotide (reduced)
NaOH	sodium hydroxide
ng	nanograms, 10^{-9} g
NirC	Nitrite transporter
nm	nanometers, 10^{-9} m

nmol	nanomoles, 10^{-9} mol, nanomole per Liter
NTA	nitrilotriacetic acid
N-term	amine protein extremity
NTP	Nucleoside triphosphate
OD	Optical Density
P	Proline (Pro), amino acid
p=	p value =
<i>P.</i>	<i>Plasmodium</i>
PAGE	Polyacrylamide gel electrophoresis
PBS	Phosphate Buffer Saline
PCR	Polymerase Chain reaction
PDB	Protein Data Bank
PEG	polyethylene glycol
PEP	Phosphoenolpyruvate
PfFNT	<i>Plasmodium falciparum</i> Formate Nitrite Transporter
<i>Pfu</i>	<i>Pyrococcus furiosus</i> (polymerase)
pH	potential of hydrogen (acidity)
Phe	Phenylalanine (F), amino acid
P_i	Phosphate ion
pI	Isoelectric point
pK _a	acid dissociation constant
PPP	parasite-induced permeation pathways
Pro	Proline (P), amino acid
psi	Pound per square inch (pressure, 1 psi = 6895 Pascal)
PV	Parasitophorous vacuole
PVDF	Polyvinylidendifluoride
Q	Glutamine (Gln), amino acid
R	Arginine (Arg), amino acid
RBC	Red blood cell / erythrocyte
rcf	Relative centrifugal force (centrifugational strength)
RCWMDE	Amino acid mix
RNA	Ribonucleic acid
rpm	rounds per minutes (relative centrifugational strength)
S	Serine (Ser), amino acid
s	seconds (Time)
S30	<i>E. coli</i> ribosomal extract (30 000 g)
SD	Synthetic defined (media)
SDS	sodium dodecyl sulphate
SEC	Size Exclusion Chromatography
SEM	Standard Error of the Mean
Ser	Serine (S), amino acid
SLC	Solute Carrier
Strep	Streptavidin
t=	Time=
T, t	Thymine (nucleotide)

T° annealing	Temperature of oligonucleotides annealing
T4	<i>E. coli</i> phage T4
T7	<i>E. coli</i> phage T7
TBS	Tris Buffer Saline
TBS-T	Tris buffer saline (pH=7.6) with 0.1 % Tween20®
TCA	Trichloroacetic acid
TE	Tris EDTA (buffer)
TEA	Tris, EDTA, Acetic acid (buffer)
TEMED	Tetramethylethylenediamine
Tet	Tetracyclin
Tm	(oligonucleotides) melting temperature
Tris	2-Amino-2-hydroxymethyl-propane-1,3-diol
tRNA	Transfer RNA
Trp	Tryptophan (W), amino acid
Tyr	Tyrosine (Y), amino acid
u	unit (enzymes)
UTP	Uridine triphosphate
V	Volt
v/v	volume per volume
V196L	Valine 196 to Leucine mutant
Val	Valine (V)
W	Tryptophane (Trp), amino acid
W	Watt
w/v	weight per volume
W303-1A	<i>Saccharomyces cerevisiae</i> genotype
WHO	World Health Organization
WT	Wild-Type
Y	Tyrosine (Tyr), amino acid
Y281F	Tyrosine 281 to Phenylalanine mutant
YPD	Yeast extract peptone dextrose (media)
λ_{em}	emission wavelength (Spectroscopy)
λ_{ex}	excitation wavelength (Spectroscopy)

ABSTRACT

Some cells rely intensively on the coupled activity of glycolysis and lactate dehydrogenase to constantly generate ATP. This process releases lactate and protons, the accumulation of which would become detrimental to the cell's survival. Therefore, the removal of these metabolites is critical to maintain the cells energy generation. This is ensured by monocarboxylate transporters (MCT), such as the human MCT and the *Plasmodium falciparum* formate nitrite transporter (PfFNT).

In the case of human MCT, it has been established that their transport activity was modulated by partner proteins: its chaperone Basigin and carbonic anhydrases enzymes. The surface of such proteins act as proton and substrate collecting antennas, generating microenvironments of greater substrate concentration close to the transport sites. This work set out to investigate how such antennas were involved in the modulation of the monocarboxylate transport functionality of MCT1 and PfFNT.

Initial attempts of expressing fusion constructs of carbonic anhydrase, Basigin chaperone and MCT1 transporter proved unsuccessful. Then, alternative methods of protein production were explored to observe interaction between the transporter and the proton antenna. Moreover, this work identified that C-terminal poly-Histidine tag initially intended for protein purification and identification would affect the transport capacity of such MCT1 transporter.

This work also hypothesized that the PfFNT C-terminal helix, highly conserved among all human-infecting *Plasmodia*, plays the role of an endogenous proton collecting antenna facilitating the proton/lactate cotransport. Experimental results suggested that this terminus does modulate the substrate transport (radiolabeled lactate influx capacity was increased in acidic extracellular pH upon its deletion), but it remains to be determined whenever this collecting antenna increases the local concentration of protons or lactate.

ZUSAMMENFASSUNG

Einige Zellen sind intensiv auf die gekoppelte Aktivität von Glykolyse und Laktatdehydrogenase angewiesen, um ständig ATP zu erzeugen. Bei diesem Prozess werden Laktat und Protonen freigesetzt, deren Anhäufung für das Überleben der Zelle schädlich wäre. Daher ist die Beseitigung dieser Stoffwechselprodukte entscheidend für die Aufrechterhaltung der Energieerzeugung der Zelle. Dies wird durch Monocarboxylat-Transporter (MCT) wie den menschlichen MCT und den Formiat-Nitrit-Transporter (FNT) von *Plasmodium falciparum* gewährleistet.

Im Falle der menschlichen MCT wurde festgestellt, dass ihre Transportaktivität durch Partnerproteine moduliert wird: das Chaperon Basigin und die Enzyme der Kohlensäureanhydrasen. Die Oberfläche dieser Proteine fungiert als Protonen- und Substratsammelantennen, die in der Nähe der Transportstellen Mikroumgebungen mit hoher Substratkonzentration erzeugen. In dieser Arbeit sollte untersucht werden, wie solche Antennen an der Modulation der Monocarboxylat-Transportfunktion von MCT1 und PfFNT beteiligt sind.

Als erste Versuche, Fusionskonstrukte von Kohlensäureanhydrase, Basigin-Chaperon und MCT1-Transporter zu exprimieren, nicht erfolgreich waren, wurden alternative Methoden der Proteinproduktion erforscht, um die Interaktion zwischen dem Transporter und der Protonenantenne zu beobachten. Darüber hinaus wurde festgestellt, dass ein terminaler Poly-Histidine-Tag die Transportkapazität eines solchen MCT1-Transporters beeinträchtigt.

In dieser Arbeit wurde auch die Hypothese aufgestellt, dass die C-terminale Helix von PfFNT, die bei allen menschlichen Plasmodien hoch konserviert ist, die Rolle einer endogenen protonensammelnden Antenne spielen könnte, die den Protonen-/Laktat-Cotransport erleichtert. Die experimentellen Ergebnisse deuten darauf hin, dass dieser Terminus den Substrattransport moduliert (die Kapazität des radioaktiv markierten Laktateinstroms wurde bei saurem extrazellulärem pH-Wert nach seiner Deletion erhöht), aber es bleibt zu klären, wann diese Sammelantenne die lokale Konzentration von Protonen oder Laktat erhöht.

Translated from English with www.DeepL.com/Translator (free version)

1. INTRODUCTION

Cells are the fundamental units of life as we know it. Delimited by lipid membranes isolating an intracellular cytosol, the cells must expend a significant amount of work and energy to maintain their homeostasis, metabolism and functions.

Many cells break down glucose through a process known as glycolysis (1.1.) to generate such energy. The uptake of glucose and the export of the metabolic products rely on transporters, *i.e.* membrane proteins facilitating the passage of such molecules and products through the cell membrane.

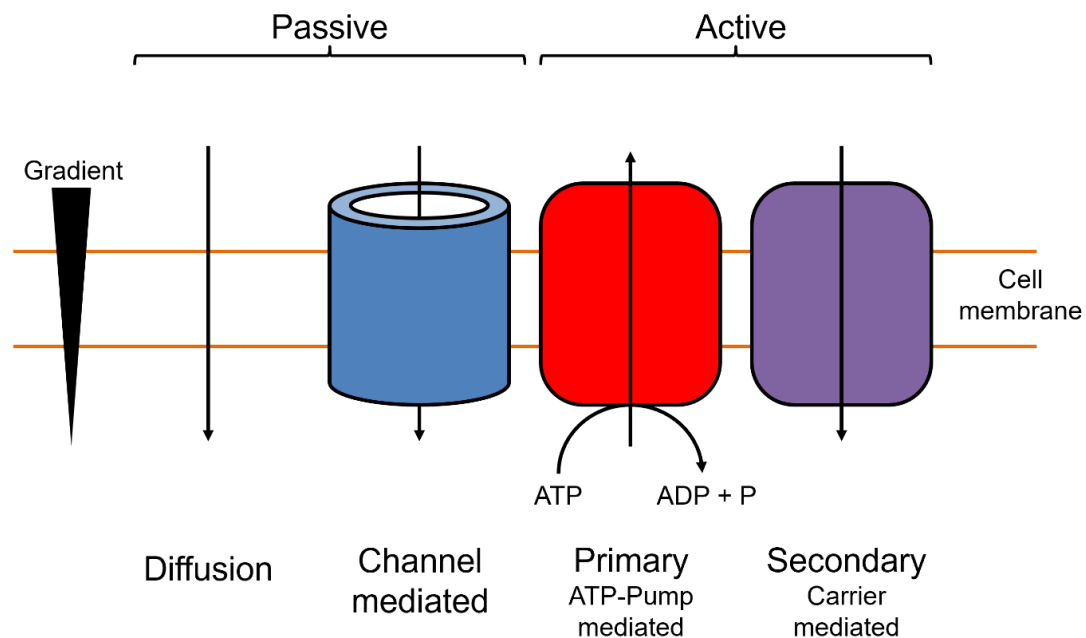


Figure 1. 1: Schematic representation of the type of transports through membranes.

1.1. Glycolysis produces lactate and proton

Also referred to as the Embden-Meyerhof-Parnas pathway, the glycolysis is the first (and sometimes last) step of the energy generation in cells. It occurs in the cytosol [1].

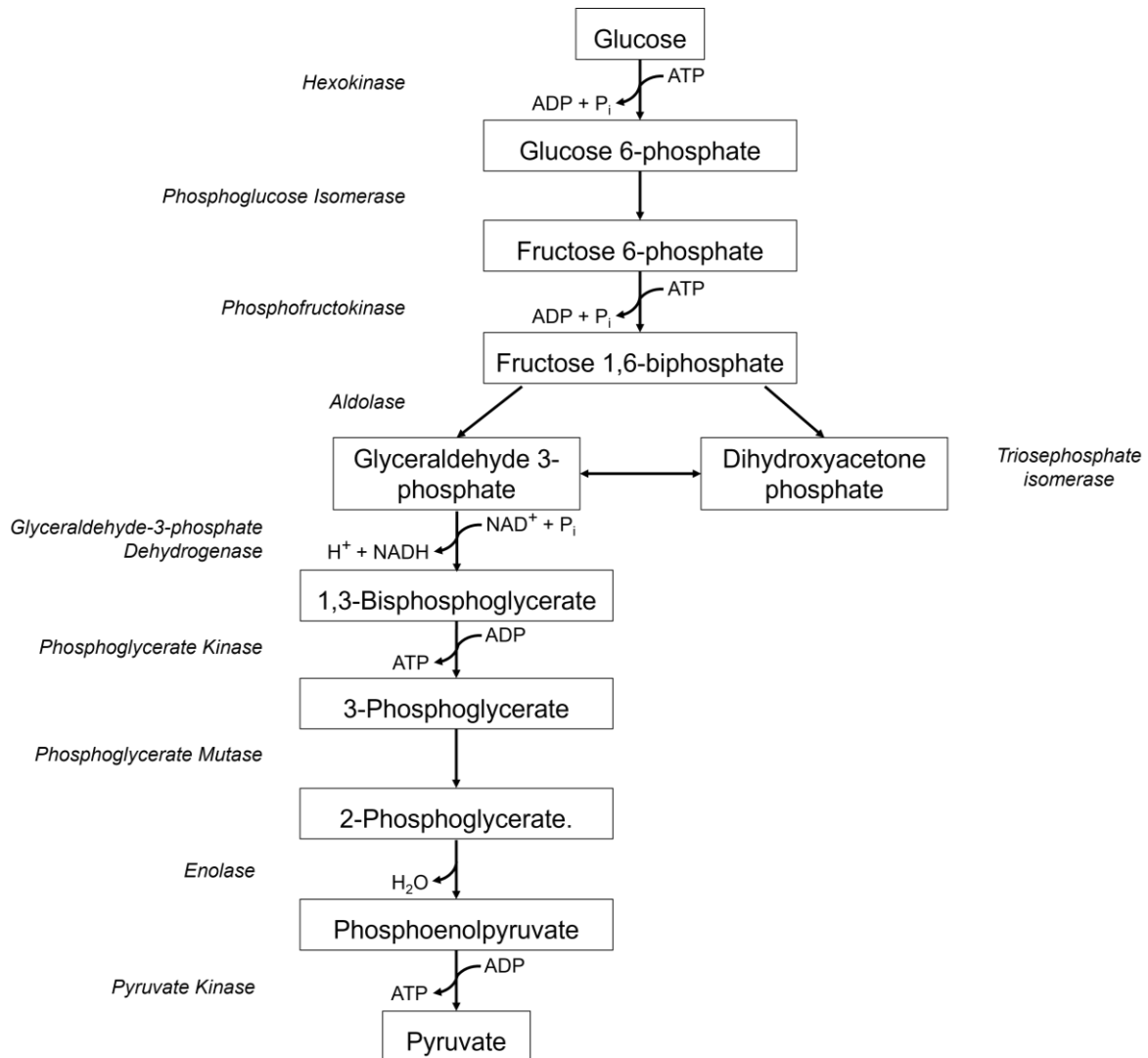
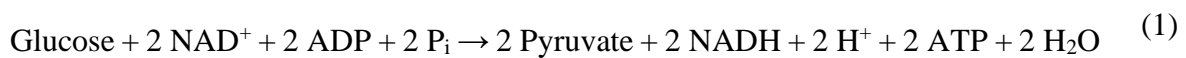


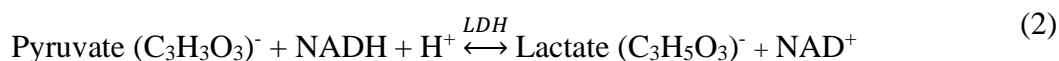
Figure 1. 2: Schematic representation of the glycolysis process.

The net product of glycolysis may be summarized as such [2]:

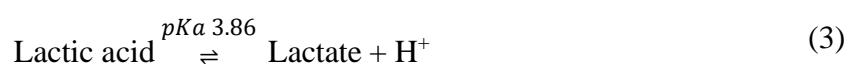


Glycolysis involves a great number of enzymatic steps, detailed in Figure 1.2. Briefly, at the price of an initial investment of two ATP to phosphorylate intermediate products, it ends up generating four ATP from ADP + P_i. Two protons are released as byproducts of the glycerhaldehyde-3-phosphate dehydrogenase activity.

Glycolysis uses the reduction of NAD⁺ to NADH to generate its 2 ATP payoff and pyruvate. NADH can be re-oxidized by the Lactate dehydrogenases (LDH) activity, reducing the produced pyruvate into lactate, oxidizing NADH in NAD⁺ on the way [3]. The LDH activity catalyzes the following reaction [2]:



This reaction is reversible (equation 2) but favors pyruvate as substrate and lactate as product [4]–[6]. However, if the cellular concentration of lactate were to become significantly greater, the LDH activity would occur in reverse, regenerating pyruvate from lactate. This would hamper the recycling of the NADH into NAD⁺ and in time, this concentration of lactate inhibits glycolysis. In order to maintain glycolytic flow to generate ATP, cells need to export the excess lactate. With a pK_a of 3.86, most of the lactate remains in its anionic form in physiological conditions.

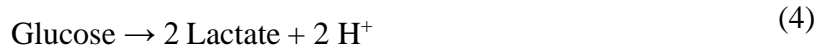


Of the two different enantiomers that can be produced by glycolysis and LDH activity, the L-lactate form is majorly represented compared to the D-lactate [7]–[9]. Further mentions of lactate will refer to the L-lactate enantiomer.

In oxidative cells (that express all the required enzymes) the products of glycolysis are transported to the mitochondria, where pyruvate dehydrogenases turn pyruvate into acetyl-CoA, used to fuel the Krebs cycle (also called tricarboxylic or citric acid cycle). This cycle drives a series of oxidations in the mitochondrial respiratory chain, which generates a steep proton gradient between the mitochondria lumen and intramembranous space. ATP synthases use this gradient as mechanical energy for the phosphorylation ADP into ATP. The combined glycolysis and oxidative phosphorylation would generate a total of 38 ATP from a single glucose molecule. It is a highly efficient process that is favored in most cells [3], [10]. In humans, part of the lactate released in the bloodstream is converted into oxaloacetate, which is used in liver cells where neoglucogenesis converts it back to glucose [11]. This process was coined the Cori cycle [12]. However, the cells that do not have access to oxygen (or do not express key enzymes) only rely on the glycolysis to generate their ATP.

The origin of the protons generated during this lactate production by the glycolysis is the subject of a controversy. Physiologists argue that the proton generation observed during glycolysis (in the context of skeletal muscle exercise-induced acidosis) is not directly caused by lactate production, as the LDH conversion of pyruvate to lactate removes protons from the cytosol.

Instead, they propose that the release of protons comes from the ATPase hydrolysis of the produced ATP caused by the cell's reliance on glycolysis [2]. In any case, the consensus is to summarize the net product of the conjoined glycolysis and LDH activity as the following equation:



In the context of this work, the pathways that should be considered are the coupled activity of glycolysis and LDH. For glycolytic cells, the transport of lactate (and protons) is critical to maintain the LDH activity, NAD^+ to NADH oxidation, and maintaining the glycolytic flux.

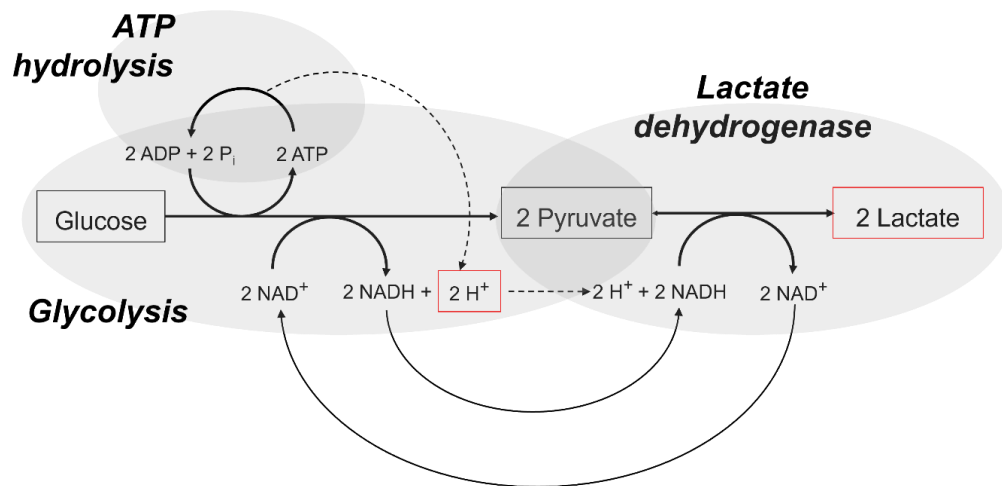


Figure 1. 3: Simplified schematic representation of the glycolysis of Glucose leading to the generation of energy, Lactate and protons as metabolic final products.

Historically, lactate was considered only as byproduct of the hypoxic glycolysis, the accumulation of which may become detrimental to the cell. In more recent studies however, have identified lactate as a critical metabolic product and signaling molecule [4], [7], [8], [13]. In either case, the trafficking of this weak acid is required for maintaining the cells activity.

The present work focuses on two distinct proteins: the *Plasmodium falciparum* formate nitrite transporter (PfFNT) and the human monocarboxylate transporter 1 (MCT1). As an interesting example of convergent evolution, these two proteins share little to no structural similarities, yet serve the same function. Both proteins are facilitating the proton-mediated transport of monocarboxylates through the cell membranes, albeit using different mechanisms.

1.2. *Plasmodium falciparum* FNT

1.2.1. Malaria

Plasmodia are the parasites responsible for malaria, one of the three most prevalent infectious diseases in humans [14]. In 2021, the WHO estimated the number of malaria cases to be 257 million (between 224 and 276), with a death toll of 619 000 (between 577 000 and 754 000) [15]. Children under 5 years old represent the majority of these deaths [16]. Estimations suggest that this disease alone is responsible for 2 to 5 % of the deaths across the planet during the 20th century [17]. Malaria plagues the developing countries, with Sub-Saharan Africa bearing the brunt of the infection.

Of the five subspecies that affect humans (*P. falciparum*, *P. vivax*, *P. malariae*, *P. ovale* and *P. knowlesi*), most infections are caused by *P. vivax* (most prevalent outside Africa) and *P. falciparum*. This latter specie is the most virulent.

Despite colossal efforts and initial major gains, the fight against malaria progresses slower than anticipated, and may even be stalling [18]. On a pharmaceutical level, the parasite's resistance to the established antibiotics is on the rise [19], [20], which stresses the need to widen our therapeutic arsenal with new drugs.

1.2.2. *Plasmodium* lifecycle

Plasmodia are protozoan, *i.e.* unicellular parasites. Their primary host and transmission vectors is the female *Anopheles* mosquitoes. The sexually differentiated parasites (gametocytes) are ingested by mosquitoes feeding on infected patients. In the guts of the mosquito, oocytes issued from sexual reproduction ruptures into sporozoites. These are then injected in a new host *via* the mosquito saliva during feeding. The sporozoites infect hepatic cells, where they undergo asexual reproduction. There, they turn into schizonts (*i.e.* multinuclear cells) that splits into daughter cells. At this stage, plasmodia of the *P. ovale* and *P. vivax* species are capable to form hypnozoites, *i.e.* dormant cells that can remain sleeping for weeks to years before triggering a new wave of infection [21]. After about a month, the rupture of the schizonts releases

merozoites that infect the erythrocytes (*i.e.* red blood cells), recognizing the extracellular domains of the Basigin membrane proteins to invade red blood cells [22].

During this erythrocytic phase, the parasite undergoes further asexual reproduction with cycles of schizonts releasing more merozoites, infecting more erythrocytes. Ultimately, the parasite differentiate into sexuated gametocytes, ready to be ingested by the mosquito and begin the cycle anew.

Blood stage plasmodia are responsible for the symptoms of malaria. Infected erythrocytes membranes will contain cytoadhering proteins expressed by the parasite. It forces the cell to adhere to the host blood vessels endothelium [23]. The resulting agglutination leads to microvascular occlusion, metabolic dysregulation and acidosis, triggering symptoms such as acute respiratory distress syndrome, renal insufficiency and acidosis, triggering symptoms such as acute respiratory distress syndrome, renal insufficiency and cerebral malaria [21]. The parasites feeding on the red blood cell hemoglobin may also lead to anemia, or exacerbate already present iron deficiency [24].

1.2.3. *Plasmodium* glycolytic pathway

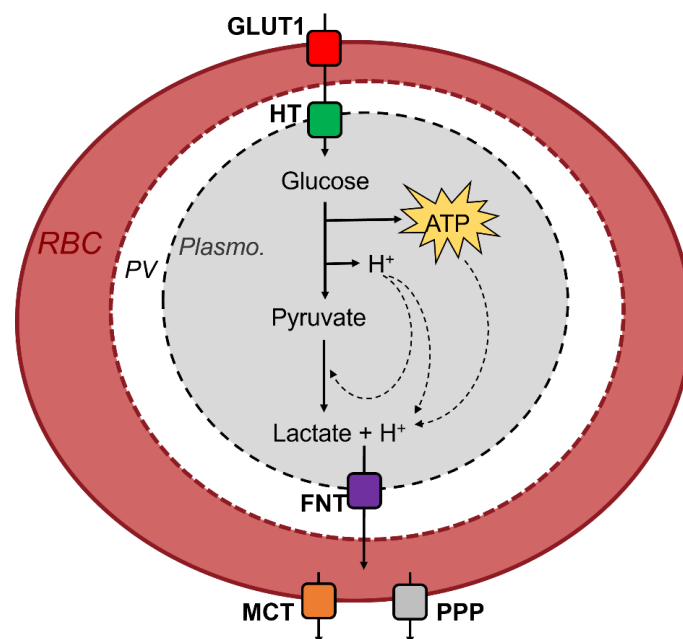


Figure 1. 4: Schematic representation of the generation and transport of lactate and protons during glycolysis in *Plasmodium* in its erythrocyte phase. Adapted from Nerlich *et al.* [25]. The Red Blood Cell (RBC) is represented infected by a *Plasmodium* parasite (*Plasmo.*), inside its parasitophorous vacuole (PV).

In *Plasmodium* infected erythrocytes, D-glucose is taken up via the glucose transporter GLUT1 [26], [27]. Nutrient permeable channels ensure that it can diffuse into the parasitophorous vacuole [28], [29], where it is transported by the *Plasmodium* hexose transporter, HT [30]–[32] (Figure 1.4). In the parasite cytosol, each molecule of glucose is metabolized into two molecules of pyruvate by the glycolysis, which generates two ATP molecules and two protons. Pyruvates are then turned into two molecules of lactate through the activity of the lactate dehydrogenase. (Figure 1.3, Equation 4).

The single mitochondrion of the *Plasmodium* is capable of expressing all the enzyme required for the Krebs cycle and respiratory chain [33]. However, the pyruvate dehydrogenase enzyme turning pyruvate in acetyl-CoA is expressed in a separate organelle, *i.e.* the apicoplast, where it appears involved with fatty acid synthesis [34], [35]. During the human blood stages, the parasite can dispense with the Krebs cycle activity. It only needs it in the mosquito, after the formation of gametes [36]. In these conditions, the parasite is using its mitochondria pathways for the biosynthesis of other metabolites [37], [38] or uses glutamine as its Krebs cycle carbon source [36]. At this stages, the parasite's generation of energy using glucose is through glycolysis alone [39]–[41].

Since the generation of pyruvate from glucose is isolated from the oxidative phosphorylation pathways in *Plasmodium*, the accumulating lactate produced by glycolysis and LDH activity (Figure 1.2.) can be considered a metabolic waste that needs to be discarded for the parasite energy mechanism to continue [42]. Lactate and protons are transported out of the parasite cytosol by the FNT, then diffuse from the parasitophorous vacuole to the red blood cell cytosol [28], [29]. There, they are exported in the plasma by endogenous transporter (*e.g.* MCT) and parasite-induced permeation pathways (PPP) [43], leading to a sharp increase in the patient lactate blood concentration from around 0.3-1.3 mM [3] to about 5 mM [44].

1.2.4. PfFNT structure and transport mechanism

It was observed that not only did *Plasmodium* infected erythrocytes consume much more glucose and displayed higher glycolytic activity than their healthy counterparts [27], [45], [46], they also displayed a lactate/proton cotransport that suggested a 1:1 stoichiometry [47]–[49]. Later, the protein responsible for this transport was identified to be the formate nitrite

transporter (FNT) [50], [51]. The structure of such protein has recently been solved at high resolution using cryo-electron microscopy (PDB#6QQV [52] and PDB#7E26 [53]).

The FNT of *P. falciparum* shows up to 84 % of protein sequence identity with the proteins from the other plasmodia [54]. Moreover, this plasmodial transporter show a high sequence identity (about 40%) with bacterial FNT, *e.g.* *E. coli* FocA and NirC [51], [55]. The members of the FNT family form homopentamers. The structure of their protomers mimic almost perfectly that of the aquaporins (AQP) [56] *i.e.* channel-mediated passive transporters. Despite their channel-like appearance, each FNT protomer acts as a bidirectional [56], [57] secondary-active transporter (Figure 1.1.) for monocarboxylates such as lactate, but also, formate or acetate [58], using protons as cotransport substrate.

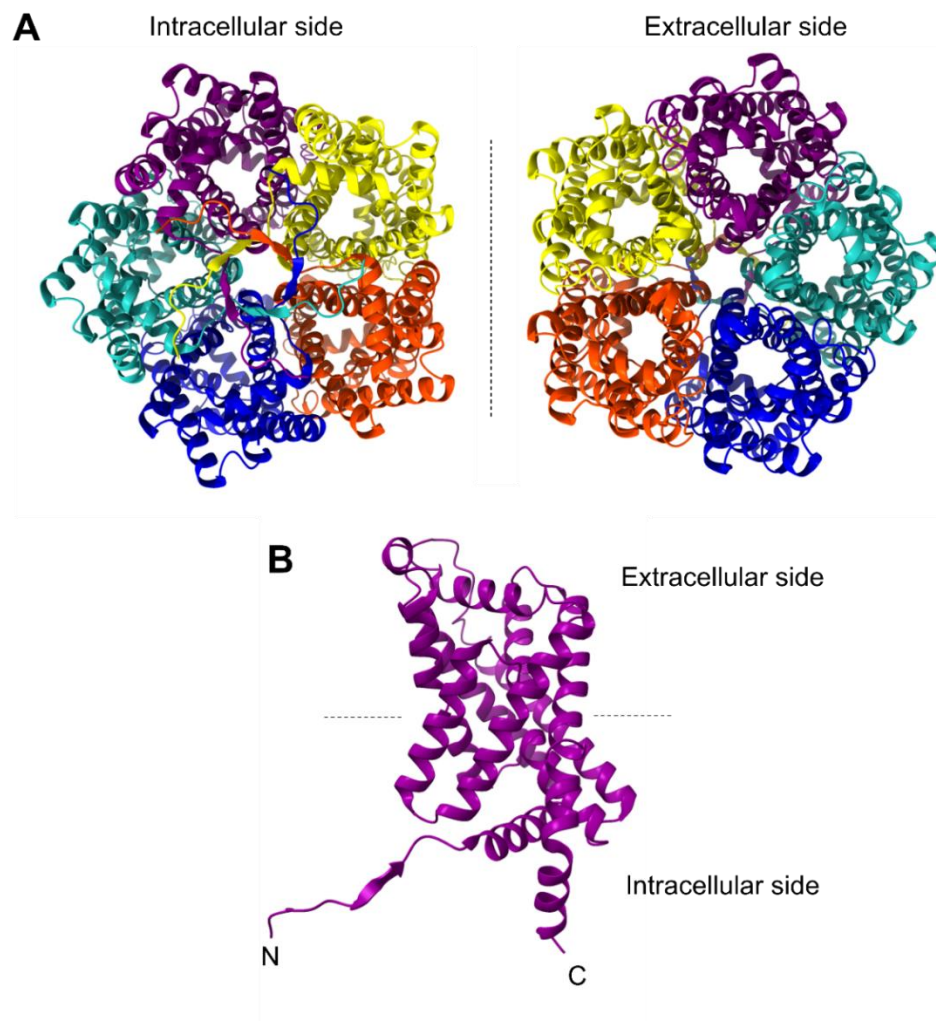


Figure 1. 5: Structure of the PfFNT pentamer (A), oriented facing the intracellular or extracellular side, and monomer (B). PfFNT monomer, with N and C-termini are labeled as such. Adapted from PDB#7E26 [53] using ChimeraX 1.5.

Their structure consists of six transmembrane helices around a symmetrical narrow transport path, composed of two hydrophobic constrictions isolating a highly conserved central histidine residue from wider vestibules at both proteins entrances [52], [53], [56], [59], [60]. These constrictions exclude the passage of charged compounds at physiological pH [58], [61] but allow for the passage of the protonated monocarboxylic acids.

Positive amino-acid clusters on the external protein surface steer the weak acid anion by charge attraction into the increasingly hydrophobic environment of the protein vestibules. As a consequence, at a certain point along the pathway, the decreasing permittivity of the dielectric environment decreases the acidity of the substrate, leading to substrate protonation from the bulk and allowing the neutralized weak acid to cross the constrictions [55], [60]. This transport mechanism has been termed the “dielectric slide” [59].

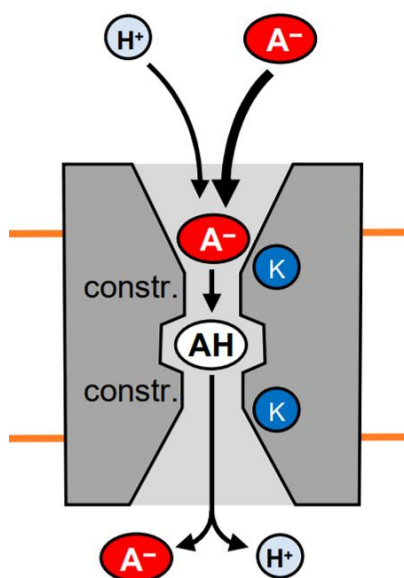


Figure 1. 6: Schematic representation of the PfFNT (grey) monocarboxylic acids (red) and proton (light blue) cotransport across the membrane. Lysines responsible for substrate binding are represented in blue. Adapted from Epalle and Beitz. [62].

1.2.5. Therapeutic target

As the *Plasmodium* lactate/proton cotransporter is so dissimilar to the human endogenous monocarboxylate transporters, it represents an interesting therapeutic target. Specific inhibitors could block the lactate efflux in the parasite, while sparing the activity of the human host MCTs.

Screening compounds of the Malaria Box [63] using two different expression systems (*Saccharomyces cerevisiae* [64] and *Xenopus laevis* oocytes [65]) identified that PfFNT transport was inhibited by MMV007839, which served as a good lead structure for drug design.

The development of the BH296 and BH267.*meta* from the MMV007839 precursor [25], [54], [64], [66], [67] has been reviewed in Nerlich *et al.* [25].

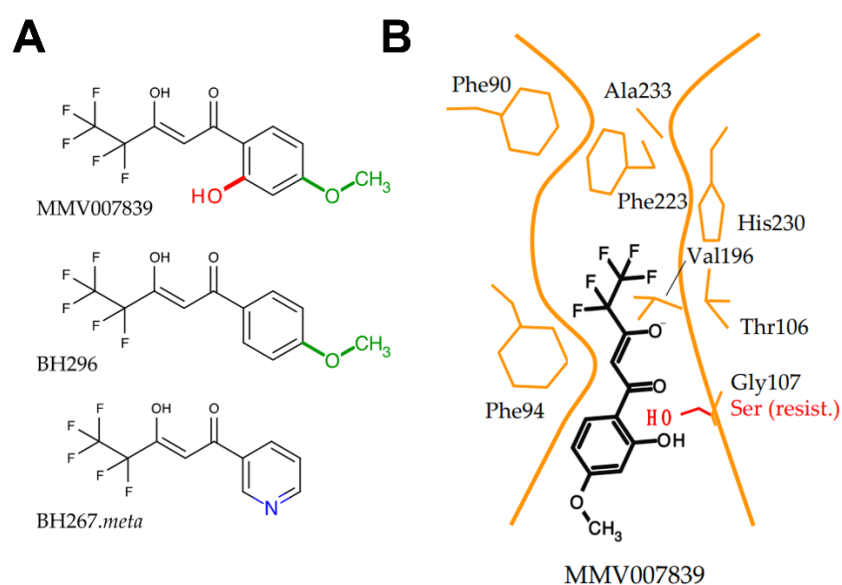


Figure 1. 7: (A) Chemical structure of the MMV007839 PfFNT inhibitors and its derivatives. (B) Model of the binding mode of MMV007839 to PfFNT intracellular vestibule and constriction region. Adapted from Nerlich *et al.* [25].

Growing *Plasmodium falciparum* infected erythrocytes in sublethal concentrations of the MMV007839 lead to the apparition of the following resistance mutations: Gly21 to Glu (G21E), Val196 to Leu (V196L) and most importantly Gly107 to Ser (G107S) (Figure 1.7) [64].

While the wild type PfFNT had been resolved in complex with the MMV007839 (PDB#6VQR [52] and PDB#7E27 [53]), observing the true interaction between the resistance mutants and the inhibitors would provide a better insight into the binding mechanism.

1.3. Human MCT1

1.3.1. The MCT family

The monocarboxylate transporters (MCT) are part of the solute carrier 16 protein family (SLC16) [68], [69]. Of the fourteen different MCTs, MCT1 to 4 (SLC16a 1, 7, 8 and 3 respectively [70]) have been characterized as proton-coupled monocarboxylate secondary active transporters [68]. They are involved with the transport and trafficking of endogenous metabolites such as lactate and pyruvate,

Table 1. 1: Literature reports of the lactate/proton transport affinity of MCT, measured at physiological pH

MCT	Influx	Efflux
Rat or hamster MCT1	3.5 ± 0.5 mM [71] 7.7 ± 0.5 mM [72] ~ 8.3 mM [73]	~ 6.4 mM [71]
Rat MCT2	0.74 ± 0.07 mM [74]	
<i>Gallus gallus</i> MCT3		5.8 mM [75]
Rat MCT4		17 ± 3 or 34 ± 5 mM [76] 28 mM [77]

The MCT 1 to 4 isoforms facilitate both the influx and the efflux of monocarboxylates [70], [78]. However, while MCT1 operates equally well in both directions [71], [78], MCT4 (and MCT3) favorize efflux [75], [76] and MCT2 influx [74].

In humans, MCT1 is almost ubiquitously expressed. The high affinity MCT2 is found expressed in the kidney, liver cells, in neurons and other cells that requires fast uptake. MCT3 is uniquely expressed in the retina. MCT4 is expressed in the skeletal muscle, tumor cells and other highly glycolytic cells [70], [78], [79].

1.3.2. MCT lactate transport in human cells

Usually in aerobic conditions, human cells rely on glycolysis followed by oxidative phosphorylation to generate their ATP, as described previously (1.1.). Under anaerobic conditions, when the oxygen is lacking, the coupled activities of glycolysis and LDH become the only energy source of the cells, generating lactate and protons (Equation 4, Figure 1.3.).

However, in some cases, cells remain glycolytic despite having access to oxygen.

Feeding the brain with glucose and oxygen is critical to maintain neural activity. There, a type of glial cells, the astrocytes, perform an aerobic glycolysis, despite having access to oxygen and active mitochondria [80], [81]. Pellerin *et al.* [82] propose that the astrocytes release lactate (presumably using MCT1 and MCT4) for the neurons to absorb (using MCT2) and convert to pyruvate. This would be feeding the neurons Krebs cycle and oxidative phosphorylation, in addition to performing their own glycolysis [83], [84]. Despite some debate around this mechanism of a astrocyte-neuron lactate shuttle [85], there exists a wealth of experimental and physiological evidence of these cells exchanging lactate through their monocarboxylate transporters [86], [87].

A similar partnership between glycolytic and oxidative cells can also be observed in cancer, albeit with more sinister implications. Tumors contain oxygenated and hypoxic regions. Cancer cells situated in the later switch their metabolism to be fueled by glycolysis [88]. It has also been observed that aerobic cancer cells also remained glycolytic, an effect that was termed the “Warburg effect” [89], [90]. These cells generate high concentrations of lactate, which is exported to the bloodstream via MCT1 and MCT4, contributing to an acidification of the tumor domain, which in turn promotes angiogenesis and evasion from the immune system [91]–[93]. Moreover, oxidative cancer cells are capable to feed their Krebs cycle with the excess lactate they recover from the bloodstream using MCT1 or MCT2 [94], [95] in a process termed the “reverse Warburg effect” [96], [97].

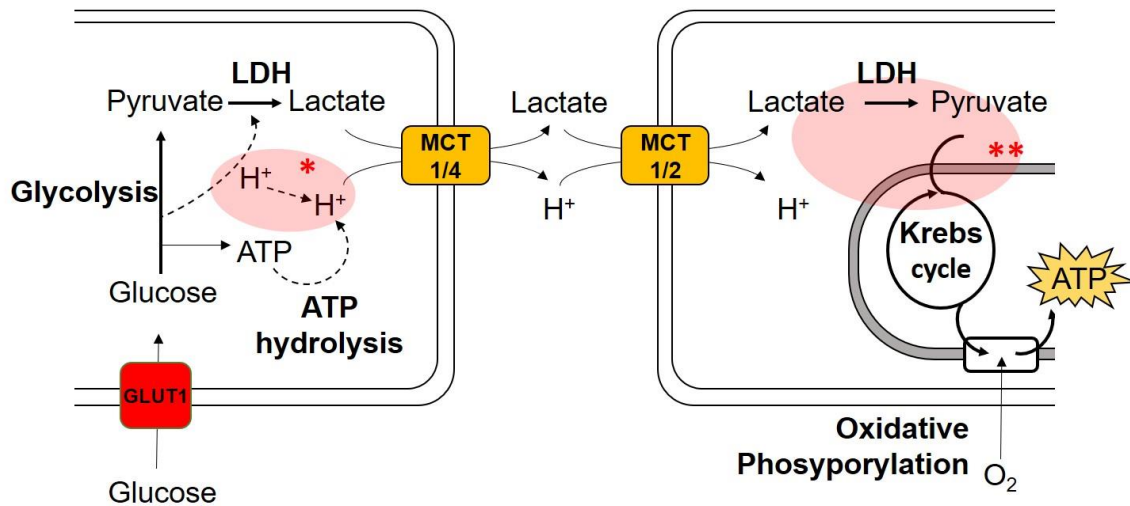


Figure 1. 8: Schematic representation of the lactate shuttle through MCTs mediating a cooperation between glycolytic (left) and oxidative (right) cells. The true source of the protons generated during the glycolysis process (*) [2] and the transfer mechanism of lactate to feed the mitochondrial Krebs cycle (intracellular lactate shuttle **) [98] are subject to controversies.

What becomes of the lactate in the oxidative cell cytosol is the subject to debate (Figure 1.8 **). Some studies argue that lactate is directly transported in the mitochondria by MCT1 (in skeletal muscle cells and cancer cells cultures) where it is then converted into pyruvate by LDH [98]–[101]. Some argue against the feasibility of this process, as the oxidation of lactate to pyruvate would be energetically unfavorable in the mitochondrial matrix and the redox conditions unsuitable [70]. Other reports state that the observation of MCT1 and LDH in mitochondria are due to experimental biases [102]. In either case, the pyruvate generated in the cell cytosol can be transported to the mitochondria *via* pyruvate carriers (MPC) [70].

Considering these findings, MCT1, 2 and 4 trafficking of lactate across the cells appear a critical component of the energy metabolism.

1.3.3. Structure and mechanism of MCT1

Initial models of MCT1 structures were based on the homologous *Syntrophobacter fumaroxidans* MCT structure (PDB#6HCL [103]). More recently, the cryo-EM structure of MCT1 was resolved as a complex with the chaperone Basigin in the presence of lactate (PDB#6LZ0 [104]).

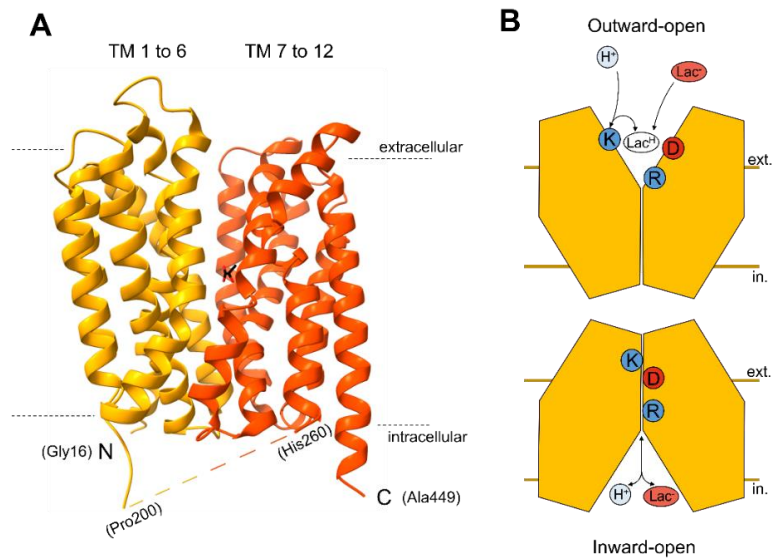


Figure 1. 9: (A) Structure of the MCT1 (PDB#6LZ0 [104]) in complex with lactate. The N and C terminal ends of the resolved structure were labeled as such. (B) Mechanism of the alternative access transport of lactate and proton by alternation between an outward open (up) and inward open (down) conformations. Lys38, Asp309 and Arg313 are represented by K, D and R respectively.

MCT1 is composed of twelve transmembrane α -helices (TM), arranged in N - terminal and C - terminal 6-helix bundles, connected together by the flexible Pro200-His260 sequence. The first 15, last 51 and intermediary 60 amino acids positions were not resolved, as they composed flexible and disorganized regions. The resolved structure of MCT1 is displayed in Figure 1.9 A.

The model of monocarboxylate transport through MCT is presented as follows [103], [105] and described in Figure 1.9 B. The substrate anion is attracted in the outward-open transport site by the positive charge of the lysine 38 and the neutralized by a proton donated by the same residue. A proton is then transferred from the monocarboxylic acid to aspartate 309, thus breaking the hydrogen bonding between the aspartate carboxyl and the arginine 313 amine groups, triggering a shift of the protein toward an inward-open conformation. The monocarboxylate and the Asp309-bound proton are released in the cell cytosol, the protein recovers its outward-open conformation and Lys38 is protonated again.

1.3.4. Partner proteins

It has been well documented that MCTs are expressed and localized in the cell membrane in complex with the Basigin or Embigin chaperones [104], [106], [107]. Basigin (also called CD174, EMMPRIN, or BSG) and Embigin (also called GP70 or EMB) are members of the immunoglobulin superfamily [108], [109]. They are composed of a C-terminal transmembrane α -helix, followed by two extracellular Ig-like N-terminal domains: IgI and Ig C2 for Basigin or Ig V1 and Ig V2 for Embigin. MCT1 and MCT4 preferentially associate with Basigin [106], [110], [111] and MCT2 with Embigin [107], [112].

Structural evidence [104] confirmed experimental data [113] suggesting the Basigin most common isoform, variant 2, was bound to the MCT through its Glu218. Moreover, Wang *et al.* [104] identified that the Basigin Glu218 interacts with the Asn187 of the MCT1 transmembrane helix 6, contrarily to the Asn86 that was previously hypothesized. This Asn187 is conserved among MCT1,2 and 4, while the Embigin chaperone carries an equivalent to Glu218 [104]. Mutation of this Glu to Arg in a Basigin – MCT1 fusion construct expressed in yeasts led to a loss of transport functionality [114].

Moreover, Köpnick *et al.* [114] demonstrated that two amino acid patches situated in the Basigin IgI domain were responsible for an increase of the MCT1 transport capacity. These charged patches lead to the local accumulation of the monocarboxylate substrate, as well as acting as proton collecting antenna [62], [114], [115], (Figure 1.10).

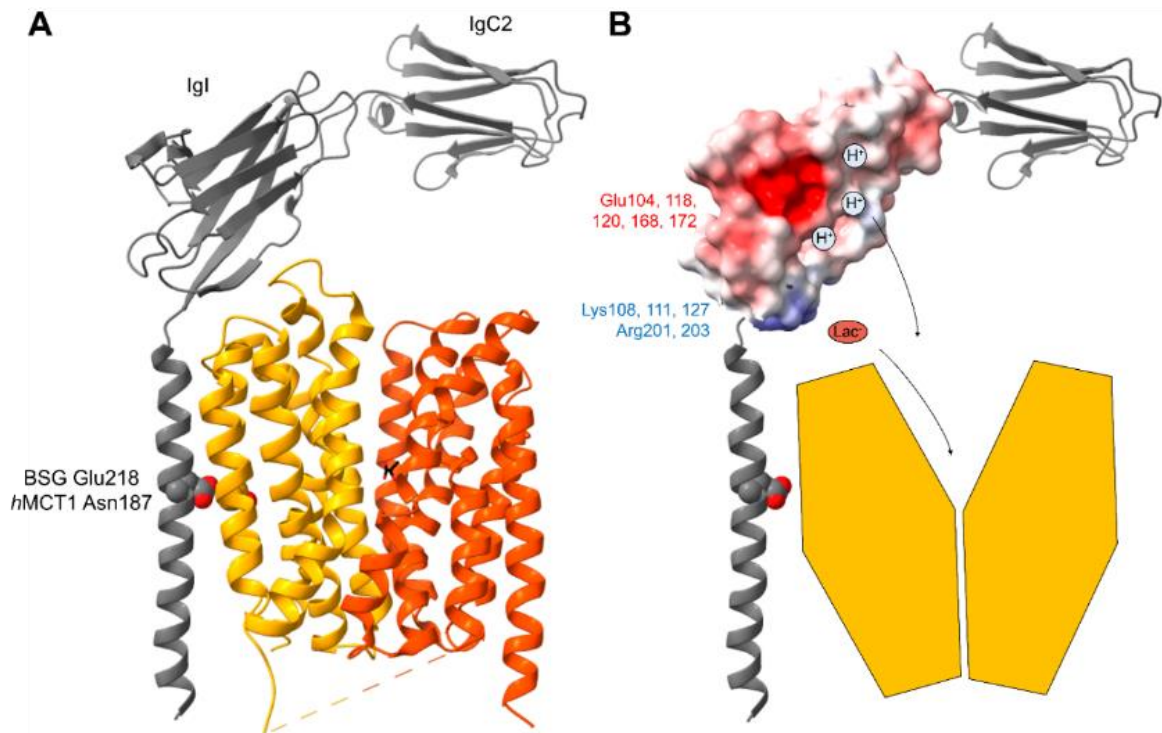


Figure 1. 10: (A) Structure of the MCT1 (PDB#6LZ0 [104], yellow and orange) in complex with lactate (black and red sticks representation) and Basigin (grey). (B) Representation of the Coulombic electrostatic potential at the surface of the Basigin IgI domain, attracting the monocarboxylate (lactate, Lac⁻) and proton substrate. Generated using Chimera antechamber 20.0 (Amber20). The reddest patch displays a surface charge of - 24.45, the bluest + 8.57.

1.4. Proton antenna

The millimolar cytosolic concentration of metabolites such as lactate (usually 0.5 to 1 mM in resting human muscles [13]) makes it impossible for the relatively slow MCT to deplete the concentration around their transport site before being regenerated by the Brownian diffusion [116]. For these high-concentration of metabolites, the cytosol is comparable to a well-mixed compartment of homogenous concentration. However, the same is not true for the co - transported protons. Their lower concentrations appears at odds with the high turnover of transporters (85 protons s⁻¹ for MCT1 [117]). Such transporter activity should deplete the substrate concentration around the entry sites. This suggests that weak acid metabolite transporters replenish the local concentration of their substrate and protons faster than simple diffusion would allow for [118], by processes such as the proximity to proton collecting antenna.

Proton collecting antennas are characterized by charged surface residues capable to electrostatically attract and bind the protons [119]–[121]. Their presence generates microenvironments containing greater proton concentrations than the bulk solvent. Protein proton wires [122]–[124] and proton exchange with the membrane bilayer [125]–[130] are facilitating the transport of protons between collection and transport sites of membrane proteins.

As previously discussed (1.3.4.), the Basigin IgI glutamate-rich patch serves this purpose for MCT. The electrostatic attraction of protons to these amino acids increases the local concentration of substrate for monocarboxylate transport. But this is not the only way Basigin increases the transport functionality of MCT. In fact, the Ig C2 Glu73 was identified as the binding site of the carbonic anhydrases (CA) (IV [131] and IX [132]). In Embigin, this binding site is a pair of aspartate/arginine [131], [133]. On the intracellular side, the carbonic anhydrase II was also found do directly bind to the C-terminus of MCT1 [134] and MCT4 [135] (but not MCT2 [133]). The presence and proximity of these enzymes, whose activities are unrelated to lactate transport appeared to improve the MCT transport, in a non-catalytic manner [132], [136]–[138], by attracting protons close to the transport path. The contribution of carbonic anhydrases to monocarboxylate transport has been extensively reviewed [62], [132]–[142].

Moreover, Noor *et al.* [143] reported that the addition of 6 histidines close to the MCT4 C - terminal had a positive effect on transport akin to the cooperation with intracellular CAII. This finding suggested that the expression of transporter with immobilized metal ion chromatography (IMAC) affinity tags may affect their transport.

Since PfFNT serve a function similar to that of MCTs (*i.e.* lactate/proton cotransport), would their transport functionality be also modulated by their own set of proton antennas or partner proteins? The PfFNT C-terminal extremity, for example, appear to protrude in the cytosolic side and carry several positively and negatively residues. Peng *et al.* [53] noticed the uniqueness of this structural features compared to other FNT, yet no functional role was identified. Could it serve to accumulate the transported substrates close to the channel?

1.5. Aims of this work

Part of this work supported C. Hansen's project of solving the structures of the resistant PfFNT mutant (G21E, G107S, V196L) in complex with inhibitors. First, membrane scaffold proteins (MSP) were purified to reconstitute PfFNT in lipid nanodiscs. Then, this work investigated methods of protein productions that would yield functional PfFNT. As the cell-free produced protein did not clearly appear functional after reconstitution in proteoliposomes and stopped-flow spectroscopy, this work established human embryonic kidney cells stable cell lines that expressed mutant PfFNT.

Moreover, investigations of the PfFNT C-terminus set-out to determine if this transporter was associated with its own proton antenna.

This work also attempted to observe and identify the contribution of known proton collecting antenna (such as Basigin, Embigin or carbonic anhydrases) in the transport of MCT1.

To investigate how the carbonic anhydrase affects the MCT1 transport, this work aimed to produce complexes formed by MCT1, Basigin and the CAIV in our lab yeast system. First, fusion constructs of the three proteins were prepared and tested. Alternatively, production of soluble CAIV was attempted. The objective was to add extracellular soluble and purified CAIV to yeasts expressing the Basigin-MCT1 fusion construct in order to form the Basigin-CAIV complex and observe how it impacts MCT1 transport.

Finally, this work investigated if the tags routinely used for protein identification and purification (*e.g.* poly-histidine and hemagglutinin tags) affected the proteins transport.

2. MATERIAL

2.1. Protein coding sequences

The DNA sequences and subsequently expressed protein amino acid sequences can be found in the supplementary materials (Supp. 1).

2.1.1. PfFNT

The coding sequence of the formate nitrite transporter from *Plasmodium falciparum* (NCBI Gen-ID: 814480) had been codon-optimized (GC, Genart/Lifetechnologies) to allow for a better expression by yeasts and *E. coli* [51], [144]. For this work, the optimized PfFNT coding sequence inserted in the plasmids pDR196 and pIVEX 2.3w were provided by A. Fuchs and A. Jansen respectively.

2.1.2. MCT1

For this work, the coding sequence of the *Homo sapiens* wild type MCT1 (NCBI Gen ID NM_001166496) was provided in the a pDR196 derivate plasmid by A-L. Köpnick. The coding sequence of the K38M mutant was provided in the same vector by K. Geistlinger.

2.1.3. Basigin chaperone

The coding sequence of the *Homo sapiens* Basigin (Isoform 2) was derived from the GenBank NM_001728 mRNA. For this work, the coding sequence was kindly provided by A-L. Köpnick, inserted upstream of the MCT1 coding sequence in a pDR196 derived plasmid.

2.1.4. Embigin chaperone

The coding sequence of the *Homo sapiens* Embigin (variant 1) was derived from the GenBank NM_198449.3 mRNA. For this work, the coding sequence was provided by A - L. Köpnick, inserted upstream of the MCT1 coding sequence in a pDR196 derived plasmid.

2.1.5. Carbonic anhydrase 4

The coding sequence of the *Homo sapiens* carbonic anhydrase 4 (CAIV) was derived from the NCBI Gene ID: 762. Its open reading frame was bought from Genscript, inserted in a pcDNA3.1⁺/C-(K)-DYK plasmid.

2.1.6. MSP1E3D1

MSP1E3D1 is a membrane scaffold protein that mimics the function of the human ApoA-1, first developed by Bayburt *et al.* [145]. The coding sequence of MSP1E3D1 was provided in the expression plasmid pET28a(+) by C. Hansen.

2.2. Plasmids

More detailed maps of the plasmids are represented in the supplementary materials (Supp. 2).

2.2.1. pDR196 derivatives for expression in yeast

The pDR196 plasmid [146], [147] is a derivative of pDR195 [148]. It allows for the production of proteins in yeasts. The DNA sequences of interests can be inserted between a PMA promoter and ADH terminator. An AmpR gene allows transformed bacteria to resist ampicillin selective condition. A URA3 gene allows the transformed yeast to grow in restrictive conditions, in media devoid of uracil.

2.2.1.1. pDRTXa

The pDR196 plasmid had previously been modified to encode for an N-terminal haemagglutinin tag (HA) and a C-terminal 10× Histidine tag (His₁₀). A Factor Xa. cleavage site separates the Multiple Cloning Site (MCS) in which the protein coding sequence is inserted from the C - terminal His₁₀ tag. The coding sequence is controlled by the PMA promoter and ADH terminator [51]. This plasmid, named pDRTXa, has been used in most previous experiments involving yeasts and was the base for the other derivatives. Protein coding sequences are typically inserted in this vector using the SpeI and XhoI restriction sites. The detailed map of this plasmid is available in Supp. 2.1.

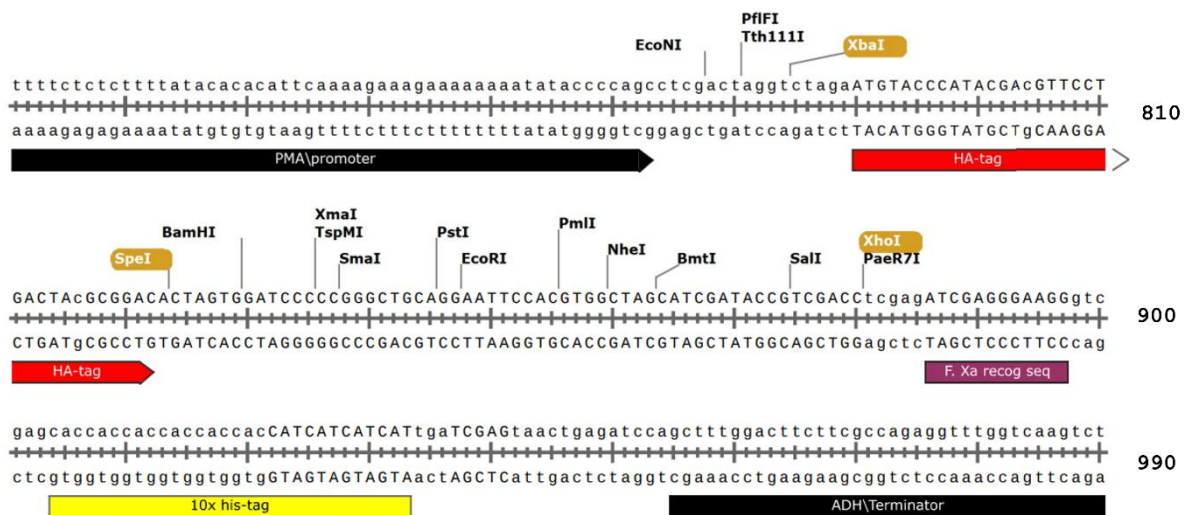


Figure 2. 1: DNA sequence of the pDRTXa plasmid between the promoter and terminator, generated using SnapGene® Viewer. The restriction sites most relevant for cloning are highlighted (gold).

2.2.1.2. pDRTXa_LK_MCT1

Prepared by A-L. Köpnick [115], this derivative of the pDRTXa (with inserted MCT1 coding sequence) contains an additional PstI site between the SpeI site and the MCT1 sequence. These two restriction sites are typically used to insert the coding sequences of Basigins or emibigin variants upstream of the MCT1 sequence. The detailed map of this plasmid is available in Supp. 2.2.



Figure 2. 2: DNA sequence of the pDRTXa_LK_MCT1 plasmid between the promoter and the beginning of the MCT1 coding sequence, generated using SnapGene® Viewer. The restriction sites most relevant for cloning are highlighted (gold)

2.2.1.3. pDRTXa_LK_BamHI_MCT1

Derived from the pDRTXa_LK_MCT1 plasmid, this vector had additional restriction sites added between the N-terminal HA-tag and the MCT1 coding sequence by inserting the oligonucleotides BamHI_insert_s and BamHI_insert_as (2.3.2. Table 2.2) in a vector digested with SpeI and PflMI.

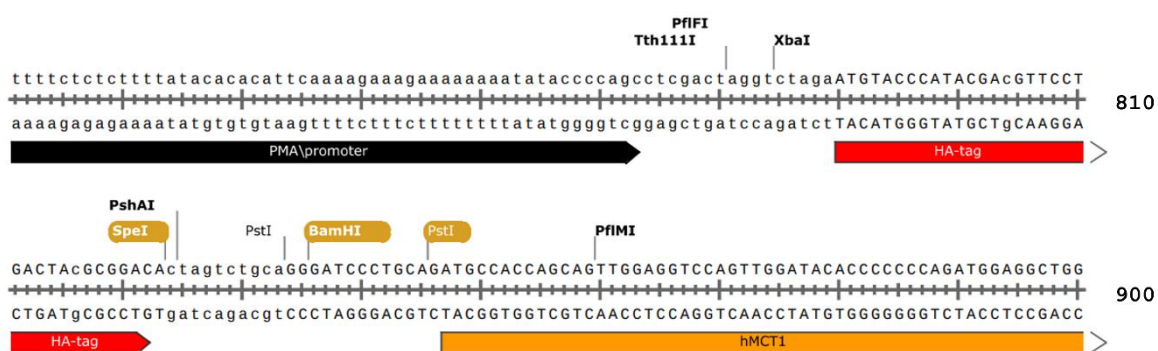


Figure 2. 3: DNA sequence of the pDRTXa_LK_BamHI_MCT1 plasmid between the promoter and the beginning of the MCT1 coding sequence, generated using SnapGene® Viewer. The restriction sites most relevant for cloning are highlighted (gold)

2.2.1.4. pDR(oTags)

The pDRTXa plasmid was reverted to a plasmid allowing for the expression of proteins without terminal tags. First, a PCR was used to amplify the ADH terminator with the primers PCR_pDRTXaDtag_s and PCR_pDRTXaDtag_as (2.3.4. Table 2.4). Both the PCR product and the pDRTXa plasmid were digested with the restriction enzymes XbaI and SphI, and they were ligated together to replace the entire HA and multiple cloning site sequence. The new plasmid was sequenced using the Seq_fullADHterm_rev primer (2.3.1. Table 2.1) to ensure a correct insertion and no unwanted mutations. The detailed map of this plasmid is available in Supp. 2.3.

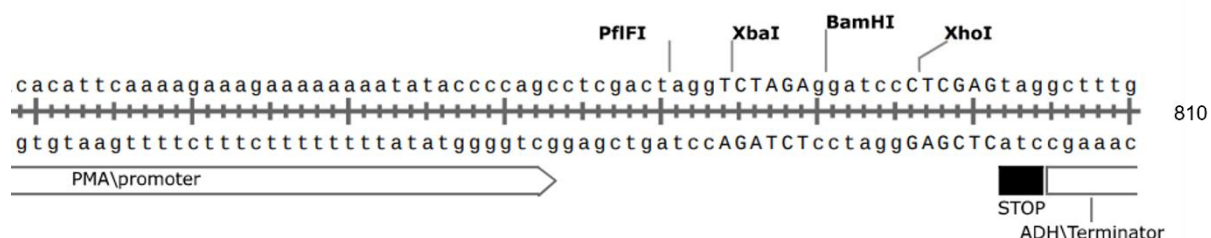


Figure 2. 4: DNA sequence of the pDR(oTags) plasmid between the promoter and the terminator, generated using SnapGene® Viewer.

2.2.2. IPTG inducible plasmid for expression in *E. coli*

These plasmids control the expression of the coding sequence of interest by expressing the *lacI* gene, which encodes for the *lac* repressor protein. It represses the expression of the T7 promoters in the absence of lactate or analogues (IPTG).

2.2.2.1. pET28a(+)

The commercially available pET28 a(+) plasmid was used to express the MSP1E3D1 coding sequence, fused to an N-terminal His₆ tag separated from the protein coding sequence by a TEV cleavage site. The plasmid contains a KanR gene allowing the transformed bacteria to grow on kanamycin selective conditions (40 ng/mL). The map of this plasmid is available in Supp. 2.4.

2.2.2.2. pET21X

The pET21X plasmid is derived from the commercially available pET21a. It contains the coding sequence expressing AmpR, allowing the bacteria transformed with this plasmid to bacteria to resist ampicillin selective condition (100 ng/mL). The expression of the coding sequence of interest (typically inserted between the SpeI and XhoI restriction sites) is controlled by T7 promoter and terminator. The map of this plasmid is available in Supp. 2.5.

2.2.3. pIVEX 2.3w and derivatives for cell-free protein production

2.2.3.1. pIVEX 2.3w

Derived from the commercially available pIVEX 2.3 (Roche), this plasmid was modified by A. Müller-Lucks [149]. It expresses the protein sequence inserted in the coding frame between an N-terminal hemagglutinin tag and a C-terminal His₁₀ tag, controlled by a T7 polymerase promoter and terminator. A protease cleavage site (Factor Xa.) separates the C-terminal tag from the protein sequence. Such plasmids were typically used for the cell-free expression of proteins. The detailed map of this plasmid is available in Supp. 2.6.

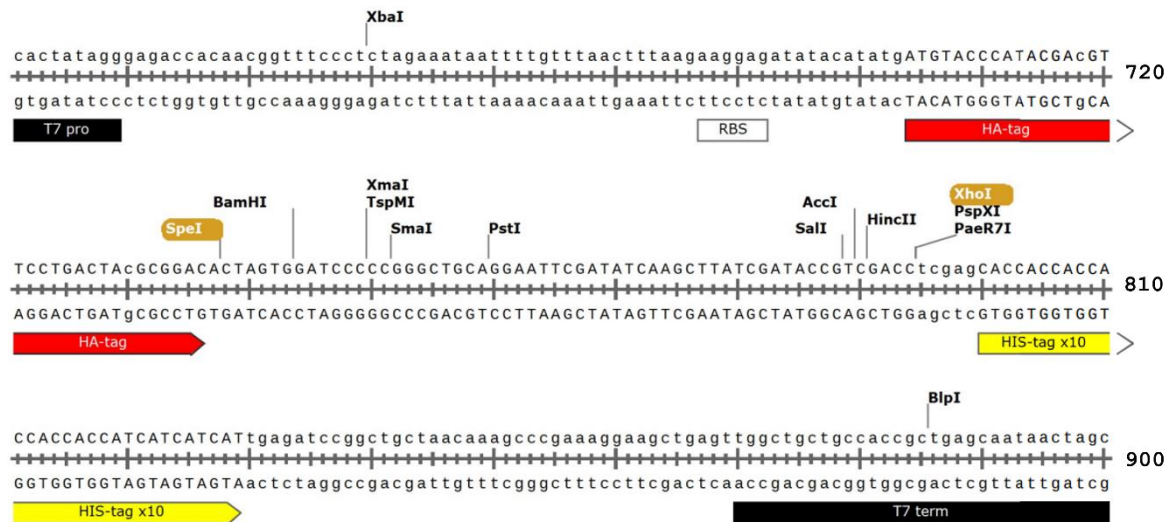


Figure 2. 5: DNA sequence of the pIVEX 2.3w plasmid between the promoter and terminator, generated using SnapGene® Viewer. The restriction sites most relevant for cloning are highlighted (gold).

2.2.3.2. pIVEX 2.3w Strep

Derived from the pIVEX 2.3w, this plasmid had its N-terminal HA-tag replaced by a Streptavidin tag. The oligomers XbaI-strepII-Xa-BamHI_TDPCR_s and XbaI-strepII-Xa-BamHI_TDPCR_as (2.3.2. Table 2.2), encoding the N-terminal Strep II tag were annealed together (Figure 3.1 B) and were inserted in a pIVEX 2.3w vector digested between the XbaI and SpeI sites. The proper insertion of the N-terminal tag was validated by Sanger sequencing.

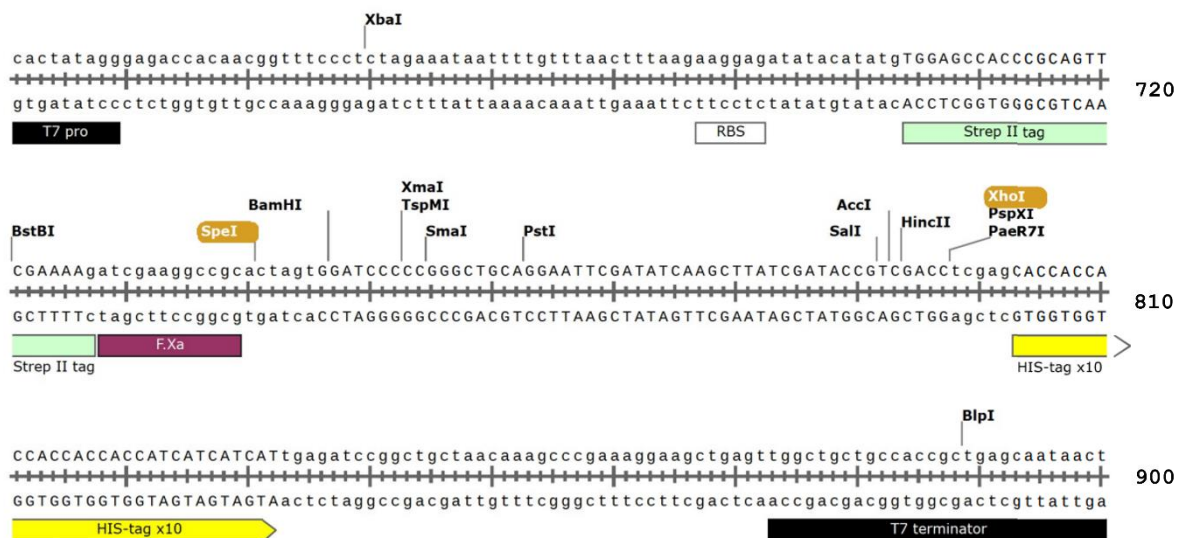


Figure 2. 6: DNA sequence of the pIVEX 2.3w Strep plasmid between the promoter and terminator, generated using SnapGene® Viewer. The restriction sites most relevant for cloning are highlighted (gold).

2.2.3.3. *pIVEX 2.3w oHA*

Derived from the *pIVEX 2.3w* plasmid, this plasmid was modified by J. Holm-Bertelsen [150] to remove the N-terminal HA tag.



Figure 2. 7: DNA sequence of the *pIVEX 2.3w oHA* plasmid between the promoter and terminator, generated using SnapGene® Viewer. The restriction sites most relevant for cloning are highlighted (gold).

2.2.3.4. *pIVEX2.3w GFPΔMI*

Derived from the *pIVEX 2.3w* plasmid, this plasmid was modified to express the proteins of interest fused to a C-terminal green fluorescent protein (GFP). The original start codon of the GFP coding sequence had been deleted. The fusion construct is expressed between an N-terminal HA-tag and a C-terminal His₁₀ tag. The map of this plasmid is available in Supp. 2.7.

2.2.4. pcDNA 3.1 derivatives for human cells protein production

pcDNA is a plasmid used for mammalian cells expression of proteins. An AmpR gene allows transformed bacteria to resist ampicillin selective condition. In this work, the pcDNA plasmids were only the initial vector of the bought human carbonic anhydrase 4 (provider) and the distant precursor to the pCGTO-GFP-myc plasmid used in Intana Bioscience GmbH.

2.2.4.1. pCGTO-GFP-myc

The pcDNA 3.1 plasmid had been modified to encode a GFP fused to the N-terminal end of the protein of interest by a flexible linker (triple glycine: GGG). It also encodes for a myc C - terminal tag, separated from the GFP coding sequence by another flexible linker (GGG) and a PreScission protease cleavage site (LEVLFQ/GP). Contrarily to pcDNA 3.1, pCGTO GFP - myc contains the gene from *Streptoalloteichus hindustanus*, encoding the BleoR protein, which confers a resistance to ZeocinTM, allowing transformed mammalian cells to grow on selective conditions (100 ng/mL Zeocin).

The pCGTO-GFP-myc was kindly provided by I. Jakóbowska and Intana Bioscience GmbH and were the base for the other derivatives. The map of this plasmid is available in Supp. 2.8.

2.2.4.2. pCGTO-His₁₀

Based on pCGTO-GFP-myc, this plasmid encodes the protein of interest fused to a C-terminal 10 Histidine tag, separated from the protein of interest by a factor Xa. protease cleavage site. The plasmid was prepared by inserting the oligonucleotides pair HindIII-Xa-10His-KpnI_s and H-Xa-X-10His-K_as (2.3.2. Table 2.2) in vector digested with HindIII and KpnI.

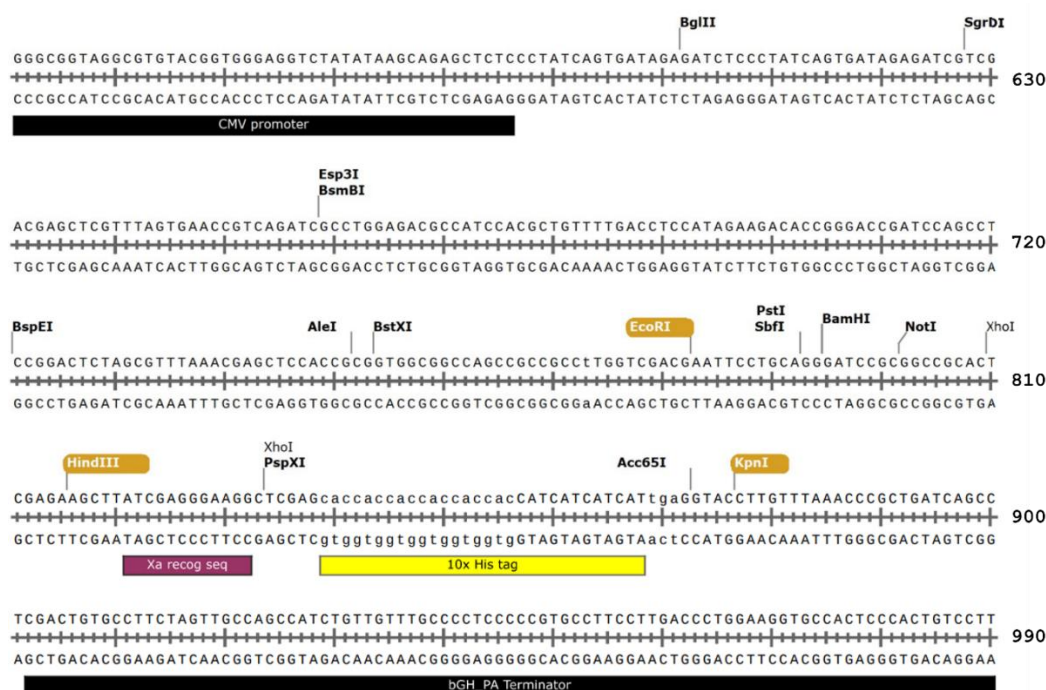


Figure 2. 8: DNA sequence of the pCGTO-His₁₀ plasmid between the promoter and terminator, generated using SnapGene® Viewer. The restriction sites most relevant for cloning are highlighted (gold).

2.3.3. Mutagenesis

Table 2.3: Mutagenesis oligonucleotides. Substituted nucleotides are labeled in bold.

Primer	DNA sequence (5'-3')
SDM_PfFNT-Y285A_s	ACAAAGAACAC g cCTACAACCTTCG
SDM_PfFNT-Y285F_s	ACAAAGAACA C tCTACAACCTTCG
SDM_PfFNT-Y285_as	AAATGAAATACAGCGGCAGTCC
SDM_PfFNT-E289Q_s	ACTACAAC T TcAACGCAGTAAACG
SDM_PfFNT-E289_as	AGTGT T C T TTGTAAATGAAATACAGCG

2.3.4. PCR

Table 2. 4: Primers for PCR

Primer	DNA sequence (5'-3')
CAIVp-XbaI_PCR4_s	taTCTAGAGCAGAGTCACACTGGTGC
CAIVp-SpeI-BamHI_PCR3_as	tttGGATCCACTAGTGGACTTTATCACCGTGCG
SpeI-SacI-BSGd308_PCR_s	TTTACTAGTATTGAGCTCTCCGACCAGGCCATCATCACGC
hBSG_BamHI_PstI_as *	ttctgcagggatccGGAAGAGTTCCTCTGGCGGACG
SpeI-M-EMBvar1deltaTM_PCR_s	TTTACTAGTATGGACGGCAGTGCCCCAG
SpeI-EMB_IgV1-2_deltaTM_PCR_s	TTTACTAGTATGCCAGTAGAAAAAATATCACTTTAG
SpeI-M-EMB_IgV2_deltaTM_PCR_s	TTTACTAGTATGCCTGAACTTCATGGGAAAAACAAG
EMBDeltaTM-SacI_PCR_as	TTTGAGCTCGGGCACCAAATAGCTCAGC
PCR_EcoRI-PfFNT_s	TTTGAATTCGCCATGCCTCCCAACAACCTCG
PCR_10His-KpnI_as	aaaGGTAC C tcaATGATGATGATGgtggtgg
PCR_PfFNT-HindIII_as_2	TTTAAGCTTGTTCGCGAGTTCAATGctcaggg
PCR_mCAIVp_s	TTTActagtATGGCAGAGTCACACTGGTGC
PCR_CAIVp-3G-XhoI_as	ttCTCGAGtcctcctccGGACTTTATCACCGTC
PCR_pDRTXaDtag_s	tttTCTAGAggatccCTCGAGtagGCTttggacttcttcgcc
PCR_pDRTXaDtag_as	tttGCATGCcggtagaggtgtggtcaataagagcgacctc
PCR_SpeI-PfFNTnter_s	TTTactagtATGCCTCCCAACAACCTCGAAATATG
PfFNT_Δ299-term_XhoI_as **	TTCTCGAGTCATTGCGCATCATTGTTGTCGCGTTTACTGCG
PCR_PfFNTd282-XhoI_as2	aaaaCTCGAGctaTTTGTAAATGAAATACAGCGGCAG
PCR_10His-KpnI_as	aaaGGTAC C tcaATGATGATGATGgtggtgg

* Designed by A-L. Köpnick [115] ,** A. Jansen [151]

2.4. Molecular biology, enzymes and buffers

2.4.1. Restriction enzymes

Thermo Fisher Scientific

BamHI	DpnI	EcoRI	HindIII	PfI
G/GATCC	GA ^{CH₃} /TC	G/AATTC	A/AGCTT	CCANNNN/NTGG
CCTAG/G	CT/A ^{CH₃} G	CTTAA/G	TTCGA/A	GGTN/NNNNACC
PstI	SpeI	SphI (PaeI)	XbaI	XhoI
CTGCA/G	A/CTAGT	G/CATGC	T/CTAGA	C/TCGAG
G/ACGTC	TGATC/A	GCTAC/G	AGATC/T	GAGCT/C

Fermentas (Thermo Fisher Scientific)

EcoRV	KpnI	SacI
GAT/ATC	GGTAC/C	GAGCT/C
CTA/TAG	C/CATGG	C/TCGAG

New England BioLabs® GmbH

EcoRI-HF	KpnI-HF
G/AATTC	GGTAC/C
CTTAA/G	C/CATGG

2.4.2. Restriction enzymes buffers

10× Tango Buffer (BSA)

330 mM Tris-acetate
(pH=7.9 at 37°C),
100 mM Magnesium acetate,
660 mM Potassium acetate,
1 mg/ml BSA.

10× Tango Buffer (BSA)

330 mM Tris-acetate
(pH=7.9 at 37°C),
100 mM Magnesium acetate,
660 mM Potassium acetate,
1 mg/ml BSA.

10× Red Buffer (BSA)

100 mM Tris-HCl (pH=8.5 at 37°C),
100 mM MgCl₂,
1 M KCl,
1 mg/ml BSA.
1 mg/ml BSA

10× Orange Buffer (BSA)

500 mM Tris-HCl (pH=7.5 at 37°C),
100 mM MgCl₂,
500 mM NaCl,
1 mg/ml BSA

10× Blue Buffer (with BSA)

100 mM Tris-HCl (pH=7.5 at 37°C),
100 mM MgCl₂,
1 mg/ml BSA

10× KpnI

10× Buffer Blue
+ 0.02% Triton X-100

10× BamHI, Lsp1109I, SgeI

100 mM Tris-HCl (pH=8 at 37°C),
50 mM MgCl₂,
1 M KCl
0.02% Triton X-100,

These enzyme buffers were bought from Thermo Scientist, except 10× KpnI, kindly prepared by A. Fuchs. They were used diluted 1:10, in accordance to the enzyme compatibility (Table 3.1)

2.4.3. Other enzymes

FastAP Thermosensitive Alkaline Phosphatase (1 u/μL) 10× FastAP™ Buffer	<i>Thermo Fisher Scientific, Schwerte</i>
T4 DNA Ligase 5 u/μ ^l 10× T4 DNA ligase buffer	<i>Thermo Fisher Scientific, Schwerte</i>
OneTaq® DNA polymerase (5 u/μL) OneTaq® Standard Reaction Buffer (5×)	<i>New England Biolabs, Frankfurt a. M</i>
PfuTurbo DNA polymerase (2.5 u/μl) Cloned Pfu reaction buffer (10×)	<i>Agilent Technologies, Waldbronn</i>

2.5. Organisms and strains

Table 2. 5: Living organismes

Organism	Genotype	Source
<i>Escherichia coli</i> (DH5 α) [152]	F ⁻ <i>endA1 glnV44 thi-1 recA1 relA1 gyrA96 deoR nupG purB20</i> ϕ 80 <i>dlacZ</i> Δ M15 Δ (<i>lacZYA-argF</i>)U169, <i>hsdR17</i> (<i>rK⁻mK⁺</i>), λ ⁻	Roche
<i>Escherichia coli</i> (BL21 DE3) [153]	<i>E. coli</i> str. B F ⁻ <i>ompT gal dcm lon hsdS_B</i> (<i>r_B⁻m_B⁻</i>) λ (DE3 [<i>lacI lacUV5-T7p07 ind1 sam7 nin5</i>]) [<i>malB⁺</i>] _{K-12} (λ ^S)	
<i>Saccharomyces cerevisiae</i> (W303-1A Δ <i>jen1</i> Δ <i>ady2</i>) [154]–[156]	MATa, <i>can1-100, ade2-1oc, his3-11-15, leu2-3,-112, trp1-1-1, ura3-1, jen1::kanMX4, ady2::hphMX4</i>	Kindly provided by M. Casal
Human embryonic kidney cells (HEK 293 T - RE \times)	Clonal; stably expressing DHFR.ATF6, Tet-XBP1s, and the tetracycline repressor	Kindly provided by I. Jakóbowska and Intana Bioscience GmbH.

2.6. Antibodies

Table 2. 6: Antibodies

Product		Provider
Penta-His antibody, BSA free (0.2 mg/mL)	mouse	QIAGEN
Anti HA 12CA5 mouse, monoclonal antibody	mouse	Roche
Anti-PfFNT C-terminus	rabbit	
Peroxidase AffiniPure Goat anti-Mouse IgG, HRP conjugate (0.4 mg/mL)	goat	Jackson Immuno Research
Peroxidase AffiniPure Goat anti-Rabbit IgG, HRP conjugate (0.4 mg/mL)	goat	Jackson Immuno Research
THE TM His-tag Antibody, mAb, + Atto488	mouse	GenScript

2.7. Chemicals list and provider

Product	Provider
2-(4'-hydroxy-benzeneazo)benzoic acid (HABA)	<i>Sigma Aldrich, Austria</i>
2-(N-morpholino)ethanesulfonic acid (MES)	<i>Carl Roth, Karlsruhe</i>
2'-Deoxyadenosine-5'-triphosphate (dATP, 100 mM)	<i>Thermo Fisher Scientific, Schwerte</i>
2'-Deoxycytidine-5'-triphosphate (dCTP, 100 mM)	<i>Thermo Fisher Scientific, Schwerte</i>
2'-Deoxyguanosine-5'-triphosphate (dGTP, 100 mM)	<i>Thermo Fisher Scientific, Schwerte</i>
2'-Deoxythymidine-5'-triphosphate (dTTP, 100 mM)	<i>Thermo Fisher Scientific, Schwerte</i>
HEPES, $\geq 99.5\%$	<i>Carl Roth, Karlsruhe</i>
4ME 16:0 PC	<i>Avanti Polar Lipids</i>
CFDA-SE	<i>Sigma Aldrich</i>
Acetic acid	<i>VWR</i>
Acetyl phosphate (Li ⁺ /K ⁺ salt)	<i>Sigma Aldrich, München</i>
Adenine hemisulfate salt	<i>Sigma Aldrich, München</i>
Adenosine-5'-triphosphate disodium salt (ATP, hydrate)	<i>Sigma Aldrich, München</i>
Agar bacteriological	<i>Oxoid, Basingstoke, USA</i>
Agarose LE	<i>Genaxxon BioScience, Ulm</i>
Albumin Fraction V (BSA)	<i>Carl Roth, Karlsruhe</i>
Ammonium Persulfate	<i>Sigma Aldrich, München</i>
Ammonium sulfate	<i>Carl Roth, Karlsruhe</i>
Ampicillin (sodium salt)	<i>Genaxxon BioScience, Ulm</i>
AZD3965	<i>Selleckchem.com</i>
Bacto™ Peptone	<i>BD Biosciences, San Jose, USA</i>
Bacto™ Yeast Extract	<i>BD Biosciences, San Jose, USA</i>
Blasticidin	<i>InvivoGen, Toulouse, France</i>
Brij®78	<i>Sigma Aldrich, München</i>
Bromophenol Blue (sodium salt)	<i>Carl Roth, Karlsruhe</i>
Calcium chloride (dihydrate, $\geq 99\%$)	<i>Carl Roth, Karlsruhe</i>
Cholic acid	<i>Carl Roth, Karlsruhe</i>
Citric acid	<i>Carl Roth, Karlsruhe</i>
Clarity™ ECL Western blotting substrate	<i>Bio-Rad, München</i>
COmplete™ EDTA-free protease inhibitor	<i>Roche</i>
Cytidin-5'-triphosphate disodium salt (CTP)	<i>Sigma Aldrich, München</i>
D(+)-Glucose (monohydrate)	<i>Carl Roth, Karlsruhe</i>
d-Desthiobiotine	<i>Sigma Aldrich</i>
Difco™ Yeast Nitrogen Base	<i>BD Biosciences, San Jose, USA</i>
Dimethyl sulphoxide (DMSO, $\geq 99.8\%$)	<i>Sigma Aldrich, München</i>
Diodium hydrogen Phosphate dihydrate	<i>Carl Roth, Karlsruhe</i>
Dithiothreitol (DTT)	<i>Carl Roth, Karlsruhe</i>
DNA Sodium Salt Type III from salmon Testes	<i>Sigma Aldrich</i>
Dodecyl- β -D-Maltoside	<i>Glycon Bioch. GmbH Biotechnology</i>
<i>E. coli</i> polar lipids	<i>Avanti Polar Lipids</i>
Ethanol ($\geq 99.8\%$)	<i>Carl Roth, Karlsruhe</i>
Ethidium bromide	<i>MP Biomedicals, Illkirch, France</i>
Foetal Bovin Serum Premium	<i>PAN Biotech</i>

Product	Provider
Gibco™ DMEM, high glucose, pyruvate, 10 x 500 mL	<i>Life Technologies</i>
Folinic acid (calcium salt)	<i>Sigma Aldrich</i>
Gibco™ Penicillin-Streptomycin (10,000 U/mL), 100 mL	<i>Life Technologies</i>
Gibco™ Trypsin-EDTA (0.05%), phenol red, 100 mL	<i>Life Technologies</i>
Glycerol (≥ 98 %, anhydrous)	<i>Carl Roth, Karlsruhe</i>
Glycin	<i>Carl Roth, Karlsruhe</i>
Gramicidin (<i>Bacillus brevis</i>)	<i>Sigma Aldrich</i>
Guanosine 5'-triphosphate sodium salt (hydrate, GTP)	<i>Sigma Aldrich, München</i>
HEPES	<i>Carl Roth, Karlsruhe</i>
Hydrochloric acid	<i>J. T. Baker, München</i>
Imidazole	<i>Sigma Aldrich, München</i>
IPTG	<i>Carl Roth, Karlsruhe</i>
Isopropanol	<i>Carl Roth, Karlsruhe</i>
L-(+)-Lactate (Na ⁺ salt)	<i>AppliChem, Darmstadt</i>
L-[¹⁴ C]-Lactic acid (sodium salt, 55 mCi mmol ⁻¹)	<i>Hartmann Analytic, Braunschweig</i>
L-Alanine	<i>Fluka Chemie, Buchs, Switzerland</i>
Lambda DNA	<i>Thermo Fisher Scientific, Schwerte</i>
L-Arginine monohydrochloride	<i>Sigma Aldrich, München</i>
L-Asparagine monohydrate	<i>Sigma Aldrich, München</i>
L-Aspartic acid sodium salt monohydrate	<i>Sigma Aldrich, München</i>
LB agar (Lenox)	<i>Carl Roth, Karlsruhe</i>
LB medium (Lenox)	<i>Carl Roth, Karlsruhe</i>
L-Cysteine	<i>Sigma Aldrich, München</i>
L-Glutamic acid monopotassium salt monohydrate	<i>Fluka Chemie, Buchs, Switzerland</i>
L-Histidine monohydrochloride monohydrate	<i>Carl Roth, Karlsruhe</i>
L-Isoleucine	<i>Sigma Aldrich, München</i>
Lithium acetate	<i>Carl Roth, Karlsruhe</i>
L-Leucine	<i>Carl Roth, Karlsruhe</i>
L-Lysine monohydrochloride	<i>Sigma Aldrich, München</i>
L-Methionine	<i>Sigma Aldrich, München</i>
L-Phenylalanine	<i>Sigma Aldrich, München</i>
L-Proline	<i>Carl Roth, Karlsruhe</i>
L-Serine	<i>Fluka Chemie, Buchs, Switzerland</i>
L-Threonine	<i>Sigma Aldrich, München</i>
L-Tryptophane	<i>Sigma Aldrich, München</i>
L-Tyrosine	<i>Sigma Aldrich, München</i>
L-Valine	<i>Sigma Aldrich, München</i>
lysozyme	<i>Thermo Scientific</i>
Magnesium acetate	<i>Sigma Aldrich, München</i>
Magnesium acetate tetrahydrate	<i>Sigma-Aldrich</i>
MES	<i>Carl Roth, Karlsruhe</i>
Metformin Hydrochloride	<i>MP Biomedical LLC, China</i>
Methanol (HPLC grade)	<i>J. T. Baker, München</i>
Milk powder (blotting grade)	<i>Carl Roth, Karlsruhe</i>
Monosodium dihydrogen phosphate monohydrate	<i>Carl Roth, Karlsruhe</i>
MOPS	<i>Carl Roth, Karlsruhe</i>
N,N,N',N'-tetramethylethane-1,2-diamine (TEMED)	<i>Genaxxon bioscience, Ulm</i>

Product	Provider
Ni ²⁺ -NTA agarose	<i>Qiagen, Hilden</i>
N-lauroylsarcosine	<i>Tokyo Chemical Industry Co. Ltd</i>
Orange G	<i>Carl Roth, Karlsruhe</i>
Phosphoenolpyruvate (PEP, potassium salt)	<i>AppliChem, Darmstadt</i>
Polyethylenglycol (PEG) 3350	<i>Sigma Aldrich, München</i>
Polyethylenglycol (PEG) 8000	<i>Sigma Aldrich, München</i>
Ponceau red	<i>Carl Roth, Karlsruhe</i>
Potassium chloride	<i>Carl Roth, Karlsruhe</i>
Potassium acetate	<i>Carl Roth, Karlsruhe</i>
Potassium hydroxide (KOH)	<i>AppliChem, Darmstadt</i>
preqGOLD Marker III	<i>VWR</i>
Pyranine (HPTS)	<i>Life technologies™</i>
Pyruvate kinase (10 mg ml ⁻¹)	<i>Roche Diagnostics, Mannheim</i>
Q Sepharose® FastFlow resin	<i>Sigma Aldrich</i>
RiboLock RNase inhibitor (40 U·µL ⁻¹)	<i>Thermo Fisher Scientific, Schwerte</i>
Rotiphorese® Gel 40 (40 %, 29:1)	<i>Carl Roth, Karlsruhe</i>
Roti®-Quant concentrate (5X)	<i>Carl Roth, Karlsruhe</i>
Rotiphorese® Blue R concentrate	<i>Carl Roth, Karlsruhe</i>
Saccharose	<i>Merck</i>
Scintillation cocktail (Quicksafe A)	<i>Zinsser Analytic, Frankfurt</i>
Sodium azide (NaN ₃)	<i>Carl Roth, Karlsruhe</i>
Sodium chloride (NaCl)	<i>Carl Roth, Karlsruhe</i>
Sodium dihydrogen phosphate (monohydrate)	<i>Carl Roth, Karlsruhe</i>
Sodium dodecyl sulfate (SDS)	<i>AppliChem, Darmstadt</i>
Sodium Formate	<i>Sigma Aldrich, München</i>
Sodium hydroxide (NaOH)	<i>Carl Roth, Karlsruhe</i>
Tetracycline Hydrochloride	<i>Life Technologies</i>
Tetramethylethylenediamine	<i>Genaxxon bioscience, Biberach</i>
Trichloroacetic acid	<i>Carl Roth, Karlsruhe</i>
Tris(hydroxymethyl)aminomethane (Tris)	<i>Carl Roth, Karlsruhe</i>
Tritiplex® (EDTA)	<i>Merck</i>
Triton X-100	<i>Carl Roth, Karlsruhe</i>
tRNA (<i>E. coli</i> , MRE 600)	<i>Roche Diagnostics, Mannheim</i>
Tween® 20	<i>AppliChem, Darmstadt</i>
Uridine-5'-triphosphate trisodium salt (UTP, hydrate)	<i>Sigma Aldrich, München</i>
Zeocin™ powder	<i>InvivoGen</i>
Zymolase® 20t	<i>Carl Roth, Karlsruhe</i>
β-Mercaptoethanol	<i>Carl Roth, Karlsruhe</i>

2.8. Culture media

2.8.1. Bacteria cultures

Ampicillin 1000

1 g Ampicillin
Diluted in 10 mL in ddH₂O
Filtered sterile (0.2 μm)

LB (lysogeny broth)

20 g LB medium (Lennox)
Up to 1 L in ddH₂O
Autoclaved sterile
Stored at room temperature

IPTG:

2.383 g dissolved in 10 mL ddH₂O (1 M)
0.2383 g dissolved in 10 mL ddH₂O (100 mM)
Aliquoted as 1 mL, stored at -20°C

LB, Amp (100 ng/mL)

20 g LB medium (Lennox)
Up to 1 L in ddH₂O
Autoclaved sterile, cool down to room temperature
+ 1 mL Ampicillin 1000×
Stored at 4°C

LB agar, Amp (100 ng/mL)

35 g LB agar (Lennox)
Up to 1 L in ddH₂O
Autoclaved sterile, cool down to 60°C
+ 1 mL Ampicillin 1000×
Cast on 9 cm dishes

2.8.2. Yeast cultures

Adenine (200×)

1 g Adenine hemisulfate salt
Up to 200 mL in ddH₂O (5 g/L)
Filtrated sterile (0.2 μm)
Stored at room temperature.

L-Leucine (200×)

4 g L-Leucine
Up to 200 mL in ddH₂O (20 g/L)
Filtrated sterile (0.2 μm)
Stored at room temperature.

L-Tryptophan (500×)

1 g L-Tryptophan
Up to 200 mL in ddH₂O (5 g/L)
Filtrated sterile (0.2 μm)
Stored at 4°C

L-Histidine (1000×)

4 g L-Histidine monohydro-chloride
Up to 200 mL in ddH₂O (20g/L)
Filtrated sterile (0.2 μm)
Stored at 4°C

SD media (Synthetic defined media)

1.7 g Difco™ Yeast Nitrogen Base

5 g Ammonium sulfate

20 g D-Glucose

+ NaOH

Up to 1 L in ddH₂O

Autoclaved sterile

Stored at room temperature.

SD-ALWH media

1 L SD media (autoclaved)

+ 5 mL Adenine (200×), 25 mg/L

+ 5 mL L-Leucine (200×), 100 mg/L

+ 2 mL L-Tryptophan (500×), 10 mg/mL

+ 1 mL L-Histidine (1000×), 20 mg/mL

SD-AWLH agar

1.7 g Difco™ Yeast Nitrogen Base Autoclaved sterile, cooled down to 60°C

5 g Ammonium sulfate + 5 mL Adenine (200×) (25 mg/L)

20 g D-Glucose + 5 mL L-Leucine (200×) (100 mg/L)

20 g Agar bacteriological + 2 mL L-Tryptophan (500×) (10 mg/mL)

+ NaOH + 1 mL L-Histidine (1000×) (20 mg/mL)

Up to 1 L in ddH₂O

Cast on 9 cm diameter dishes.

YPD ± agar

20 g Bacto™ Peptone

10 g Bacto™ Yeast Extract

20 g D-Glucose

(±20 g Agar bacteriological)

Up to 1L in ddH₂O

Autoclaved sterile

(±Cast on 9 cm diameter dishes.)

2.8.3. HEK293T cells media and buffers**Blasticidin 5 mg/mL**diluted in ddH₂O, Stored at 4 °C**Blasticidine 10 mg/mL (InvivoGen)**

Stored at -20°C, or 4°C while in use.

Tetracycline 10 000×

10 mg/mL

70% Ethanol

Filtrated sterile (0.2 μm), aliquoted in 1 mL.

Stored at -20°C, or 4°C while in use.

AZD3965 10 mM

1 mg AZD3965 (0.00194 mmol)

Diluted in 194 μL DMSO.

Stored at -20 °C

Metformin 40 mM

50 mg Metformin Hydrochloride
Dissolved in 7.547 mL ddH₂O
Filtered sterile (0.2 µm), stored at -20 °C

Zeocin™ 1000× (0.1 g/mL)

1 g Zeocin™ powder (InvivoGen)
Dissolved in 10 mL ddH₂O autoclaved.
Filtered sterile (0.2 µm), stored at -20°C.

5 mM EDTA solution

0.9306 g Tritoplex® (Merk)
Dissolved in 0.5 L ddH₂O
Autoclaved sterile, stored at room T°

HBSS, 20 mM HEPES

47 mg HEPES
Dissolved in 10 mL Hank's Balanced Salt
Solution.

2% Copper^(II) sulfate

10 g CuSO₄ dissolved in 0.5 L ddH₂O
Autoclaved sterile, stored at room T°

10×PBS pH=7.4

1.37 M NaCl
27 mM KCl
100 mM Na₂HPO₄
18 mM KH₂PO₄
pH set to 7.4
Up to 100 mL in ddH₂O

10×TBS pH=7.4

0.5 M Tris
1.50 M NaCl
pH adjusted to 7.4 using HCl
Up to 100 mL in ddH₂O

Stock culture media

Gibco™ Dulbecco's Modified Eagle Media (DMEM)
10% FBS Premium (PAN Biotech).
1% (100 u/µL) Gibco™ Penicillin-Streptomycin (10.000 u/mL)
Mixed and stored at 4°C.
For the cultures of transfected cells: +100 ng/mL Zeocin™, 5 µg/mL Blastocidin

PfFNT activity selection media:

90 % DMEM
9% FBS Premium (PAN Biotech).
0.9 % (90 u/µL) Gibco™ Penicillin-Streptomycin (10.000 u/mL)
4 mM metformin hydrochloride
1 µg/mL Tetracycline
0.1 µM AZD3965, 0.01% DMSO
100 ng/mL Zeocin™
5 µg/mL Blastocidin

2.9. Buffers and solutions

2.9.1. Molecular Biology

0.5 M EDTA: 93.06 g Tritiplex III dissolved in 0.5 L ddH₂O

50× TEA buffer stock

2 M Tris base
1 M glacial acetic acid
0.5 M EDTA
pH=8.5
Up to 1 L in ddH₂O

Ethidium Bromide

(10 mg/mL)
5 tablets (0.1 µg)
Dissolved in 50 mL ddH₂O

10× Orange G loading buffer

0.4% Orange G
30% Glycerol
100 mM EDTA
Stored at 4°C

PEG 3350 (50% w/v)

50 g Polyethylene glycol 3350
Up to 100 mL in ddH₂O

2.5 mM dNTPs

0.25 mL dATP (100 mM)
0.25 mL dGTP (100 mM)
0.25 mL dCTP (100 mM)
0.25 mL dTTP (100 mM)
up to 10 mL in ddH₂O
stored at -20°C

Lambda DNA PstI digest

200 µL Lambda DNA
108 µL 10× buffer Orange G
12 µL PstI (120 u)
760 µL ddH₂O
Incubated overnight, 37°C
+120 µL 10× Orange G loading buffer
Stored at -20°C

Lithium Acetate (1 M)

33 g Lithium Acetate
Up to 500 mL in ddH₂O
Autoclaved sterile

Single-stranded carrier DNA (2 mg/mL)

200 mg DNA from salmon testes
Up to 100 mL in buffer TE. Aliquoted.
Stored a -20 °C
Boil 5 min before use

2.9.2. Cell-free expression system

2.9.2.1. Buffers and stocks

NaN₃ (10% w/v)

100 mg Sodium Azide
Dissolved in 1 mL ddH₂O
Aliquoted in 0.5 mL. Stored at -20 °C.

Mg(OAc)₂ (1 000 mM)

3.216 g Magnesium acetate tetrahydrate
Dissolved in 15 mL ddH₂O, Filtered sterile.
Aliquoted in 0.5 mL. Stored at -20 °C.

DTT (500 mM)

154.26 mg Dithiothreitol
Dissolved in 2 mL ddH₂O
Filtered sterile, aliquoted in 0.5 mL.
Stored at -20 °C

Folinic acid

10 mg Folinic acid calcium acetate
Dissolved in 1 mL ddH₂O
Stored at -20 °C

PEP (1 000 mM)

412.2 mg Phosphoenolpyruvate (K⁺ salt)
pH set to 7 (+317 µL 10 M KOH)
up to 2 mL in ddH₂O, stored at -20 °C

Brij 78 (15% w/v)

7.5 g Brij 78, dissolved in 50 mL ddH₂O
(at 30°C or 37°C)
Stored at -20 °C.

PEG8000 (40% w/v)

20 g Polyethylene Glycol 8000
Dissolved in 50 mL ddH₂O at 30 °C
Stored at -20 °C

Protease inhibitor 50×

Tablet of COMplete™ (Roche) EDTA-free
protease inhibitor, dissolved in 1 mL ddH₂O.
Stored for 1 to 2 months at -20 °C.

Buffer H-E

2.4 M HEPES	28.596 g
20 mM EDTA	0.2923 g

Adjusted to pH=8 with KOH
Up to 50 mL in ddH₂O
Filtered sterile, stored at -20°C

KAc (4 000 mM)

19.626 g Potassium acetate
Dissolved in 50 mL ddH₂O
Filtered sterile, stored at -20 °C

AcP (1 000 mM)

368.2 mg Acetyl phosphate (K⁺/Li⁺ salt)
pH set to 7
up to 2 mL in ddH₂O, stored at -20 °C

***E. coli* tRNA (40 mg/mL)**

46 mg tRNA (*E. coli*)
Dissolved in 1.2 mL ddH₂O, filtered sterile
Aliquoted in 100 µL. Stored at -20 °C

S30 buffer 50×

0.5 M Tris base 60.6 g
 0.7 M Magnesium acetate tetrahydrate 150.1 g
 30 mM Potassium acetate 2.9 g
 pH set to 8.2 using acetic acid
 up to 1 L with ddH₂O, filtered sterile.

NTP 75×

360 mM ATP 409.7 mg
 240 mM GTP 251.1 mg
 240 mM CTP 253.0 mg
 240 mM UTP 272.6 mg
 Dissolved each nucleotide in 1 mL ddH₂O,
 pooled together, pH adjusted to 7 with
 NaOH, up to 8 mL in ddH₂O.
 Aliquoted in 0.5 mL, stored at -20 °C.

*2.9.2.2. Amino acids stocks***Table 2. 7:** Amino acids stocks for cell-free expression. Dissolved in ddH₂O.

Amino acid	Concentration (mM)	Mass (mg)	Volume (mL)	
L-Arginine	100	316.1	15	
L-Asparagine	100	225.3	15	
L-Alanine	100	133.6	15	
L-Aspartate	100	259.7	15	
L-Glutamate	100	304.9	15	
L-Glutamine	100	219.2	15	
Glycine	100	112.6	15	
L-Histidine	100	314.4	15	
L-Isoleucine	100	196.8	15	
L-Leucine	100	196.8	15	
L-Lysine	100	274.1	15	
L-Serine	100	157.7	15	
L-Threonine	100	178.7	15	
L-Valine	100	175.7	15	
L-Cysteine	100	181.8	15	
L-Methionine	100	223.8	15	
L-Tryptophan	100	306.3	15	20 min at 75°C in a sonication bath
L-Tyrosine	20	181.2	50	20 min at 75°C in a sonication bath

AA-Mix (4 mM each): for 50 mL

Mixed 2 mL of each amino-acids 100 mM preparation except L-Tryptophan and L-Tyrosine. Added 2 mL ddH₂O and filtered sterile (0.2 μm).

Added 2 mL 100 mM L-Tryptophan and 10 mL 20 mM L-Tyrosine.

Aliquoted in 10 mL, stored at -20 °C.

RCWMDE mix (16.7 mM each): for 24 ml

Mixed 4 mL of 100 mM L-Arginine, L-Cysteine, L-Methionine, L-Aspartate and L-Glutamate. Filtered sterile (0.2 μm).

Add 4 mL of 100 mM L-Tryptophan.

Aliquoted in 2 mL, stored at -20 °C.

2.9.2.3 Bacterial extracts

S30 *E. coli* extracts were kindly prepared and provided by B. Höger, C: Hansen and Moira Möller. **T7 polymerase** was kindly prepared by F. Helmstetter [157].

2.9.3. SDS-PAGE

4× Running Buffer

1.5 M Tris pH=8.8 54.4 g
0.4 % SDS 1.2 g
ddH₂O up to 300 mL

4× Stacking Buffer

0.5 M Tris pH=6.8 12.1 g
0.4 % SDS 0.8 g
ddH₂O up to 200 mL

10 % APS

Dissolving 10 g Ammonium persulfate in 100 mL ddH₂O. Aliquoted as 1 mL and stored at -20 °C

10×Cathode buffer

2 M Glycin
0.25 M Tris
1% SDS
pH=8.2 - 8.6

4× SDS buffer

250 mM Tris pH=6.8
40% Glycerol
0.02% Bromophenol Blue
8 % SDS
400 mM DTT

Staining solution

Diluting Rotiphorese® Blue R concentrate 6:4 in ddH₂O

Destaining solution

10% Acetic acid
30% Ethanol

2.9.4. Western blot

5× Transfer buffer stock

25 mM Tris
192 mM Glycine
0.0375% SDS

10× TBS pH=7.6

1.35 M NaCl
0.2 M Tris
pH set to 7.6 using HCl

10× Ponceau Red solution

0.5 % Ponceau red
30 % Acetic acid

2.9.5. Radiolabeled substrate transport assay

Table 2. 8: 10× pH buffers stocks.

pH	Composition	pH	Composition
pH=7.4	500 mM HEPES	pH=5.8	500 mM MES
pH=7.2	500 mM Tris	pH=5.3	500 mM Tris
pH=6.8	+ HCl	pH=4.8	+ HCl
pH=4.3	500 mM citric acid		500 mM citric acid
pH=3.8	500 mM Tris + NaOH	pH=2.8	500 mM Tris + HCl

50 mM sodium lactate stock solution

0.05603 g sodium L-lactate diluted in 10 mL ddH₂O

5× L-lactate substrate solution

100 nmol sodium L-lactate

0.04 μCi (20 μL) ¹⁴C radiolabeled L-lactate

1× pH buffer, or ddH₂O

2.9.6 Protoplasts solutions

0.2 M CaCl₂

0.29404 g in 10 mL ddH₂O

2.5 M NaCl

3.6525 g in 250 mL ddH₂O

5× MOPS

250 mM MOPS

pH set to 7.2

Protoplast buffer

50 mM MOPS pH=7.2,

Dissolved in 1.8 M saccharose using a heating magnetic stirrer (Ikamag® Ret-GS)

Volume adjusted with ddH₂O and filtrated sterile (0.2 μm)

Protoplast storage buffer

10 mM MOPS pH=7.2, 1.2 M , 50 mM NaCl, 50 mM CaCl₂,

Dissolved in 1.2 M saccharose using a heating magnetic stirrer (Ikamag® Ret-GS)

Volume adjusted with ddH₂O and filtrated sterile (0.2 μm)

2.9.7 Protein purifications

1 M Imidazole pH=8

3.404 g imidazole
+ 700 μ L 25% HCl, pH=8
Dissolved in up to 50 mL ddH₂O
Stored at room temperature or 4°C

15% Brij 78 (w/v)

1.5 g Brij 78
Dissolved in 10 mL ddH₂O
Agitated at 37°C for a few hours
Stored at -20 C

200 mM β -Mercaptoethanol

0.1399 mL 14.3 M β -mercaptoethanol diluted in 10 mL ddH₂O
Stored sealed at 4°C

50 mM EDTA: 0.75 g Tritiplex III, dissolved in 40 mL ddH₂O

10 % N-lauroylsarcosine

3 g dissolved in 30 mL ddH₂O

2.9.8. Liposomes buffers

1 M Sodium Formate

3.4005 g Sodium Formate
Dissolved in 50 mL ddH₂O
Filtered sterile (0.2 μ m)

5 mM pyranine

0.026185 g pyranine
dissolved in 10 mL ddH₂O

0.4 M HEPES pH=6.8

9.532 g HEPES
Dissolved in 100 mL ddH₂O
+ 1.2 mL 5 N NaOH

1 M NaH₂PO₄

6.9 g NaH₂PO₄
Dissolved in 50 mL ddH₂O

0.5 M Na₂HPO₄

4.45 g Na₂HPO₄
Dissolved in 50 mL ddH₂O

5 mM Sodium Phosphate pH=6.8

231.5 μ L 0.5 M Na₂HPO₄
268.5 μ L 1 M NaH₂PO₄
pH adjusted to 6.8
diluted up to 50 mL in ddH₂O

5 mM Sodium Phosphate pH=5.8

39.5 μ L 0.5 M Na₂HPO₄
230.2 mL 1 M NaH₂PO₄
pH adjusted to 5.8
diluted up to 50 mL in ddH₂O

5 mM Sodium Phosphate pH=7.8

448.75 μ L 0.5 M Na₂HPO₄
26 μ L NaH₂PO₄
pH adjusted to 7.8
diluted up to 50 mL in ddH₂O

0.1 M HEPES/MES pH=6.8

1.1915 g HEPES
 0.976 g MES
 Dissolved in 50 mL ddH₂O,
 adjusting the pH to 6.8

1 M KCl

3.728 g KCl
 Dissolved into
 50 mL ddH₂O

1 M sucrose

17.115 g sucrose
 Dissolved into 50 mL ddH₂O
 Filtered sterile (0.2 μm),
 stored at 4°C

Sucrose-HEPES pH=6.8 gradient

50 mM HEPES pH=6.8	2.5 mL 4× HEPES pH=6.8					
% sucrose (w/v)	0 %	5 %	15 %	20 %	25 %	60 %
	0 g	0.5 g	1.5 g	2 g	2.5 g	6 g

Volume adjusted to 10 mL in ddH₂O
 Filtrated sterile (0.2 μm) and stored at 4°C

TCA solution

10 g TCA, dissolved in 4 mL ice cold ddH₂O. Stored at -20°C

10× PBS pH=7.4

1.37 M NaCl
 27 mM KCl
 100 mM Na₂HPO₄
 18 mM KH₂PO₄
 pH set to 7.4
 Up to 100 mL in ddH₂O

2.10. Commercial kits

Product	Provider
Wizard® Plus SV Minipreps DNA Purification System	<i>Promega, Mannheim</i>
HiYield® PCR Clean-up/Gel Extraction	<i>Süd-Laborbedarf, Gauting</i>
NucleoBond® PC 500	<i>Machery-Nagel, Düren</i>
Clarity™ Western ECL Substrate	<i>Bio-Rad, München</i>
Quick Start™ Bradford Protein Assay	<i>Bio-Rad, München</i>
Pierce™ BCA Protein Assay Kit	<i>Thermo Scientific™</i>
JetPRIME® transfection reagents	<i>Polyplus</i>

2.11. Consumables

Product	Provider
1 mL single-use syringes	<i>CB Healthcare, Hambourgh, Germany</i>
12 and 96-wells plates	<i>Sarstedt, Nümbrecht, Germany</i>
15 ml and 50 ml polypropen, sterile centrifuge tubes	<i>Sarstedt, Nümbrecht, Germany</i>
2, 5, 10 and 20 mL Norm-Ject® syringes	<i>Eydam Labor Technik & Lehrmittel</i>
20 mL Henke-Ject® syringes	<i>Henke Sass Wolk, Tuttlingen, Germany</i>
50 mL centrifuge tube with scew cap, polypropene	<i>Carl Roth, Karlsruhe</i>
Amersham™ Hybond™ P 0.45 PVDF membrane	<i>GE Healthcare, Freiburg</i>
Amicon® Ultra-4 centrifugal filters Ultracell (100K and 30K)	<i>Merck Millipore Ltd.</i>
Cellstar® tissue culture flasks, (550 mL 175 cm ² and 250 mL 75cm ²)	<i>Sarstedt, Nümbrecht, Germany</i>
Cellstar®Tubes, 15 and 50 mL	<i>Greiner bio-one</i>
Cryo.s™ polypropen tubes with screw cap	<i>Greiner bio-one</i>
Cuvettes, polystyrol (10 × 4 × 45 mm)	<i>Sarstedt, Nümbrecht, Germany</i>
Dialysis tubing, Visking® (14 kDa MWCO)	<i>Carl Roth, Karlsruhe</i>
Fine-Ject® (276 × 3/4" 0.40×20 mm and 236 × 1/4" 0.6×30 mm)	<i>Henke Sass Wolk, Tuttlingen, Germany</i>
Glass beads (acid-washed, Ø 425-600 µm)	<i>Sigma Aldrich, München</i>
K65HM-CE/KP65HM-CE High density paper	<i>Mitsubishi electric corporation, Japan</i>
Kimtech Science precision wipes	<i>Kimberley-Clark® Professional</i>
Micro tubes (1.5 ml, 2 ml)	<i>Sarstedt, Nümbrecht, Germany</i>
Parafilm “M”	<i>American National Can, Chicago, USA</i>
PCR strips (8-strip opt. clear flat caps)	<i>Sarstedt, Nümbrecht, Germany</i>
PCR tubes Multiply®-Pro 0.2 ml, PP	<i>Sarstedt, Nümbrecht, Germany</i>
PD-10 columns	<i>GE Healthcare</i>
Perha-Soft® nitrile gloves	<i>Hartmann</i>
Pipette tips	<i>Sarstedt, Nümbrecht, Germany</i>
Poly-Prep® Chromatography Columns	<i>Bio-Rad, München</i>
Scintillation vials, Snaptwist® (6.5 ml, HDPE tube)	<i>VWR, Darmstadt</i>
Serological pipettes	<i>Sarstedt, Nümbrecht, Germany</i>
Slide-A-Lyzer™ Dialysis Cassette (10 kDa MWCO, 3 ml)	<i>Thermo Fisher Scientific, Schwerte</i>
Sterile filter, Filtropur S 0.2	<i>Sarstedt, Nümbrecht, Germany</i>
Sterile filter, Filtropur S 0.45	<i>Sarstedt, Nümbrecht, Germany</i>
TC Dish 100, Standard	<i>Sarstedt, Nümbrecht, Germany</i>
Ultracentrifuge polypropylene tubes (1.5 ml)	<i>Beckman Coulter, Krefeld</i>
Whatman Grade GF/C Glass Micro-fiber filter (25 mm)	<i>GE Healthcare, Freiburg</i>
Whatman™ Grade 3MM CHR Blotting Paper	<i>GE Healthcare, Freiburg</i>

2.12. Equipment

ÄKTA purifier™ 10 Superdex 200 10/30 GL	<i>GE Healthcare, Freiburg, Germany</i>
Cell-free reaction chambers (preparative and analytical)	<i>Beitz lab, CAU Kiel, Germany (Supp. 5)</i>
Centrifuges and rotors	
Optima™ XL-80K Ultracentrifuge 50.2 Ti and SW60 Ti Rotors 26.3 mL, Polycarbonate Bottle, 25 × 89 mm	<i>Beckman Coulter, Krefeld, Germany</i>
Multifuge 1S-R 75002006 Fixed Angle Rotor 75002000 Swinging Bucket Rotor 75002002 Centrifuge Buckets	<i>Heraeus, Hanau, Germany</i>
Centrifuge 5424 R	<i>Eppendorf, Hamburg, Germany</i>
Perfectspin 24 Plus	<i>Peqlab, Erlangen, Germany</i>
DNA 110 SpeedVac®	<i>Savant Instruments, Farmingdale, USA</i>
Biofuge™ Pico	<i>Heraeus, Hanau, Germany</i>
WiseSpin, type CF-10	<i>PMI Labortechnik, Wettingen, Germany</i>
Clean benches	
HeraGuard HeraSafe	<i>Heraeus, Hanau, Germany</i>
DNA electrophoresis and imaging	
VV-E 24W Microwave	<i>Panasonic</i>
Electrophoresis Power Supply EPS 300	<i>Pharmacia Biotech, Stockholm, Sweden</i>
UV-Transilluminator UVT-20 S/M	<i>Herolab, Wiesloch, Germany</i>
IDA Image Documentation & Analysis 1.2 9-inch Monitor, model EM-09	<i>Elysia-Raytest, Straubenhardt, Germany</i>
BI Video copy processor	<i>Chugai Boyeki Co. LTD</i>
Freezing container: Mr. Frosty™	<i>Mitsubishi</i> <i>Thermo Fisher Scientific</i>
Fridges and refrigerators	
Ultra low temperature Freezer	<i>New Brunswick Scientific, Edison, USA.</i>
Comfort NoFrost Premium NoFrost	<i>Liebherr, Germany</i>
Heat blocks	
Techne Dri-Block® DB-2D QBT heatblock	<i>Fisher Scientific, Schwerte</i> <i>Grant</i>

Incubators

Incubator Kelvitron® t
Minitron and Ecotron incubators
Incubator WTC Binder 9010-0021
APT.line™ C 150 (E2) CO² Incubators

Heraeus, Hanau, Germany
Infors HT, Bottmingen, Germany
Binder, Tuttlingen, Germany

Lysis

French® Press Cell disrupter
French® Pressure Cell
Sonopuls mini20 homogeniser

Thermo Electron Corporation
Bandelin

Magnetic stirrers

Ikamag® Ret-GS
Variomag mono

IKA-Werke, Staufen, Germany
Variomag-USA, Daytona Beach, USA

Microscopes

Confocor2
AxioVert.A1 microscope
IX50 Inverted Phase Contrast Microscope
Fuchs-Rosenthal counting chamber
Neubrand Improved counting cell

Zeiss
Olympus
Superior, Germany
Blau Brand, Germany

PAGE and Imaging

PerfectBlue Dual Gel System Twin S
Gel casting bases
Power Pac 200 Power Supply
Trans-Blot® SD Semi-Dry Transfer Cell

Peqlab, Erlangen, Germany
Bio-Rad, München, Germany

pHmeters

Digital pH meter Lab 850
Seven Compact

Schott Instruments, Mainz, Germany
Mettler Toledo

Photometers and Spectrometers

BioPhotometer 6131
Infinite F200 plate reader
LS 5S Fluorescent Spectrometer
Quartz cuvette
UV/Vis Spectroscopy cells

Eppendorf, Hamburg, Germany
TECAN
Perkin Elmer
Helma, Jena
Perkin Elmer

Pipettes, pipetting aids

0.2-2 µL UA 56553
2-20 µL NC 50610
20-200 µL NC 52197
0.1-1 mL NC 52032
RF3000 Pipette Controller

Gilson, Middleton, USA
Heathrow Scientific

accu-jet® pro Pipette Controller
FORTUNA ® POLYFIX ® Dispenser

*Brand GmbH + CO. KG, Wertheim
Poulten&Graf, Wertheim, Germany*

Printer and Scanner

MS510DN Printer
Photographic Scanner HP Scanjet G4050

*Lexmark
HP*

Pump: Diaphragm Pumps 400171

ILMVAC GmbH, Ilmenau Germany

Scales/Balances

Electronic balance ABS 120-4
PB3002-S Delta Ranger
Cubis®

*Kern & Sohn, Balingen, Germany
Mettler-Toledo, Gießen, Germany
Satorius. Göttingen, Germany*

Shakers

Dual-Action Shaker KL 2
Tilt Shaker WS 10
TC-7 rotator
Grant Bio PTR-30 360-degree Rotator
 PRS-4/12, platform
Certomat® MoII
Certomat®

*Edmund Bükler, Bodelshausen, Germany
Edmund Bükler, Hechingen, Germany
New Brunswick Scientific. Edison, USA.
Keison International, Essex, Great Britain
Biosan
Satorius, Göttingen, Germany
B. Braun Biotech International*

Scintillation Counter: Tri-Carb 2900TR

Packard, Downers Grove, USA

Sonication baths

Sonorex RK514 sonication bath
Sonorex Super RK514 BH

Bandelin

Stopped-flow

Stopped-flow mixing system SFM 2000
Microprocessor unit MPS 70/2
Monochromator BH-10-61
UV/Vis-Photometer MOS-200
Power Supply ALX 250
Signal Amplifier PMS 250
Cuvette FC-15/7,5
AD (v.2) and F12 temperature controls

*BioLogic Science Instruments,
Claix, France*

JULABO Labortechnik GmbH, Germany

Thermocyclers

Thermocycler Primus HT 25
Biometra TRIO Thermocycler

*Clemens, Waldbüttelbrunn, Germany
Analytik Jena, Jena*

Vortex: Vortex® Genie 2

Scientific Industries, Bohemia, USA

Water bath: GLF 1083

Gesellschaft für Labortechnik. Burgwedel, Germany

Water source

Water purification system Puraninity TU
PURELAB® Flex

VWR, Darmstadt, Germany
ELGA

2.13. Software

2.13.1. Laboratory software

Software	Producer
Bio-Kine Version 4.74.2	<i>BioLogic, Claix, France</i>
Chimera 1.14	<i>Resource for Biocomputing, Visualization, and Informatics at the University of California</i>
ChimeraX 1.5 [158], [159]	<i>National Institutes of Health</i>
ImageJ	<i>DNASTAR®</i>
Lasergene 7.2.1	<i>Microsoft Corporation, Redmond, USA</i>
Microsoft Office 365, Version 2010	<i>OriginLab Corporation, Northampton, MA, USA</i>
Origin 2020 9.7.0.185	<i>Schrödinger, LLC</i>
PyMOL 1.7.4.1	<i>Adobe Systems Inc.</i>
Photoshop® Elements 11.0	<i>Systat Software Inc</i>
SigmaPlot 11.0	<i>Dotmatics</i>
SnapGene® Viewer	

2.13.2 Online software

DeepL translator (free version) [cited in May 2023],
Accessible at <https://www.deepl.com/translator>

Adaptive Poisson-Boltzmann Solver and PDB2PQR [160], [cited in March 2023],
Accessible at <https://server.poissonboltzmann.org/>

3Dmol [161] , [cited in March 2023].

OligoCalc [162], [cited in March 2023].
Accessible at <http://biotools.nubic.northwestern.edu/OligoCalc.html>

The Sequence Manipulation Suite [163], [cited in March 2023] .
Accessible at <https://www.bioinformatics.org/sms/index.html>

ExPASy ProtParam [164], [cited in March 2023].
Accessible at <https://web.expasy.org/protparam/>

ExPASy Translate, [cited in March 2023].

Accessible at <https://web.expasy.org/translate/>

NCBI protein BLAST, [cited in March 2023].

Accessible at <https://blast.ncbi.nlm.nih.gov/Blast.cgi?PAGE=Proteins>

AlphaFold [165], [166], [cited in April 2023].

Accessible at <https://alphafold.ebi.ac.uk/>

EMBL-EBI Clustal Omega [167], [cited in March 2023].

Accessible at <https://www.ebi.ac.uk/Tools/msa/clustalo/>

Prot pi | Protein Tool [cited in March 2023].

Accessible at <https://www.protpi.ch/Calculator/ProteinTool>

3. METHODS

3.1. Molecular biology

3.1.1. Restriction enzyme digestion

Digestion of DNA was done with the appropriate restriction enzymes corresponding to the sites present in the sequence, using the appropriate buffer condition (as specified by the manufacturer, detailed in 2.4.2.). 1 to 10 μg of DNA and about 1 unit of enzymes (u) were mixed in a 1.5 mL Eppendorf tube with buffer stock and diluted in H_2O . The total reaction volumes were comprised between 10 and 20 μL . Digestion occurred at 37 °C from 1 h to overnight. When applicable, double digestions were done by using two enzymes together in a compatible buffer. Otherwise, the digestion was done in two steps, with either a DNA clean-up step or a heat inactivation of the previous enzymes, and the adjustment of the buffer conditions between each digestion.

**Table 3. 1: Appropriate buffers for restriction enzymes,
provided by Thermo Fisher Scientist**

Buffer	Compatible restriction enzyme
Tango	DpnI, PstI, SpeI, XbaI
Green	BamHI, EcoRV, HindIII, SpeI, SphI(PaeI), XbaI, XhoI
Red	EcoRV, HindIII, PflMI, SacI, XhoI
Orange	EcoRI
Blue	SphI(PaeI)
Unique	BamHI, KpnI

3.1.2. Polymerase Chain Reaction (PCR).

Polymerase Chain Reaction (PCR) was used to amplify divers DNA sequence, serving a variety of purposes such as replicating plasmids for Site-directed mutagenesis, amplifying genes between restriction sites for cloning, or introducing new sites for plasmid editing.

Different polymerases were used, each necessitating a different reaction mix, as described below:

Pfu PCR

1.5 μ L 25 μ M Primer sense
 1.5 μ L 25 μ M Primer antisense
 1.5 μ L DMSO
 4 μ L 2.5 mM dNTPs
 0.5 μ L template DNA
 5 μ L 10 \times Cloned *Pfu* reaction buffer AD
 34.2 μ L ddH₂O
 1.8 μ L Turbo *Pfu* Polymerase

OneTaq PCR

1.5 μ L 25 μ M Primer sense
 1.5 μ L 25 μ M Primer antisense
 1.5 μ L DMSO
 4 μ L 2.5 mM dNTPs
 0.5 μ L template DNA
 10 μ L 5 \times OneTaq buffer
 30.5 μ L ddH₂O
 0.5 μ L OneTaq Polymerase

The *Pfu* polymerase has a higher replication fidelity than OneTaq. The addition of DMSO slightly improved primer binding specificity but it's volume could be replaced by ddH₂O without loss of PCR efficiency. The template DNA concentration ranged from 0.5 to 500 ng depending on the experiment. Controls were done by replacing template volume with ddH₂O. The PCR reaction mixes were gently homogenised using a pipette before the addition of polymerase. DNA sequences were amplified by cycles of melting, annealing and extension:

Table 3. 2: Typical program used for PCR

Initial denaturation	95-98°C for 5 min
~ 30 cycles	Melting 95-98°C for 30 s
	Annealing Annealing temperature for 30 s
	Elongation 68°C for the elongation time
Final elongation	68°C for the elongation time
Storage	4-16°C indefinitely

The elongation time was adjusted for each amplified DNA sequence, considering that the polymerases can replicate about 1000 base pair per minute. Each primer pair was designed in such way that their melting temperatures were within 5 °C of each other. The annealing temperature for PCR was defined approximately 5 °C below the lowest melting temperature of the pair. Melting temperatures were determined either by the oligonucleotide manufacturer or by using the online software OligoCalc [162]. For primers smaller than 13 nucleotides, the following equation is used to calculate the basic melting temperature:

$$Tm (^{\circ}C) = (wA + xT) \times 2 + (yG + zC) \times 4 \quad (5)$$

Where w, x, y, z are the respective number of the A, T, G and C nucleotides in the sequence [162], [168].

For primers longer than 13 nucleotides, the following equation was used:

$$Tm (^{\circ}C) = 64.9 + 41 \times \frac{yG + zC - 16.4}{wA + xT + yG + zC} \quad (6)$$

Where w, x, y, z are the respective number of the A, T, G and C nucleotides in the sequence [162], [169].

After PCR, the amplified DNA was most of the time separated on an agarose gel and extracted (3.1.4).

3.1.3. Site-directed mutagenesis.

Exchanging single amino acids in the coding sequence of a protein (PffNT) were achieved using Site-directed mutagenesis. PCR reactions were done as described (3.1.2.) with the distinction of using a longer elongation time as the primer used are intended to elongate the entire plasmid and introduce a few nucleotide mismatches. The PCR method was the same as described in the OneTaq PCR (Table 3.2. Using the proofreading *Pfu* polymerase would have been more appropriated. After the amplification of the plasmid, the methylated initial plasmid templates are digested overnight using DpnI (either in 1× Tango or added directly into the PCR mix).

Table 3.3: Annealing temperatures of the oligonucleotides pairs used for Site-directed Mutagenesis.

Primer	Tm Provider	Tm OligoCalc	T° annealing
SDM_PffNT-Y285A_s	61	55.7	
SDM_PffNT-Y285F_s	58	52.3	54
SDM_PffNT-Y285_as	58	53	
SDM_PffNT-E289Q_s	61	56	54
SDM_PffNT-E289_as	59	53.7	

DNA strands were separated according to their size using agarose gel electrophoresis. Agarose powder was mixed in 50 mL TEA buffer and melted in a microwave. After adjusting the volume back to 50 mL with ddH₂O and ensuring the agarose was properly dissolved, 1 µL of DNA-intercalating ethidium bromide (10 mg/mL) was mixed to the solution once it had cooled down to be handled manually. After mixing, the gel was cast and let to cool down, either at room temperature or on a cold aluminium plate before placing in an electrophoresis chamber filled with TAE buffer. Percentages of agarose varied between 0.5 and 2 % w/v depending on the size of the DNA to isolate. Orange G buffer was added to the DNA samples (1:10) before loading on the gel wells. Electrophoresis was done at 120 V and 0.4 A for 15 to 40 min, depending on the desired resolution. DNA fragments size were estimated by comparison with λ phage DNA digested overnight with PstI (Supp. 3).

3.1.4. DNA extraction from agarose gels

To recover pure DNA after a digestion or a PCR and extracting a DNA band from an agarose gel, the HiYield® PCR Clean-up/Gel Extraction kit was used, following the manufacturer protocol.

3.1.5. Introduction of DNA fragments into plasmids

To introduce DNA fragments in digested vectors, complementary primer pairs were dissolved in ddH₂O to a concentration of 1 µM and mixed together in a 1:1 ratio (up to a volume of 50 µL). Using a Thermocycler, these primers were heated at 95 to 98 °C for 5 min and gradually cooled down to 8 to 16 °C. The following table details the primer pairs annealed together.

Table 3. 4: Primer pairs for self-annealing

	Primer sens (s)	Primer anti-sens (as)
A	BamHI_insert_s	BamHI_insert_as
B	XbaI-strepII-Xa-BamHI_TDPCR_s	XbaI-strepII-Xa-BamHI_TDPCR_as
C	HindIII-Xa-X-10His-KpnI_s	H-Xa-X-10His-K_as

of undigested vector or self-religation, controls are prepared using ddH₂O instead of the DNA insert.

Table 3. 6: composition of a typical ligation mix.

Digested DNA vector:	1-3 μ L
Water control/Digested DNA insert:	7-4 μ L
10 \times T4 DNA ligase buffer:	1 μ L
Autoclaved ddH ₂ O:	up to 9 μ L
T4 DNA ligase:	1 μ L

3.1.8. *E. coli* transformation

Aliquots of 100 to 50 μ L frozen competent cells (brought from Roche or kindly prepared by A. Fuchs [170]), previously stored at - 80 °C, were thawed on ice for 3-5 min until liquid. Then 10 to 20 μ L of ligation mix was added and mixed using a pipette. The cells were incubated on ice at least 30 min before being heat-shocked 1 min at 42°C. The cells were then kept on ice for a few minutes until adding 0.9 mL of LB culture media and incubating 45 to 60 min at 37 °C. Finally, cells were pelleted using 30 s of centrifugation at maximum speed and resuspended in 100 μ L. These cells were plated on LB agar plates containing the appropriate selection antibiotics (in most cases, ampicillin) and incubated overnight at 37 °C or at room temperature for a few days. Once colonies had grown, such plates were stored at 4 °C for a few weeks.

For the long-term storage of transformed *E. coli*, bacteria cultures were mixed with autoclaved 80 % glycerol (up to a final concentration of 27 to 40 %), then flash-frozen in liquid nitrogen before being stored at -80 °C. To start cultures from these glycerol stocks, scraps of the frozen cells could be plated onto LB agar plates (supplemented with the appropriated selection antibiotic, usually Ampicillin) or could be used to inoculate LB media for cultures.

3.1.9. *E. coli* plasmid extraction

3.1.9.1. DNA Minipreps and Maxipreps

The DH5 α *E. coli* strain was exclusively used for the expression and extractions of plasmid DNA. Small-scale DNA extractions (100-400 μ g/mL) were done by using Wizard® Plus SV Minipreps DNA Purification kit (Promega) and adapting the manufacturers indications.

Large - scale DNA extractions were done using the NucleoBond™ PC 500 kit (Macherey - Nagel) and adapting the manufacturer's instructions.

3.1.9.2. Determining DNA concentrations

Once extracted as described below, the DNA concentration of the plasmid preparations were determined using Optic Spectroscopy, measuring their absorbance at 260 nm according to the following equation:

$$DNA\ concentration\ (\mu g \cdot mL^{-1}) = 50\ (\mu g \cdot mL^{-1}) \times A_{260nm} \times dilution\ factor \quad (7)$$

The purity of DNA was assessed by calculating the ratio of A_{260nm}/A_{280nm} , with values higher than 1.8 denoting pure DNA.

3.1.9.3. Ethanol precipitation of plasmid DNA

To increase the purity of a plasmid preparation, the DNA could be precipitated. In an Eppendorf tube, for 1 volume of DNA solution, 0.1 volumes of 3 M sodium acetate pH=4.5 solution and 2.5 volumes of ice-cold ethanol (99%) were added. The DNA was left to precipitate at -20 °C for at least 20 min, then was pelleted at 12,000 g for 15 min at 4 °C. After discarding the supernatant, the pellets were washed with 200 μ L of 70 % ethanol and centrifuged again under the same conditions. After removing the ethanol, the DNA pellets were dried in a vacuum centrifuge and resuspended in 20 μ L ddH₂O.

3.2. Methods for protein identification

3.2.1. Bradford protein quantification assay

When applicable, the protein concentration in samples was determined using the Quick Start™ Bradford Protein Assay (Bio-Rad) [171]. Briefly, when the Coomassie molecules contained in the staining solution forms complexes with the protein's amino acids, their maximal absorbance shifts from 465 nm to 595 nm. 2 to 10 μ L of samples containing 1 to 20 μ g of protein were diluted in ddH₂O up to a volume of 800 μ L. 200 μ L of 5 \times Roti®-Quant concentrate was added. The samples were mixed by vortexing and incubated at room temperature for 5 to 15 min. The absorbances at 595 nm were measured using a light spectrometer against a blank prepared the

same way using only buffer. The corresponding protein concentration was determined by comparison with a calibration curve of BSA standard solution ranging from 1 to 20 $\mu\text{g/mL}$, according to the following calibration curve:

$$f(x) = 0.0312x - 0.0077 \quad (8)$$

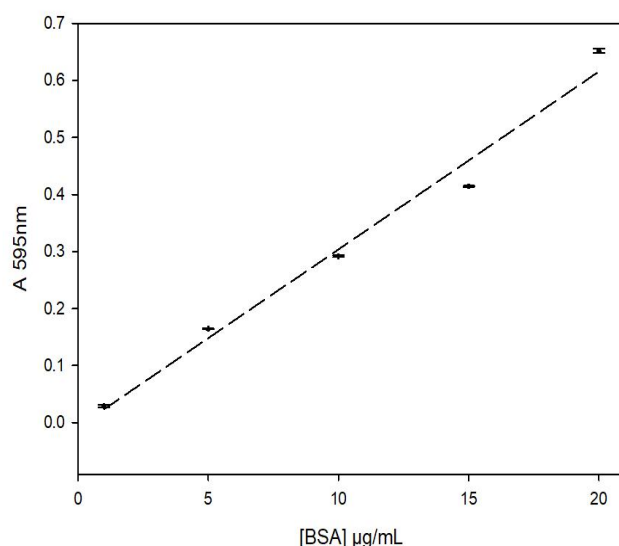


Figure 3. 2 : Calibration curve of BSA measured with the Bradford assay. The error bars denote SEM (n=3).

3.2.2. BCA

The protein concentration of CAIV samples could be assessed using the Pierce™ BCA Protein Assay Kit (Thermo Scientist™) according to the manufacturer's instructions.

Briefly, a set of calibration samples containing 1 mg/mL, 0.75 mg/mL, 0.5 mg/mL, 0.25 mg/mL, 0,125 mg/mL and 0 mg/mL of BSA were prepared. 50 μL of these probes were precipitated, dissolved in reagent solution, incubated at 60°C for 20 min and finally loaded in a 96 well plate. The absorbance of these samples was then measured at 595 nm (instead of the optimal 562 nm) using a plate reader (Infinite F200, TECAN). A calibration curve correlating the BSA standards concentration and absorbance could be determined, and used to determine the protein concentration in the other samples.

3.2.3. TCA precipitation

To increase the concentration of a protein sample, usually in order to load it in a SDS gel, the proteins could be precipitated using Trichloroacetic acid (TCA).

2.5 g of Trichloroacetic acid were dissolved in 1 mL of H₂O in preparation of the precipitation and stored at -20°C. For each protein sample to concentrate, it was diluted 4:1 with the ice-cold TCA solution (typically: 700 µL of protein samples and 175 µL of TCA solution) and incubated for 30 min at 4 °C until a white protein precipitates forms. Then, the samples were centrifuged at maximal speed (Centrifuge 5424 R, Eppendorf) and 4°C for 30 min and the supernatants discarded. The pellets were washed three times with cold acetone. Each time, 875 µL of acetone were added, the samples were incubated 5 min at room temperature, then pelleted by centrifuging 5 min at 4°C and maximal speed. Removing the acetone without washing away the pellet was critical.

Finally, each precipitated protein pellet was resuspended in 20 µL PBS and incubated either 1 h on ice or overnight at 4°C, before being used for Bradford assays and SDS-PAGE.

Occasionally, the TCA precipitated samples may be too acidic if the TCA was not thoroughly washed away. It is noticed when the SDS-PAGE sample turns yellow upon mixing and incubating the precipitated protein with 4× SDS buffer. This high acidity can prevent the sample from running properly in the PAGE gel and can be corrected by adding a few µL of base (KOH or NaOH) until the sample turns blue again.

3.2.4. SDS-PAGE

SDS-denatured proteins were separated depending to their charge and size in vertical, two-dimensional polyacrylamide gel electrophoresis (PAGE).

Polyacrylamide gels were cast by assembling a glass and ceramic plates, separated by 1 mm by two plastic spacers, and loading the polymerizing gel (after the addition of TEMED). First, 5 cm of running gel are loaded onto the cast and a thin layer of isopropanol was added on top of it to smooth the meniscus. After about 30 min of polymerization, the layer of isopropanol was removed (by inverting the cast) and the polymerizing loading gel was loaded. A plastic comb was added to form the wells (10 or 12 wells). Once fully set, the comb was removed and the gel could be either used immediately or stored covered in a wet paper towel in a plastic bag, at 4 °C for about a week.

Table 3. 7: Preparation for two gels

<u>Running gel</u>	7.5 %	10 %	12.5 %	15 %	20 %
ddH₂O (mL)	6.75	6	5.25	4.5	1
4× Running gel buffer (mL)	3	3	3	3	3
40 % Acrylamide (29:1) (mL)	2.25	3	3.75	4.5	8
10 % APS (μL)	80	80	80	80	80
TEMED (μL)	10	10	10	10	10

<u>Stacking gel</u>	5 %
ddH₂O (mL)	2.4
4× Stacking gel buffer (mL)	1
40 % Acrylamide (29:1) (mL)	0.6
10 % APS (μL)	25
TEMED (μL)	6

Protein samples were prepared for SDS-PAGE by diluting them in 4× SDS-PAGE buffer and denaturing the protein either 1 h at 37°C, 20 minutes at 60°C (for membrane proteins) or 5 min at 95°C (for soluble protein). Under the combined action of the DTT (reducing the disulfide bonds), the SDS (disrupting the non-covalent protein bonds) and heat, the protein unfolds and are coated with negatively charged SDS molecules.

The samples were loaded on the gels alongside 5 to 7 μL of protein ladder, usually PeqGOLD Protein Marker III, Peqlab (see supplementary materials Supp. 4). First, the electrophoresis is run at 160-170 V, 2 A for 15-20 min to concentrate the proteins in the stacking gel. Then, the voltage is increased to 200 V for 30 to 50 min while the proteins separate according to their sizes through the running gel.

3.2.4.1. Coomassie staining

SDS-PAGE gels were stained for at least 1 h in Rotiphorese® Blue R solution, at room temperature, agitated in a rotary shaker while the proteins are stained with Coomassie molecules. The gels were then washed with water and incubated 10-30 min in destaining solution until the protein bands were visible. To improve the removal of the background Coomassie, the stained gels could be left to soak in water overnight (with the optional addition of a paper towel to soak up the dye) or could be briefly boiled up in water in a microwave.

3.2.4.2. Western Blot

The proteins separated in SDS-PAGE gels could be identified by Western Blot, using a semi-dry system to transfer it on a membrane.

Polyvinylidene difluoride (PVDF) membranes were first activated for 30 s in methanol then soaked in Transfer buffer (5 mM Tris, 38.4 mM Glycine, 0.0075% SDS, 20% Methanol) alongside two stacks of three pieces of Whatman paper each (6.5 × 9 cm) (Figure 3.3). The stack is gently pressed with a roll to ensure all air bubbles were removed then wetted again with a few mL of transfer buffer. These stacks were sandwiched between the anode and cathode plates and the proteins were transferred from the gel to the membrane by applying a voltage of 17 V, a tension of 2 A, for 30 min in the case of soluble proteins, 1 h for membrane proteins.

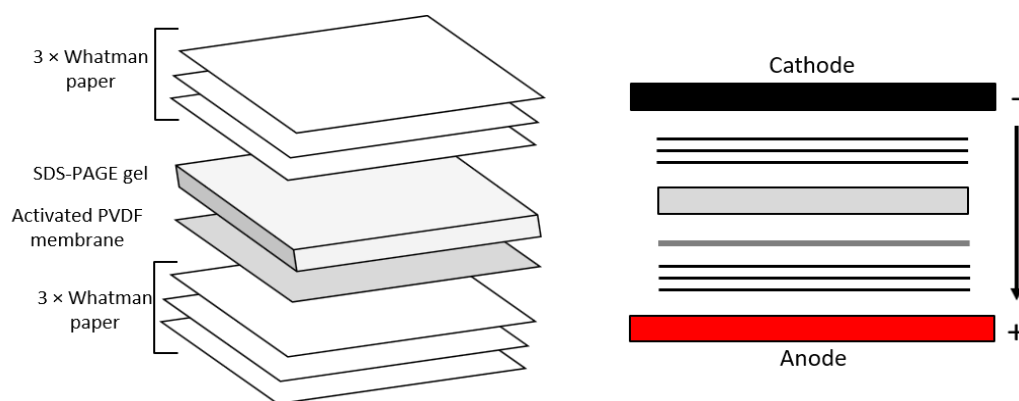


Figure 3. 3: Schematic representation of the blotting step of a Western Blot.

The membranes were blocked for 1 h at room temperature in 20 mL of a saturated solution of milk proteins TBS pH=7.6, 0.1% Tween, 5% milk powder (TBS-T, 5% milk) under constant agitation (tilt-shaking). Then, the blocking solution was replaced with 10-20 mL TBS-T, 5% milk containing the appropriate concentrations of primary antibodies. The membranes were incubated between 4 h and overnight at 4°C under constant agitation (tilt-shaking), then rinsed three times with 10 to 20 mL TBS-T for 10 min at room temperature under constant agitation (tilt-shaking) to remove non-specifically bound antibodies. The primary antibody solutions were recovered and stored at -20 °C before reuses. After the rinses, the membranes were incubated for 1 to 2 h, at room temperature under constant agitation (tilt-shaking) in 10-20 mL TBS-T, 5% milk containing the appropriate concentrations of horseradish peroxidase (HRP) conjugated secondary antibodies. These secondary antibody solutions were also recovered, frozen at - 20 °C before reuses. The membranes were once again rinsed 10-20 mL TBS-T for 10 minutes at room temperature under constant agitation (tilt-shaking).

The presence of the proteins of interest in the membrane was revealed by coating it in a 1:1 mix of Clarity™ ECL Western blotting substrates (Bio-Rad) containing luminol and hydrogen peroxide. The Electro Chemo Luminescent (ECL) activity of HRP catalyze these two substrates into 3-aminophthalate weakly emits light at 425 nm that is detected using a Chemostar Touch ECL & Fluorescence Imager (INTAS Science Imaging Instruments, Göttingen) (Figure 3.4).

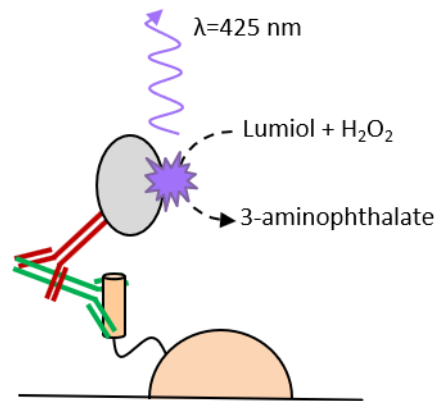


Figure 3. 4: Schematic representation of the Western Blot principle. The epitope of the protein (beige) blotted on the PVDF membrane (black horizontal line) are recognized by the primary antibodies (green), themselves recognized by secondary antibodies (red) bound to horse radish peroxidase (Grey).

3.2.4.3. Ponceau Red staining

To verify that the blotting of the SDS-PAGE proteins was efficient and homogenous, the membranes could be stained by incubating in 10 mL of 1× Ponceau Red solution for 10 min at room temperature, under constant agitation (tilt-shaking). Once stained, the membranes were rinsed with 10-20 mL water until most of the dye got removed. This step could be done before the blotting or after the ECL revealing.

3.2.4.4. Observing the in-gel fluorescence

The fluorescence of GFP protein that resisted denaturation during SDS-PAGE was monitored using the Chemostar Touch ECL & Fluorescence Imager (INTAS Science Imaging Instruments, Göttingen).

3.3. Methods for protein purification

3.3.1. Immobilized metallic anion chromatography

Most of the recombinant proteins expressed in our lab are fused to a terminal poly-Histidine tag (His₁₀) for Immobilized metallic anion Chromatography (IMAC) purification.

A volume of agarose beads chelating nickel (II) cations using nitrilotriacetic acid (NTA) bought as a 50% slurry stored in 30% ethanol (HisPur™, Thermo Fisher) was loaded in a Poly-Prep® Chromatography column (BioRad). After eluting the storage solution, the resin was washed with at least six to ten column volumes of washing buffer (usually composed of 50 mM Tris pH=8, 150 mM NaCl, appropriate detergent concentrations and eventually protease inhibitors). The rest of these steps were then done in the cold (4°C or on ice).

Once the resin was equilibrated, it was recovered in a small volume of washing buffer and mixed with the cell lysate to purify. The binding of the proteins of interests to the resin occurs by incubating this mixture for at least 30 minutes, under gentle agitation. When dealing with samples containing a high amount of endogenous histidine-rich proteins, a low concentration of imidazole (5 to 20 mM) was added. The resin-lysate mix was then loaded back onto the chromatography column, and the non-binding proteins are left to elute by gravity in the flow-through.

Then, the resin was washed with 4 to 7 column volumes of elution buffer: 50 mM Tris pH=8, 150 to 300 mM NaCl, ± detergents, containing increasing concentrations of imidazole. In this work, proteins tags with His-tags eluted upon reaching between 100 and 300 mM imidazole. After the elution was over, the resin was recovered in a volume of buffer to verify that no more proteins of interest stayed trapped in it. Every collected fraction could have its protein concentration measured (generally using the Bradford assay) and used to prepare SDS-PAGE that would allow to estimate the purity of the recovered proteins.

For further analysis, the proteins fractions of interests were pooled and concentrated. Since high concentrations of imidazole can affect further analysis, the buffer was changed, either by diluting down the imidazole during protein concentration or by dialysis.

3.3.2. Streptavidin-purification

The proteins labeled with the Strep II -tag peptide (Trp-Ser-His-Pro-Gln-Phe-Glu-Lys) can be trapped in resins of agarose beads bound to engineered streptavidin from *Streptomyces avidinii* for streptavidin purification.

Streptavidin Agarose Resin (Thermo Fisher) 50% slurry in 0.02% sodium azide was loaded in a Poly-Prep® Chromatography column (BioRad) and washed with 10 resin volumes of 20 mM Tris pH=8, 150 mM NaCl, 0.05% Brij78. The equilibrated resin was then mixed with the crude extract containing the proteins of interests for 30 min to 1 h at room temperature.

The resin-protein mix was then loaded back onto the chromatography column and eluted by gravity flow. The flow-through, containing the contaminant proteins were collected for analysis. Proteins remaining in the resin through non-specific interaction were washed away with 5 volumes of 20 mM Tris pH=8, 150 mM NaCl, 0.05% Brij78, then eluted in at least 5 volumes of the same buffer containing 2.5 mM then 5 mM desthiobiotin.

Finally, the resin could be regenerated by addition of at least 5 resin volumes of buffer containing 1 mM HABA (2-(4'-hydroxy-benzeneazo)benzoic acid turning the resin color from yellow to red in the process. The regenerated resin was then washed with Strep-Wash buffer until the red color disappears.

3.3.3. Ion Exchange chromatography

The Ion Exchange Chromatography (IEX) is used to separate proteins according to their surface charge. The resin used (Q Sepharose® FastFlow, Sigma Aldrich) is composed of 90 µm agarose beads cross-linked to quaternary ammonium cations. After equilibrating the resin in buffer containing a minimal concentration of sodium chloride (20 mM Tris pH=8, 100 mM NaCl), the proteins were loaded and the flow through discarded. They were then eluted with buffer containing increasing concentration of sodium chloride and were collected for further analysis.

3.4. Production of proteins in *E. coli*

3.4.1. Culture conditions and induction

The production of protein can be induced in the *E. coli* BL21 (DE3) [153] cultures by the addition of Isopropyl β -D-1-thiogalactopyranoside (IPTG).

During this work, two types of plasmids could be used to transform the BL21 (DE3). The pET21X or pET28a(+), carrying a LacI gene that allows for the repression of the polymerase expression and the lacO regulated protein of interest (which prevents expression leakage before induction), and pIVEX 2.3w, whose T7 promoter allows the expression of protein of interest (when the addition of IPTG induces the T7 polymerase expression).

This production system was used for the expression of two different proteins: membrane scaffold protein and soluble carbonic anhydrase. The details depend on which protein were expressed, as described in the following table:

Table 3. 8: Summary of the methods used for the of BL21(DE3) expression of proteins

Protein expressed	(m)CAIV(p)	MSP
Adapted method	Idrees <i>et al.</i> [172]	Rues <i>et al.</i> [173]
Induction OD_{600 nm} =	0.6	1
Culture media	LB	LB +0.5% glucose,
Selective antibiotic	100 ng/mL Amp	40 ng/mL Kan
IPTG concentration	+ 0.5 mM (or less)	+ 1 mM
Incubation time		1 h 37°C
and temperature	16°C for 15 h	28°C for 4-5 h

The resulting cultures were pelleted using centrifugation and the pellets frozen at -80 °C before protein extraction and purification.

3.4.2. Cell lysis

3.4.2.1. Sonication:

In the case of expression tests and small volumes of pellets, the cells were lysed using sonication. Once resuspended in 1.5 mL of appropriate lysis buffers, the cell suspensions were lysed on ice with twelve cycles of 30 s sonication at 750 joules and 30 s of cooling. The

suspended proteins were separated from the cellular waste by centrifugation at maximal speed for 10 min at 4°C.

3.4.2.2. French Press lysis

Larger pellets resuspended in 20-40 mL of appropriate cell lysis buffer were lysed using a hydraulic French pressure cell press following the manufacturer's instruction (Figure 3.5). Briefly, the suspended cells were loaded in the cell body, sealed with the piston and the plug. The sample was then pressed up to 1500-2000 psi. Pressure was released by slightly opening the valve and the flowing lysate was collected. The samples typically went through 3 to 4 cycles of pressure to achieve an efficient lysis, noted when the turbid white suspension turned translucent and brownish. The suspended proteins were separated from the cellular waste by centrifugation 30 000 g for 30 min at 4°C (50.2Ti rotor).

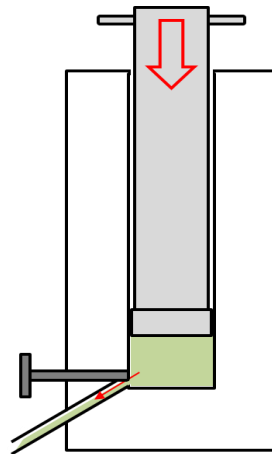


Figure 3. 5: Schematic representation of the French press Lysis. A hydraulic press applies pressure to the device via the piston (light grey) and compresses the cell suspension (green) through the small opening left by the screw (dark grey).

The soluble proteins present in the lysate would later be purified, according to the methods previously described (3.3.).

3.5. Protein production in yeast

3.5.1. Yeast transformation

To study the transport activity of heterologous monocarboxylate transporter, the yeast strain used in this work had been modified so it does not express the endogenous lactate transporter Jen1 and Ady2 [155], [174] and was kindly provided by M. Casal [154]–[156].

The protocol for the chemical transformation of yeasts was adapted from Gietz, R.D. and Woods [175] by B. Wu [176]. Naïve yeast cells are grown on YPD agar plates and incubated at 29°C for 3-5 days until colonies form. A single colony was picked to inoculate 5 mL YPD and incubated overnight at 29°C with shaking at 200-220 rpm. The preculture was used to inoculate 50 mL YPD in a 250 mL Erlenmeyer flask to an OD₆₀₀ of 0.2. The culture was incubated at 29°C, 200-220 rpm until it reached an OD₆₀₀ of 0.6. The culture was harvested by centrifugation at 2500-4000 g for 5 min at 4°C. The cell pellet was washed with 25 mL water, collected, resuspended in 1 mL water, and split in 100 µL aliquots in 1.5 mL Eppendorf tubes. The yeast cells were pelleted by centrifuging for 30 s at maximal speed using a benchtop centrifuge and the supernatant removed. Each pellet was re-suspended in 360 µL of transformation mix composed of 240 µL polyethylene glycol 3500, 36 µL 1 M lithium acetate, 34 µL water and 50 µL boiled single-stranded carrier DNA (2 mg/mL DNA sodium salt type III from salmon testes, in 10 mM Tris-HCl, pH=8.0, and 1 mM EDTA), and placed on ice. Up to 1 µL of plasmid solution containing 100 to 200 ng DNA was added. The cells were heat - shocked at 42°C for 45-60 min, and immediately cooled on ice. For plating, the cell suspension was pelleted (30 s at max speed, benchtop centrifuge) and re-suspended in 1 mL water. 50 to 200 µL were plated on SD-ALWH agar plates and incubated at 29°C for 3 to 5 days until colonies formed. These plates can later be stored at 4°C up to a few months.

3.5.2. Yeast culture cultures

Yeasts colonies growing on SD ALWH agar plates were picked to inoculate 5 mL SD ALWH liquid media, and incubated at 29°C, 200-220 rpm for 20-24 h. Main cultures of 50 mL SD ALWH were inoculated such that an OD_{600 nm} of 1 was reached after an overnight incubation

at 29°C, 220-220 rpm. The inoculating OD was calculated using the equation (where *time* is the incubation time and *d* is the doubling time of the yeast):

$$initial\ OD_{600\ nm} = \frac{1}{2^{\frac{time}{d}}} \quad (9)$$

3.5.3. Yeast glycerol stocks

For the long-term storage of transformed yeasts, overnight cultures (prepared as described above) were mixed in a 1:1 ratio with autoclaved 80 % glycerol (up to a final 40 % glycerol), then flash-frozen in liquid nitrogen before being stored at -80 °C. To start cultures from these glycerol stocks, the frozen cells could be plated onto SD-ALWH or YPD agar plates and incubating at 29°C for several days, or could be used to inoculate SD media for cultures, incubated at 29°C and 220 rpm for at least two days.

3.5.4. Extraction of the microsomal fraction from *S. cerevisiae*

50 to 100 mL of yeast culture at an optical density of 600_{nm} of 1 ± 0.1 are harvested in 50 mL tubes by centrifuging at 4 000 g for 5 min, at 4°C two times and discarding the supernatant. The yeast pellets are washed by resuspending in 10 mL 10 mM Tris-NaOH pH=8, 1 mM EDTA, centrifuging at 4 000 g for 5 min, at 4°C and discarding the supernatant, then frozen at -80 °C for at least 30 min, usually overnight. The yeast pellets are thawed on ice, resuspended in 0.5 mL of buffer TE and 0.5 g of acid-washed glass beads are added. The cells were broken by twelve cycles of 30 s of vortexing then 30 s on ice. The solution was then centrifuged at 1 000 g for 5 min at 4 °C to recover a cleared suspension of disrupted cells. This step could be repeated after adding 0.5 mL of 10 mM Tris-NaOH pH=8, 1 mM EDTA. The high-density cellular wastes are removed by centrifuging at 10 000 g for 5 min at 4 °C and only recovering the supernatant. Microsomal fractions were collected by ultracentrifugation at 100 000 g for 45 min at 4 °C, resuspending the membrane pellet in 100 µL of PBS pH=7.4. Such proteins could be analysed using SDS - PAGE.

3.5.5. Intracellular yeast pH determination

To monitor intracellular pH in yeast transporting L-lactate, the cells were loaded with the pH-sensitive 5'(6')-carboxyfluorescein-diacetatesuccinimidyl-ester (CFDA-SE, Sigma Aldrich). A. Jansen [57], [151] adapted the protocol developed by Bracey *et al.* [177].

Cultures of the Yeast cells expressing the proteins of interest were collected at an OD_{600 nm} of 0.8 ± 0.05 , washed in an equal volume of ddH₂O, and resuspended in 50 mM HEPES/Tris, pH=6.8, prepared from the corresponding 10× pH buffer stock. The cells were subsequently incubated at 37°C for 24 h under agitation in an equal volume of 100 μM CFDA-SE in 50 mM HEPES/Tris, pH=6.8, with 2% DMSO. Extracellular CFDA-SE was removed by centrifugation at 10,000 g for 5 min, and yeasts cells were resuspended in 50 mM HEPES/Tris, pH=6.8, three times, ensuring the absence of excess or leaked dye in the buffer. Fluorescence was excited at $\lambda_{ex1} = 435$ nm (isosbestic point, pH-independent) and $\lambda_{ex2} = 495$ nm (pH-dependent), and emission intensity was determined at $\lambda_{em} = 525$ nm (LS 55 fluorometer with a QS 4/4 mm quartz cuvette, Perkin Elmer) before and after the addition of 1 mM L-lactate at room temperature. Each expression construct was measured in triplicate. The internal pH values were determined from the emission ratios by using the previously established calibration function determined by A. Jansen [57]:

$$f(pH_i) = -3.4238 + 5.4077x - 1.9197x^2 + 0.2033x^3 \quad (10)$$

Where x is the time and pH_i the internal pH value. The resulting points were fitted as linear polynomial curves curve (SigmaPlot 14.5, Polynomial linear) using the following equation:

$$f(x) = y_0 + ax \quad (11)$$

Where x is the time, $y_0 = f(0)$, and a the variation for each time point, determined during fitting.

3.5.6. Preparation of yeasts protoplasts

Yeast protoplasts were prepared by following and adapting the protocol described by L. Petersen [219]. 100 mL of MCT1 expressing yeasts cultures were incubated overnight in SD-AWLH media, at 29°C, 220 rpm. Upon reaching an OD₆₀₀ $\approx 1 \pm 0.1$, these cultures were harvested in 50 mL tubes by centrifuging 5 min at 2000 g and 4°C: Then the pellet was resuspended in 3 mL of 50 mM MOPS pH=7.2, 0.2% β-mercaptoethanol, centrifuged again

under the same conditions and after carefully discarding the supernatant, the pellets were weighted and kept on ice. Then, the pellets suspended in 2 mL 50 mM MOPS pH=7.2, 0.2% β -mercaptoethanol and were incubated 15 min at 30°C, gently agitated. After that, the volumes were adjusted up to 6 mL with Protoplast buffer (50 mM MOPS pH=7.2, 1.8 M saccharose, 2.9.6.) containing 600 units of Zymolase® 20t (ROTH) per g of pellet, 100 mg of Albumin Fraction V (BSA, ROTH) and incubated 60 min at 30°C, gently agitated to digest the yeast cell walls. The yeast protoplasts were recovered by centrifuging 5 min at 2000 g and 4°C, gently resuspending the pellets in 5 mL Protoplast storage buffer (10 mM MOPS pH=7.2, 1.2 M saccharose, 50 mM NaCl and CaCl₂, 2.9.6.), by centrifuging again 5 min at 2000 g at 4°C and finally gently resuspending the pellet in the same storage buffer. Such protoplasts were stored at 4°C for no more than a day.

3.6. Radiolabeled substrate transport assay in yeasts

The following methods have been adapted from the protocol developed by J. Rambow [178] and B. Wu [176]. Briefly, the activity of the yeast expressed lactate transporters were assayed by measuring the intracellular amount of radiolabeled substrate in yeasts expressing the proteins of interests. L-lactate was labeled with ¹⁴C. min⁻¹)

3.6.1. Uptake of radiolabeled substrate

3.6.1.1. Uptake assay

Yeast cultures were harvested at an OD₆₀₀ of 1 ± 0.1 , in 50 mL tubes (4000 g, 5 min, 4°C). The yeast pellets were washed with 25 mL ice-cold water, and re-suspended in ice-cold 1× pH buffer (Table 2.8) to a final OD_{600 nm} of 50 ± 5 . These yeast cells suspensions were kept on ice at all times before measures and appeared to remain fit for measurements for a few hours [115]. In 1.5 mL Eppendorf tubes, 80 μ L of yeast suspension were warmed to room temperature (18 to 20 °C) in an aluminium block for 2 to 5 min before initiating the import of substrate by mixing with 20 μ L of 5× L-lactate substrate solution (2.9.5.). The final suspension contained 1 mM of lactate spiked with radiolabeled substrate (0.04 μ Ci, Hartmann Analytic, Braunschweig, Germany) in an OD_{600 nm} of 40. The substrate uptake was stopped by diluting the cells in 1 mL of ice-cold water and immediately transferring onto GF/C glass microfiber filters (GE

Healthcare, Solingen, Germany) for vacuum filtration. The filters were washed with 5 to 7 ml of ice-cold water, transferred into scintillation vials containing 3 mL of scintillation cocktail ROTISZINTeco plus (Carl Roth, Karlsruhe, Germany), and dissolved overnight.

The radioactive isotope $^{14}_6\text{C}$ decays into $^{14}_7\text{N}$, emitting β^- radiation (electrons). The proprietary scintillation cocktail contains aromatic molecules that emit fluorescence when exposed to β radiations, thus allowing to measure the relative amount of radioactive isotope in each sample using the Packard TriCarb 2900TR liquid scintillation counter over 2 min. It generates for each sample the value of their counts per minutes (cpm). These values are later used to calculate the corresponding concentrations of transported substrate.

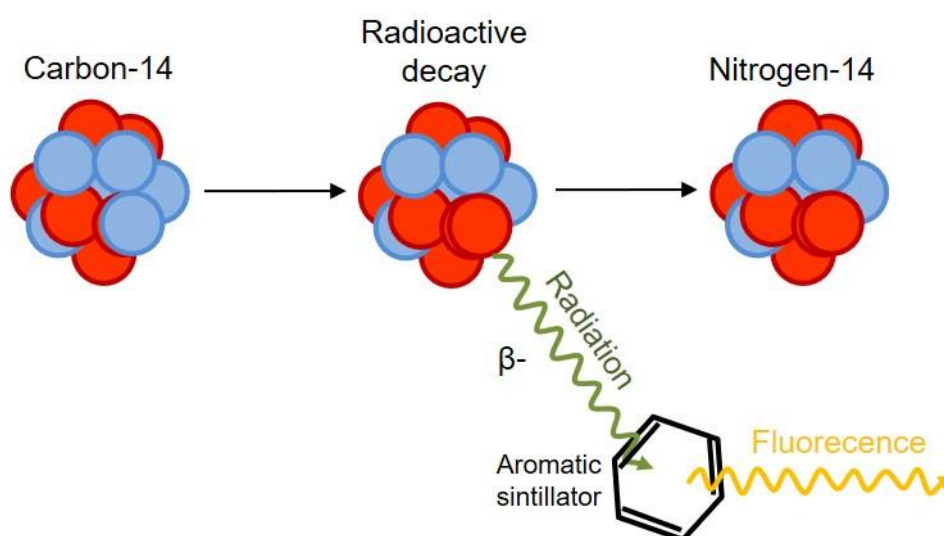


Figure 3. 6: Schematic representation of the principles behind β radiation detection

3.6.1.2 Calculating the intracellular substrate concentrations

For each experiment, duplicates of 20 μL of $5\times$ L-lactate substrate solution were also directly injected in 3 mL of scintillation cocktails. The average cpm measured in these samples (max) represents 100.72 nmol of total lactate substrate (their variations were considered negligible). Therefore, the cpm counts of the other samples were translated into nmol units using the following equation:

$$\text{substrate}_{(nmol)} = \frac{\text{cpm sample}}{\text{cpm max}} \times 100.72 \text{ nmol} \quad (12)$$

This amount of substrate measured in the yeasts of each sample was normalised to the mass of yeast pellets. It had been previously determined by A-L Köpnick that 80 μL of yeast suspensions at an OD_{600} of 50 contains 5.6 mg of dry cell mass [115]. Therefore:

$$[\textit{substrate}]_{\textit{nmol} \cdot \textit{mg}^{-1}} = \frac{\textit{substrate}_{(\textit{nmol})}}{5.6 \textit{mg}} \quad (13)$$

A. Jansen determined that in the yeast system, a cytosolic L-lactate concentration of $0.28 \pm 0.03 \text{ nmol} \cdot \text{mg}^{-1}$ corresponds to 1 mM of transported substrate [151], meaning that the concentration units can be converted as follows:

$$[\textit{substrate}]_{\textit{mM}} = \frac{[\textit{substrate}]_{\textit{nmol} \cdot \textit{mg}^{-1}} \times 1_{\textit{mM}}}{0.28_{\textit{nmol} \cdot \textit{mg}^{-1}} (\pm 0.03)} \quad (14)$$

To simplify calculations and better appreciate the experimental variation, the errors of the yeast cell pellets and cytosolic L-Lactate concentration to 1 mM were usually considered negligible.

For each experimental condition, values were measured from biological and technical duplicates or triplicates. The substrates concentrations were expressed as an average of these values. Their error was expressed as standard error of the mean (SEM, equation 16, where N is the number of replicates), itself calculated from the sample standard deviation (σ , equation 15), using the Windows Excel function STDV.S.

$$\sigma = \sqrt{\frac{\sum_{i=1}^N ([\textit{substrate}]_{\textit{sample}} - [\textit{substrate}]_{\textit{average}})^2}{N - 1}} \quad (15)$$

$$\textit{SEM} = \frac{\sigma}{\sqrt{N}} \quad (16)$$

For each experimental condition, a set of control values (duplicates or triplicates) were collected by applying the same experimental process to a suspension of yeast that does not express lactate transporter: Such yeasts are W303-IA $\Delta\textit{jen1} \Delta\textit{ady2}$, transformed with an empty pDRTXa (or derivative) plasmids that encodes for the URA selection gene. The amount of radioactivity measured in such samples is not representative of any transport but of the experimental background noise, created by radioactive molecules staying trapped in the yeast cell walls or filter despite the washes. Such background values are subtracted from the transported substrate concentrations, carrying the error across the calculations.

3.6.1.3. Substrate uptake curves

The substrate influx was measured at fixed pH, with variable transport times from 30 seconds to 32 min. After calculating the background-subtracted concentrations of intracellular substrate, the data points were fitted (SigmaPlot 14.5, exponential rise to a maximum, single, 2 parameters) using the following equation:

$$f(t) = a \times (1 - e^{-bt}) \quad (17)$$

Where a is the limit and b the rate constant.

From the equation, the initial rate of transport was determined from the slope of the curve during the initial phase, at $t=0$. These measured rates depend on the level of transporter expression as well as their activity. The plateau of the curve represents the maximal uptake capacity at the transport equilibrium.

3.6.2. Substrate efflux

Measuring the efflux was similar to the measures and calculation of influx transport but differs in two points. First,

The yeast cells were initially loaded with substrate spiked with radiolabeled isotopes by adding $5 \times$ L-lactate substrate solution to room temperature yeast suspension (OD_{600} of 40 ± 4) and incubated for a definite amount of time, at a defined pH. Incubating for 8 min was enough to load the cells with radiolabeled substrate. Setting the pH to 4.8 helped increase the initial uptake. Then, the yeast cells are pelleted by centrifugation (13 500 g, room temperature), the supernatant removed and the pellet resuspended in $1 \times$ pH buffer (Table 2.8), thus initiating the efflux transport. Then, the substrate efflux was stopped at the desired time point by removing 100 μ L of sample, centrifuging it quickly, discarding the supernatant and resuspending the yeast pellet in 1 mL ice-cold water. Finally, vacuum filtrated in GF/C glass microfiber filters and dissolved in scintillation cocktail overnight. Counting and calculating the background-subtracted intracellular concentration of substrate in these samples was done as previously described (3.6.1.2.).

The data points were fitted as an exponential decay (SigmaPlot 14.5, exponential decay, single, 3 parameters) as the following equation:

$$f(t) = y_0 + ae^{-bt} \quad (18)$$

Where t is the efflux time.

The intracellular substrate can be expressed in nmol · mg⁻¹, or in percentages of the initial load, by determining $f(t = 0) = y_0 + a = 100\%$.

3.6.3. IC₅₀ measures

Measurements of the half-maximal inhibitory concentration (IC₅₀) of inhibitors were done by following the method developed by A. Goldack [179]. Radiolabeled substrate uptake is measured at fixed pH and a fixed transport time (30 s to 3 min). Before initiating the substrate transport, the yeast cells suspensions are mixed and incubated at room temperature with increasing concentrations of inhibitors dissolved in 1 μL DMSO (1.25% final DMSO concentration). Counting the intracellular concentration of substrate in these samples was done as previously described. The data points are fitted to sigmoidal curves (Sigma Plot 14.5, Sigmoidal, 4 parameters):

$$f([inhibitor]) = y_0 + \frac{a}{1 + e^{-\left(\frac{[inhibitor]-x_0}{b}\right)}} \quad (19)$$

Where y₀, x₀, a and b are parameters determined during the fitting.

A typical inhibition curve should be composed of maximal transport plateau at lower inhibitor concentrations (maximum plateau = y₀ + a, equation 19) and a minimal transport plateau at higher inhibitor concentration (minimum plateau = y₀, equation 19).

The transport values can be translated in percentages of transport activities for each inhibitor concentration according to the following equation:

$$\text{Activity } \% = 100 \times \frac{\text{sample} - \text{minimum}}{\text{maximum} - \text{minimum}} \quad (20)$$

The IC₅₀ value is determined by calculating the inhibitor concentration corresponding to the halfway point on the inhibition curve between the minimum and the maximum plateaus.

3.6.4. pH dependency of transport

Measuring the effect of external pH on transport uptake was done by using a fixed transport time (during which the transport rate can be fitted linearly) at different pH. After the yeast cultures were pelleted and washed in ddH₂O they were resuspended in ddH₂O up to an OD_{600 nm} of 55 ± 5. To prepare equivalent yeasts suspensions at different pH values, 9 volumes of yeasts are mixed with 1 volume of 10× pH buffer stock (Table 2.8), reaching a final OD_{600 nm} of 50 ± 5.

After incubating the yeast suspension at room temperature for 2-5 min, transport was initiated by the addition of 5× L-lactate substrate solution (2.9.5.). The substrate uptake was stopped by diluting the cells in 1 mL of ice-cold water, transferring onto GF/C glass microfiber filters (GE Healthcare, Solingen, Germany) for vacuum filtration, washing with 5-7 ml of ice-cold water, transferred into scintillation vials containing 3 mL of scintillation cocktail ROTISZINTeco plus (Carl Roth, Karlsruhe, Germany), and dissolved overnight. Counting and calculating the background-subtracted intracellular concentration of substrate in these samples was done as previously described (3.6.1.2.).

The *P_fFNT* pH dependent rates are expected to display a peak [51], [57], [60]. They are therefore fitted as such (Sigma Plot 14.5, peak, Gaussian, 3 parameters) according to the following equation:

$$f(pH) = ae^{(-\frac{1}{2} \times (\frac{pH-x_0}{b})^2)} \quad (21)$$

Where x_0 , a and b are parameters determined during the fitting.

The curves corresponding to MCT1 protein constructs were reported to have more complex patterns [180].

3.7. Cell-free production of proteins

The cell-free transcription and translation system was adapted by A. Müller-Lucks [149] and S. Bock [144] from the protocol of Schwarz *et al.* [181], [182].

The DNA encoding the proteins of interests was inserted into pIVEX 2.3w with a T7 promoter. The transcription of the plasmid DNA into RNA was done by the phage T7 polymerase. Stocks were kindly prepared by F. Helmstetter and stored at -80°C. The protein translation machinery (ribosomes and translation factors) was extracted from *E. coli* fermenter cultures. The 30 000 g (S30) extract were kindly prepared by B. Höger, M. Möller and C. Hansen and stored aliquoted at -80°C.

The cell-free synthesis was done in specialized purpose-build chambers (described in Supp. 5), separating a reaction mix from a feeding mix by semipermeable membranes (10-14 kDa MWCO). Ribosomes, polymerases and other enzymes are kept in the reaction mix, while the feeding mix supply amino acids and other reaction precursors, while dialyzing small molecular weights byproducts that could impede the protein synthesis.

The cell-free reactions are incubated at 30 °C in a shaking water bath for 20 to 24 h.

Small-scale cell-free protein syntheses were prepared to screen for optimal reaction conditions, such as magnesium and potassium concentrations, or detergents. 70 µL of reaction mix are separated from 900 µL of feeding mix by a piece of 10 kDa MWCO dialysis membrane. Such protein synthesis reaction produces enough proteins to observe GFP fluorescence and proteins in SDS-PAGE.

For the preparation of large-scale cell-free protein syntheses, up to 3 mL of reaction mix are loaded onto a 3 mL Slide-A-Lyzer™ dialysis cassettes with semipermeable membranes (10 kDa MWCO), separated from 17 to 32 mL of feeding mix. To stop the expression, the reaction mix was extracted from the cassette and placed on ice for 1 h. Such reaction typically produces between 0.5 and 1.5 mg of proteins, further purified using IMAC.

The preparation of the reaction and feeding mixes are detailed in the following tables:

Table 3. 9: Preparative cell -free expression Master mix

	Stock concentration	Final concentration
NaN ₃	10 %	0.05 %
PEG8000	40 %	2 %
KAc	4000 mM	150.8 mM
Mg(OAc) ₂	1000 mM	variable *
Buffer H-E	24 ×	1 ×
Protease inhibitor	50 ×	1 ×
Folinic acid	10 mg/mL	0.1 mg/mL
DTT	500 mM	2 mM
NTP	75 ×	1 ×
PEP	1000 mM	20 mM
AcP	1000 mM	20 mM
AA-Mix	4 mM	0.5 mM
RCWMDE	16,67 mM	1 mM
detergent		variable [†]
H ₂ O		variable

Table 3. 10: Preparative cell -free expression Feeding mix

	Stock concentration	Final concentration
Master mix		
H ₂ O		
AA-Mix	4 mM	1.05 mM
S30 Buffer	1×	0.35 ×

Table 3. 11: Preparative cell -free expression Feeding mix

	Stock concentration	Final concentration
Master mix		
Pyruvate kinase	10 mg/mL	0.08 mg/mL
E.coli tRNA	40 mg/mL	0.7 mg/mL
T7-RNA polymerase	350 u/μL	15 u/μL
RNAse inhibitor	40 u/μL	0.3 u/μL
DNA template	variable	0.023 mg/mL
S30-Extract	1×	0.35
H ₂ O		

* The optimal concentration of Magnesium ions for each S30 Extracts stocks were previously determined to be 7.1 mM by B Höger, M. Möller and C. Hansen.

† PffNT was expressed in the presence of 0.8% Brij78 which had previously been established as the optimal detergent composition [144], [183], [184]. During the cell-free syntheses of soluble proteins such as mCAIVp, the detergent volume was replaced by water.

3.8. Protein production in human embryonic kidney cells

These following methods were applied following the methods of I. Jakóbowska [185].

3.8.1. HEK 293 T-REx cell cultures conditions

Human embryonic kidney cells (HEK) 293 T-REx had previously been stably transfected with a pcDNATM6/TR vector (Invitrogen, USA) encoding for a tetracycline (Tet) repressor and a blasticidin resistance gene. They are cultured on 10 cm plates in 10 mL of Dulbecco's Modified Eagle Media (DMEM) with 4.5 g/L D-glucose and L-glutamine (Gibco) enriched with 10% (v/v) fetal bovine serum (FBS) (FBS Premium, PAN Biotech), 1% penicillin (100 u/mL) and streptomycin (100 μg/mL) (Gibco) and 5 μg/mL blasticidin. The cells plates were incubated at 37°C, 5% CO₂ in humid conditions provided by a water pan filled with 5 mM EDTA or

2% Copper(II) sulfate solution. The cells transfected with pCGTO plasmids were selected by the addition of 100 ng/mL of Zeocin (inVivoGen). Some other antibiotics and inhibitors could be added to the culture media for further selections.

HEK 293 cells doubling time is approximately one day. Once cells reached confluence on a plate they needed to be split. Their culture media was removed, the cells washed with 5 mL Dulbecco's Phosphate Buffer Saline (DPBS) containing CaCl_2 and MgCl_2 (Gibco) and detached by incubating 3 to 5 min at 37°C in 1 mL of 0.05% trypsin-EDTA (Gibco). Once detached, the trypsin-EDTA volume is diluted 1:8 with 7 mL of culture media, cells were separated by pipetting with serological pipette and diluted in a new plate with fresh media. While the cells were growing, the media was regularly removed and replaced.

3.8.2. Determination of HEK 293 T-REx cell culture density

Once cells were suspended using trypsin, as described above, the cell numbers can be determined. A volume of cell suspension (10 μL) was added between the glass slits of a 0.1 mm deep Neubrand Improved counting cell (Blau Brand, Germany). The counting cells contains 4 area of 4×4 squares of 0.0025 mm^2 each (0.04 mm^2 in total). By counting the number of cells in the 0.04 mm^2 surface, the cell density is determined as follows:

$$\text{Cell density (cells/mL)} = \text{cells in } 0.04 \text{ mm}^2 \times 10\,000 \quad (22)$$

3.8.3. Preparation of plasmids for HEK 293 T-REx production

The DNA encoding P_fFNT carrying the mutations G107S, G21E or V196L, each responsible to the resistance to the BH296 inhibitor had been designed in pDRTXa by J.D.R Schmidt. These sequences were amplified by PCR, flanked by EcoRI and HindIII consensus sequences (PCR_EcoRI-P_fFNT_s and PCR_P_fFNT-HindIII_as_2, Table 2.4) and cloned into the pCGTO-GFP-myc vector. These plasmids were sent to I. Jakóbowska who measured the inhibitor affinity for the different mutants [67], [185].

To construct a pCGTO plasmid that would encode for the expression of His-tagged protein, the HindIII-Xa-X-10His-KpnI_s and H-Xa-X-10His-K_as oligonucleotides were annealed then inserted in pCGTO plasmid (Table 3.8, C and Figure 3.1, C). In parallel, P_fFNT mutant coding sequences from pDRTXa plasmids were amplified by PCR using the PCR_EcoRI-P_fFNT_s and PCR_10His-KpnI_as primers (Table 2.4). The resulting products were extracted, digested

and inserted in pCGTO, thus replacing the coding sequence of the GFP, linkers and tags from the original plasmids. These plasmids encode PffNT mutants tagged with a C-terminal His₁₀.

3.8.4. HEK 293 T-REx cells transformation

Naïve HEK 293 T-REx cells were seeded on a 10 cm plate to a density of 2×10^6 cells/mL and incubated overnight at 37 °C 5% CO₂. The next day, the cells were transfected using the JetPRIME® Transfection reagent kit (Polyplus) and following the manufacturer instructions, described below. First, 4 µg of the DNA of interest were diluted up to 244 µL in the proprietary JetPRIME® transfection buffer, briefly vortexed to mix then pelleted. 6 µL of proprietary JetPRIME® reagent were added, briefly vortexed to mix then pelleted, then incubated 30 min at room temperature.

Finally, the mix was added drop by drop to the naïve cells plate and swirled to homogenize. The cells were incubated overnight at 37 °C, 5% CO₂ before starting the screening process.

3.8.5. Screening for genomic integration and protein expression

The plasmids used in HEK 293 T-REx transfection were pCGTO plasmids, encoding encodes the *Sh ble* gene (from *Streptoalloteichus hindustanus*), conferring resistance to Zeocin®. Therefore, to screen for the proper integration of the plasmid during transfection, the cells were cultured in media containing 100 ng/mL Zeocin® for three weeks, splitting the cells when necessary.

PffNT protein expression in transformed HEK 293 T-REx cells was induced by the addition of 1 µg/mL tetracycline upon reaching 40 to 60% confluence and were incubated overnight (37 °C, 5% CO₂).

To use these cell lines to produce PffNT, we needed to ensure the cell line neither over nor underproduce the PffNT mutants. Overexpression of protein can have a detrimental effect on the cell growth and can also lead to the formation of inclusion bodies. In the absence of a GFP domain allowing to visualize the expression and localization of PffNT in the cell, indirect methods were employed to ensure the His₁₀-tagged PffNT was functional.

Benjamin *et al.* [186] described how to induce lethality in cancer cells by exposing them to metformin hydrochloride (inhibiting the regeneration of NADH into NAD⁺ by the mitochondrial complex I) and the MCT1 and MCT4 inhibitor syrosingopine (which leads the accumulation of cytosolic lactate, eventually inhibiting the lactate dehydrogenase activity). Together, these two inhibitors make the accumulation of cytosolic lactate, usually cytostatic, into a complete inhibition of the main pathways regenerating NAD⁺, which leads to cell death. By using this principle, F. Becker devised a culture condition (0.1 μM AZD3965 and 4 mM metformin hydrochloride) that should kill all cells unable to transport lactate out of their cytosol. The MCT1 inhibitor AZD3965 was used instead of syrosingopine [112]. Thus, only the cells expressing functional PffNT would be able to grow.

Such selection was applied to the transformed cells for about two to three weeks.

3.8.6. Storage of HEK 293 T-REx cells

Confluent HEK 293 T-REx cells were detached using trypsin (3.8.1.) and transferred in a 15 mL tube. The cells were centrifuged at 600 to 1000 g for 5 min at room temperature, the supernatant discarded and the cell pellet resuspended in 3 mL cell freezing medium (90% FBS, 10% DMSO). The suspension was split in two 1.5 mL screw-cap cryo-tubes, placed in a Mr. Frosty™ freezing container filled with isopropanol and placed in a -80 °C freezer for a few days. For long-term storage (more than a week), the frozen cells were stored in liquid nitrogen.

To start a culture from such frozen cells, the cryo-tubes were briefly thawed at room temperature and their content added to culture media before incubating the cells overnight (37 °C, 5% CO₂). The culture media was replaced the next day to remove the DMSO.

3.8.7. HEK cells membrane protein extraction

For each membrane protein of interests, transformed and selected HEK 293 T-REx were grown in culture media containing 100 ng/mL Zeocin, 1 μg/mL tetracycline, 4 mM metformin and 0.1 μM AZD3965, 0.001% DMSO. Once they reached 80-100% confluence, the media was removed and the cells were washed with 10 mL PBS pH=7.4. Then, the cells were resuspended in 10 mL PBS pH=7.4 by pipetting up and down. The cell suspensions were pooled accordingly in 50 mL Falcon tubes and pelleted by centrifuging around 1000 and 4000 g for 5 min. Then

the supernatant was carefully discarded and the cell pellet frozen at - 80 °C for at least 1 h. The cell pellets, once thawed on ice, were resuspended in 2 mL ice-cold TBS pH=7.4 or TBS pH=8, supplemented with protease inhibitor (cOmplete EDTA-free, Roche) and lysed by sonication. Using the Sonopuls sonicator equipped with a MS 1.5 tip (Bandelin), the suspensions were lysed by alternating 30 s of sonication at 8 W, followed by a period of cooling down on ice, for no less than 30 s. Several cycles were repeated until the suspensions turned from turbid to translucent, which usually took between 15 and 30 cycles. After clearing the lysate from wastes and debris, the membranes were pelleted by ultracentrifugation (100 000 g, 1 h, 4°C). The resulting pellets were dissolved in TBS pH=8 mixed with protease inhibitor, their protein concentration estimated using the Bradford assay, then frozen at -20°C

3.9. Protein reconstitution in proteoliposomes

The liposomes prepared in this work were unilamellar lipid vesicles in which detergent micelles-suspended proteins could be reconstituted. Cell-free expressed transporters were reconstituted in such proteoliposomes to assess their transport functionality using stopped-flow spectroscopy.

3.9.1. Lipid preparation

The lipids used were either a mix of *E. coli* polar lipids extracts or 1,2-diphytanoyl-sn-glycero-3-phosphocholine (abbreviated as 4ME 16:0 PC), both bought from Avanti polar Lipids, Inc, or a suspension of 25 mg/mL of powder *E. coli* lipid extract bought from Avanti polar Lipids, Inc dissolved in chloroform.

A volume of 1 mL of lipids dissolved in chloroform at a concentration of 25 mg/mL were transferred in a glass tube, filled with nitrogen and briefly stored on ice sealed with a cork. The tubes were inclined on ice and span while applying a constant stream of gaseous nitrogen, to evaporate the chloroform until a lipid film formed at the bottom and sides of the tubes. These lipid films were dried at room temperature in an exicator at - 600 to - 650 mbar for at least 4 h. 1 mL of buffer containing 2 mM of β -mercaptoethanol was added to the dried lipid film, left 2 h at room temperature to rehydrate then vortexed to resuspend, until the solution became milky white. During these stages, the solution was kept a sealed tube containing nitrogen in order to prevent lipid oxidation. Finally, the lipid suspension was split in 200 μ L aliquots in

1.5 mL Eppendorf tubes filled with nitrogen, incubated 10 min on ice to remove air bubbles, flash-frozen in liquid nitrogen and stored at - 80°C

3.9.2. (Proteo)Liposome preparation

200 µL aliquots of prepared lipids (as described above) were thawed on ice and diluted up to 500 µL in the appropriate buffer (usually 20 mM HEPES pH=6.8). The lipids were then sonicated in a cool water bath, 30 min three times, changing the water between each step. Then the volume was adjusted to 1 mL (for liposomes) or nearly 1 mL (for proteoliposomes, excluding the volume of protein suspension to be added later), set in a specific buffer with a specific detergent concentration (in most cases, 0.05% Brij-78). The lipids were then sonicated in a cool water bath, 30 min three times, changing the water between each step. During this step, the sample became more translucent. Correspondence with S. Brescia was critical to identify the significance of this step.

While preparing proteoliposomes, proteins were integrated in the lipid environment by adding to the sonicated lipids the appropriate amount of detergent. This volume would be adapted depending on the protein concentration and the desired lipid to protein ratio (usually 50:1, *i.e.* 100 µg of protein). Once the proteins are added, the sample was mixed (by vortexing at medium speed) and incubated on ice for 30 min. To prepare empty liposomes (usually used as controls), the same steps were applied, replacing the volume of protein suspension by an equal volume of buffer of equivalent composition.

The detergent was removed from the liposomes by abruptly diluting them in cold buffer (1:25). Typically, centrifuge tubes (50.2 Ti, Beckman Coulter) were filled with 24 mL of buffer and kept in the fridge, then the 1 mL of liposomes was injected in using a Gauge 23 syringe. These centrifuge tubes were agitated at room temperature for 20 min then centrifuged at 140 000 *g* for 45 min, 4°C (SW60 Ti, Beckman Coulter). After centrifugation, the supernatants are discarded and the round white pellets containing the liposomes are resuspended in 2 mL of buffer by gently vortexing.

3.9.3. Extrusion

Once resuspended, the liposomes were homogenized by extrusion. Briefly, two gastight syringes (Hamilton. Co, #1750) were connected through a membrane (Nucleopore® Track-Etched membranes, Polyester, Whatman) of various pore sizes (typically 200 nm). Then, the

whole set-up was washed with 70% ethanol, then with ddH₂O, then equilibrated in buffer, 0.5 mL of the liposome suspension was loaded into one syringe and passed back and forth through the filter for a total of eleven times.

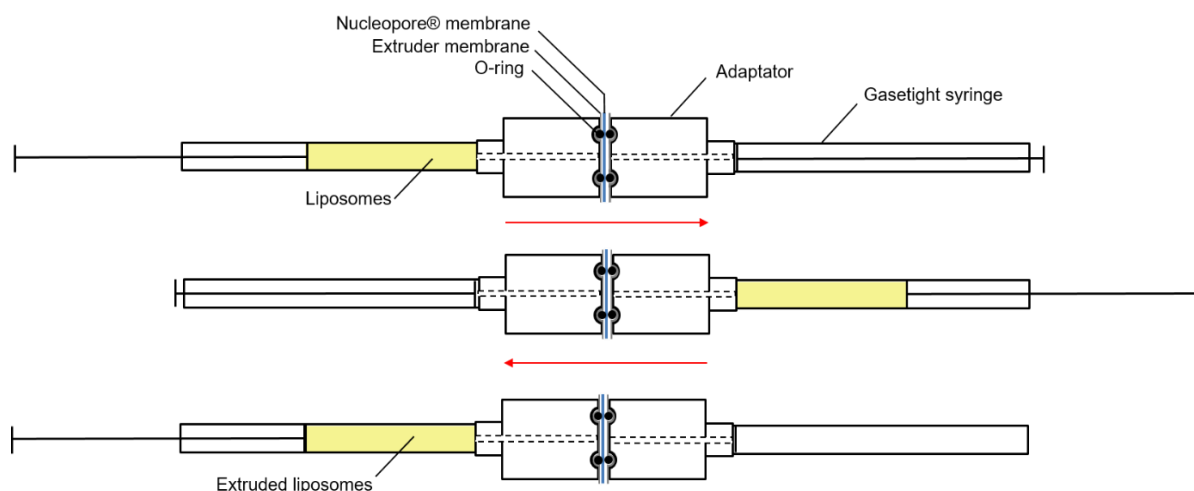


Figure 3. 7: Schematic representation of the extrusion process. The liposome preparation (yellow) is pushed through the nucleopore membrane (blue), sealed between the two gastight syringes thanks to a set of adaptors (white) and O-rings (black). The steps represented are repeated eleven times for each 0.5 mL of liposome preparations.

3.9.4. Pyranine loaded liposomes preparation

To monitor the change of intravesicular pH generated by the cotransport of substrate and protons, liposomes were prepared in such a manner to include a pH-sensitive probe in their intravesicular space. Pyranine was chosen as it exhibits a decrease in fluorescence as the concentration of proton increases when using an excitation wavelength of 450 nm [187], [188]. Working concentrations of pyranine used were between 1 and 5 mM [189].

Pyranine was loaded in liposomes either during sonication or extrusion. In order to remove the extravesicular pyranine from the final liposomes they were loaded on disposable PD10 desalting columns (GE Healthcare) equilibrated with the liposome buffer of choice (containing no pyranine). Once the liposomes entered the packed bed, liposome buffer was added to elute.

The free pyranine, eluting much earlier than the liposomes making their way through the resin was thus removed.

3.9.5. Stopped-flow measurement of substrate transport

Stopped-flow measurements were done using a SFM 2000 device (Biologic).

Briefly, the liposome preparation and buffer were filled in chambers controlled by pumps (MPS 70/20, Biologic) and mixed by injection through a mixer block into the measuring cuvette (Figure 3.8. A). A light beam, generated a set wavelength (ALX 250, Biologic) was sent through the sample and the intensity of the light diffracted or emitted by the sample was detected (by a PMS 250, Biologis). Scattering at 524 nm indicates swelling or shrinking of the liposomes (Figure 3.8. B) while fluorescence emitted at 450 nm shows acidification (Figure 3.8. C).

The measured traces were averaged and usually normalized by setting the maximal signal value to approximately 1 V.

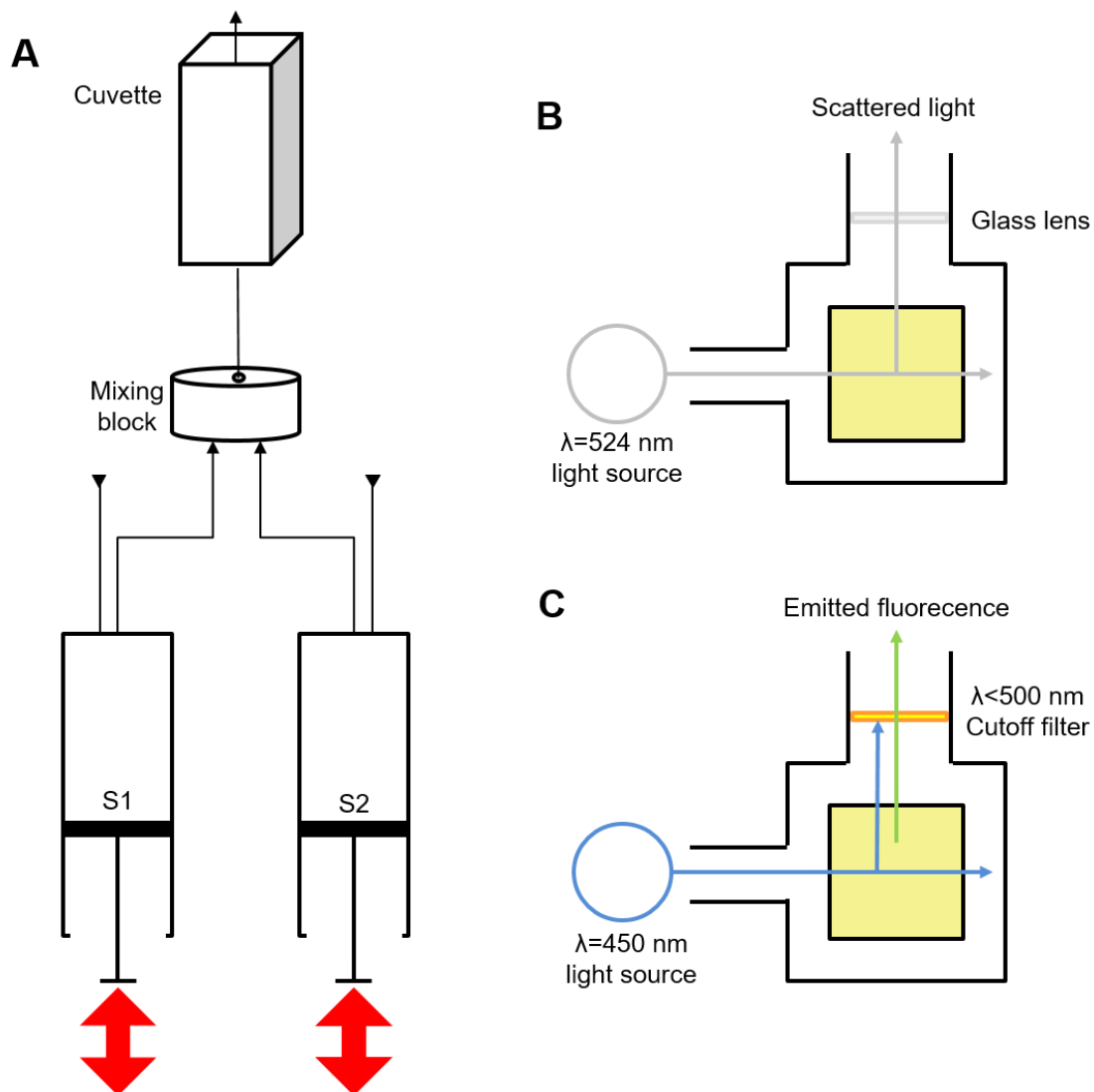


Figure 3. 8: Schematic representation of the Stopped-flow measurement principles.

3.9.5.1 Measurement of light scattering

As the liposome and the substrate are mixed in the chamber, the concentration of substrate outside the lipid bilayer is much greater than inside. In response to the hypertonic pressure, the water contained in the liposomes rushes out of the liposome by osmosis, leading to a sharp decrease of the liposomes volume, which is characterized by an initial increase in light scattering intensity. This typically occurs within 10 ms. Then, depending if the liposome membranes are impermeable to the free diffusion of the substrate and that functional transport proteins are reconstituted in the bilayer, the substrate starts to be transported inward alongside the gradient. While the inner concentration of substrate increases, the liposome size starts to increase again, characterized by a decrease of the signal, whose velocity depends on the reconstituted transporters number and their transport rate.

3.9.5.2. Measures of fluorescence

Pyranine has two main excitation wavelengths ($\lambda_{ex} = 405 \text{ nm}$ and $\lambda_{ex} = 460 \text{ nm}$) leading to a fluorescence emission at $\lambda_{em} = 510 \text{ nm}$, which respectively depending on the pH (Figure 3.9 B). The pyranine isobestic point (pH independent) is at an excitation wavelength around 415 nm (Figure 3.9 A) [187].

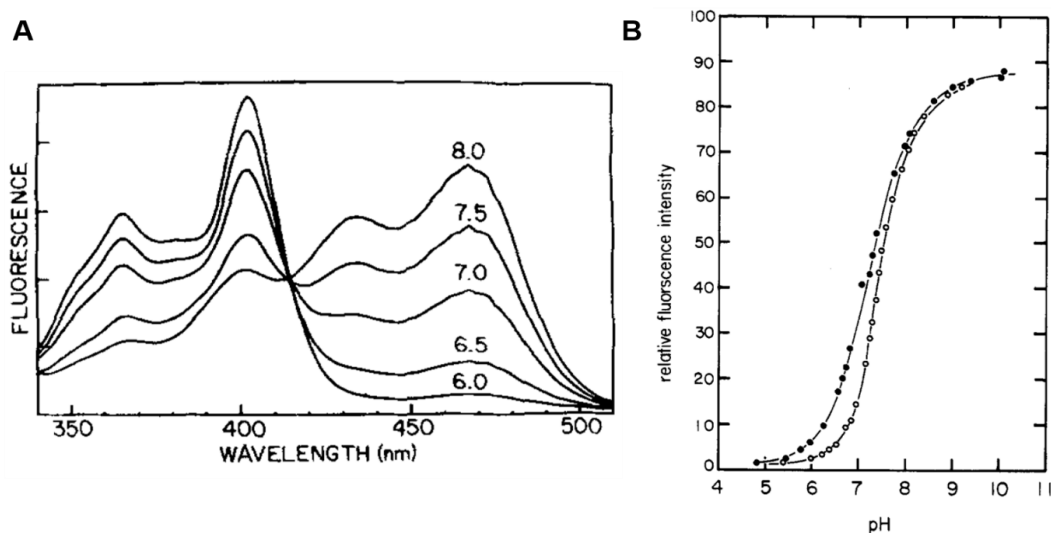


Figure 3. 9: (A) *In vitro* fluorescence excitation pH titration of pyranine in nigericin buffer. Excitation spectra were collected using an emission wavelength of 514 nm. Adapted from Giuliano and Gilles [187]. (B) Variation of the fluorescence intensity (excitation $\lambda = 460 \text{ nm}$; emission $\lambda = 520 \text{ nm}$) of 1 μM pyranine (black) or pyranine-containing phospholipid vesicles (white) (containing 5 μM valinomycin and 200 nM gramicidin to facilitate transmembrane H^+ equilibration) in different pH conditions. Adapted from Clement and Goult [188].

To measure excitation fluorescence in pyranine labeled liposomes using stopped-flow spectroscopy, the wavelength was adjusted to 450 nm. Emission was followed at $\lambda_{em} > 500$ nm cut-off (Figure 3.8 C).

3.9.6. Sucrose gradient-density centrifugation

The liposomes can be separated according to their specific weight in a sucrose gradient. The liposome samples were diluted to 350 μ L in 50 mM HEPES pH=6.8, then mixed with 350 μ L of 50 mM HEPES pH=6.8, 60 % sucrose (for a total of 30 % sucrose) in a 11 \times 60 mm Ultra-Clear™ tube (Beckmann Coulter). A sucrose gradient from 30 % to 0% was created by layering 700 μ L volumes of 50 mM HEPES pH=6.8 Sucrose solutions (from 25 to 5 %), from the higher sucrose concentration to the lower, on top of the previous one. Pipetting on a small piece of cork floating at the surface of each layer prevented mixing.

By centrifuging at 164 000 g, 4°C for 6 h, the liposomes migrated in different density layers depending on their specific weight. Empty liposomes are expected to concentrate in the 5% sucrose step, while the heavier proteoliposomes are expected to be found in the 15% sucrose layer (Figure 3.10).

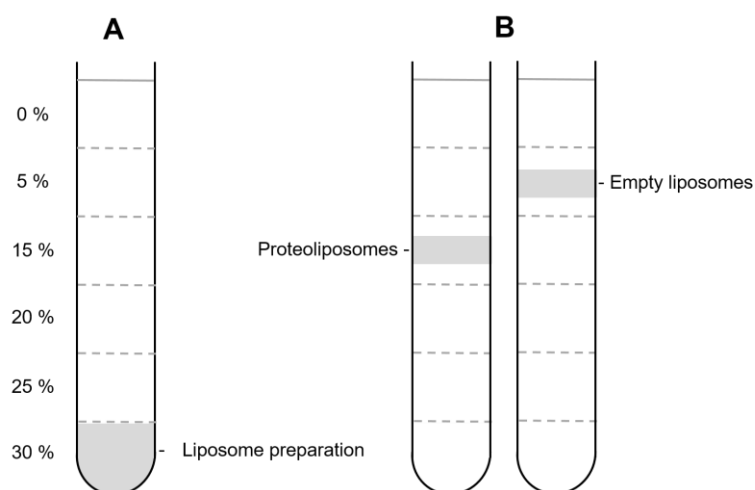


Figure 3. 10: Schematic representation of the sucrose gradient separation of liposomes preparation, before (A) and after (B) centrifugation.

The individual layers were pipetted separately and the protein content of each fraction was concentrated using TCA precipitation (3.2.3.) then visualized using SDS-PAGE and Western Blot (3.2.4.2.).

4. RESULTS

4.1. Producing functional PffNT for structure determination

Solving the structure of PffNT mutants in complex with inhibitors would allow for a better understanding of the protein resistance mechanism and improve the development of inhibitors. Part of the present work assisted the project of C. Hansen to solve the structure of such PffNT.

A well-established method for solving the structure of membrane proteins consists in reconstituting them in a lipid nanodisc. Such nanodiscs are composed of a small lipid bilayer, maintained by a ring of two membrane scaffold proteins (MSP). The membrane proteins of interest can be reconstituted in such a bilayer and the structure later resolved using Cryo - Electron Microscopy.

4.1.1. Membrane scaffold protein production and purification

The MSP used in this work was MSP1E3D1 (2.1.6.), expressed and purified based on the method described by Rues *et al.* [173]. After expressing the proteins in BL21 (DE3) (Table 3.8), the pellets were unfrozen and resuspended in Tris buffer saline (40 mM Tris pH=8, 300 mM NaCl), at 1 to 2 mL per gram of pellet, supplemented with protease inhibitor (Complete EDTA free, Roche). Triton X-100 was added to a final concentration of 1%.

The French press was used for the lysis of the resuspended cell pellets (3.4.2.). The lysate was centrifuged for 30 min at 30 000 g and 4°C to separate the supernatant containing the soluble proteins of interest. The content was visualized using SDS-PAGE (Figure 4.1 A).

For purification, the recovered supernatant was filtrated (0.45 µm), loaded on an IMAC column (typically 1.2 mL of volume), equilibrated in 5 column volumes of buffer solution containing 1% Triton X-100, then 50 mM of cholic acid. Proteins weakly bound to the resin were washed by rinsing with 5 volumes of buffer solution. The MSP protein was eluted in 5 volumes of buffer solution containing increasing concentrations of imidazole (from 20 to 300 mM). Fractions of each step were recovered for analysis using SDS-PAGE (Figure 4.1 B).

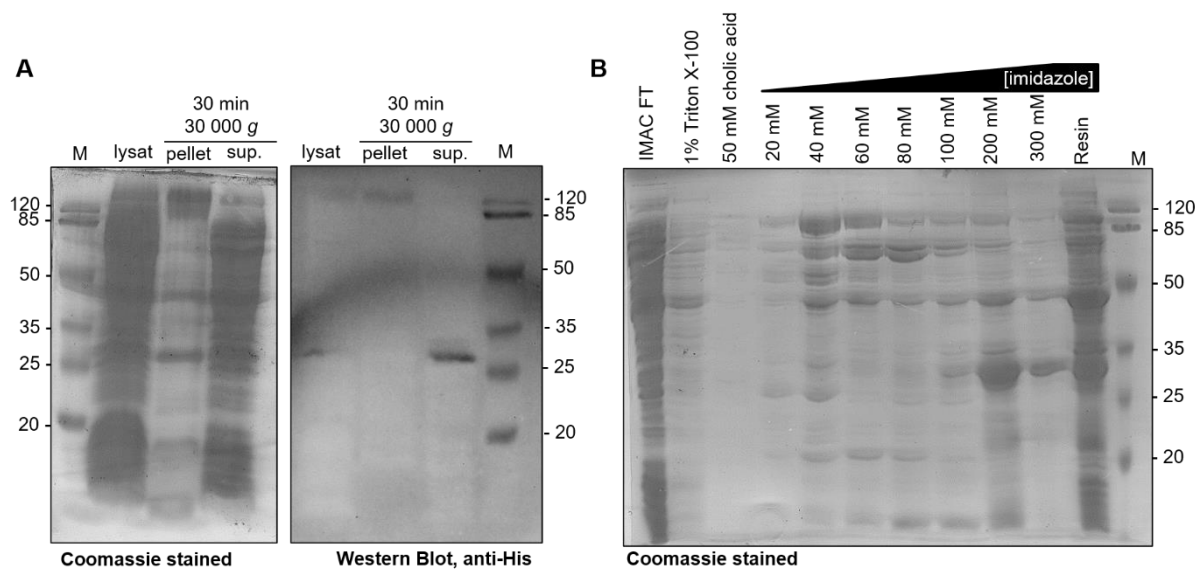


Figure 4. 1: SDS-PAGE of the proteins separated during the MSP1E3D1 extraction (A) and IMAC purification (B). Protein marker (M) was used to estimate the protein sizes (units are in kDa)

The expected molecular mass of the His₆-tagged MSP1E3D1 is 31.2 kDa and the protein was detected between the 25 and 35 kDa markers, using both Western Blot targeting the His₆ tag (Figure 4.1 A) and Coomassie staining (Figure 4.1 B).

This method of IMAC purification did not seem to elute all the resin-bound protein of interests, as a large amount of MSP remained on the resin. Moreover, contaminant proteins were eluted alongside the MSP. To decrease the amount of contaminant proteins, the eluted proteins (Fractions 100-300 mM imidazole) were collected, pooled and dialyzed overnight to decrease the imidazole concentration (>1 mM). Then they were used to perform a second IMAC purification.

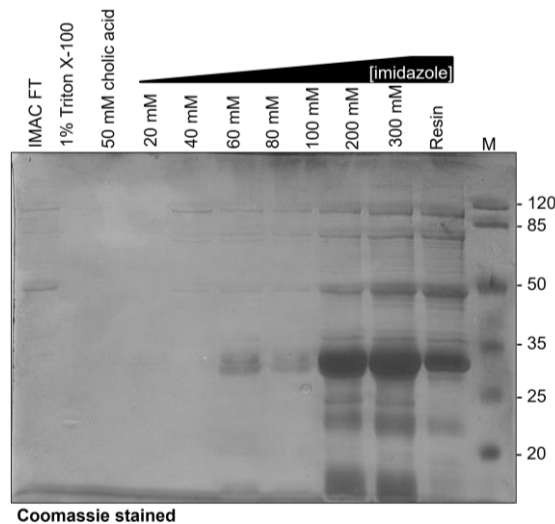


Figure 4. 2: SDS-PAGE, Coomassie staining of the second IMAC of purification, after pooling and dialyzing the fractions 100 to 300 mM imidazole from the previous IMAC (Figure 4.1 B). Protein marker (M) was used to estimate the protein sizes (units are in kDa).

Neither a second IMAC purification step, nor increasing the volume of the washing and elution fractions managed to properly remove the contaminants that appeared to strongly bind to the resin. To improve the purity of the recovered MSP, an additional purification step was done using the Ion Exchange (IEX) principle (3.3.3.).

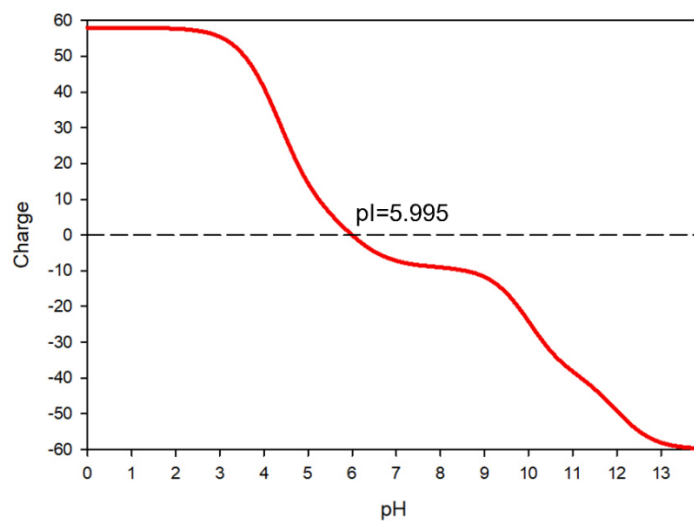


Figure 4. 3: Total electric charges of the His-tagged MSP1E3D1, depending on the pH. Calculated using the “Prot pi | Protein Tool” web application, using ExPASy pK_a values

In the buffer condition previously used (pH=8), the charge of the MSP1E3D1 proteins was calculated to be of -9.063. They can therefore be further purified using the Q Sepharose[®] FastFlow resin (Sigma Aldrich) containing ammonium quaternary cations (anion exchanger).

The dialyzed proteins were loaded on an equilibrated Q Sepharose FastFlow resin, then eluted with 20 column volumes (2 ml) of buffers containing 40 mM Tris pH=8 and increasing

concentrations of NaCl (from 100 to 400 mM). The protein concentration of the elution fractions was quantified using the Bradford assay, and visualized by SDS-PAGE (Figure 4.4). Since there was more fractions than wells on the PAGE gels, some SDS-PAGE samples were composed of equal volumes of two different elution fractions (Figure 4.4 C).

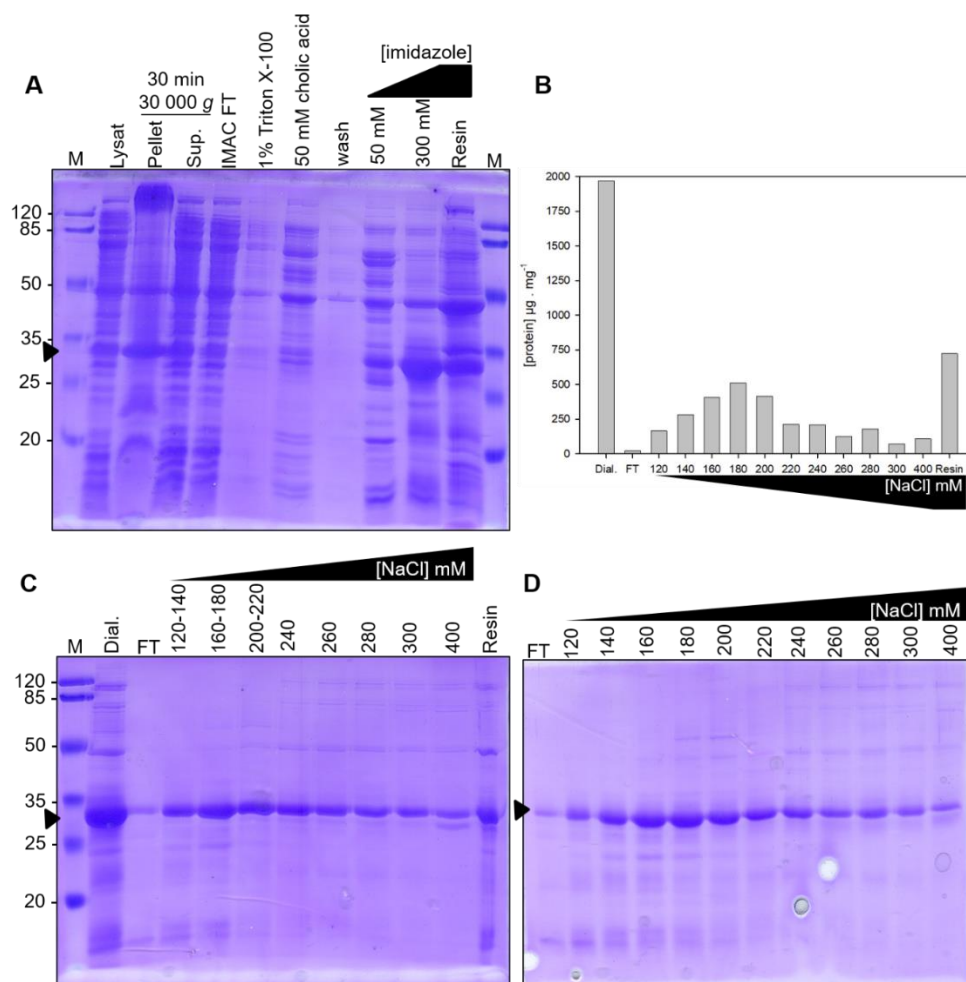


Figure 4. 4: (A) SDS-PAGE of the MSP extraction and initial IMAC purification. The eluted fraction (300 mM imidazole) was dialyzed overnight then used for IEX purification (B-C). The protein concentrations in each fraction were determined with Bradford assay (B) then visualized on SDS-PAGE, Coomassie stained (C and D). Protein marker (M) was used to estimate the protein sizes (units are in kDa)

The IEX was very efficient at separating the contaminants present in the IMAC purified proteins. The MSP contained in the elution peak (160- to 200 mM) could be subsequently used for nanodiscs production.

C. Hanssen had also investigated alternative methods of measuring PffNT structures using cryo-EM: reconstituting the pentamers in detergent micelles. It is this method that is being investigated at time of writing.

4.1.2. Cell-free production of PfFNT

The next challenge in reconstituting PfFNT pentamers in nanodiscs or detergent micelles consisted in expressing functional proteins.

For the cell-free production of proteins, the PfFNT coding sequences were inserted in pIVEX 2.3w derivatives. The three mutant PfFNT coding sequences carrying either the G107S, G21E or V196L mutations were prepared by J.D.R. Schmidt in the pDRTXa plasmids. These DNA fragments were transferred into the pIVEX 2.3w plasmid by using the SpeI and XhoI restriction enzymes. These plasmids were amplified in DH5 α *E. coli*, extracted using Maxiprep (3.1.9.1.) and used for preparative cell-free expression (3.7.2.). Afterwards, the reaction mix was purified using IMAC (3.3.1.).

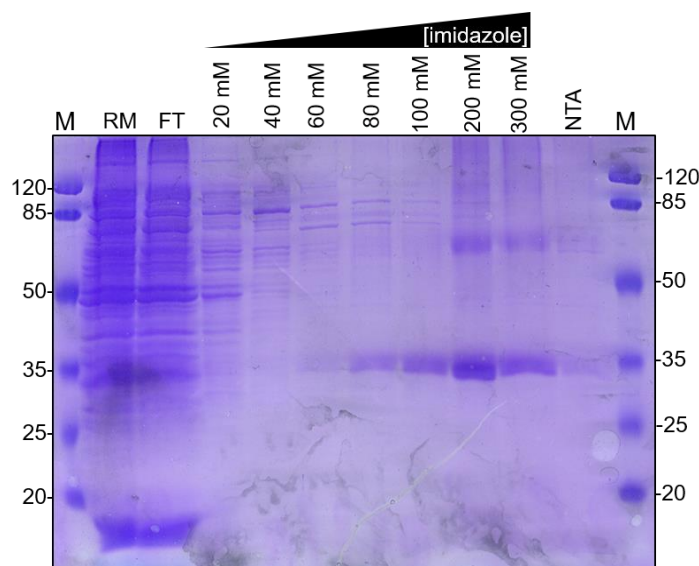


Figure 4. 5: Typical SDS-PAGE (Coomassie stained) gel from the IMAC purification of cell-free expressed PfFNT. “RM” represents the diluted reaction mix after the cell-free protein expression, “FT” the IMAC flow-through and “NTA” the resin resuspended in equivalent volume of elution buffer. The other fractions are the IMAC elution at different imidazole concentrations. All gels lanes were loaded with the same volume of samples diluted in 4 \times SDS buffer, except “RM” that was initially diluted 1:1 in equilibration buffer. Protein marker (M) was used to estimate the protein sizes (units are in kDa)

The cell-free expressed His₁₀-tagged PfFNT proteins (37.6 kDa) mainly eluted between 100 and 300 mM of imidazole. Most of the cell-free reaction contaminants washed away with lower concentrations. In Figure 4.5, it can be observed that the protein complexes were not entirely denatured during the SDS-PAGE, as protein bands corresponding to proteins dimers (75.18 kDa, in the 200 to 300 mM fraction) and even traces of trimers (112.77 kDa, in the

200 mM fraction) were observed. After the IMAC, the pooled fractions containing the most purified proteins of interest are concentrated by centrifugation (several cycles at 500-750 g, 5 min, 4°C) in an equilibrated Amicon Ultra-4 centrifugal filter (100 kDa MWCO). At this stage, the buffer was gradually replaced with 150 mM NaCl, 20 mM Tris pH=8, 0.05 % Brij78 to dilute the imidazole concentration (below 1 mM).

Green fluorescent protein (GFP)-PfFNT fusions were expressed and purified according to the same protocol, except the fluorescence activity of GFP could be used to visualize the proteins during the purification and reconstitution processes.

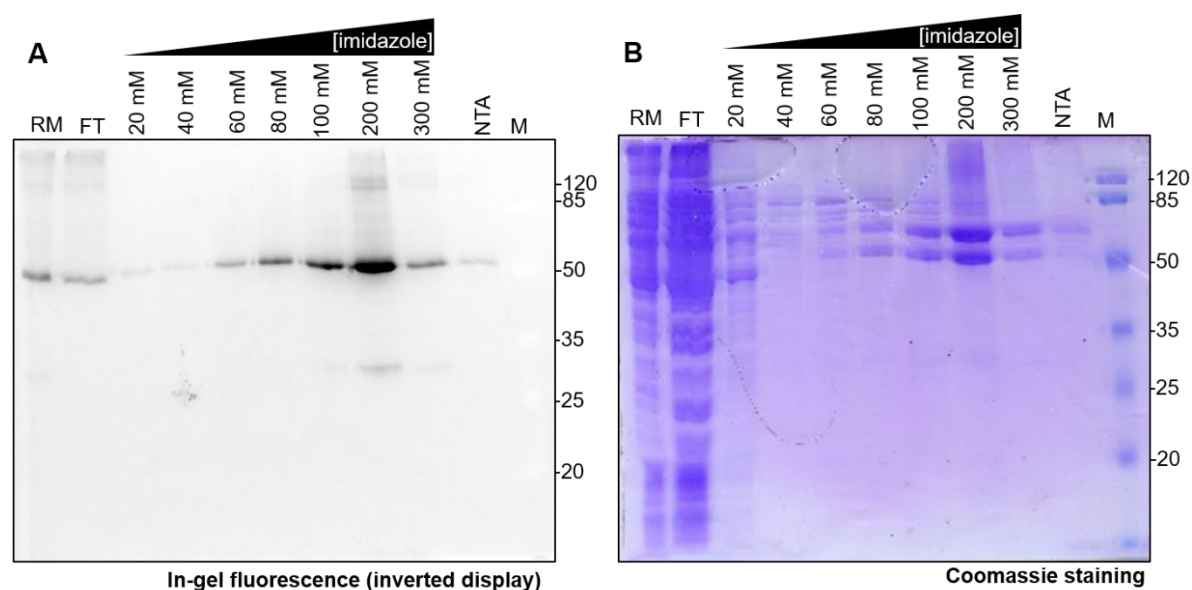


Figure 4. 6: Typical SDS-PAGE (In-gel fluorescence, then Coomassie stained) gel from the IMAC purification of cell-free expressed PfFNT (G107S)-GFP. “RM” represents the diluted reaction mix after the cell-free protein expression, “FT” the IMAC Flow-through and “NTA” the resuspended resin. The other fractions are the IMAC elution at different imidazole concentrations. All gels lanes were loaded with samples diluted in 4× SDS buffer, except “RM” that was initially diluted. Protein marker (M) was used to estimate the protein sizes (units are in kDa)

The expected molecular weight of the GFP tagged PfFNT was 67.1 kDa. The in-gel fluorescence (Figure 4.6 A) shows that two signals can be observed: one slightly above the 50 kDa ladder, the other between 25 and 35 kDa. The former corresponds to PfFNT-GFP with an intact secondary structure, allowing GFP fluorescence. The latter should be some soluble GFP, expressed without PfFNT. Figure 4.6 B shows that the PfFNT-GFP appeared in the gel as two bands, one slightly above the 50 kDa ladder and the other corresponding to the expected 67.1 kDa. Only the lower band displayed fluorescence; as the fluorophore was intact. These proteins that were not fully denatured migrated down the gel faster during electrophoresis.

To reconstitute PffNT in lipid nanodiscs then separate between filled or empty discs, the PffNT needed to be expressed fused to a different purification tag that of the MSP proteins. To that effect, it was decided to replace the N-terminal HA tag from the pIVEX 2.3w plasmid with a Strep II tag.

To facilitate establishing the expression and purification process, it was decided to express the N-terminal Strep II tagged protein in the pIVEX 2.3w GFP Δ M1 plasmid (2.2.3.2. and 2.2.3.4.), as the fluorescent proteins would allow to visualize more easily what becomes of the tagged proteins during the purification process.

The Strep-tagged PffNT (G107S) GFP fusion was expressed using the cell-free system as described previously (3.7.). After the reaction, the produced proteins were split in two and purified using either IMAC (3.3.1) or Streptavidin purification (3.3.2.). The content of each fraction was visualized by monitoring the GFP fluorescence, then SDS-PAGE and Western Blots.

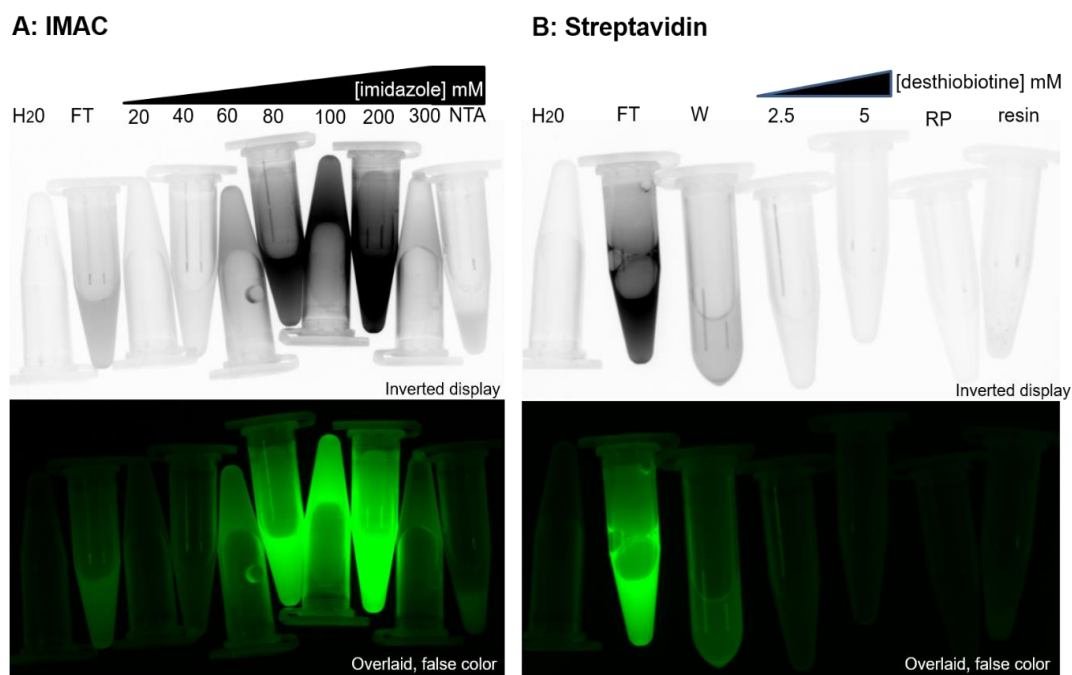


Figure 4. 7: GFP fluorescence measured in the samples from the cell-free produced N-terminal Strep II-tagged PffNT (G107S) GFP, purified with IMAC (A) or Strep-Tactin[®] (B). The test tubes containing the fractions were visualised using inverted display or an overlay of the signals with fake colors. A test tube filled with water was used as a negative control (H₂O).

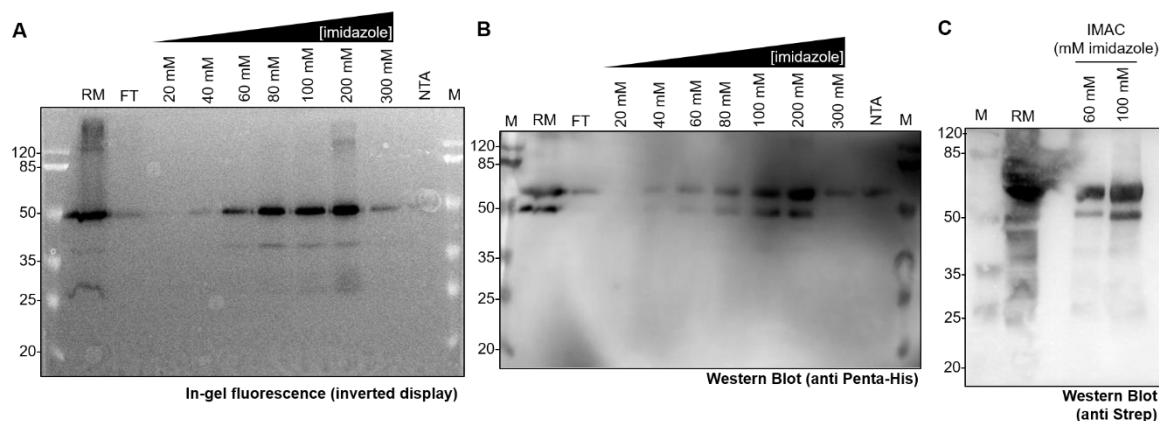


Figure 4. 8: SDS-PAGE of the fractions from the Strep II-tagged PfFNT (G107S) GFP proteins IMAC purification. Visualised by in-gel fluorescence (A) or Western Blot detecting the His (B) and Strep II tags (C). All gels lanes were loaded with samples diluted in 4× SDS buffer, except “RM” that was initially diluted 1/1 in equilibration buffer. Protein marker (M) was used to estimate the protein sizes (units are in kDa)

From the IMAC purification, the GFP fused proteins were recovered in the elution fractions containing 100 to 300 mM imidazole. However, the streptavidin purification was not successful, as all the fluorescence could only be detected in the flow-through of the resin (“FT”, Figure 4.7 B). The results of the SDS-PAGE showed that the expressed protein had the expected molecular weight (Figure 4.8 A and B), were tagged with the C-terminal His₁₀-tag (Figure 4.8 B) and the N-terminal Strep II-tag (Figure 4.8 C). Hypotheses for the lack of streptavidin binding are discussed later (5.1.2.).

4.1.3. Reconstitution of PfFNT in proteoliposomes.

These results (4.1.2) showed that production of cell-free expressed high yield protein. However, it remained necessary to measure PfFNT transport functionality to validate that the cell-free produced protein was properly folded. To do so, PfFNT was reconstituted in proteoliposomes (3.9.) to observe transport functionality using stopped-flow spectroscopy (3.9.5.).

After trying and adjusting different methods, the protocol adapted from Borgnia and Agre [190] by J. Holm-Bertelsen [150], [183] (using 20 mM HEPES pH=6.8 as buffer, and *E. coli* polar lipid extracts as source of lipids) was employed. The first successful experiments were prepared using cell-free expressed PfFNT-GFP.

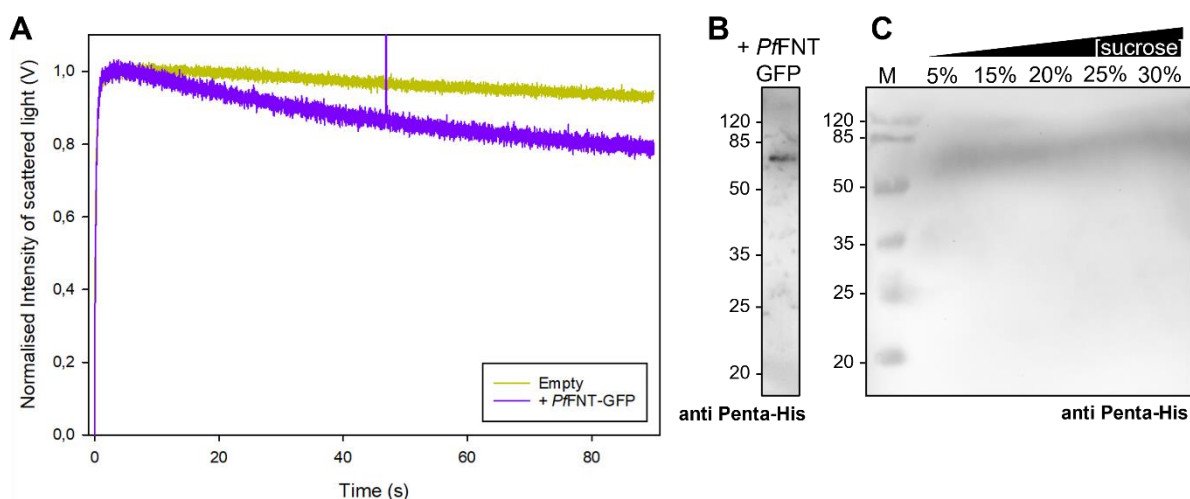


Figure 4. 9: (A) Stopped-flow measurements of the light scattering of empty liposomes (yellow) and PfFNT-GFP reconstituted proteoliposomes (purple). Liposomes composed of polar *E. coli* lipids liposomes were prepared using 0.05% Brij 78, \pm addition of PfFNT-GFP in a 1:50 protein to lipids ratio, extruded to 200 nm. Measured at $\lambda=524$ nm in 20 mM HEPES pH=6.8, 0 to 50 mM sodium formate gradient. Traces are the normalized averages of 5 curves. The presence of proteins in the liposome was assessed by Western Blot, before (B) or after sucrose gradient separation and TCA precipitation (C). Protein marker (M) was used to estimate the protein sizes (units are in kDa).

The scattered light intensity (3.9.5.1.) appeared to decrease over time in the liposomes prepared with PfFNT-GFP. This is caused by the liposomes swelling back after the initial shrinkage caused by the fast water efflux (itself caused by the strong hypertonic gradient). It suggests that the gradient between the outside and the inside of the liposomes equilibrate over time, which could be caused by the transport of formate through the lipid bilayer by PfFNT-GFP.

The presence of PfFNT-GFP proteins in the liposomes was assessed by Western Blot before and after separation in a glycerol gradient (3.9.6.) and TCA precipitation (3.2.3.). The Western blot prepared with the crude liposome preparation (Figure 4.9. B) displayed a signal at the level corresponding to the expected molecular weight of PfFNT-GFP. The separation in a glycerol gradient resulted in a loss of the liposome and after TCA precipitation and Western Blot, no protein-specific signal could be observed (Figure 4.9. C). This was likely caused by an experimental error.

Visualising a Western Blot signal at the expected protein molecular weight in the sucrose gradient in which liposomes were recovered is the proof of a successful proteoliposome reconstitution. However, as failed protein reconstitution never showed protein signals in Western Blots, the presence of a signal in Figure 4.9. B led to the conclusion that this PfFNT - GFP proteoliposomes reconstitution had been a success.

Following up on these results, the same method was applied to reconstitute cell-free expressed and purified PfFNT in liposomes. Several attempts appeared successful, as they generated liposomes that appeared to transport formate and would yield expected protein signal when loaded on a gel for Western Blot, before or after sucrose gradient separation (3.9.6.) and TCA precipitation (3.2.3.) (Figure 4.10 B). It was further attempted to inhibit its activity by incubating the liposomes 5 min with 10 μ M of the BH267.*meta* PfFNT inhibitor (Figure 4.10 A).

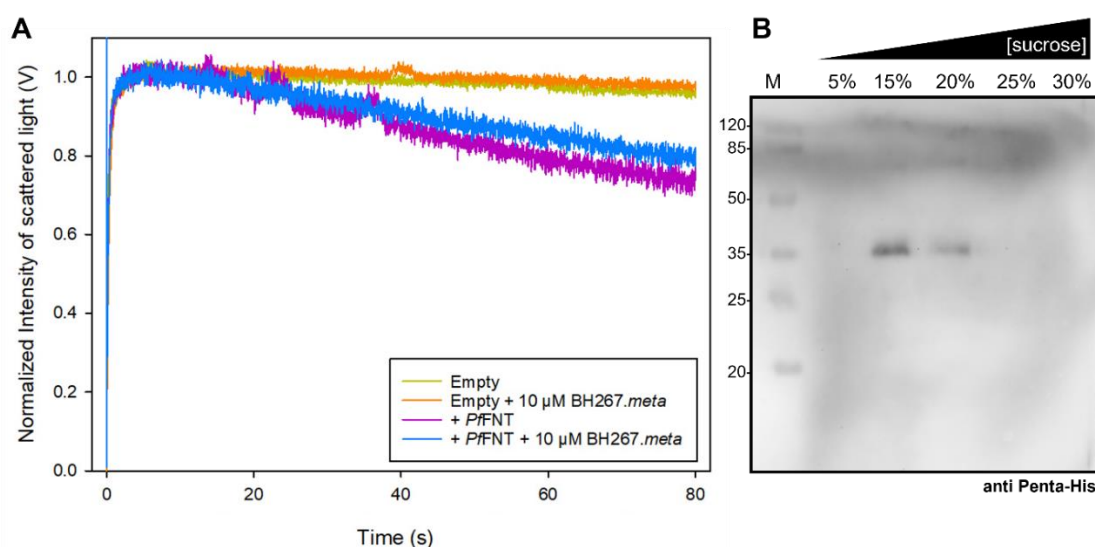


Figure 4. 10: (A) Stopped-flow measurements of the light scattering of empty liposomes before (dark yellow) and after (orange) the addition of 10 μ M BH267.*meta* and PfFNT reconstituted proteoliposomes before (purple) and after (blue) the addition of 10 μ M BH267.*meta*. Liposomes composed of polar *E. coli* lipids liposomes were prepared using 0.05% Brij 78, \pm addition of PfFNT in a 1:50 protein to lipids ratio, extruded to 200 nm. Measured at $\lambda=524$ nm in 20 mM HEPES pH=6.8, 0 to 50 mM sodium formate gradient. Traces are the normalized averages of 8, 6, 6 and 6 curves respectively. The liposomes samples were incubated for about 5 min in 10 μ M PfFNT inhibitors at room temperature before the stopped-flow spectroscopy measurements. (B) The presence of proteins in the liposome was assessed by Western Blot after sucrose gradient-density centrifugation and TCA precipitation. Protein marker (M) was used to estimate the protein sizes (units are in kDa).

The proteoliposomes appeared to equilibrate the 50 mM formate gradient over time (Figure 4.10 A, purple) and contained PfFNT reconstituted in the lipid bilayers (Figure 4.10 B). However, the addition of inhibitor barely appeared to decrease this supposed transport functionality (Figure 4.10 A, blue). The initial concentrations of 10 μ M BH267.*meta* became 5 μ M after the 1:1 dilution caused by the stopped-flow measurement, but it still represented over 50 times the IC_{50} observed in yeast [25]. The addition of inhibitor did not affect the integrity of the lipid membranes (Figure 4.10 A, orange).

The addition of PfFNT inhibitor did not decrease the formate transport. The stocks of inhibitor were tested by P. Walloch using the radiolabeled substrate assay and it appeared they could inhibit the lactate transport in PfFNT expressing yeast during radiolabelled substrate assay. It could be that the observed gradient equilibration was unrelated to the PfFNT transport functionality (*e.g.* by some leakage). Or it could be that the inhibitors could not access their binding site. An additional experiment was designed to identify the most appropriate explanation.

F. Helmstetter had observed that PfFNT mainly reconstituted with their terminal inside the liposomes [58]. The BH267.*meta* inhibitors access its binding site from the cytosolic side [25], [52], [53], [67]. To test if the formate transport inhibition would be more efficient when the inhibitor is present inside the liposomes, 10 μ M of BH267.*meta* were added to the extrusion buffer.

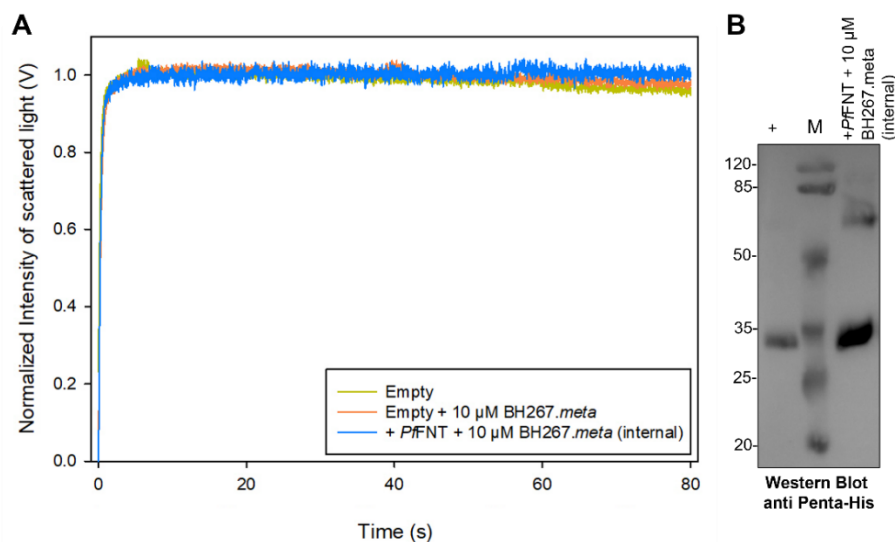


Figure 4. 11: (A) Stopped-flow measurements of the light scattering of empty liposomes before (dark yellow) and after (orange) the addition of 10 μ M BH267.*meta* and PfFNT reconstituted proteoliposomes prepared with internal 10 μ M BH267.*meta* (blue). Liposomes composed of polar *E.coli* lipids liposomes were prepared using 0.05% Brij 78, \pm addition of PfFNT in a 1:50 protein to lipids ratio, extruded to 200 nm. Measured at $\lambda=524$ nm in 20 mM HEPES pH=6.8, 0 to 50 mM sodium formate gradient. Traces are the normalized averages of 8 ,6 and 8 curves respectively. (B) The presence of proteins in the liposome was assessed by Western Blot, in comparison with 1 μ g of cell-free expressed PfFNT (+) used as positive control. Protein marker (M) was used to estimate the protein sizes (units are in kDa).

The PfFNT proteoliposomes prepared with internal inhibitor did not show any formate transport, as the measured curves appeared identical to the empty liposomes (Figure 4.11 A, blue). Moreover, these liposomes appeared to properly contain the PfFNT protein (Figure

4.11 B). Due to the low volume of remaining samples, it was not possible to separate the liposomes on a sucrose gradient to show that the proteins were present in the liposomes. However, it had previously been observed that directly loading liposomes from unsuccessful reconstitutions onto SDS gels would not show any Western Blot signal (not shown) but loading successful reconstitutions would (Figure 4.9 B).

Noteworthy, it also appeared that the successful reconstitution of PfFNT in liposomes did not necessarily translate into formate transport in all experiments (Figure 4.12).

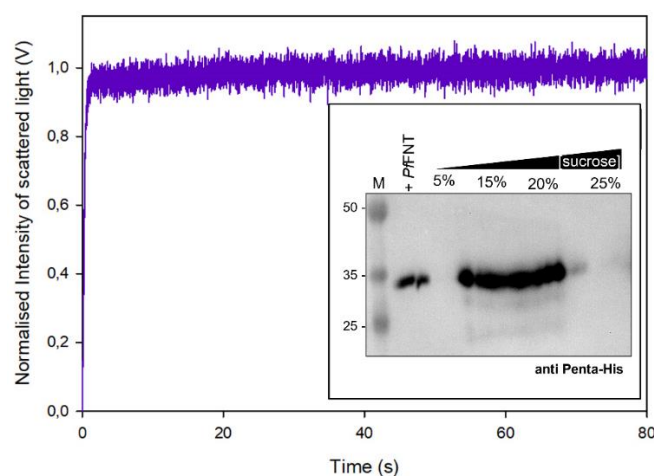


Figure 4. 12: Stopped-flow measurements of the light scattering of PfFNT reconstituted proteoliposomes (purple). Liposomes composed of polar *E. coli* lipids liposomes were prepared using 0.05% Brij 78, \pm addition of PfFNT in a 1:50 protein to lipids ratio, extruded to 200 nm. Measured at $\lambda=524$ in 20 mM HEPES pH=6.8, 0 to 50 mM sodium formate gradient. The trace is the normalized average of 5 curves. The presence of proteins in the liposome was assessed by Western Blot after sucrose gradient and TCA precipitation, in comparison with 1 μ g of cell-free expressed PfFNT (+PfFNT) used as positive control. Protein marker (M) was used to estimate the protein sizes (units are in kDa).

This work also attempted to produce pyranine loaded liposomes to measure the intravesicular pH changes caused by the cotransport of protons and lactate, by monitoring the pH-sensitive probe fluorescence. In order to act as a proper intravesicular pH probe, the pyranine loading needed to meet several requirements. First, the concentration of pyranine should be enough to accurately measure fluorescence signal. Then, the dye fluorescence should change in a distinctive and measurable manner when a change of intravesicular pH occurs. Finally, the prepared liposomes should be impermeable to proton diffusion. To address these issues, pyranine-loaded liposomes were prepared using 1,2-diphytanoyl-sn-glycero-3-phosphocholine (4ME 16:0 PC). It was hypothesized that such liposomes would be more impermeable to proton diffusion thanks to the methyl groups of the lipid tails. 4ME 16:0 PC liposomes were prepared in a weakly buffered solution (5 mM sodium phosphate, pH=6.8) and extruded in buffer

containing 0.5 mM soluble pyranine [188], [189]. The extravesicular probe was removed by using a PD-10 desalting column (3.9.4). These loaded liposomes ($\text{pH}_{\text{in}}=6.8$) were diluted 1:1 using stopped-flow, in 5 mM sodium phosphate buffered at $\text{pH}=6.8$ ($\text{pH}_{\text{out}}=6.8$), $\text{pH}=5.8$ ($\text{pH}_{\text{out}}=6.4$) and $\text{pH}=7.8$ ($\text{pH}_{\text{out}}=7.2$) (Figure 4.13).

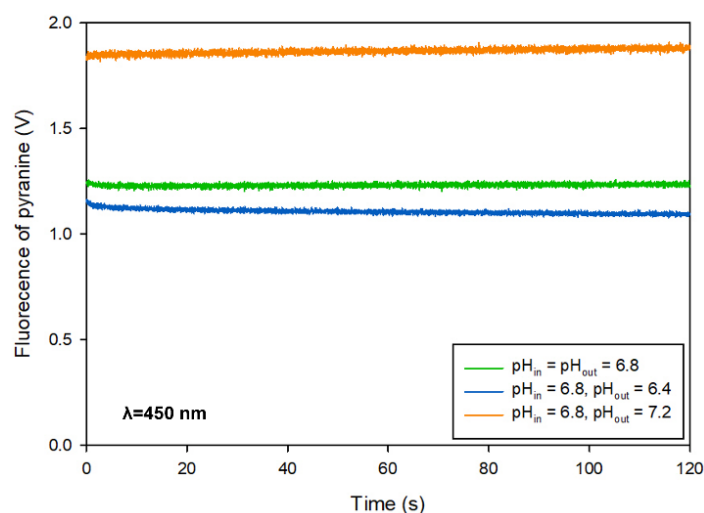


Figure 4. 13: Stopped-flow measurements of the pyranine fluorescence in empty liposomes composed of 4ME 16:0 lipids, loaded with 0.5 mM of probe. Measured in external 5 mM sodium phosphate buffers at $\text{pH}=6.8$, 6.4 and 7.2 (pH_{out}). Averages of 3, 4 and 3 curves respectively.

These experiments showed that the fluorescence of the pH probe changed depending on the extravesicular pH. When mixed in a more basic buffer, the internal pyranine fluorescence increased (Figure 4.13, orange) and when mixed in a more acidic buffer, it decreased (Figure 4.13, blue) compared to when the pH inside and outside of the vesicles were equivalent (Figure 4.13, green). It suggests these concentrations of pyranine are suitable to measure changes in the pH. However, such changes of fluorescence occurred without ionophores or proton transporters. It means that these initial liposomes were permeable for proton diffusion, allowing the pH gradient to equilibrate during the experimental dead time (1.4 ms).

Further attempts were made to produce liposomes that would be impermeable to proton diffusion while also attempting to reconstitute PfFNT in probe-loaded liposomes. Two behaviors were measured with the probe-loaded proteoliposomes. The water permeability was monitored with the scattered light ($\lambda=524$ nm) and the evolution of the proton transport was monitored by measuring the pyranine fluorescence ($\lambda=450$ nm).

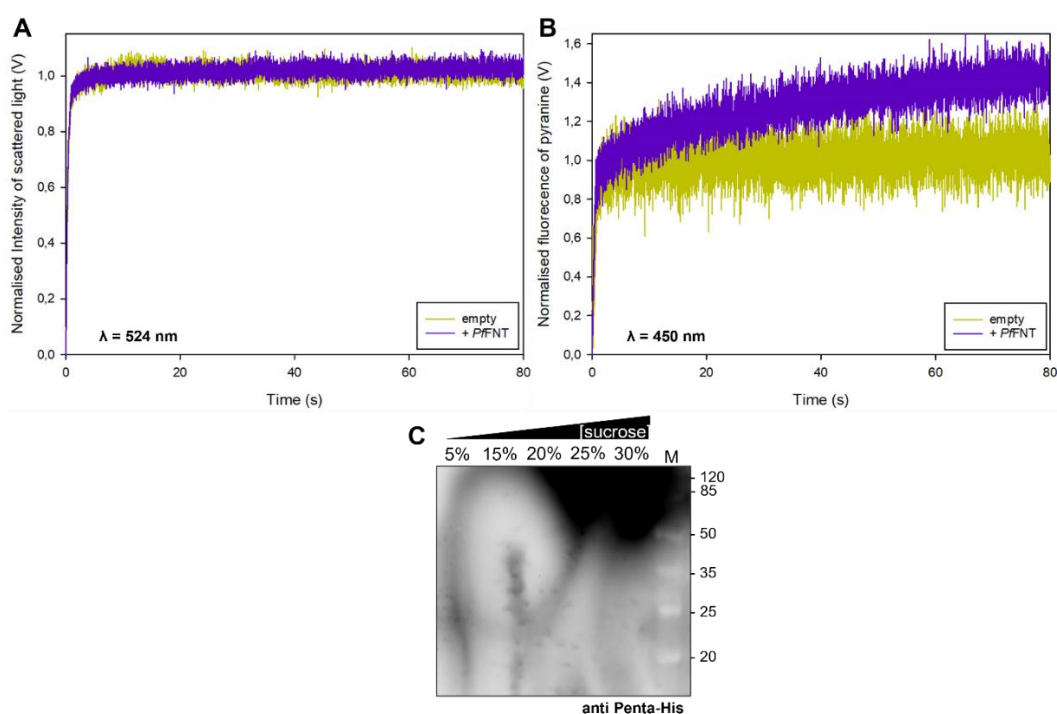


Figure 4. 14: Stopped-flow measurements of the light scattering (**A**) or pyranine fluorescence (**B**) of empty liposomes (dark yellow) and PffNT reconstituted proteoliposomes (purple) composed of 4ME 16:0 lipides \pm addition of PffNT in a 1:50 protein to lipids ratio. Measured at $\lambda=524$ and 450 nm respectively in 20 mM HEPES pH=6.8, 0 to 50 mM sodium formate gradient. Traces are normalized averages of 4 and 7 or 4 and 9 curves respectively. The presence of proteins in the liposome was assessed by Western Blot after sucrose gradient and TCA precipitation (**C**). Protein marker (M) was used to estimate the protein sizes (units are in kDa).

Despite multiple attempts, no reconstituted PffNT was found in pyranine-loaded liposomes, as stopped-flow spectroscopy never visualized formate gradient equilibration and Western blots of liposomes never showed protein-specific signals. However, reconstitution procedure appeared to affect the pyranine fluorescence during the stopped-flow measure (Figure 4.14 B). The initial water efflux should be equivalent between the liposomes and was used to overlay the curves. The liposomes resulting from reconstitution attempts appeared to have their internal pyranine fluorescence increase over time. An increase of pyranine fluorescence is correlated with an alkalization of the buffer, which is the opposite of the expected transport of formate and protons inside the probe-loaded liposomes, which should have resulted in an acidification.

Perhaps the addition of the pyranine impacted the ability of the PffNT-detergent micelles to reconstitute into the membranes, or perhaps the additional buffer exchange step (using PD-10 columns) was detrimental to the reconstituted liposomes integrity.

To further analyze the pyranine-loaded liposomes, they were mixed with gramicidin, circular peptides extracted from *Bacillus brevis* that form pore-like channels through lipids membranes [191]. Such pores allow the passage of water molecules and cations [192].

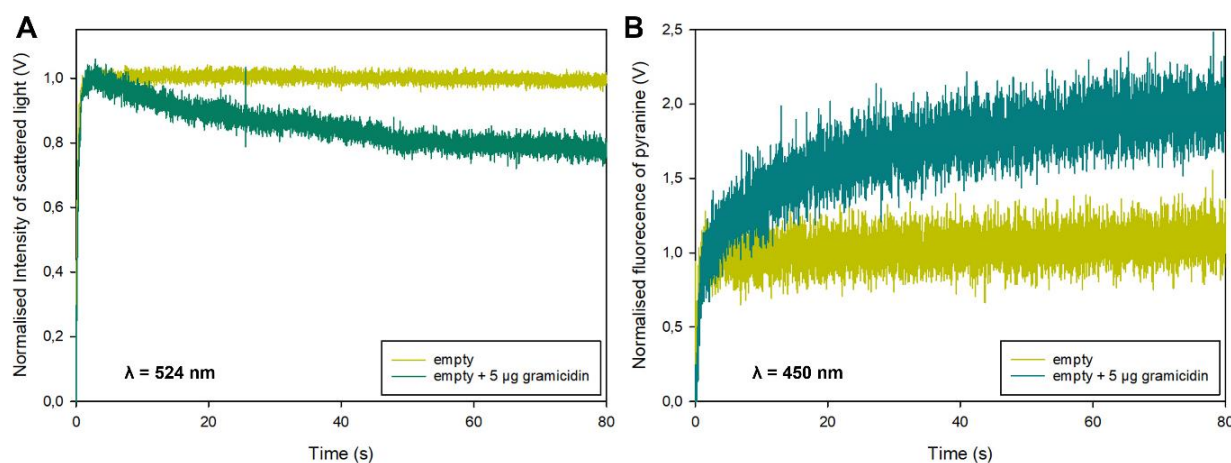


Figure 4. 15: Stopped-flow measurements of the light scattering (A) or pyranine fluorescence (B) of empty liposomes before (dark yellow) and after the addition of 5 µg of gramicidin (teal). Measured at $\lambda=524$ and 450 nm respectively in 20 mM HEPES pH=6.8, 0 to 50 mM sodium formate gradient. Traces are normalized averages of 5 and 4 or 4 and 3 curves respectively. The sample was incubated 10 min on ice after the addition of gramicidin

After the addition of pore-forming gramicidin; the hypertonic pressure exerted on the liposome appeared to decrease over time, as they appear to swell back after the initial water efflux (Figure 4.15 A). Gramicidin pores should not allow the passage of formate ions, but it nonetheless allowed for the hypertonic pressure to equilibrate over time by allowing water molecules to pass from the inside to the outside of the liposomes. Addition of gramicidin also leads to an increased in the internal pyranine fluorescence (Figure 4.15 B), at a faster rate than the previously observed increase (Figure 4.14 B). The part of the curves corresponding to the effect of the water efflux should be equivalent between the samples and was used to normalize and overlay the two different curves.

Hypotheses to explain the cause of such liposome pressure equilibration and alkalization are discussed later (5.1.3.)

4.1.4. Producing PffNT in human embryonic kidney cells.

As an alternative to the cell-free expression system, the methods to express PffNT in human embryonic kidney cells (HEK) were established.

4.1.4.1. Testing and validating the HEK 293 T-REx selection process

After designing and producing the plasmids of interests (3.8.3.), the following transformation and selection of human embryonic kidney cells were done at Intana Bioscience GmbH with the help of I. Jakóbowka, F. Becker and S. Hannus, K. Hansen and S. Minguzzi.

The objective was to produce stable cell lines that would be able to express functional PffNT mutants back in our lab in Kiel.

Ensuring that the pCGTO plasmids were correctly integrated in the cells genome was the first step of the selection process. Naïve HEK 293 T-RExTM cells were transformed with the pCGTO plasmids encoding mutant PffNT tagged with C - terminal His₁₀ by using the JetPRIME® kit (Polyplus) (3.8.4). These cells were cultivated on media supplemented with 100 µg/mL Zeocin®. Once the cells reached confluence, they were split (3.8.1) and the selective condition was maintained for two to three weeks. After this time, the Zeocin® selected cells were stored (3.8.6) and entered the second step of the selection process (3.8.5.) to ensure the cell lines expressed suitable levels of PffNT.

In the following experiments, HEK 293 T-REx cells transformed with the original pCGTO PffNT-GFP-myc and selected to express functional PffNT-GFP were used as positive control.

Lethality Assay

To verify that it was the PffNT activity that kept the cells alive under selective conditions 100 µL of media containing 2000 cells were added in the wells of a 96-well plates. 10 µM of PffNT inhibitor (BH267.*meta*) were added to some wells and the cells were left to grow at 37°C 5% CO₂. Images of the cells growth were taken after a few days using AxioVert.A1 microscope (Zeiss). This experiment was only carried out with the cell lines expressing PffNT-GFP (positive control), PffNT G107S-His₁₀ and PffNT G21E-His₁₀.

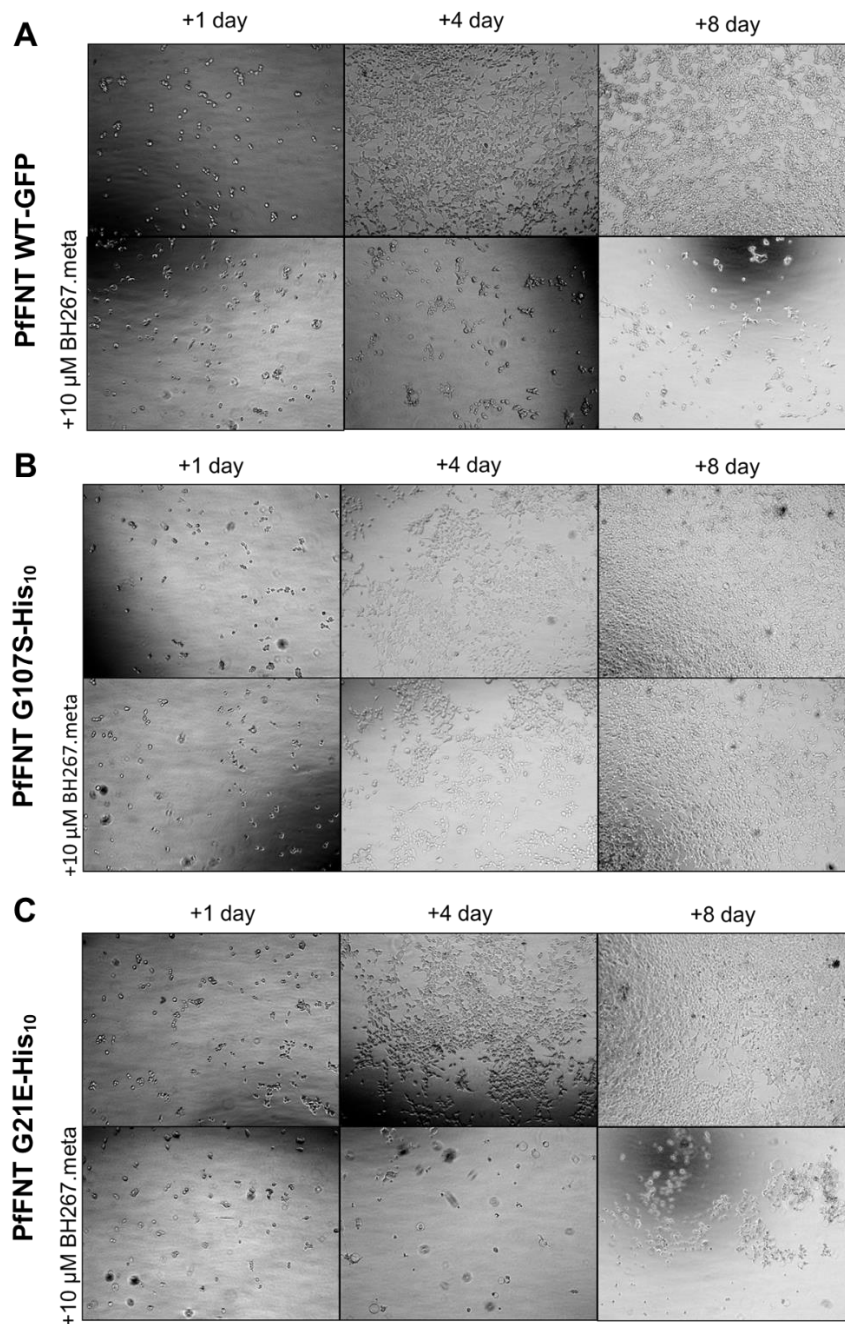


Figure 4. 16: Inhibition of the PfFNT activity leads to cell lethality under selective conditions (4 mM Metformin hydrochloride, 0.1 μ M AZD3965) in cultures of **A:** PfFNT-GFP (control), **B:** PfFNT G107S-His₁₀ and **C:** PfFNT G21E-His₁₀.

The cells expressing PfFNT-GFP and PfFNT G21E-His₁₀ behaved the same way. Here, the addition of the PfFNT inhibitor made the intracellular accumulation of lactate lethal for the cells that were growing in selective condition. However, the cells expressing PfFNT G107S-His₁₀ grew at the same rate, regardless of the presence of PfFNT inhibitor. This would suggest that for this cell line, the selective pressure of metformin hydrochloride and AZD3965 no longer applied. Beside the possibility of experimental errors, it could also have been caused by the development of a resistance to the AZD3965 inhibitor [193].

Intracellular pH assay with pHrodo™

To verify that the selected cell lines expressed surface PffNT, the pH-rodo™ indicator (Invitrogen) was used to compare the intracellular pH of cells with or without addition of BH267.*meta* PffNT inhibitor. An increase of pHrodo™ fluorescence at $\lambda_{540\text{ nm}}$ corresponds to an increase of intracellular pH. Under the selection media growth condition (with AZD3965 inhibiting MCTs transport) and the addition of PffNT inhibitor, it was expected that the inhibition of all major lactate transporters would lead to an accumulation of cytosolic lactate, resulting in an intracellular pH increase and therefore an increase of the probe fluorescence.

AZD3965/Metformin selected cells and a positive control cell line expressing PffNT-GFP were seeded in 96-wells plate, with 10^5 cells incubated overnight at 37°C, 5% CO₂ in 100 μ L DMEM 10% FCS 1% Pen/Strep, 0.005 μ g/mL blasticidin, 0.01% Zeocin, 4 mM methformin, 0.1 μ M AZD3965, 1 μ g/mL tetracyline. The next day, 1 μ L of 1 mM BH267.*meta* PffNT inhibitor in DMSO (final concentration of 10 μ M) or DMSO were added to some wells and incubated for 3 h at 37°C % CO₂. The intracellular increase of pH driven by the inhibition of PffNT was monitored using pHrodo™. For a 500 μ L volume of pHrodo™ solution 0.5 μ L of pHrodo™ are mixed with 5 μ L of PowerLoad™ concentrate 1000 \times (Invitrogen) then diluted up to 500 μ L with 20 mM HEPES Hank's balanced salt solution (HBSS). After the incubation period, the media of the cells is removed, 50 μ L of 20 mM HEPES HBSS are added then removed to wash the cell layer, the 20 μ L of pHrodo™ solution are carefully loaded on the cells then incubated 30-60 min at 37°C. The intracellular pH is later monitored by exiting the pHrodo™ at 540 nm and measuring the fluorescence emitted using a Confocor2 confocal microscope (Zeiss).

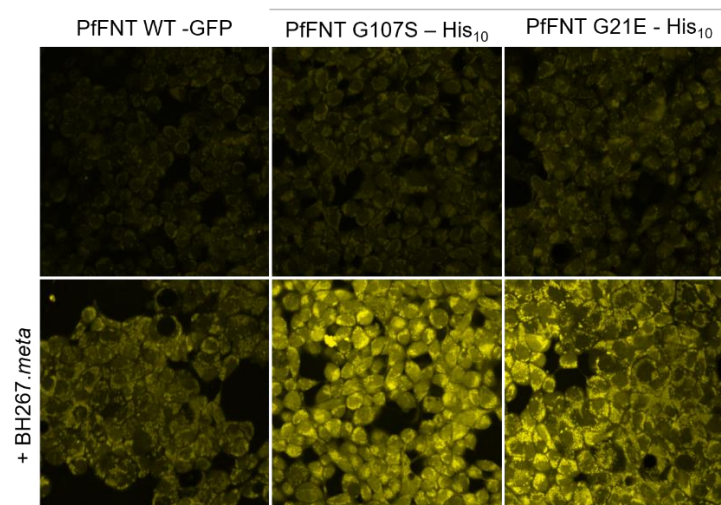


Figure 4. 17: Visualisation of the of pHrodo™ fluorescence at $\lambda_{540\text{ nm}}$. An increase of the fluorescence (yellow) corresponds to an increase of intracellular pH.

All observed cells showed an increased fluorescence after the addition of PfFNT inhibitor. This suggests that these cells rely on the PfFNT activity to avoid the intracellular lactate and proton accumulation. Therefore, these cells are likely to express functional PfFNT. These results complement previous lethality assay. Even if the cells transformed and selected to express PfFNT G107S-His₁₀ appeared to grow at the same rate regardless of the PfFNT activity, this fluorescent measurement of the intracellular pH shows that the inhibition of the lactate transporters did lead to intracellular pH increase.

Western Blots

After determining that the cell lines expressed functional PfFNT proteins, the amount of proteins present in their membranes was visualised using Western Blot. To estimate if growing the cell line in selective condition successfully increased the PfFNT expression compared to the transient expression of unselected cells, the expression levels of PfFNT produced by cell lines selected 1 week in Zeocine™ containing media, then 2 weeks in selective conditions (Metformin/ AZD3965) was compared to that of cells selected 1 week in Zeocine™ containing media (transient transfection).

These cells membranes were extracted as described earlier (3.8.7) and diluted in 4× SDS buffer and used in the same Western Blot. The blotted and blocked PVDF membrane was incubated overnight in 400 ng/mL of rabbit primary antibodies targeting the PfFNT C-terminal end (in TBS-T 5% Milk° then 80 ng/mL of anti-rabbit, HRP conjugated secondary antibodies. The ECL activity of HRP was monitored over 1 h 30 min.

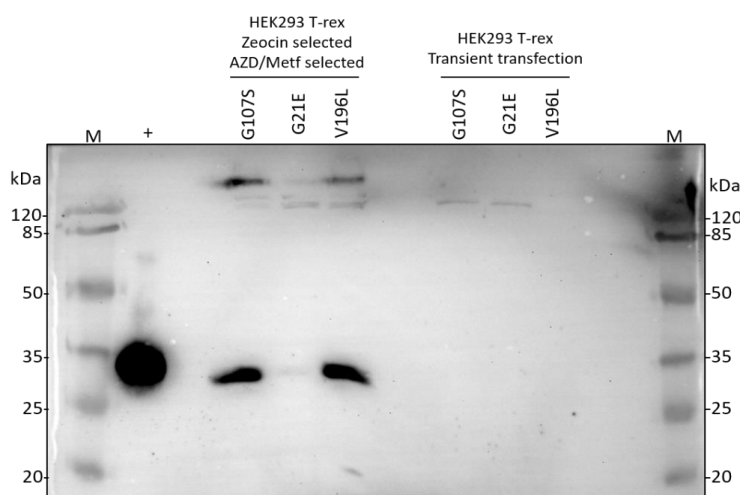


Figure 4. 18: Western Blot of the protein expressed in HEK 293 T-REx either freshly transformed with PfFNT encoding plasmids (transient transfection) or selected into a stable cell line after selections. The positive control lane (+) contained purified cell-free expressed PfFNT G107S, whose concentration was determined using the Bradford assay, kindly provided by C. Hansen. Protein marker (M) was used to estimate the protein sizes (units are in kDa).

The cell lines selected in media containing metformin and AZD3965 appeared to have expressed PffFNT, as a signal could be observed at the same level as the positive control, indicating the presence of PffFNT monomers (about 36.7 kDa, appearing between the 25 and 35 kDa protein ladders). Higher bands could be observed, above the 120 kDa protein ladder, which indicates the presence of multimers, possibly pentamers (183.3 kDa). Such signals were not detected in the other lanes of the gel. Interestingly, the PffFNT G21E-His₁₀ sample shows very little expression, despite being the cell line that responded the best to the previous lethality tests (Figure 4.16). A faint signal could be detected at the level of the 120 kDa protein ladder. It could be PffFNT trimers or tetramers (110 or 146.6 kDa) as they were targeted by the highly specific primary antibodies (targeting PffFNT C - terminal end), or it could be caused by non-specific interaction (discussed later, 5.1.4.3.).

This Western Blot showed that the expression of PffFNT in HEK T-REx was greatly improved by the selection process. It is worth noting that for this Western Blot, the total concentrations of protein loaded in each well were not normalised: this is simply an indicator of how much PffFNT could be detected in equivalent volumes of cell membrane protein extraction.

4.1.4.2. Establishing stable HEK 293 T-RExTM cell lines

After determining that the selection process increased the expression levels of PffFNT in the HEK 293 T-REx cells, stable cell lines were generated expressing the different PffFNT mutants.

The cell lines expressing the PffFNT carrying the mutations were cultivated for two to three weeks. Their protein expression levels were compared using Western Blots. Their membrane proteins were extracted before and after the selection process (0, 2 or 3 weeks growing in selective media), with or without induction of their PffFNT expression by addition of tetracycline (+ or – Tet).

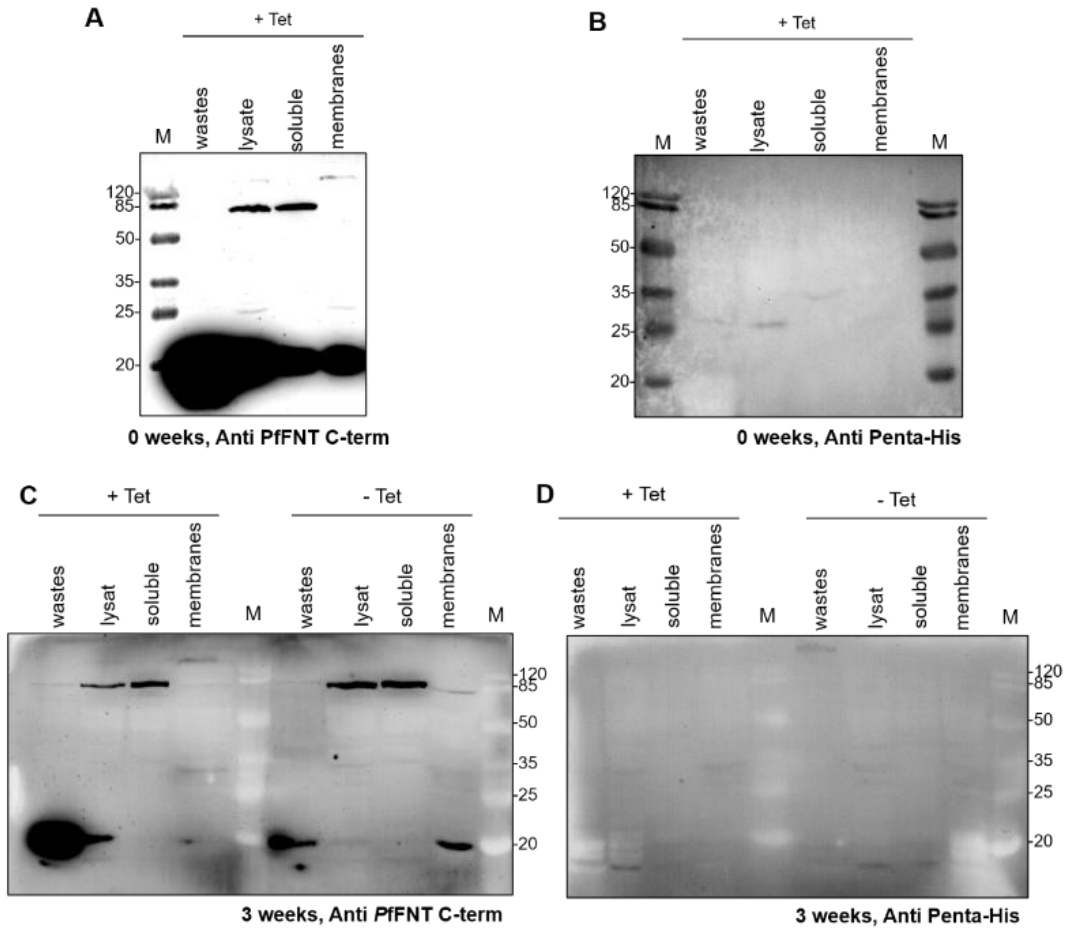


Figure 4. 19: SDS-PAGE from the extraction of PfFNT G107S-His₁₀ expressed by HEK 293 T-REx, before (**A** and **B**) and after (**C** and **D**) three weeks of culture in selective media, with or without the PfFNT expression being induced by the addition of tetracycline during the last day of growth (+ or - Tet). Western Blots of 20 μ g of protein loaded in each lane of the gels (except in the membranes +Tet lane, which is 15 μ g), done using Anti PfFNT C-terminus (**A** and **C**) and anti Penta-His (**B** and **D**) as primary antibodies. Protein marker (M) was used to estimate the protein sizes (units are in kDa).

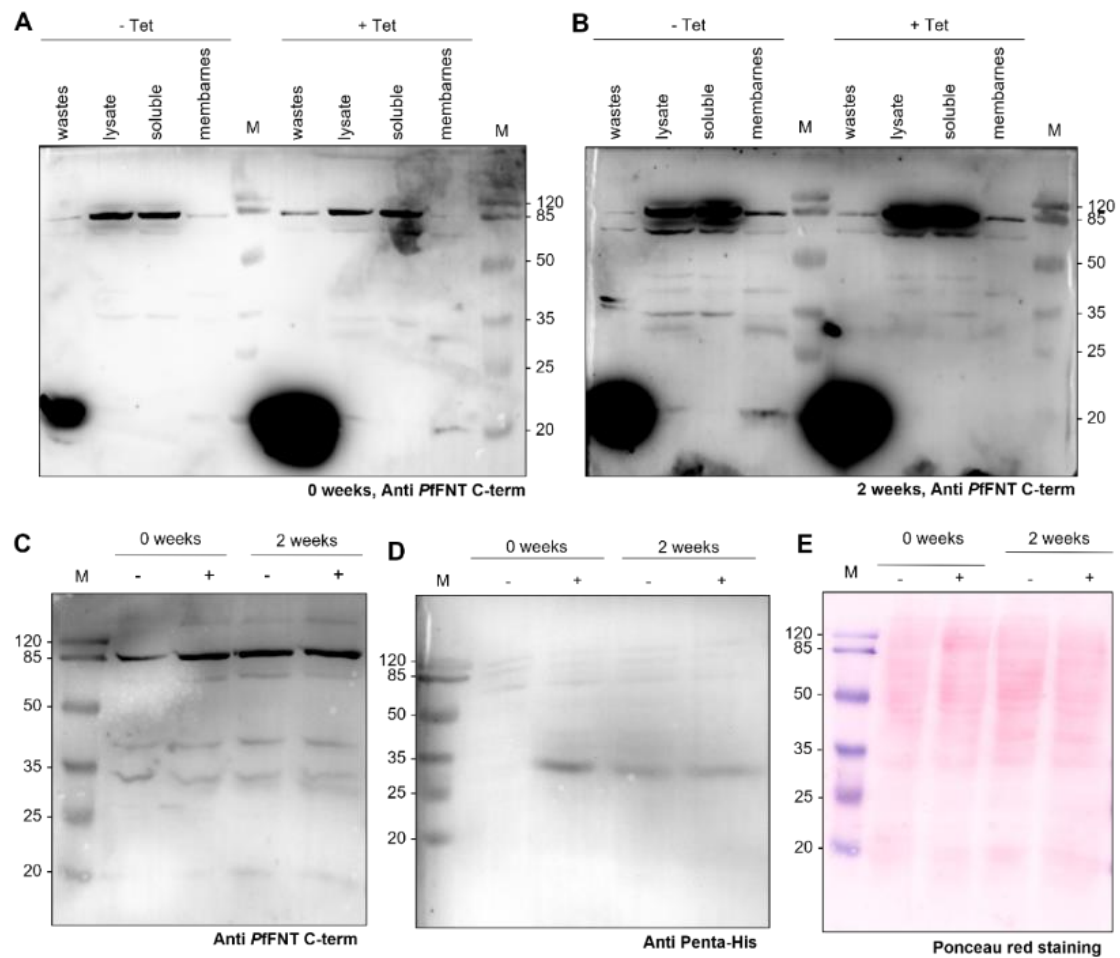


Figure 4.20: Western Blots of the proteins extracted from PpfFNT G21E-His₁₀ transformed HEK 293 T-RExTM, before (**A**, 0 weeks) and after (**B**, 2 weeks) growing under selective conditions for two weeks (**B**), with or without expression of PpfFNT by addition of tetracycline (\pm Tet). 20 μ g of protein were loaded in each well. The membrane fraction was visualised using anti PpfFNT C-term (**C**) or anti Penta-His (**D**) primary antibodies. Protein marker (M) was used to estimate the protein sizes (units are in kDa)

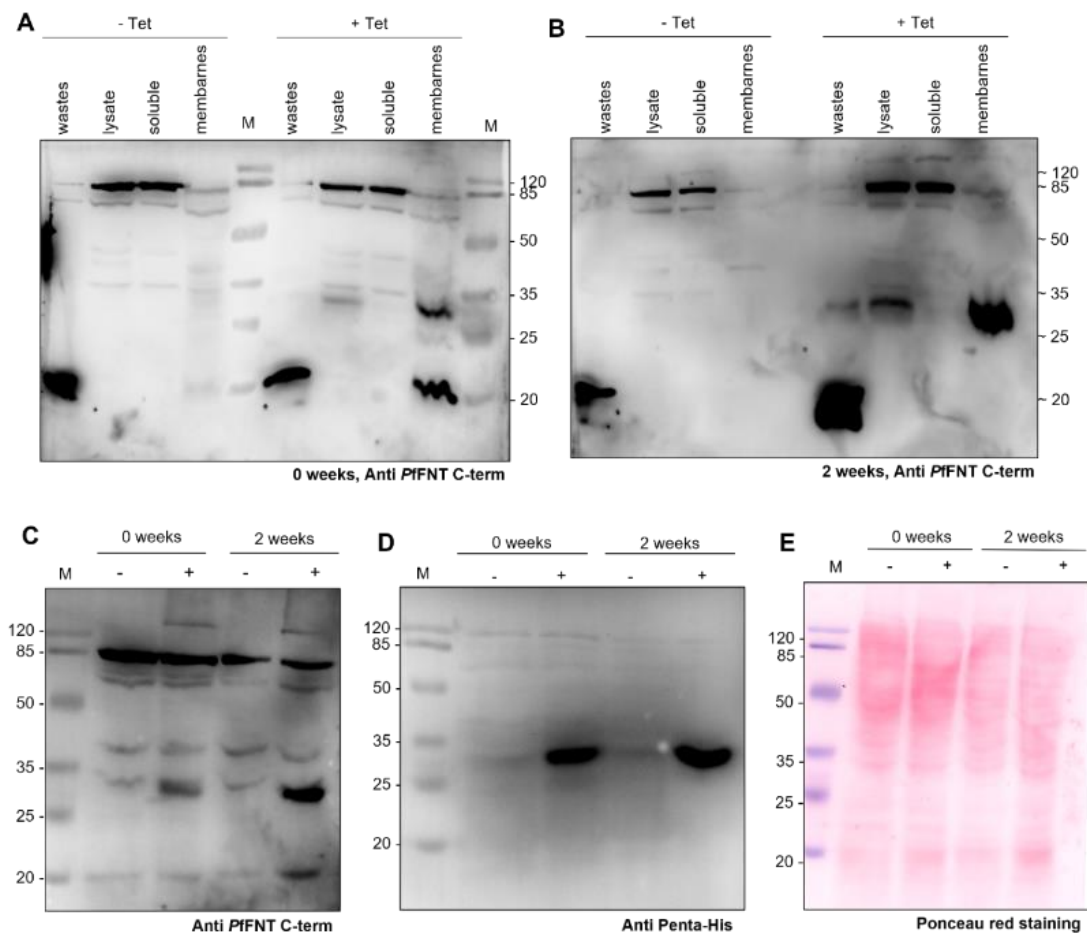


Figure 4. 21: Western Blot of the proteins extracted from PfFNT V196L- His₁₀ transformed HEK 293 T-RExTM, (**A**, 0 weeks) and after (**B**, 2 weeks) growing under selective conditions for two weeks (**B**), with or without expression of PfFNT by addition of tetracycline (\pm Tet). 30 μ g of protein were loaded in each well. The membrane fraction was visualised using anti PfFNT C-term (**C**) or anti Penta-His (**D**) primary antibodies. Protein marker (M) was used to estimate the protein sizes (units are in kDa).

Contrarily to the cell line expressing PfFNT G107S (Figure 4.19), the other cell lines were expressing a detectable amount of PfFNT before the selection process. After two weeks of selection, the PfFNT G21E-His₁₀ expressing cells appeared to express PfFNT even in the absence of tetracycline (Figure 4.20 B-D). For the PfFNT V196L-His₁₀ expressing cells, the selection process significantly increased the level of PfFNT expression (Figure 4.21 B-D). The pertinence of such selection process is discussed later (5.1.4.2.).

After the culture in selective condition, the cell expressed PfFNT, as signals corresponding to the monomers (between the 25 and 35 kDa protein markers) were detected in the Western Blots using anti PfFNT C-term and anti Penta-His primary antibodies. Many other protein bands were also detected due to non-specific interactions (5.1.4.3.). These cell lines were stored (3.8.6.) and are ready for the production of HEK cell expressed PfFNT mutants.

4.2. Investigating potential proton antenna in PfFNT

4.2.1. The PfFNT C-terminus could be acting as a proton collecting antenna

Upon the resolution of the PfFNT structure [52], [53], it appeared that the protein termini had a defined structure. The N-terminal extremity is involved with the assembly of the pentameric structure, each terminus interacting with the opposite monomers. The C-termini however, are forming helices protruding into the intracellular region.

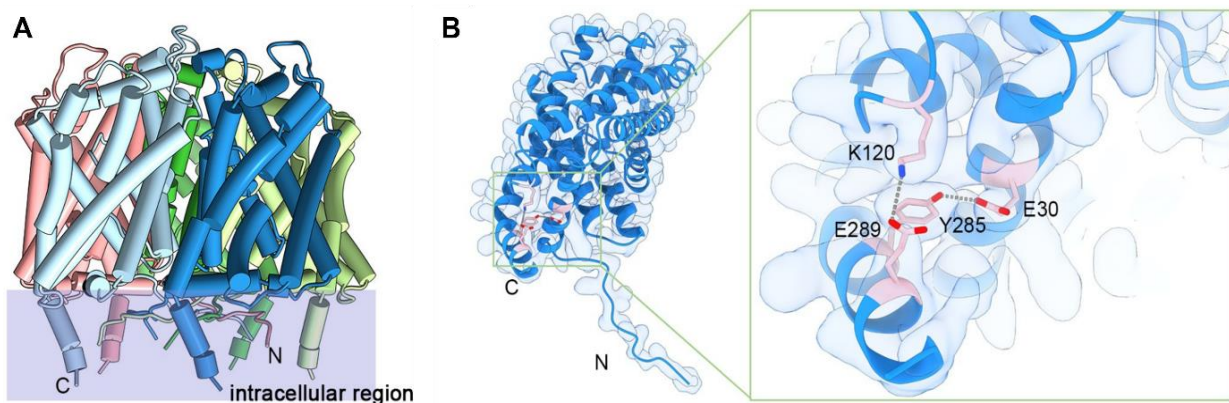


Figure 4. 22: (A) Cylinder cartoon representation of the overall PfFNT pentameric structure. (B) Schematic representation of the PfFNT monomer structure fitted to the cryo-EM electron densities. PDB#7E26. Adapted from Peng *et al.* [53].

These structured C-terminal helices appeared to be a specificity of the *Plasmodium* FNT, as other related proteins such as EcFocA do not display such features. Some reports suggest that in EcFocA, the deletion of the 6 last amino acids of the C-terminus decreased the transporter functionality [194], [195], suggesting that FNT transporters C-termini may be involved in transport, and not only in pentamer assembly. Moreover, the same group also reported that the N-terminal structure of EcFocA was involved with the regulation of the transport functionality by gating the transport path [195], [196]. This potential role of the FNT N-termini is discussed later (5.2.2).

BLASTp and protein alignment of the *Plasmodium* FNT

A protein BLAST search using the PffNT C-terminus amino acids sequence as query was used to generate an alignment of the most relevant sequence matches. It detected a high level of conservation among the C-terminal amino acids of the different *Plasmodium* FNT.

[<i>P.gaboni</i>]	KEHYYNFERSKRDGND AQMKSL SIELRN-----	309
[<i>P.sp.gorilla_clade_G3</i>]	KEHYYNFERSKRDGND AQMKSL SIELRN-----	309
[<i>P.sp.gorilla_clade_G1</i>]	KEHYYNFERSKRDND AQMKSL SIEKLS-----	305
[<i>P.falciparum</i>]	KEHYYNFERSKRDND AQMKSL SIELRN-----	309
[<i>P.reichenowi</i>]	REHYYNFERSKRDND AQMKSL SIELRN-----	309
[<i>P.berghei_ANKA</i>]	RHCYEDYETKNSSLGSMNMRGTSIEIQNDI-----	311
[<i>P.yoelii</i>]	RHYEDYEAKNSSLGSMNIRGTSIEIQNDI-----	311
[<i>P.yoelii_yoelii</i>]	RHYEDYEAKNSSLGSMNIRGFLIKNTFLIFLNWDLNLSIFY	324
[<i>P.vinckei_vinckei</i>]	NHYEDYEIKSSSLGSINMKGISIEMQND-----	274
[<i>P.chabaudi_chabaudi</i>]	SHYEDYEAKSSSLGSINMKGISIEMQND-----	310
[<i>P.vinckei_lentum</i>]	NHYEDYETKSSSLGSINMKGISIEMQND-----	274
[<i>P.vinckei_petteri</i>]	NHYEDYETKSSSLGSINMKGISIEMQND-----	310
[<i>P.knowlesi_strain_H</i>]	RNSYRDYERTRGDGNSCGLRSLSIEMQNGSNGN-----	314
[<i>P.vivax</i>]	RHSYSDYETKTRGDGNSGLKSLSIEMQNGSSGR-----	313
[<i>P.ovale_curtisi</i>]	RSYYINYEKMNPEPSG-GSLRSISIEMKNDGGAT-----	330
[<i>P.ovale</i>]	RSYYVNYEKMNELNG-GALKSISIEMKNDGGAA-----	313
[<i>P.malariae</i>]	RSCYYDYDKMDELNTVVLKTL SLELQNESNHI-----	314
[<i>P.gallinaceum</i>]	RNHYINYEKINDELNNAALKTL SIELHNGSNDLK-----	315
[<i>P.relictum</i>]	RNHYKNEYKMNDELNNAALKTL SVELHNGSNDIKDQPF GKAFK	324
	* :: : . :: :	

Figure 4. 23: Multiple protein alignment (using Clustal Omega [197]) of the different *Plasmodium* FNT C-termini identified after a protein BLAST against the PffNT C-terminal protein sequence. The conservation of the amino acids is noted in the last line.

The amino acids identified by Peng *et al.* [53] as stabilizing the C-terminal helix, Tyr285 and Glu289 (Figures 4.22 and 4.23) are among the most conserved across different species (Glu289 appears to be replaced by an equivalently charged Asp in *P. malariae*). Other conserved amino acids worthy of note are charged residues that would correspond to the PffNT Lys301 (also found as Arg in other species, this residue remains positively charged) and Glu306. Other amino acids appeared highly conserved, such as those corresponding to PffNT Asn287 (either an Asn or an Asp, which shares their structure but not their charge), Phe288 (which appear as either a Phe or a Tyr, sharing an aromatic side chain), Met300 (Met, Ile, Lys) or Ile305 (Ile, Lys, Val). These conserved amino acids might retain a common function across the different *Plasmodium* subspecies.

Poisson-Boltzmann Electrostatic Potentials

The PfFNT C-terminal end appears to be the most significant cluster of negative charges present in the surface of the protein, in the cytosolic side, as calculated using the Adaptive Poisson-Boltzmann Solver (APBS) software [160] and visualised using 3Dmol [161]. The PfFNT resolved structures did not contain the amino acids the Pro21 and past the Arg290, as the electron densities corresponding to the terminus extremities were not recorded in the Cryo-EM structures [52], [53]. AlphaFold [165], [166] was used to generate a structure prediction based on the published structures. It reported a high confidence in the prediction of the PfFNT C - terminus ($90 \geq$ per-residue confidence score > 70).

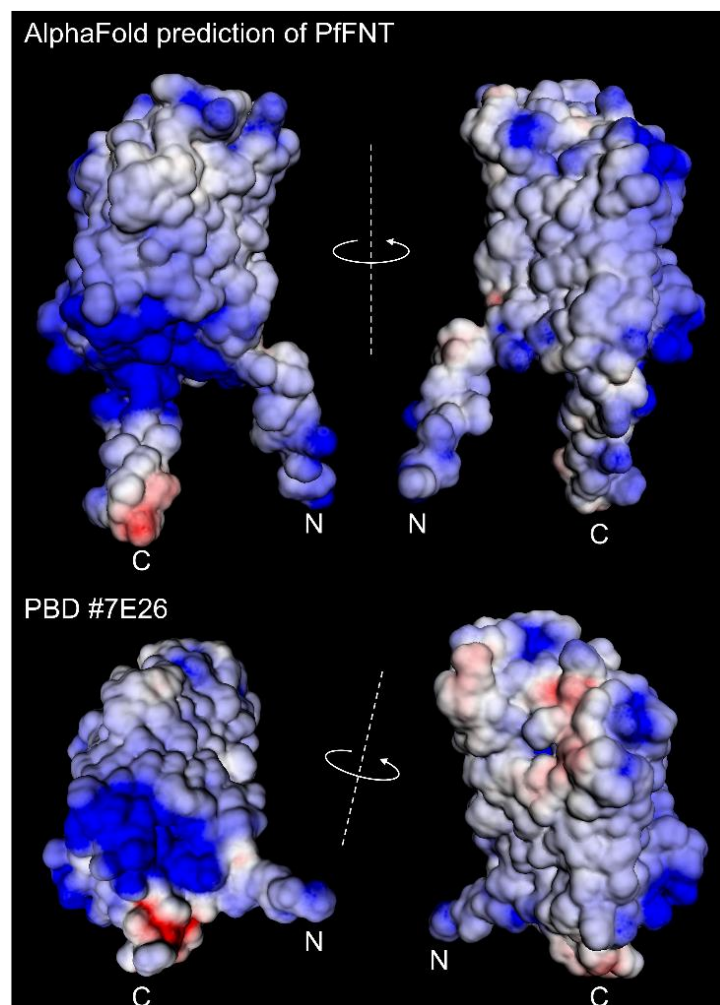


Figure 4. 24: Poisson-Boltzmann electrostatic potentials of a PfFNT monomer, from $+3ke^-$ (blue) to $-3ke^-$ (red). Calculated using the PARSE forcefield, $pH=7.2$, using AlphaFold structure prediction from 5 structures (PDB #6VQQ, #6VQR [52], #7E26, #7E27 and #7MXY [53]) or the PDB#7E26 [53]. The C and N-termini are labeled as such.

The C-terminal end of the PfFNT shortened resolved structures and prediction displayed the maximal negative surface charges (red) at physiological pH ($pH=7.2$).

Deletion of the PfFNT termini impacted substrate transport (at pH=4.8)

While studying the impact of post-translational modifications on the PfFNT transport functionality, A. Jansen had generated a truncation variant of PfFNT, excluding the first 18 amino acids of the N-terminus and the last 10 amino acids of the C-terminus ($\Delta 1-18_{\Delta 299}$). It served the purpose of deleting the regions in which phosphorylation took place (Ser17, Ser302 and Ser301, as observed using the mass spectrometry and reported by PlasmoDB [151], [198]). Although point mutations of these phosphorylation sites (to Ala or Asp) did not yield observable changes in the transport capacity at equilibrium, the deletion of both termini led to a significantly lower capacity at pH=4.8 (while no such difference was observed at pH=6.8).

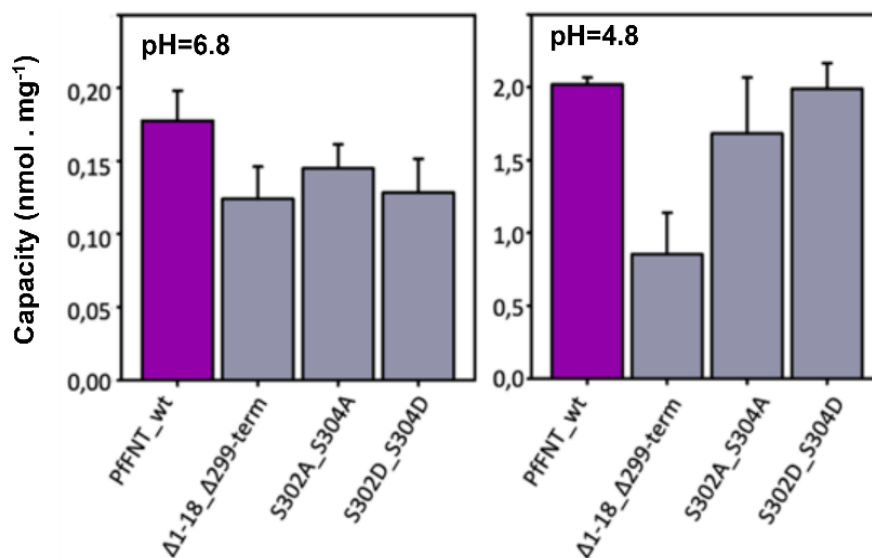


Figure 4. 25: Transport capacity of the PfFNT construct used by A. Jansen to investigate the effect of phosphorylation on transport, at pH=6.8 and 4.8. Adapted from A. Jansen doctoral thesis [151].

Such an effect could be explained by different factors. The deletion of the C-terminal could have decreased the total substrate that the FNT could transport at equilibrium because it acts as a facilitator of transport, or the deletion of the N-terminal end could be the cause of the decrease. Additional experiments were necessary to determine the source of this effect (4.2.3.). Their conclusions are discussed later (5.2.2.).

Isoelectric Point and Total Charges

Theoretical calculations of the PfFNT isoelectric point (pI) were made using the “Prot pi | Protein Tool” web application (2.13.2.) to estimate the effect of the PfFNT C-terminus and additional terminal tags on the protein charge. Overall, the amino acids 282 to 309 of PfFNT displayed a high level of identity with the other *Plasmodium* termini (Figure 4.23). A PfFNT mutant was prepared with the full length of the PfFNT termini deleted ($\Delta 282$) to investigate its potential effects.

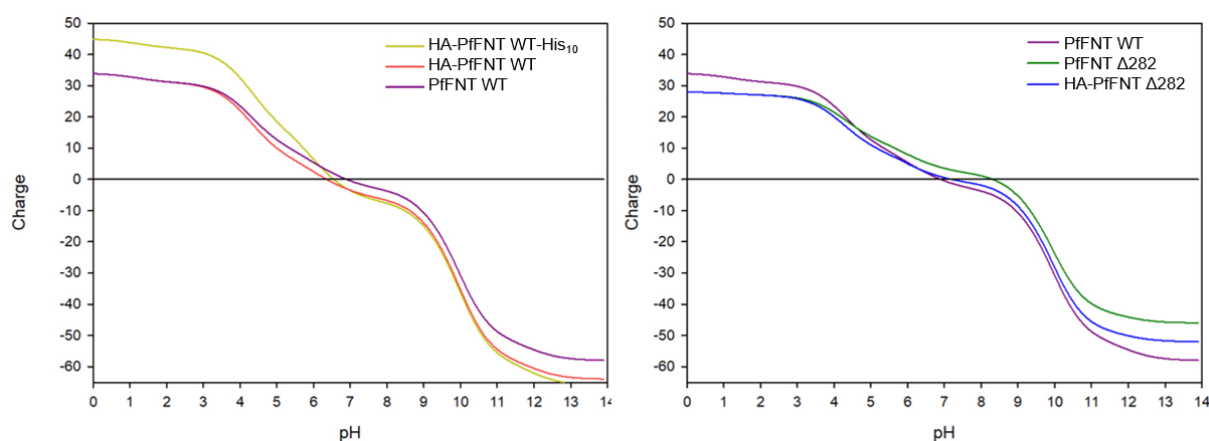


Figure 4. 26: Total electric charges in PfFNT constructs, depending on the pH. Calculated using the “Prot pi | Protein Tool” web application, using ExPASy pK_a values, assuming that the PfFNT sequence carries the observed post-translational modifications (Lys7-Acetate, Ser30-P_i, S302-P_i, S304-P_i) [151].

Table 4. 1: Isoelectric point (pI) and net charges (z) of the different PfFNT constructs.

	HA-PfFNT WT -His ₁₀	PfFNT WT -His ₁₀	HA- PfFNT WT	PfFNT WT	PfFNT $\Delta 282$	HA- PfFNT $\Delta 282$
pI	6.545	6.909	6.355	6.897	8.316	7.204
z (pH=7.2)	- 4.692	- 1.69	- 4.264	- 1.262	+ 3.012	+ 0.009
z (pH=6.8)	- 2.21	+ 0.786	- 2.534	+ 0.463	+ 4.198	+ 1.202

There does not appear to be any significant differences between the native (PfFNT WT) and the HA-tagged protein within the 1 to 3 pH range. However, such high pHs are less physiologically relevant. The presence of the HA tag appears to shift the protein pI toward more acidic values. This protein tag proved necessary for the identification of PfFNT $\Delta 282$ and its

presence is therefore required. But as it is located at the N-terminal end, it was hypothesized that it would not interfere with the observations of the C-terminal extremity.

The addition of the C-terminal His₁₀ tag to the protein sequence had a significant effect on the pI in the 1 to 6.5 pH range (Figure 4.26, yellow curve). Once the pH becomes higher than the construct pI (6.545), the total charge of the His-tagged proteins becomes greater than that of the native one. It suggests that these positively charged Histidines may bind and attract a significant concentration of substrates anions, making the presence of the His-tag detrimental to the study of the C-terminal contribution to transport. Once the pH was lower than the pI, the shape of the yellow curve matched that of the HA-tagged protein (red curve), meaning that the C - terminal His-tag might not have a significant effect in this range.

As a means of comparison, the cytosolic pH of *Plasmodium falciparum* was reported to be around 7 [199] (with the inside of the parasitophorous vacuole reaching a pH of about 5 [199], [200]). Jensen *et al.* reported that in cultures of *Plasmodium* infected erythrocytes growing in optimal pH conditions at pH>7.15. The red blood cell intracellular pH was between 6.3 and 6.85, while the pH of the parasite compartment was between 7.5 and 7.8 [201]. The human blood pH is highly buffered around 7.4 [202].

Deleting the PffNT C-terminus from the amino acid sequence would significantly increase the protein pI, as observed in the PffNT Δ 282 charge curve, in green. This further suggests that this terminus contains plenty of negative charges, reinforcing the hypothesis that it could act as proton binding sites or a proton collecting antenna.

Designing the pDR Plasmid and Derivatives.

Beside the report by Noor *et al.* that the addition of a C-terminal His-tag affected the transport functionality of monocarboxylate transporter [143], these informations justified the need to edit the pDRTXa plasmid. As it was, it expressed the proteins of interest flanked with a N - terminal HA tag and a C-terminal His₁₀ tag (separated from the protein sequence by a Factor Xa cleavage site). The pDR plasmid was thus prepared (2.2.1, Supp. 2.3.) to allow for the expression of either untagged or N - term HA-tagged PffNT. These plasmids were first used to study the eventual effect of the PffNT C-terminus without risks of artificial tags interferences. Later, such plasmid would be used to verify if these terminal HA and His-tags had an effect on transporters functionality (4.4.).

4.2.2. Point mutations of The Tyr285 and Glu289

First, the Tyr285 and Glu289 were mutated using Site-directed mutagenesis (3.1.3.) to Phenylalanine (conserving the aromatic residue, removing the polar hydroxyl group) and glutamine (identical structures, removing the negative charge by replacing the oxygen from the carboxyl group by an amid group) respectively. As these residues were identified by Peng *et al.* [53] as binding and stabilising the C-terminal helix (Figure 4.22 B), these mutations were hypothesized to disrupt the C-terminus. The point mutations were prepared as described in Supp. 1.2.

The plasmids encoding untagged FNTs were used to transform Δ jen1 Δ ady2 yeasts (3.5.1.) to measure the transport of radiolabeled substrate over time (3.6.). The expression levels of the different constructs were estimated by Western Blot using the anti-PfFNT as primary antibodies.

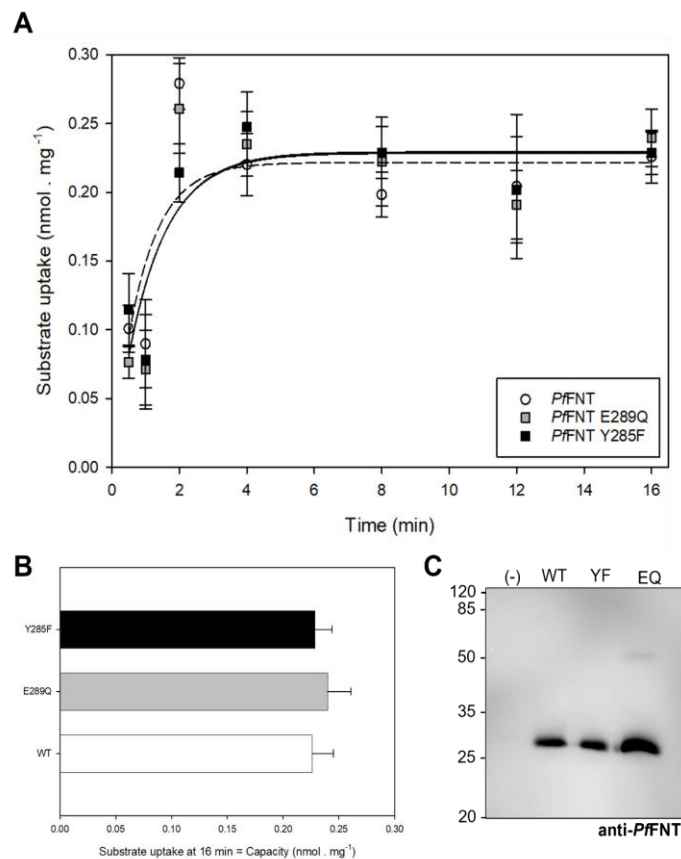


Figure 4. 27: Radiolabeled substrate uptake of the different PfFNT constructs over time (A) and at equilibrium (B), measured in Tris/HEPES pH=6.8, 1 mM L-lactate. Error bars represent SEM of experimental triplicate. Background subtracted. The protein expressions were estimated based on a Western Blot (C) containing equivalent total protein concentrations in each well. Protein marker (M) was used to estimate the protein sizes (units are in kDa).

Measuring the substrate transported (uptake) at different time points. Each curve was fitted as an exponential rise to a maximum (single, 2 parameters). The dashed line represents the wild type PfFNT fitting curve. The two solid fitting curves corresponding to PfFNT Y285F and E289Q almost overlap. As these transport curve reaches a plateau after about 8 min of transport, the substrate uptake at 16 min was used as a representation of the maximal transport capacity. (Figure 4.27 B). Comparing the capacities of the Y285F or the E289Q mutants to the wild type showed no significant differences (Student's t-test, two-tailed $p=0.919$ and 0.648 respectively). These results indicate that these point mutations did not lead to significant changes in the protein uptake functionality. Perhaps single mutations were insufficient to destabilize the C - terminus. A PfFNT construct, tagged with an N - terminal HA-tag, was generated, carrying both the Y285F and E289Q mutations at the same time. Its functionality was assayed in the same way as the single point mutants.

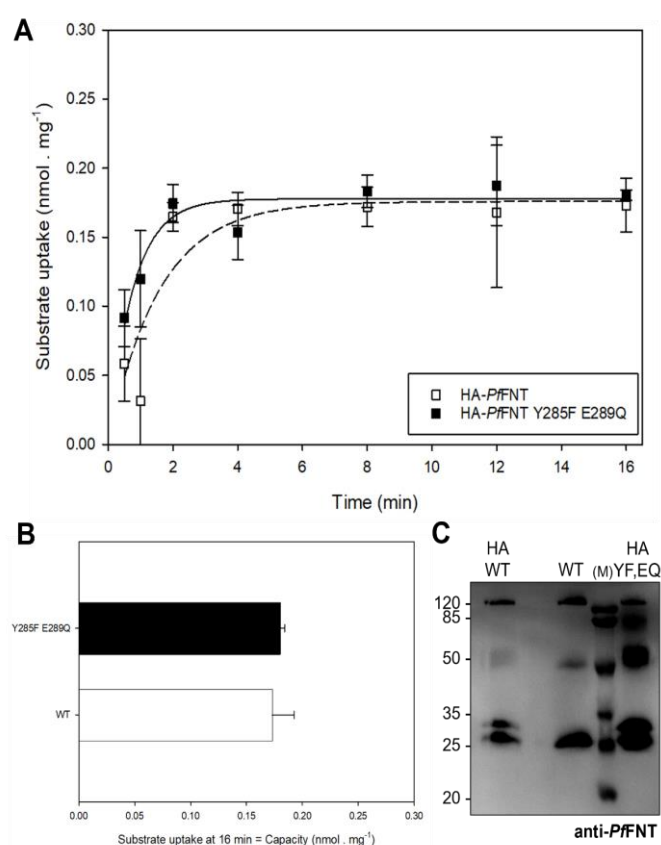


Figure 4. 28: Radiolabeled substrate uptake of the different PfFNT constructs over time (A) and at equilibrium (B), measured in 50 mM Tris/HEPES pH=6.8, 1 mM L-lactate. Error bars represent SEM of experimental duplicate (WT) or triplicate (mutant). Background subtracted. The protein expressions were estimated based on a Western Blot (C) containing equivalent total protein concentrations in each well. Protein marker (M) was used to estimate the protein sizes (units are in kDa).

Once again, the fitted transport curves (exponential rise to a maximum, single, 2 parameters) appeared to reach the same plateau, meaning the same capacity at transport equilibrium. However, the HA - PffNT WT (Figure 4.28 A, white square and dashed fitted curve) appeared to reach this equilibrium slower than the mutant (Figure 4.28 A, black squares, solid fitted curve). This can be explained by an apparent greater expression level of the mutant, as observed in the Western Blot signals (Figure 4.28 C). Past 8 min, the fitted curves appeared to have reached their maximal level, meaning that the measured substrate concentration at 16 min can be used to compare the capacities at transport equilibrium for the different FNT mutants (Figure 4.28 B), which showed no significant differences (Welch's t-test, two-tailed $p=0.775$).

After these experiments, it appeared that either the two mutations were not enough to destabilize the position of the PffNT C-terminus, or that such position is irrelevant for substrate uptake.

4.2.3. Deletion of the PffNT C-terminal.

Since simple point mutations were not enough to observe any differences, it was decided to use a more direct approach: deleting the part of the C-terminus that was hypothesized to play a role in transport functionality.

4.2.3.1. Effect of the $\Delta 299$ truncation:

The last 10 amino acids of the PffNT C-terminal were truncated ($\Delta 299$) by amplifying the PffNT gene by PCR with the primers PCR_PffNTnter_s and PffNT_ $\Delta 299$ -term_XhoI_as (Table 2.4). The extracted insert was digested and inserted in the pDR plasmid. These plasmids were used to transform Δ jen1 Δ ady2 yeasts (3.5.1.) to measure the transport of radiolabeled substrate over time (3.6.1.).

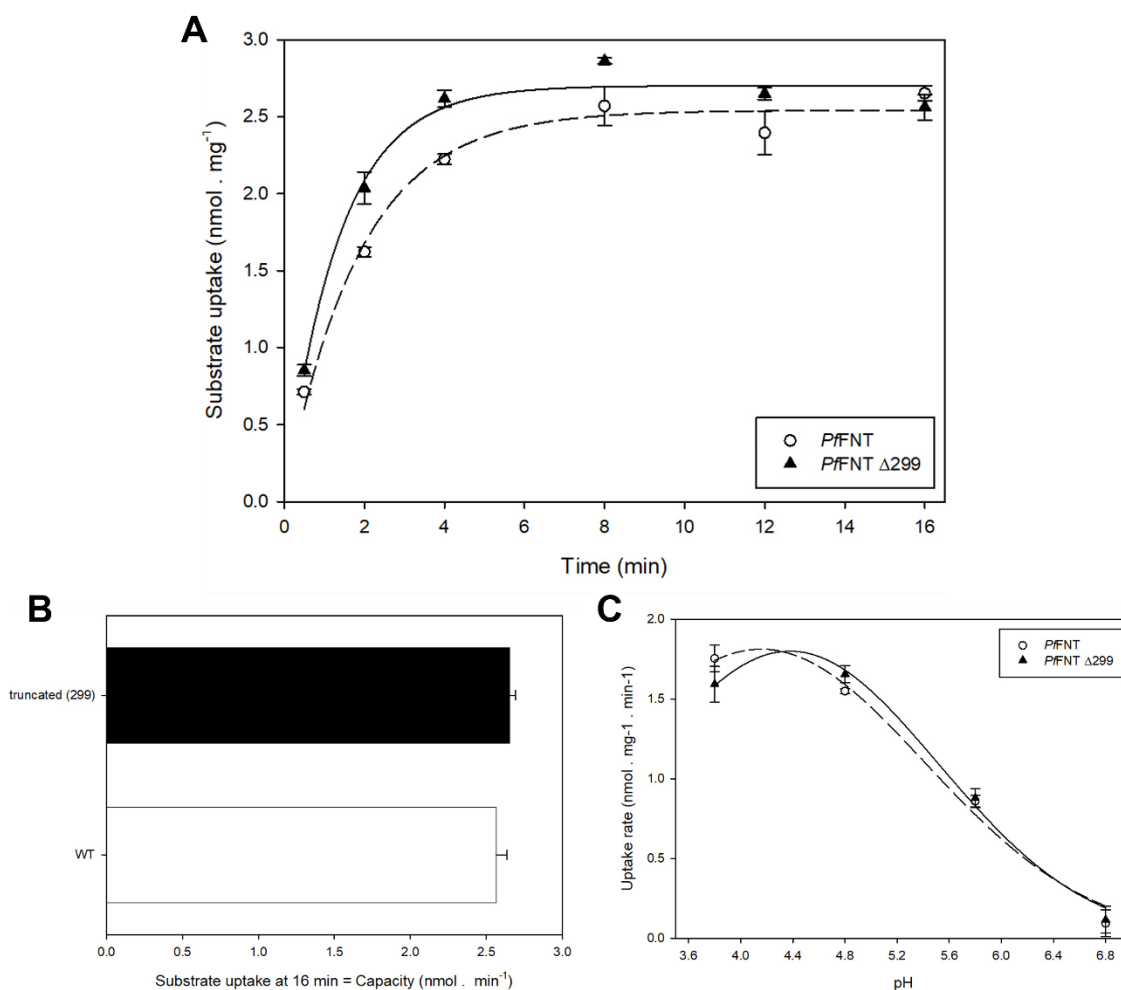


Figure 4. 29: Radiolabeled substrate uptake of the different PfFNT constructs over time (**A**) and at equilibrium (**B**), measured in 50 mM Tris/MES pH=4.8. (**C**) Radiolabeled substrate uptake rates of the different PfFNT constructs measured at different pH (over 0.5 min). 1 mM L-Lactate, Error bars represent SEM of experimental duplicate. Background subtracted.

The transport curves of the PfFNT construct (Figure 4.29 A) were fitted to exponential rises to a maximum (simple, two parameters) that appear to be reached after 16 min of transport, as the curves reach a plateau. This would represent the capacity at transport equilibrium, as represented in Figure 4.29 B. There did not appear to be significant differences between the two capacities (Student's t-test, two-tailed $p=0.393$). The uptake rates measured as a function of pHs were fitted to a peak (Gaussian, three parameters) and showed little difference between the truncated ($\Delta 299$) and the wild type PfFNT (Figure 4.29 C).

4.2.3.2. Effect of the complete C-terminus truncation ($\Delta 282$)

The full C-terminus of PffNT was truncated by amplifying the PffNT gene with PCR, using the PCR_PffNTnter_s and PCR_PffNTd282-XhoI_as2 primers (2.3.4.). The resulting coding sequence was inserted in a pDR plasmid and it was used to transform Δ jen1 Δ ady2 yeasts (3.5.1.) to measure the transport of radiolabeled substrate over time (3.6.1.)

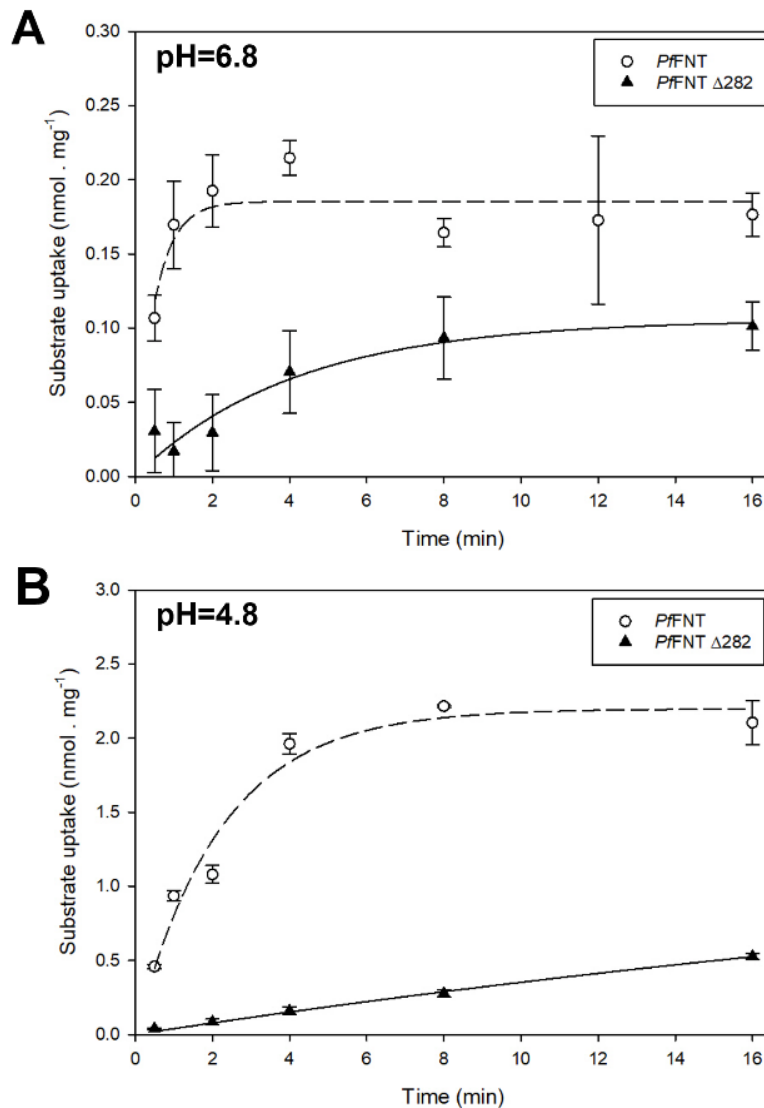


Figure 4.30: Substrate uptake curve over time of wild type PffNT (white circles) and C-terminus truncations ($\Delta 282$, black triangles) in 50 mM Tris/HEPES pH=6.8 (A) or 50 mM Tris/MES pH=4.8 (B). 1 mM L-Lactate. Error bars represent SEM of experimental triplicates. Background subtracted.

At first glance, the total deletion of the C-terminus appeared to significantly decrease the substrate uptake. The transport curves were fitted with exponential rises to a maximum (single,

two parameters) and it appeared that in both conditions the PfFNT $\Delta 282$ uptake did not reach its plateau after 16 min of transport. This could either had been caused by a low transport functionality or a low expression rate.

As this C-terminus deletion is located in the cytosolic side of the yeast, several experiments were designed to visualize the possible effects. First, the radiolabeled substrate uptake assay was modified to measure substrate efflux (3.6.2.).

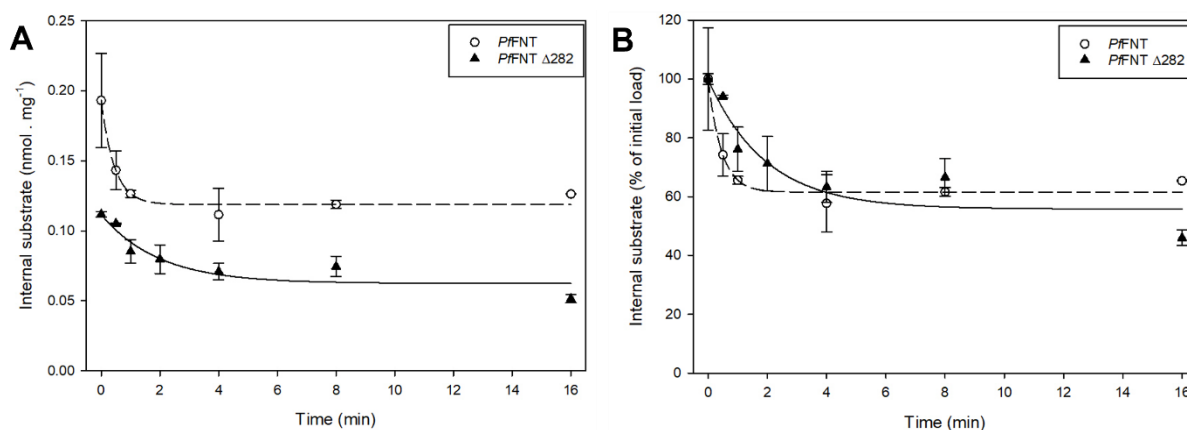


Figure 4. 31: Efflux of substrate over time of wild type PfFNT (white circles) and C-terminus truncations ($\Delta 282$, black triangles), expressed as nmol of substrate per mg of yeasts (A) or percentage of the initial load (B). The cells were loaded for 7 min and 40 seconds in 1 mM L-lactate. 50 mM Tris/HEPES pH=6.8. Error bars represent SEM from experimental duplicates. Background subtracted.

The substrate effluxes over time were fitted as exponential decay equations (Single, three parameters): There, the truncation mutant showed a lower initial substrate load (Figure 4.31 A), followed by a lower efflux rate (Figure 4.31 B) compared to the wild type. Interestingly, both PfFNT constructs displayed an efflux rate that was about twice as high as the influx rates that can be calculated from the transport curves at pH=6.8 presented in Figure 4.30 A: the WT showed an influx rate of 0.21 ± 0.03 and an efflux rate of 0.56 ± 0.53 , while the $\Delta 282$ truncation showed an influx rate of 0.08 ± 0.007 and an efflux rate of 0.15 ± 0.06 nmol · mg⁻¹. It remained to be determined whenever it was a behavior of the PfFNT or an inaccuracy of the measure. The pertinence of such efflux assay is discussed later (5.4.3.).

IC₅₀ curves of the PfFNT inhibitors BH296, which enters the transport path through the cytosolic side were measured to visualize whether modifications at the level of the C - terminus had an impact on the inhibitor affinity.

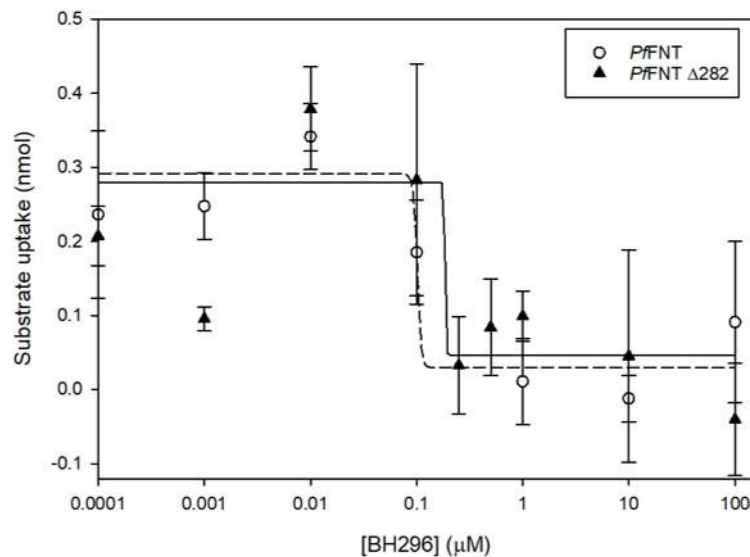


Figure 4. 32: Inhibition curves of the BH296 inhibition of PfFNT transport functionality. 1 mM L-lactate, in 50 mM Tris/HEPES pH=6.8, 1%DMSO. Measured over 30 seconds (PfFNT) or 3 min (PfFNT Δ282). Errors bars are SEM of three experimental replicates. Background subtracted.

The inhibition curves of the PfFNT construct (WT: white circles, dotted line; Δ282: black triangles, solid line) were fitted as sigmoidal curves (Sigmoid, 4 parameters). Using these curves to determine the halfway point between the maximal and minimal values of the equation, the IC_{50} of each protein was determined. 50% of the transport functionality was inhibited in presence of about 0.1035 μ M or 0.1858 μ M BH296, for the WT and truncated protein respectively. These values match the BH296 IC_{50} of 0.14 μ M reported for PfFNT WT [25]. As such, it appeared that a truncation of the C-terminals did not modify the inhibitor affinity, validating that such deletion should not significantly affect the folding of the transporter path. However, the fact that the Δ282 truncated PfFNT required 3 min of transport time to yield measurable transport values stressed that this construct PfFNT was significantly less active than the other.

A Western Blot was prepared, loading the same amount of total membrane proteins for each PfFNT constructs and comparing the signals intensity detected by rabbit anti-PfFNT and HRP - conjugated anti-rabbit antibodies.

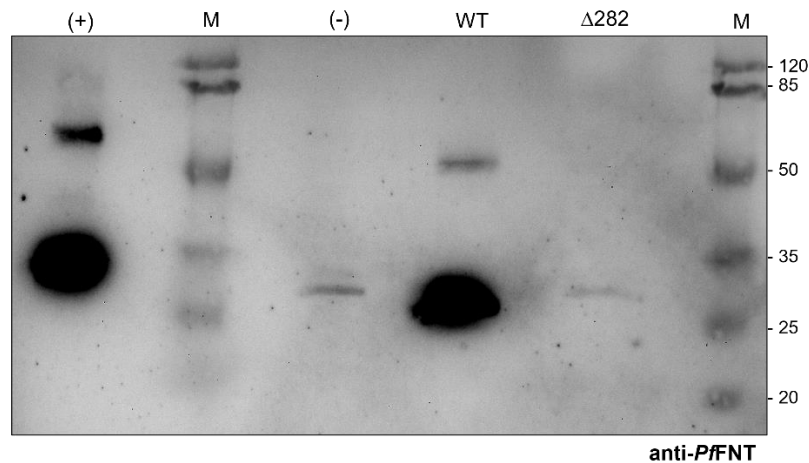


Figure 4. 33: Western blot of 10 μg yeast total membrane proteins, loaded on a 12.5% PAGE gel. Detected using the anti-PfFNT primary antibody. Protein marker (M) was used to estimate the protein sizes (units are in kDa). The PfFNT constructs were loaded alongside a positive (+: 0.5 μg of cell-free produced PfFNT) and negative (- : membrane proteins of untransformed yeasts) controls.

The expected molecular weight of the N-terminal HA-tagged and C-terminal His-tagged proteins expressed in cell-free system is 37.59 kDa. Their monomers are routinely detected just below the 35 marker. The untagged proteins were expected to weigh 34.5 kDa, which could be detected (WT) between the 25 and 35 kDa markers. However, no significant signals could be detected in the membrane proteins of the yeasts expressing the truncated PfFNT ($\Delta 282$, expected to weigh 31.11 kDa) that could not also be detected in the negative control (-). A low level of non-specific epitope recognition appeared to occur. It is unclear which yeast proteins are weakly recognized by the anti-PfFNT antibodies around the same level as the PfFNT monomers. It appeared that the antibodies raised against PfFNT could not detect the C-terminal truncations. It also appeared that the epitope of such antibodies recognizes the 15 last amino acids of the protein sequence (NNDAQMKLSIELRM). This means that the truncation mutant levels of expressions could never be assessed using Western Blot without being expressed with a tag that would be recognized by the antibodies epitope. It was therefore decided to express PfFNT $\Delta 282$ fused to the N-terminal HA tag. It is also worth mentioning that the C-terminal His-tagged PfFNT $\Delta 282$ were poorly expressed and did not appear functional.

The HA-tagged C-terminal truncated PfFNT behaves similarly to the Wild Type, except at higher extracellular pH

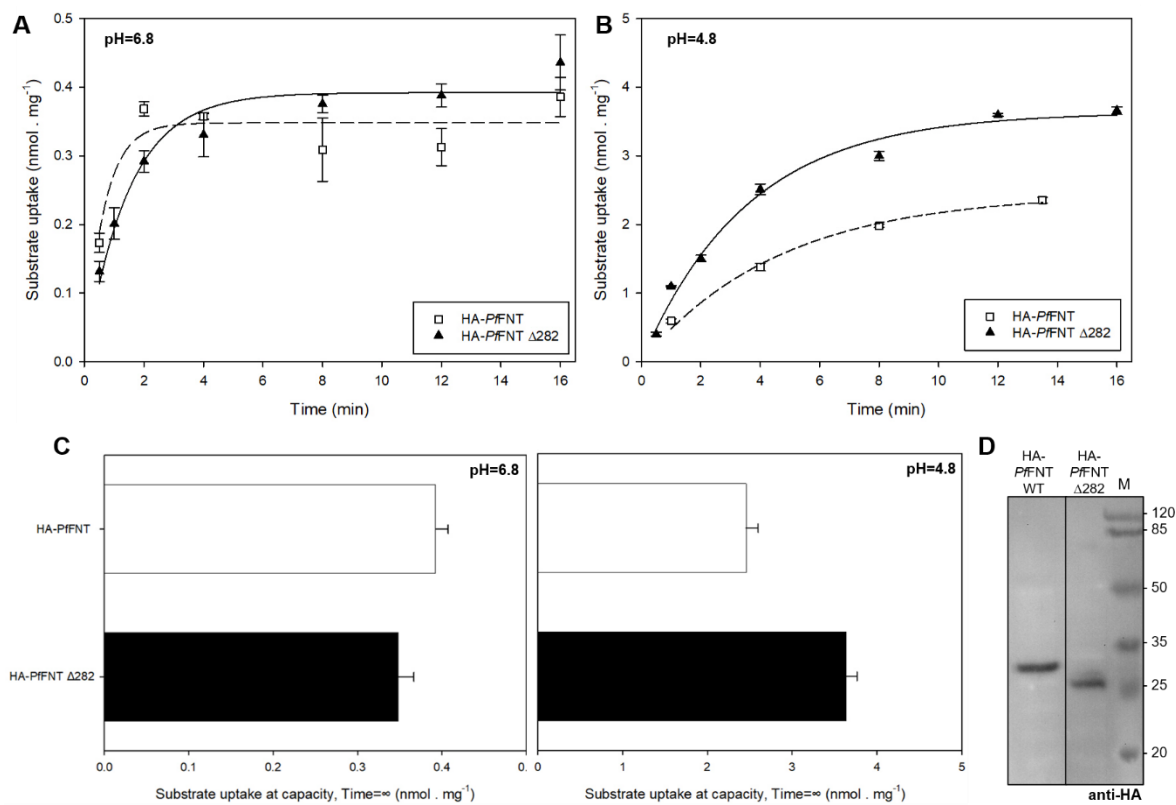


Figure 4. 34: Substrate uptake of HA-tagged wild type (white squares) and truncated C-terminus (black triangles) PfFNT expressing yeasts measured over time in 50 mM Tris/HEPES pH=6.8 (**A**) or 50 mM Tris/MES pH=4.8 (**B**). 1 mM L-Lactate, background subtracted. The substrate uptake capacity at equilibrium was determined from the fitted curves (**C**). Error bars represent SEM of experimental duplicates. The protein expressions were estimated based on a Western Blot (**D**) containing 10 μ g of membrane proteins in each well. Protein marker (M) was used to estimate the protein sizes (units are in kDa).

The HA-tagged truncated PfFNT appeared to be properly expressed, as relevant lactate uptake could be measured using radiolabeled substrate assay (Figure 4.34 A-C) and a relatively equivalent amount of signal could be observed in each well of the Western Blot (Figure 4.34 D). The substrate transport curves over time were fitted with exponential raises to a maximum (Single, 2 parameters), and the capacity at transport equilibrium deduced from the fitted curves (Figure 4.34 C). There was no statistically significant difference between the two capacities (Student's t-test, two-tailed $p=0.415$) at pH=6.8 (Figure 4.34 A, Figure 4.34 C left) but there was one at pH=4.8 (Student's t-test, two-tailed $p=0.0256$) (Figure 4.34 B, Figure 4.34 C right). The difference between these capacities is discussed later (5.2.3.).

The transport rate pH dependency of the PfFNT (HA-PfFNT $\pm\Delta 282$) was observed by measuring the L-lactate transport over 30 s in buffer solutions of different pH (3.6.4.).

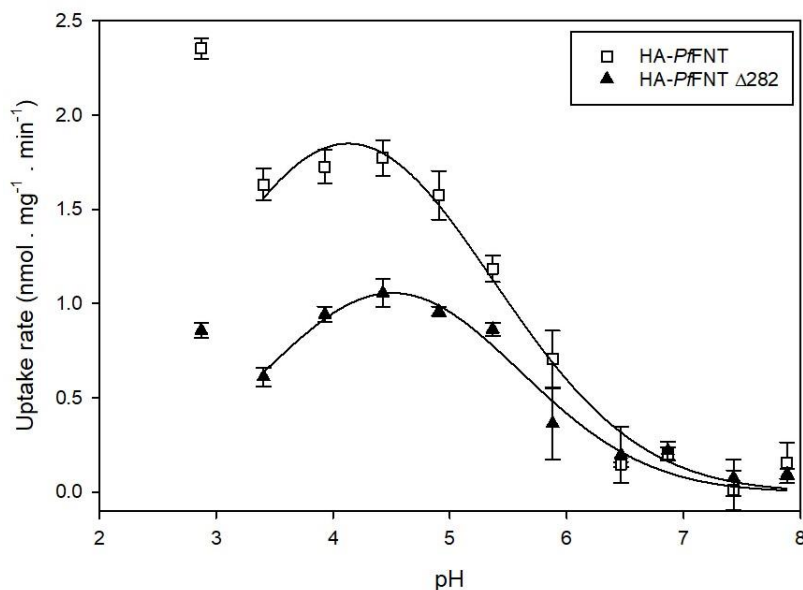


Figure 4. 35: Measures of the substrate uptake rates of HA-tagged wild type (white squares) and truncated C-terminus (black triangles) PfFNT expressing yeasts. Measured over 30 seconds in 1 mM L-Lactate, with different pH buffers. Error bars represent SEM of experimental duplicates.

While more acidic pH appeared to have an impact on the transport capacity, the pH-rate dependency of the different protein construct did not appear to be different (Figure 4.35). While the lactate uptake rates appear equivalent between the two constructs between pH of 6.5 to 7.8, those of the truncated protein appear significantly lower than the wild type at more acidic pH. As the protein signal observed in the HA-PfFNT $\Delta 282$ Western Blot lane is slightly lower than that of the HA-PfFNT (Figure 4.34 D), differences in protein expression levels could still be the reason for that difference. The rates over pH were fitted as peaks (Gaussians, 3 parameters) between pH of 3.5 and 7.8. The two curves appear to follow the same shape, but the peak of HA-PfFNT $\Delta 282$ was centered ever so slightly toward the higher pHs. Overall, beside the difference in the uptake rate, the extracellular pH-rate dependency of the transport functionality of the PfFNT uptake does not appear to be affected by the truncation of the C - terminus.

It is, however, worth noticing that the shape of the curves did not match those that were previously reported [51], [57], [60]. It was the subject of more experiments and further discussion (5.6.).

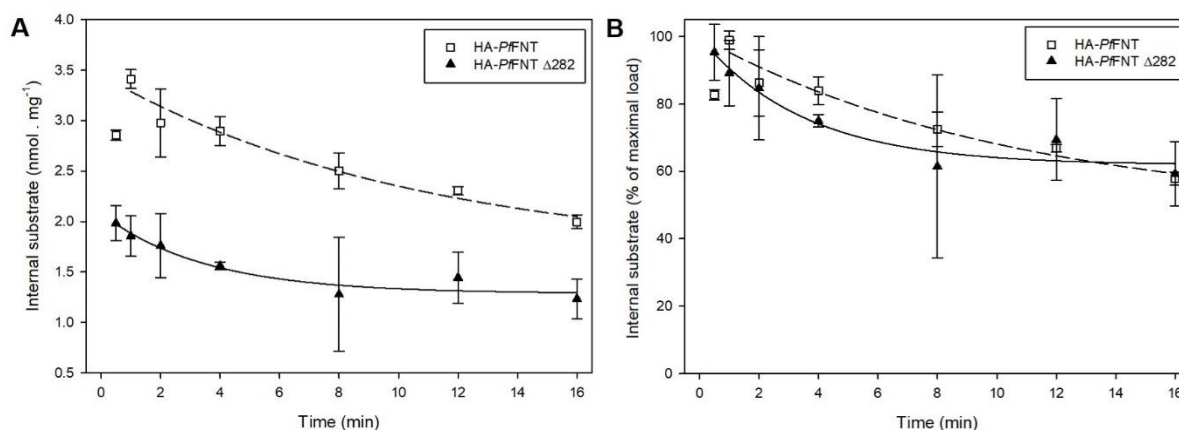


Figure 4.36: Substrate efflux of HA-tagged wild type (white squares) and truncated C-terminus (black triangles) PfFNT expressing yeasts. Measured over time in 50 mM Tris/HEPES pH=6.8. The cells were loaded for 8 min in 1 mM L-Lactate, 50 mM Tris/MES pH=4.8. Background subtracted. Error bars represent SEM of experimental duplicates.

The measured substrate efflux was fitted to exponential decays (single, 3 parameters), but the first point of the HA-PfFNT curve had to be excluded for a reasonable fit. The two protein constructs showed different initial lactate load (Figure 4.36 A) after 8 min of uptake in pH=4.8. This can be explained by the previous figure that showed that the uptake rate of the truncated protein ($\Delta 282$) was lower than the wild type (Figure 4.34 D). Once normalized to the same scale, by expressing the substrate efflux over time as a percentage of the initial load, the efflux curves of the two protein constructs appeared to overlap. Therefore, it was concluded that the C-terminal truncation did not significantly affect the transport efflux either. The pertinence of such efflux assay is discussed later (5.4.3.).

4.3. Effects of proton antenna on the MCT1 transport

4.3.1. Effects of the MCT1 chaperones (BSG and EMB)

4.3.1.1. Intracellular pH of BSG-MCT1 expressing yeasts

While A-L. Köpnick was studying the effect of the co-expression of MCT1 and its BSG chaperone as fusion constructs [114], [115], it became relevant to verify that the internal pH of the observed yeasts did not significantly change during the substrate transport measured using

the radiolabeled substrate assay. To that extent, yeast expressing the different BSG-MCT1 constructs were loaded with the pH-sensitive probe CFDA-SE, and the change in their internal pH was measured over time while transporting L-lactate (3.5.5).

The intracellular pH remained stable during 32 min (corresponding to the typical radiolabeled substrate uptake assay time) after the addition of 1 mM L-Lactate.

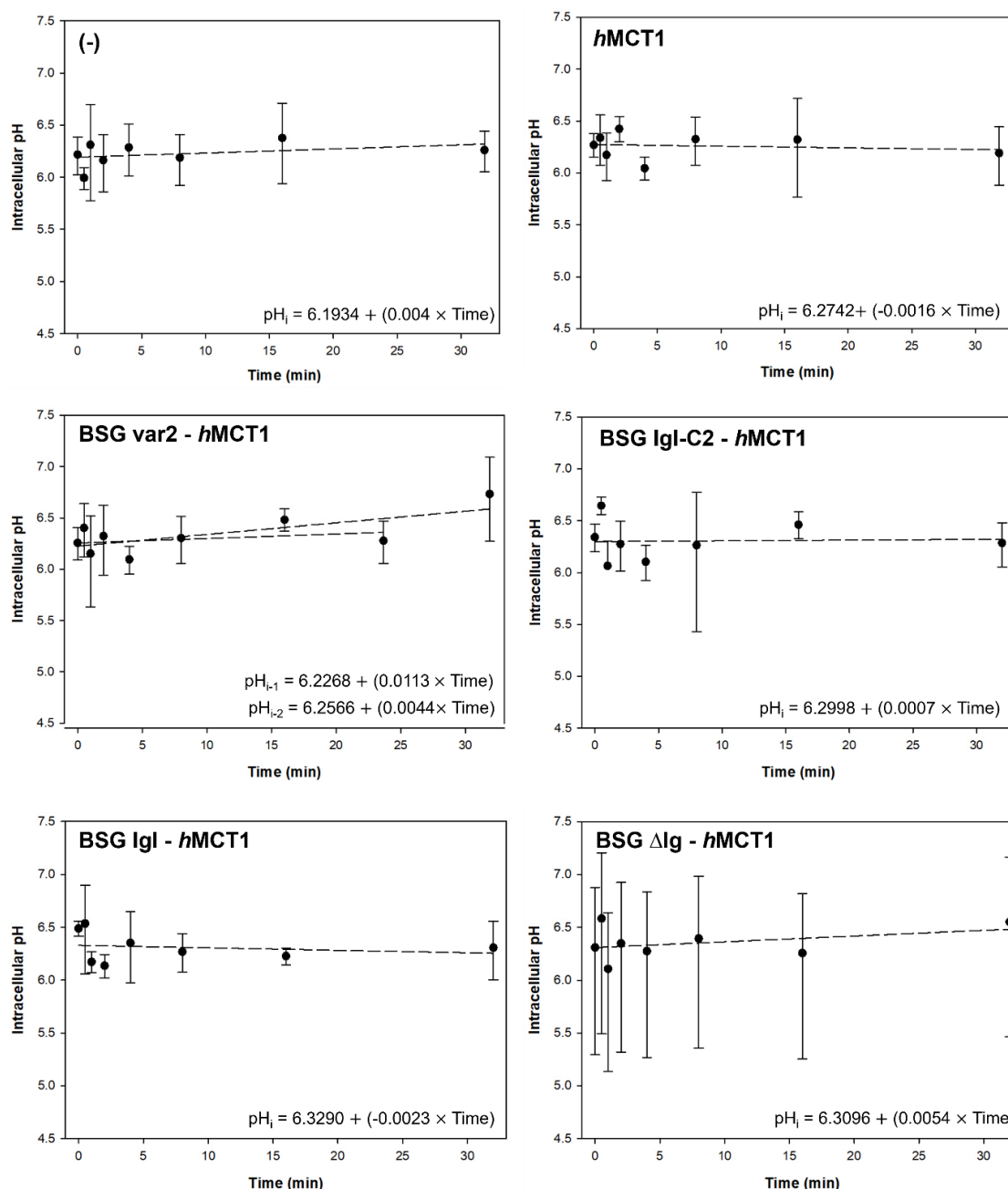


Figure 4. 37: Intracellular pH of BSG-MCT1 expressing yeasts over time. Detected by calculating the ratio of the CFDA fluorescence emitted at $\lambda_{em}=525$ nm when excited at $\lambda_{ex1} = 435$ nm (isosbestic point, pH-independent) and $\lambda_{ex2} = 495$ nm (pH-dependent). Measured in 50 mM HEPES/Tris pH=6.8, 1 mM L-lactate. Error bars represent SEM of experimental triplicates or duplicates.

4.3.1.2. pH-rate dependency of BSG-MCT1 transport

Previous measures of the pH dependency on the MCT1 transport were limited to the pH=4 to 8 range [71], [72], [203], [204]. Overall, the shape of the reported curves appeared like a single sigmoidal. However, such measures do not include more acidic pH where the substrate would be protonated as lactic acid (pK_a of 3.86, equation 3). Measure including a few of such acidic conditions suggested that the MCT1 rates pH dependency would take the shape of a bell curve [57].

To better understand the pH rate profile of MCT, K. Geistlinger measured high resolution curves of the pH rate dependencies of MCT1 expressing yeasts, using the radiolabeled substrate assay. Her findings showed that the rate of MCT1 transport was in fact behaving as a double sigmoidal curve until pH=4.5, then behaving as an exponential decrease at lower pH [180].

Additional measures were made to assess wherever the presence of the Basigin chaperone interacting with MCT1 (using the fusion constructs developed by A-L. Köpnick [115]) would behave differently than previously reported.

The MCT1 protein coding sequence had been modified by K. Geistlinger to carry the K38M mutation. The DNA encoding the BSG sequence was inserted in pDRTXaLK plasmid carrying the MCT1 sequence, WT or K38M (expressed with an N-terminal HA tag and a C-terminal His₁₀ tag, separated from the protein coding sequence by a Factor Xa. cleavage site). Such plasmids were used to transform Δ jen1 Δ ady2 yeasts (3.5.2) to measure the transport of radiolabeled substrate (3.6) in different external pH conditions, over two min. Part of the culture used for the assay was lysed to test the expression level of the different proteins.

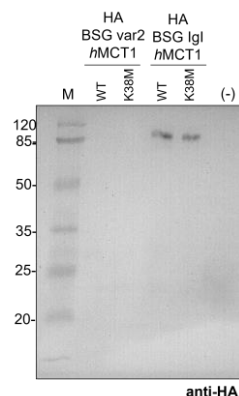


Figure 4. 38: Western Blot visualization of the BSG – MCT1 constructs expression levels. 15 μ g total protein were loaded in each well. Protein marker (M) was used to estimate the protein sizes (units are in kDa).

Only the construct expressing the shortened BSG IgI domain had a detectable level of protein expression and substrate transport over two min, which was in line with the previously observations [114], [115]. Their pH to transport rate dependency was measured using the radiolabeled substrate assay (3.6.4.).

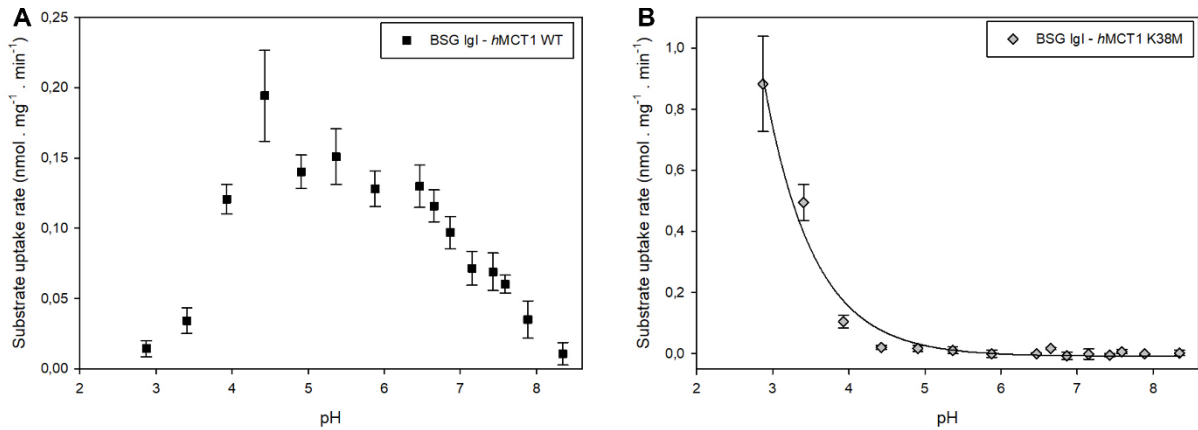


Figure 4. 39: Substrate uptake rates of BSG IgI – MCT1 WT (A) or K38M (B) expressing yeasts, measured at different extracellular pH. Measured over 2 min in 1 mM L-Lactate. Background subtracted. Error bars represent SEM of 4 (WT) or 3 (K38M) biological replicates.

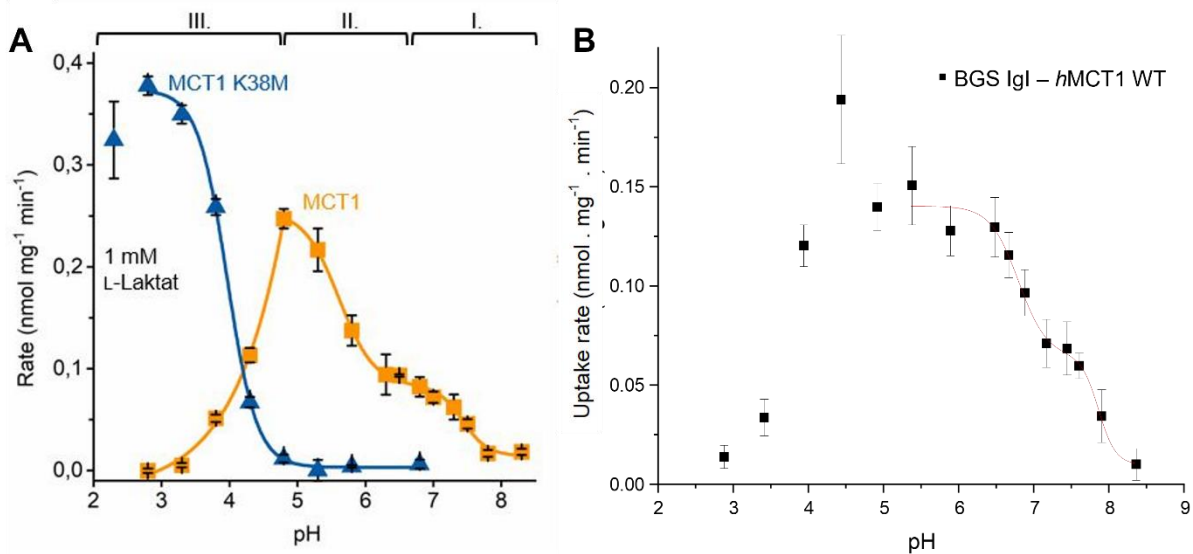


Figure 4. 40: (A) Curve fits of the pH-dependent transport rate of the WT (orange) and K38M MCT1. Adapted from K: Geistlinger doctoral thesis [180]. (B) pH-dependent transport rate of the BSG IgI – MCT1 (Black squares), fitted with a double sigmoidal curve between pH=5.3 and 8.3 using OriginLab.

The resulting pH-dependent transport rate of the BSG – MCT1 WT was fitted between pH=5.3 and 8.3 as a double sigmoidal as well (Origin Lab, Growth, Sigmoidal, double response). Overall, the presence of the BSG IgI domain appears to have shifted the shape of the curve slightly toward the more acidic pH (Figure 4.39 A and 4.40). The addition of the BSG chaperone

did not seem to affect the transport rate dependency of the MCT1 K38M mutant (Figure 3.39 B and 3.40 A).

It had been identified that the effect of the Basigin IgI domain on MCT1 transport stemmed from the two electrostatically charged patches found at its surface. Two mutant constructs had been prepared by A-L. Köpnick to investigate how these patches affected transport. The first had its positively charged patch neutralized by mutating the Lys 108, 111 and 127, as well as the Arg 201 and 203 to alanine (labeled K,R to A). The second had its negatively charged patch inverted by mutating Glu 114, 118, 120, 168 and 172 into Gln.

The mutated BSG coding sequences were inserted in pDRTXaLK carrying the MCT1 coding sequence. Such plasmids were used to transform Δ jen1 Δ ady2 yeasts (3.5.2) and their transport rate pH dependency was measured as previously described.

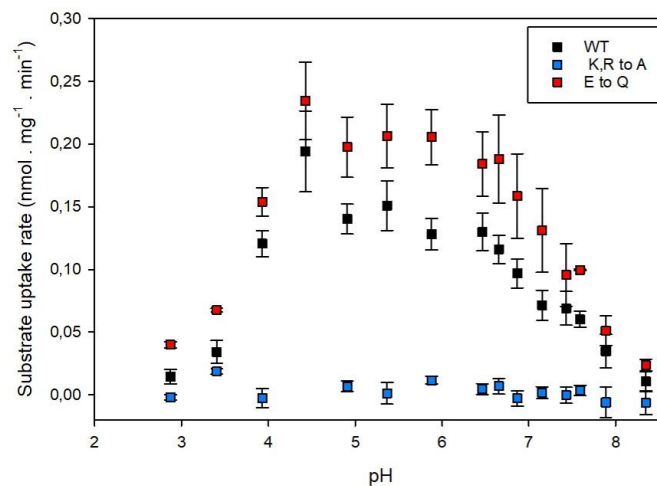


Figure 4. 41: Substrate uptake rates of BSG IgI – MCT1 WT (Black squares) compared to the constructs expressing mutated BSG IgI (K,R to A: blue; E to Q: red), measured at different extracellular pHs. Measured over 2 min in 1 mM L-Lactate. Background subtracted. Error bars represent SEM of 4 (WT) or 3 biological replicates.

The Basigin construct that had its positively charged patch neutralized (K,R to A, blue) was known to have a low level of protein expression and transport. Its transport over 2 min was not sufficient to record properly the transport rates pH dependency. The construct that had its negatively charged patch inverted (E to Q, red) had a similar pH-rate dependency curve than the WT (black). The higher rate value measured could be caused by slight differences in the expression level, and the high error makes it difficult to conclude if it also displayed a double sigmoidal fitting curve between pH=5 and 8.

Together, these results shows that the pH rate profile measured by K. Geistlinger was a property of the MCT1 transporter, independent of the presence of the Basigin chaperone. Further comparisons of the pH-rate dependencies of MCT1 and BSG-MCT1 are discussed later (5.3.1.2.).

4.3.1.3. Expression of EMB-MCT1 fusion constructs.

Embigin is as much a chaperone of MCTs as Basigin [133]. Like BSG, it is composed of a C - terminal transmembrane domain, followed by C-terminal Immunoglobulin-like domains (Ig V1 and V2). However, despite some structural similarities and sequence identities, the BSG IgI and EMB Ig V1 appeared different at the level of the residues responsible for the charged IgI patches.

```

hBSG MAAALFVLLGFAL-LGTHGASGAAGTVFTTVEDLGSKILLTCSLNDSA-TEVTGHRWLKG 58
hEMB MAN-NFSLESHNISLTHESSMPVE---KNITLERPSNVNLTQCFTTSGDLNAVNVTKKD 56

**  * * . . : * * . : . . . : * : : * * * . . . * . : . . . * * .

hBSG GVVLKEDALPG-----QKTEFKVDSDDQWGEYSCVFLPEPMGTANIQLHGPPRVKAVK 111
hEMB GEQLENNYLVSATGSTLYTQYRFTIINSKQMGSYSCFFREEKEQRGTFNFKVPE-LHGKN 115

*  * : : * . : . * . : . . * * * * * * * * . . : : : * : . . :

hBSG SSEHINEGETAMLVCKSESVPVTDWAWYKITDSEDKALMNGSESRRFFVSSS-QGRSELH 170
hEMB KPLISYVGDSTVLTCKQCNCFP-LNWTWYSSNGSVKVPVGVQ-MNKYVINGTYANETK 173

.      * : : : * * * . . . * : * * * . . * . : . . : : : : : : : : : : :

hBSG IENLNMEADPGQYRCNGTSSKGSQAIITLVRVSHLALWPFLGIVAEVLVLTIIIFIYE 230
hEMB ITQ-LLEEDGESYWCRALFQLGESEEHIELVLSYLVPLKPLVIVAEVILLVATILLCE 232

* : : * * . * * . . . * . . : * * * * * * * * * * * * * * * * * * * * * * * * * * * * *

hBSG KRRKPEDVLDLDDDDAGSAP---LKSSGQHQNDKGKNVR-Q-RNSS--- 269
hEMB KYTQKKKKHSDEGKEFEQIEQLKSDDS--NGIENNVRHRKKNESLGQ 277

* : : . * * . . . * * * . . . * . : * * : : * * *

```

Figure 4. 42: Protein alignment of the human Basigin isoform 2 and human Embigin, using Clustal Omega. The identities between amino acids are marked as “*”, and the similarities as “.” or “:” depending on their respective importance. The domains of BSG IgI or EMB Ig V1 were highlighted in grey. The charged amino acids responsible for the presence of the charged patches in the BSG IgI are represented in color (red: negative, blue: positive).

Wherever such Embigin domains would also be involved in the MCT substrate transport remained to be determined.

A-L. Köpnick had already attempted to measure the transport of MCT1 fused to the Embigin. These constructs were barely expressed or transporting [115]. Since it had also been measured that the MCT1 could be expressed fused to only the transmembrane domain of Basigin (Δ Ig) [114], fusion proteins were created to express the MCT1 fused to the EMB Ig domains through the Basigin transmembrane domain. The preparation of pDRTXa plasmids allowing the expression of such protein complexes is described in Supp. 1.5.

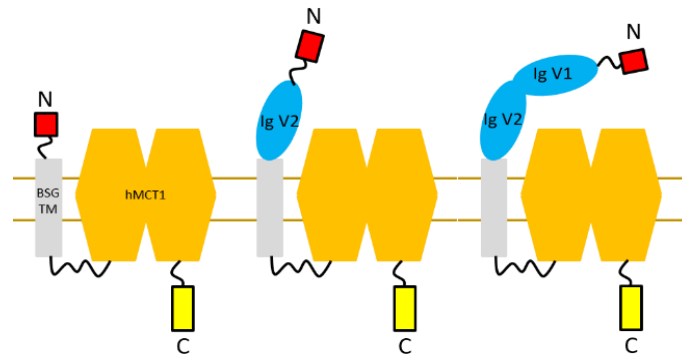


Figure 4. 43: Schematic representation of the target fusion constructs of the MCT1 transporter (orange), fused to the Embigin Ig domains (blue) through the Basigin transmembrane domain (grey). Terminal HA and His₁₀ tags are represented in red and yellow respectively.

The generated plasmids were used to transform Δ jen1 Δ ady2 yeasts (3.5.1.) to measure the transport of radiolabeled substrate over time (3.6.1.). Part of the culture used for the assay was lysed to test the expression level of the different proteins.

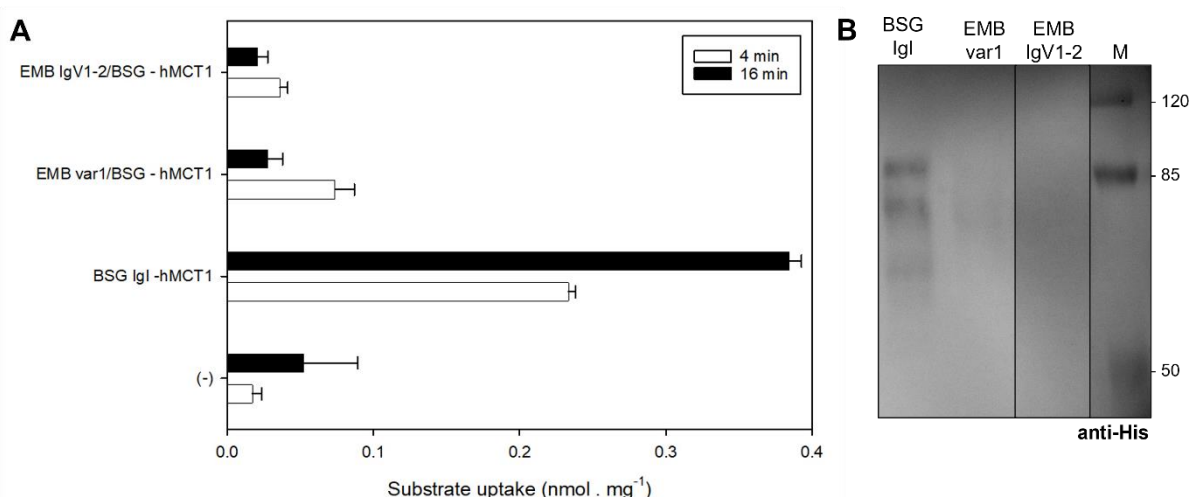


Figure 4. 44: (A) Substrate uptake of BSG IgI – MCT1 or EMBs/BSG – MCT1 expressing yeast, over 4 (white) or 16 (black) min. Measured in 50 mM HEPES/Tris pH=6.8, 1 mM L - Lactate. Error bars represent SEM of experimental duplicates. The protein expressions were estimated based on a Western Blot (B) containing 7.5 μ g total protein concentrations in each well. Protein marker (M) was used to estimate the protein sizes (units are in kDa).

Although at first the EMB expressing yeast uptakes appeared greater than the control (-) after 4 min of transport (white), it appeared that these constructs did not transport lactate, as the uptake after 16 min (black) appear insufficient compared to the control (-). Moreover, these constructs were barely expressed (only faint traces of the EMB var1/BSG – MCT1 constructs could be detected) in a relatively poor Western Blot.

These fusion proteins did not appear to be the solution for expressing the Embigin domains fused to the MCT1, so it was not investigated further. Perhaps fusion constructs including the Embigin chaperone should also include the MCT2, as EMB are their preferred chaperone: However, such a transporter had not yet been expressed in yeasts.

4.3.2 Investigating the role of carbonic anhydrase IV in MCT1 transport

To investigate how the carbonic anhydrase has an effect on the MCT1 transport, it needed to be co-expressed with the Basigin-MCT1 complex. Additional tests should ensure that the Carbonic anhydrase is capable to interact with the Basigin domain, as described in the literature [131] for this study to be relevant.

The human carbonic anhydrase IV amino acid sequence contains a signal peptide (the first 18 amino acids) and putative transmembrane protein propeptide (the last 27) that are not present in the mature form of the protein [205], [206] (Supp.1). In nature, the CAIV is bound to the extracellular side of the membrane by a Glycosylphosphatidylinositol (GPI) anchor, utilizing its Serine 284 [206]. Although the yeasts are capable of adding GPI anchors to proteins [207], it was initially decided not to rely on the yeast post-translational modifications system to correctly produce the CAIV since no good controls could be designed to ensure it was done properly.

In order to express a protein that would mimic as closely as possible the CAIV physiological state in our experimental set-up, it was decided to exclude the first 18 and the last 27 amino acids from the coding sequence. The resulting peptide sequence should be similar to the processed protein and is referred to as CAIV(p). Its proper addressing to the membrane would be assured by its expression in a fusion protein or by relying on the Basigin - CAIV interaction described in the literature [131].

4.3.2.1. Expression of carbonic anhydrase as a fusion protein

Fusion proteins of the Basigin - MCT1 complex had already been prepared by A-L. Köpnick [114], [115]. The genes encoding for these proteins were inserted in a pDRTXa plasmid and used to transform yeast. The transport functionality of these construct had been measured using the Radiolabeled substrate assay. The first step in this process of checking how the Carbonic anhydrase increased lactate transport in MCT1 was to generate a fusion construct expressing the MCT1 transporter fused to the Basigin chaperone, itself fused to the Carbonic anhydrase.

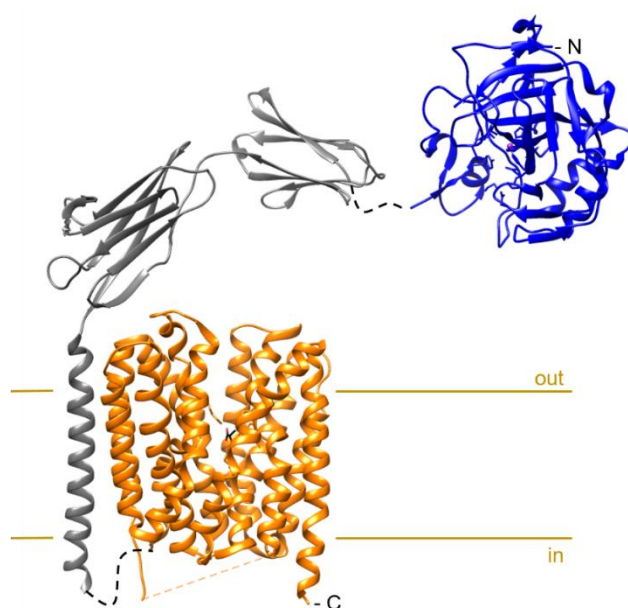


Figure 4. 45 Representation of the CAIV (PDB# 3F7B [208]) in blue, linked to the Basigin chaperone (PDB# 6LZ0 [104]) in grey and the MCT1 in orange (PDB# 6LZ0 [104]). Ligands are represented in black and red (lactate in MCT1) and purple (zinc cation chelated in CAIV). Model assembled using Chimera 1.14. The dotted black lines represent the positions of the eventual fusion linkers.

Preparing the pDRTXa plasmids encoding CAIV(p) – BSGs – MCT1

The protein construct simulating the complex of CAIV(p) – BSG – MCT1 needed to be expressed in yeasts to be investigated using the radiolabeled L-Lactate assay.

Considering that the protein complex would be composed of very different proteins artificially linked together, there was a possibility that it would not fold properly once expressed. It was hypothesized that the initial expression of a globular protein (N-terminal CAIV) could prevent the Basigin Ig domains from folding properly [209], [210]. In an attempt to address this

potential issue, in parallel to simply linking the CAIV to the Basigin-MCT1 constructs, the CAIV coding sequence was inserted in the construct, separated from the rest of the protein by a short, soluble and flexible linker. A twice-repeated sequence of Glycin-Serine-Glycine-Glycine (GSGG₂) was used for that purpose [211].

The CAIV(p) coding sequence was amplified by PCR (3.1.2.) using the CAIVp-XbaI_PCR4_s and the CAIVp-SpeI-BamHI_PCR3_as primer pair (Table 2.4.) and extracted after electrophoresis on an agarose gel (3.1.4.). The PCR product was digested using XbaI and BamHI, then ligated (3.1.7.) upstream of the MCT1 gene in pDRTXa_LK_MCT1 plasmids, linearized with the same enzymes. The different Basigin constructs (BGS var2, IgI-C2, IgI, ΔIg...) developed by A-L. Köpnick [115] was inserted between the CAIV and MCT1 coding frames, using the SpeI and BamHI restriction enzymes to ligate the digested and extracted Basigin coding sequences. The primers CAIVinsert1s, 2s, 3s, PMA 5' and ADH 3' (Table 2.1) were used in Sanger Sequencing to verify that the PCR did not introduce unrequired mutations.

Expression Tests in Yeast

After growing the transformed cells on SD-AWLH agar plate, the membranes proteins of the most relevant constructs were extracted as described earlier (3.5.4.). To visualize the expression of these clones, the protein extracts were used to prepare an SDS-PAGE followed by a Western Blot (3.2.4.2.), using 40 ng/mL of primary mouse anti Penta-His antibodies and 40 ng/mL secondary goat anti-mouse HRP-conjugated antibodies.

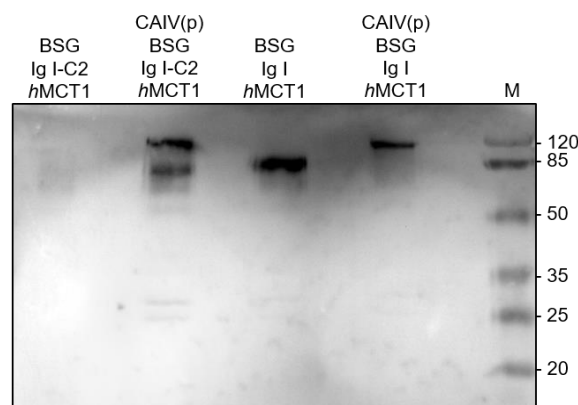


Figure 4. 46: Western Blot (anti Penta-His) of the different (CAIV)-BSG-MCT1 constructs expression levels. 10 µg of total protein were loaded in each lane. Protein marker (M) was used to estimate the protein sizes (units are in kDa).

A faint signal could be detected in the BSG IgI-C2 MCT1 lane. This observation matches those of A-L. Köpnick that this specific BSG-MCT1 construct had a lower expression rate than the others [115]. The expected protein molecular weights of the BSG - IgI-C2 - MCT1 construct, without and with fused CAIV(p) are approximately 85.7 and 116 kDa respectively. For the BSG – IgI - MCT1 constructs, they are 76.6 and 106.9 kDa (using the ExPASy Translate tool and ProtParam). Accounting for the fact that proteins migrate down an SDS-PAGE gel differently depending on their sizes and their charges, the observed protein bands approximately match the expected molecular weights.

Two protein bands could be observed in the CAIV(p) - IgI-C2 - MCT1 (corresponding to about 116 and 85.7 kDa), which is most likely explained by different starts of protein expression as two start codons were probably recognised (the first upfront of the CAIV(p) coding sequence, the second upfront of the Basigin coding sequence). However, all constructs appeared to show at least some level of protein expression, which should make them suitable for radiolabeled substrate transport assay.

Lactate Transport

Individual clones were picked and cultivated for radiolabeled substrate transport assay (3.6.1.). To verify that the fusion constructs could be used to mimic the assembly of the CAIV, Basigin and MCT1 complex, some functionality of the CAIV(p) - BSG IgI-C2 – MCT1 was measured first, as it is the protein construct most representative of the physiological state.

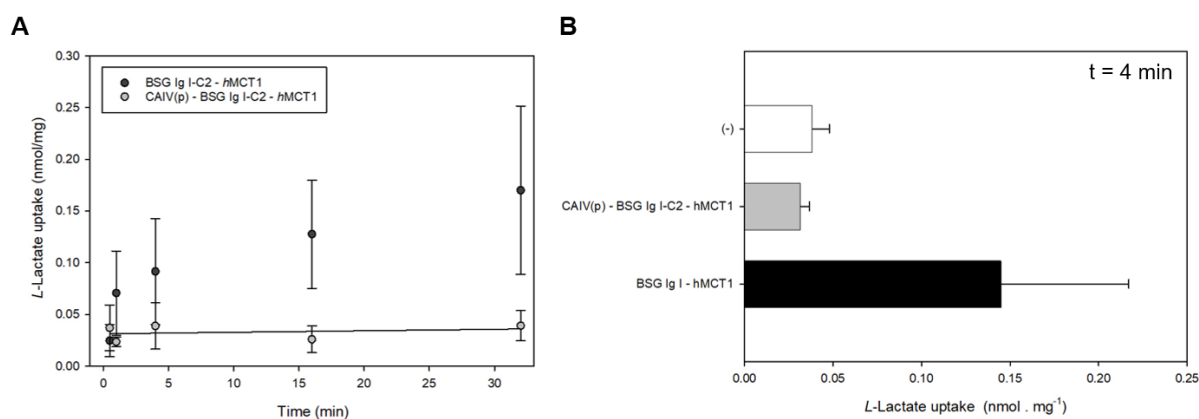


Figure 4.47: (A) Time dependent transport of 1 mM L-Lactate by yeasts expressing the BSG - IgI-C2 -MCT1 or CAIV(p) - BSG IgI-C2 -MCT1 constructs. Background subtracted. Error bars represent SEM (3 technical replicates). (B) Transport of 1 mM L-Lactate over 4 min by yeasts expressing the BSG - IgI -MCT1 constructs; the CAIV(p) - BSG IgI-C2 -MCT1 constructs or no transport protein at all (-). Measured in 50 mM Tris/HEPES pH=6.8. Error bars represent SEM (technical duplicates; 2, 5 and 2 biological replicates respectively).

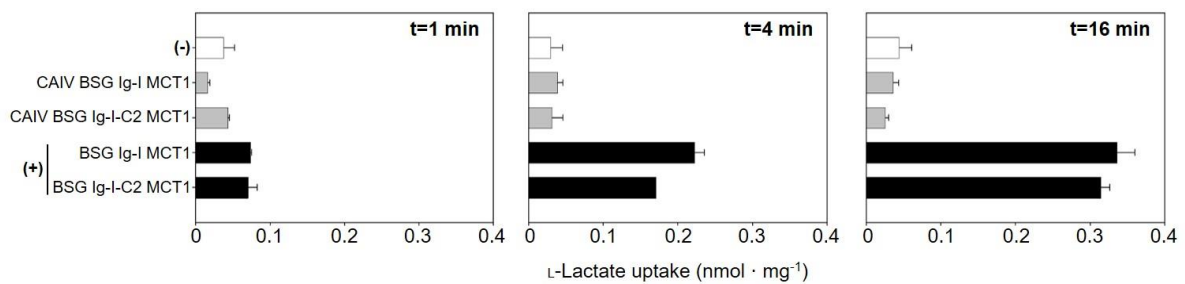


Figure 4. 48: Transport of 1 mM L-Lactate over 1, 4 and 16 min by yeasts expressing the fusion protein constructs or no transport protein at all (-). Measured in 50 mM Tris/HEPES pH=6.8. Error bars represent SEM (technical duplicates).

Figure 4.47 A shows, despite the large error bars, that the BSG - IgI-C2 – MCT1 (black dots) is active and transports more lactate over time. In contrast, the CAIV(p) - BSG IgI-C2 -MCT1 construct (grey dots) shows no increase of transport. Its transport could be fitted to a linear polynomial equation of $(0.0001 \pm 0.00003 \times x) + (0.0313 \pm 0.005)$, which is close to a straight flat line. In Figure 4.47 B, a negative control (-) and yeasts expressing the Basigin IgI -MCT1 construct (supposedly the most expressed and active construct) are showing the expected experimental range of detection. The level of L-Lactate transported by the CAIV(p) - BSG IgI-C2 - MCT1 construct (grey) do not appear different to the negative control (white), meaning that no transport occurred. Figure 4.48 confirms that this observation is also true for the CAIV(p) - BSG IgI - MCT1 construct. There, while the uptake measured in the control (white) and the yeasts expressing the BSG – IgI – MCT1 or BSG – IgI - C2 – MCT1 (black) shows a significant difference (Student’s t-test, two-tailed p-value<0.05), the difference observed when these constructs are expressed fused with CA(p) are statistically insignificant (Student’s t-test, two-tailed p-value=0.697 and 0.388 respectively).

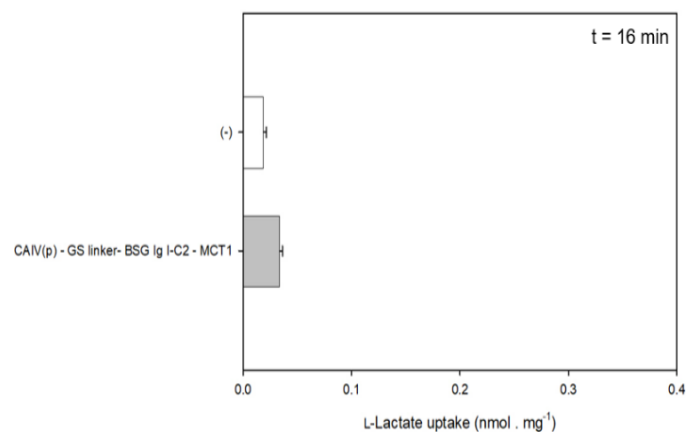


Figure 4. 49: Transport of 1 mM L-Lactate over 16 min by yeasts expressing the fusion protein construct or no transport protein at all (-). Measured in 50 mM Tris/HEPES pH=6.8. This fusion

construct had its CAIV(p) coding sequence separated from the rest of the protein by a (GSGG)₂ linker (“GS linker”). Error bars represent SEM (biological duplicates, with technical duplicates).

The transport uptake was also measured in the construct separating the CA from the BSG domains by a GS linker. Although the lactate transport observed in the yeast expressing the GS linker construct appeared to be slightly greater than the negative control (Student’s t-test, two-tailed p-value<0.05) (Figure 4.49), it is not at the same level than that of the yeast expressing functional fusion constructs (BSG IgI - MCT1 and BSG IgI-C2 - MCT1, Figures 4.48 and 4.49). The level of expression was not verified by protein extraction followed by a western blot, but such results are sufficient to conclude that this construct is not functional (or not properly expressed).

Considering these experiments, it appeared that the CAIV - BSG - MCT1 fusion complexes cannot transport lactate, probably because they cannot fold properly or cannot be transported to the yeast membrane. Therefore, these artificial constructs cannot be used to study the way in which the interaction of Basigin with CAIV would affect substrate transport.

The addition of the CAIV(p) domain to the EMB/BSG – MCT1 construct did not prove successful either. The resulting proteins were expressed, but were detected on Western Blots as having a smaller molecular weight than expected. Moreover, the yeasts expressing such constructs did not show any transport either.

4.3.2.2. *Yeast expressed Basigin - MCT1 and soluble CAIV.*

As the previous experiments demonstrated that no fusion proteins could adequately replicate the assembly of the CAIV, Basigin and MCT1 complex, another strategy had to be used. A - L. Köpnick had already prepared a fusion protein that mimicked the assembly of the Basigin - MCT1 complex that transports lactate in our experimental set-up. The next step would be to provide soluble carbonic anhydrase that would interact with the Basigin - MCT1 fusion protein.

Preparing plasmids for the expression of soluble CAIV

Two different expression systems were tested in parallel to produce and purify soluble CAIV.

A convenient production system for soluble proteins is the BL21(DE3) *E. coli*, capable to produce T7 polymerase when induced with IPTG. It requires inserting the protein coding sequence in a plasmid controlled by a T7 promoter, and repressed by the lacO operon. The plasmid pET21X fitted these criteria.

Soluble CAIV could also be expressed in a cell-free expression system. To do so, the CAIV coding sequence needed to be inserted in a pIVEX vector.

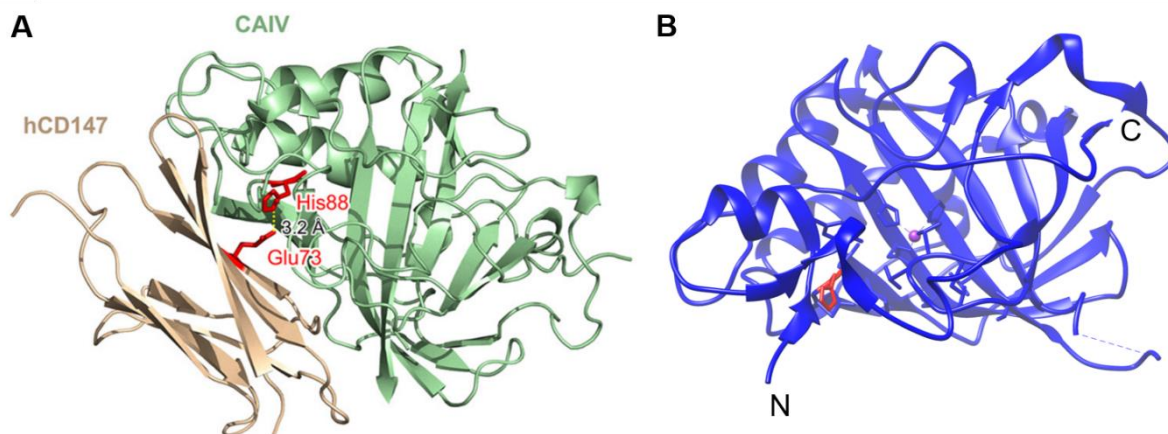


Figure 4. 50: (A) Model of the CAIV docking on the Basigin Ig C2 domain, adapted from Forero-Quintero *et al.* [131]. Based on the PDB structures of the human CD147 (Basigin) expressed in *E. coli* (PDB# 3B5H, [212]) in beige and the PDB structure of human CAIV expressed in *Cricetulus griseus* (PDB# 5JN9, [213]) in green using Coot. The amino acids hypothesized to be involved in the docking are represented in red. (B) Model of the human CAIV expressed in *E. coli* (PDB# 3F7B, [208]) using Chimera 1.14. The Histidine hypothesized to be involved in the docking is represented in red, and the protein N and C-termini are labeled as such.

As the C-terminus end of the protein appears to be tucked under a protein loop (Figure 4.50), tagging the termini of the protein necessitate some caution. To ensure that the addition of the C-terminal His₁₀ tag does not disrupt the fold of the CAIV extremity, it was decided to add a short, soluble and flexible spacer between them, composed of three Glycines (GGG). The N-terminal extremity of the CAIV is freer, but it appears extremely close to the hypothesised docking site of the Basigin - CAIV complex (His88). In order to ensure that no artificial tag would get in the way of the binding, it was decided to express the CAIV(p) without N-terminal HA tag. For identification purposes, the C-terminal His₁₀ tag would suffice. A start codon had to be inserted upfront of the CAIV(p) coding sequence to allow for the synthesis of proteins. These modifications were carried by the primer pairs of the PCR amplifying the (m)CAIV(p) coding sequence: PCR_mCAIVp_s and PCR_CAIVp-3G-XhoI_as (2.3.4. and Table 2.4).

The (m)CAIV(p) was inserted in a pIVEX 2.3w oHA (2.2.3.3.) for cell-free expression. In parallel, the same coding sequence was inserted in pET21X plasmid for IPTG inducible *E. coli* production.

Cell-free Expression of CAIV and IMAC Purification

The CAIV was expressed in a cell-free system as described previously (3.7.). Since this protein is soluble, detergents were omitted from the reaction and feeding mixes. The produced proteins were purified using IMAC as described previously (3.3.1.) in a buffer containing 150 mM NaCl, 50 mM Tris - HCl pH=8 and increasing concentrations of imidazole. After elution, the content of each fraction was used in an SDS-PAGE and the protein content were visualized using Coomassie staining and Western Blot (using 40 ng/ml of mouse anti Penta-His primary antibodies, and 40 ng/mL of goat anti-mouse HRP-conjugated secondary antibodies).

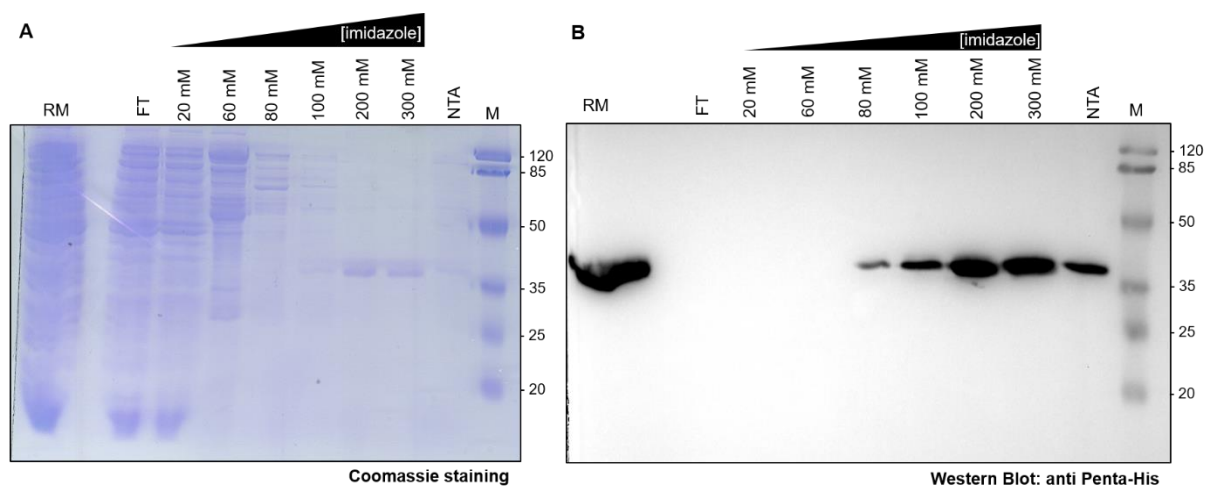


Figure 4. 51: SDS-PAGE of the soluble CAIV cell-free expression and IMAC purification visualized using Coomassie staining (A) or Western Blot anti Penta-His (B). The fractions of cell-free reaction mix (RM), IMAC Flow through (FT), elution steps with different imidazole concentrations and resuspended resin (NTA) were diluted in 4× SDS buffer before incubating at 37°C for 1 h. Protein marker (M) was used to estimate the protein sizes (units are in kDa).

Despite a low staining on the SDS-PAGE gel, the CAIV appeared to be reasonably expressed in the reaction mix of the cell-free expression system and later properly purified. It appeared to elute starting from 80 mM of imidazole, but the 200 mM and 300 mM fraction appeared to contain the greater concentration of eluted protein. Moreover, these lanes appeared clear of other contaminant proteins, suggesting that by pooling the 200 and 300 mM fraction, one could recover the best and most pure CAIV concentration.

To be mixed with Basigin expressing yeasts and to measure the resulting effect on CAIV addition on MCT1 transport using the radiolabeled, the protein buffer needed to be changed to 50 mM HEPES (pH=6.8). The pooled fraction of the IMAC containing the protein of interests were dialysed in 50 mM HEPES pH=6.8, which also served to dilute the concentration of

imidazole to a negligible amount ($>5 \times 10^{-4}$ mM). At this stage, a heavy precipitation was observed, likely caused by the removal of the NaCl that had helped the protein to stay solubilised. Finally, the protein was dialysed and concentrated using a 30 000 MWCO Amicon. More precipitation occurred at this step.

It appeared that the soluble CAIV protein concentrations could not be accurately measured using the usual Bradford assay method, even though other labs reported measuring their CAIV concentrations in this way [214]. At this stage, the BCA assay had not been considered, but would have been a suitable alternative. Instead, samples of the concentrated soluble CAIV were used for SDS-PAGE, visualised with Coomassie staining. The size of the protein band was approximately compared to that of BSA bands of known concentrations loaded on the same gel. It was entirely possible that the Coomassie of the gel staining solution would not reveal the CAIV with the same intensity as the BSA, but it would allow for a rough estimation of the CAIV protein concentration.

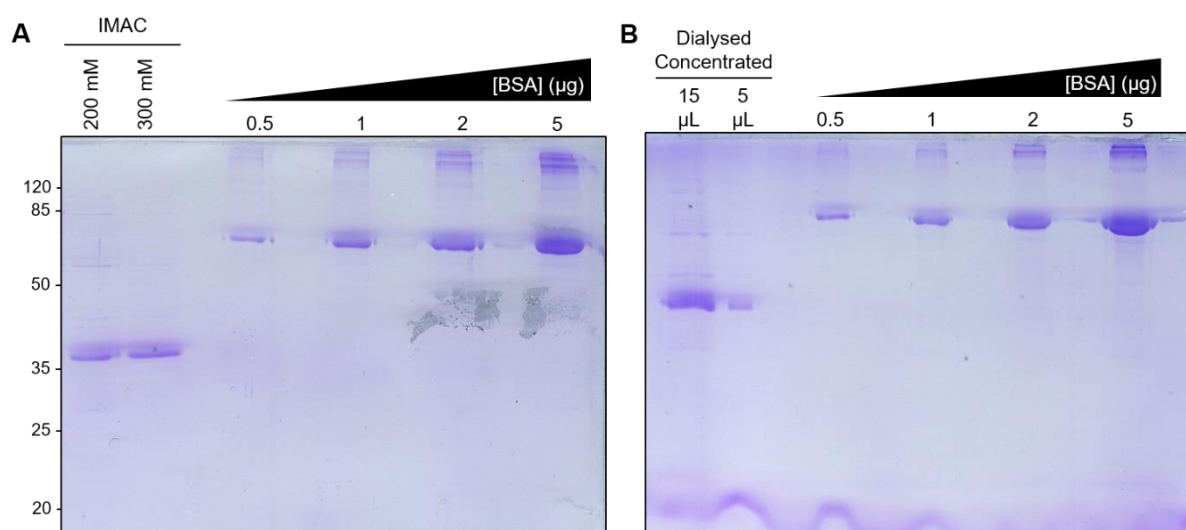


Figure 4.52: Coomassie stained SDS-PAGE gel (12.5%) used to roughly estimate the CAIV protein concentration in the IMAC fractions (A) and after dialysis and concentration by comparison (B) with known amounts of BSA.

By comparing the sizes of the protein bands, it was estimated that the 200 mM and 300 mM IMAC fraction contained each about 0.75 μg of CAIV each. This permitted to calculate that the total concentration of CAIV in the pooled IMAC fraction was about 594 μg/mL, for a total of 855 μg of pure proteins. After dialysis and concentration, it was estimated that the total protein concentration recovered was of 137 to 174 μg/mL, for a total protein yield of 50 to 122 μg.

This is significantly lower, as almost 90 % of the purified protein was lost during the dialysis and concentration process. Nevertheless, it was used for the radiolabeled substrate transport assay.

Estimating the Soluble Protein Concentration for Substrate Transport Assay

The aim of the next experiment was to force the yeast expressed Basigin-MCT1 fusion proteins to interact with the soluble cell-free expressed and purified CAIV and measure how this addition would affect the transport of the substrate. To create experimental conditions in which this binding can occur, it was first necessary to assess how many Basigin-MCT1 fusion proteins are expressed in the samples of radiolabeled substrate transport assay. It would give a general idea of how much soluble protein to add to allow the formation of a significant amount of Basigin-MCT1 fusion proteins and soluble CAIV complexes.

Two 50 mL yeasts cultures expressing the BSG IgI-C2 - MCT1 and BSG Δ Ig - MCT1 fusion constructs were cultivated up to an OD_{600 nm} of 1. The strains were chosen because they represent the biggest and smallest relevant BSG - MCT1 constructs. After extracting their membranes (3.5.4.), their total membrane protein concentrations were determined using Bradford assay. These concentrations were 2.805 mg/mL and 3.355 mg/mL respectively, which was approximated to 3 (\pm 0.4) mg/mL. Based on this, approximation, each 80 μ L of yeast suspension at an OD_{600 nm} of 50 used in the radiolabeled substrate assay would contain about 240 μ g of total membrane proteins.

It was then necessary to estimate which proportion of these membrane proteins was the BSG - MCT1 fusion proteins. To do so, an SDS-PAGE followed by Western Blot (using 40 ng/ml of mouse anti Penta-His primary antibodies, and 40 ng/mL of goat anti-mouse HRP-conjugated secondary antibodies) were conducted. 10 μ g of total membrane proteins were loaded on the lanes, alongside different concentrations of cell-free expressed and IMAC-purified His-tagged PffNT.

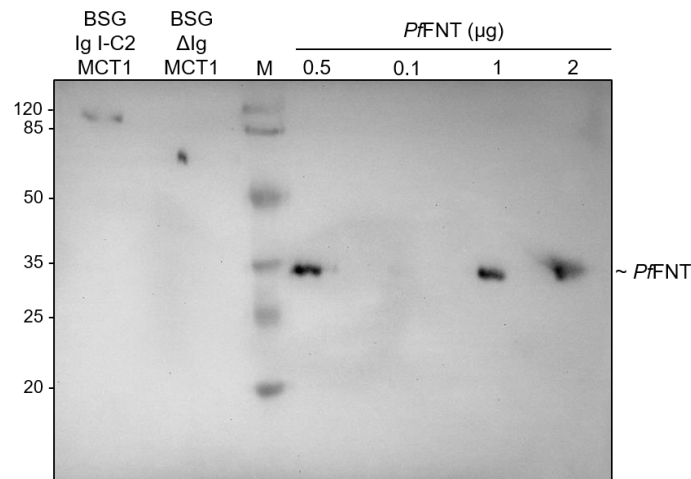


Figure 4. 53: Western Blot (anti Penta-His) of 10 μg total membrane proteins extracted from BSG IgI-C2 - MCT1 and BSG ΔIg - MCT1 expressing yeasts, compared to different concentrations of pure PfFNT. Protein marker (M) was used to estimate the protein sizes (units are in kDa).

The image analysis software ImageJ was first used to estimate the protein concentrations. However, as the Western Blot signal detection had saturated pixels, no reliable information could have come as a result. Finally, it was visually estimated that the signal intensities detected in the BSG IgI-C2 - MCT1 and BSG ΔIg - MCT1 lanes were between those detected in the 0.5 μg and the 0.1 μg PfFNT lanes (a faint signal was detected in the latter). Based on this information, it was estimated that each 80 μL of yeast suspension at an $\text{OD}_{600\text{ nm}}$ of 50 used in the radiolabeled substrate transport assay contained in total between 2.5 and 12 μg of BSG - MCT1 fusion protein.

Transport Assay of Yeast Expressed BSG - MCT1 and Soluble CAIV

Based on the previous calculations, 30 μL of the dialysed and concentrated CAIV would contain 4 to 10 μg of soluble CAIV. This would be sufficient to obtain approximately a 1:1 CAIV to BSG - MCT1 ratio.

The effect of the addition of soluble CAIV on the substrate transport of BSG - MCT1 expressing yeasts was determined using the radiolabeled substrate transport assay (3.6.) with some notable deviations from the standard protocol.

First, the yeast suspensions (in 50 mM HEPES pH=6.8) were concentrated to an $\text{OD}_{600\text{ nm}}$ of 80 (± 5), to maintain the same amount of yeast in each samples (5.6 mg of yeast fresh pellet).

50 μL of these yeast suspensions were mixed with 30 μL of buffers containing soluble CAIV or various controls, in such a way that the final dilution was similar to the 80 μL at an $\text{OD}_{600 \text{ nm}}$ of 50 (± 5) used in the other experiences. These samples were briefly vortexed and incubated 10 min at room temperature before proceeding as usual with the addition of 5 mM sodium L-lactate solution in 50 mM HEPES pH=6.8 and spiked with radiolabeled L-Lactate.

These 30 μL contained 4 to 10, 2 to 5 or 1 to 2.5 μg of soluble CAIV, dialysed in 50 mM HEPES pH=6.8. These protein concentrations respectively corresponded to a 1:1, 1:2 or 1:4 CAIV to BSG - MCT1 ratio (according to the previously described approximations). After normalization, it corresponded to 0.71 to 1.79, 0.36 to 0.89 or 0.18 to 0.45 μg of protein per mg of yeast. A control was prepared by mixing the 50 μL of yeast suspension with 30 μL of the dialysis buffer (50 mM HEPES pH=6.8) which should have the same composition as the CAIV solutions.

These measures were done using yeasts expressing the BSG IgI-C2 - MCT1, BSG IgI - MCT1 (missing the C2 domain, this construct would not interact with soluble CAIV) and transformed with an empty vector to measure the experimental background. Said background was subtracted from the measured signals.

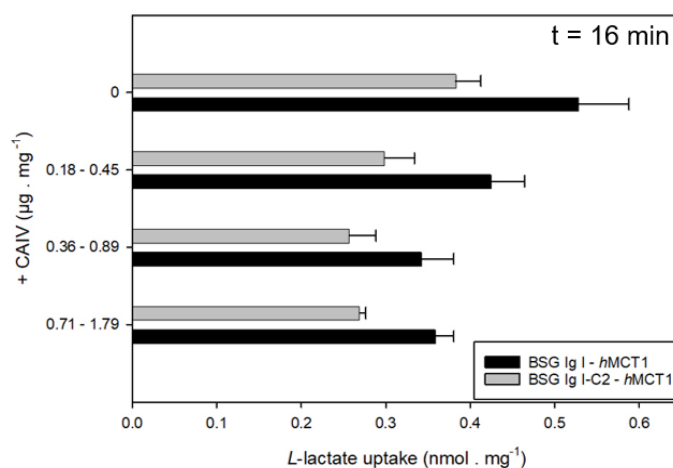


Figure 4. 54: L-Lactate uptake by BSG IgI-C2 - MCT1 (grey) and BSG IgI - MCT1 (black) expressing yeasts over 16 min after the addition of different soluble CAIV concentrations. Measured in 50 mM Tris/HEPES pH=6.8, 1 mM of external L-Lactate. Background subtracted. Errors are SEM (experimental duplicates).

It was expected that the addition of soluble CAIV would increase the transport functionality of the BSG IgI-C2 - MCT1 expressing yeasts but would not affect that of the BSG IgI - MCT1 expressing yeasts (that could not form a complex with CAIV). None of the results displayed in Figure 4.54 fitted expectations.

First, the BSG IgI - MCT1 expressing yeasts transported significantly more substrate than those expressing BSG IgI-C2 - MCT1. That effect can, however, be explained by the differences in expression levels. A-L Köpnick had observed that the BSG IgI - MCT1 was significantly more expressed than bigger constructs [114], [115], which is also noticed on Figure 4.38. Moreover, after 16 min of transports, these protein fusions barely had reached the transport equilibrium [114] which means that the differences in expression levels would be relevant.

More importantly, it appears that the addition of soluble CAIV decreased the overall amount of substrate transported by either of the tested protein constructs. If anything, it looked like the addition of CAIV had an antagonist effect on substrate transport. One possible explanation could be that the CAIV did not interact with the Ig C2 domain. Under these conditions, the surface negative charge of the CAIV could have accumulated proton-rich microenvironments in the buffer bulk. Thus, the soluble CAIV would impede the MCT1 transport by diverting protons away from the transport site. It is, however, worth noting that these results are of little to no statistical significance. A Student's t-test comparing the uptake of the BSG IgI (Figure 4.54, black) or BSG IgI-C2 (Figure 4.54, grey) expressing yeasts with the absence or the addition of 0.71-1.79 $\mu\text{g} \cdot \text{mg}^{-1}$ of carbonic anhydrase yielded two-tailed p-values of 0.116 and 0.0652 respectively.

In any cases, investigating these potential effects further would have required producing and purifying greater concentrations of CAIV. As the *E. coli* expression of protein had not produced satisfying yields yet and that the cell-free expression was relatively costly, it was important to first validate that the purified CAIV were properly folded and were interacting with the Ig C2 domain. Such conclusions could not be drawn from the previous experiments.

E. coli Production of Soluble CAIV

To attempt repeats of the previous experiment (Figure 4.5.4) and adjusting the experimental parameters, large yield of soluble CAIV should be produced for testing. The most convenient host for the large-scale expression of soluble recombinant proteins in our lab are BL21(DE3) *E. coli*, as it is relatively less resource intensive than the cell-free expression system and is highly scalable.

To verify that the transformed and BL21(DE3) *E. coli* expressed the (m)CAIV(p) protein, small-scale expression tests were conducted. The expression, lysis and purification of soluble

(m)CAIV(p) were done by adapting the protocol of Idrees *et al.* 2016 [172], who purified the His-tagged isoform CAVA and described their methods in great detail.

EMBOSS Needle pairwise sequence alignment (BLOSUM62) showed that the CAIV and CAVA amino acid sequences shared 27.1 % of identity and 39.7 % of similarities. It was assumed that the production protocol described for CAVA would also apply to CAIV.

50 mL of LB media in 250 mL Erlenmeyer flasks were inoculated at an initial OD_{600nm} of 0.2, using bacteria precultures. These cultures were incubated at 37°C 220 rpm for about 2 h, until they reached an OD_{600nm} of approximately 0.5. There, the protein expression was induced by the addition of 0.1 mM IPTG and incubated at 37°C 220 rpm for 4 h. Finally, the bacteria cultures were pelleted (5 min, 4000 g, 8°C), the pellets washed in 25 mM Tris pH=8, with protease inhibitor (5 mM EDTA or 1× Complete), pelleted once more and stored at -80°C until the lysis.

For all the small-scale expression tests, the cell pellets (typically 0.5 g of fresh weights) were unfrozen on ice in about 1.5 mL of binding buffer solution (50 mM Tris pH 8, 500 mM NaCl, 5 % glycerol, 5 mM β-mercaptoethanol, 1× Protease inhibitor, 10 mM imidazole). The cells were lysed by sonication (12 cycles of 30 s 50% amplitude, 30 s on ice) and centrifuged (10 min, 4°C, max speed) to separate between the cellular wastes from the lysate.

The purification of the soluble (m)CAIV(p) proteins was based on the IMAC principle (3.3.1.). Ni-NTA resins were equilibrated in binding solution, then the lysate and the equilibrated resin were incubated together overnight (inversion, 4°C). After loading the mixture on a chromatography column and collecting the flow through, the proteins were washed with washing buffers (50 mM Tris pH=8, 500 mM NaCl, 5 % glycerol, 5 mM β-mercaptoethanol, 1× Protease inhibitor, 20 mM imidazole) then eluted with elution buffers containing increasing concentrations of imidazole (from 120 to 300 mM).

The protein content of each fraction was visualised by diluting then 3:4 in 4× SDS-PAGE buffer, incubating 5 min at 95°C. These samples were used to prepare an SDS-PAGE, visualised with Coomassie staining and Western Blot (anti Penta-His).

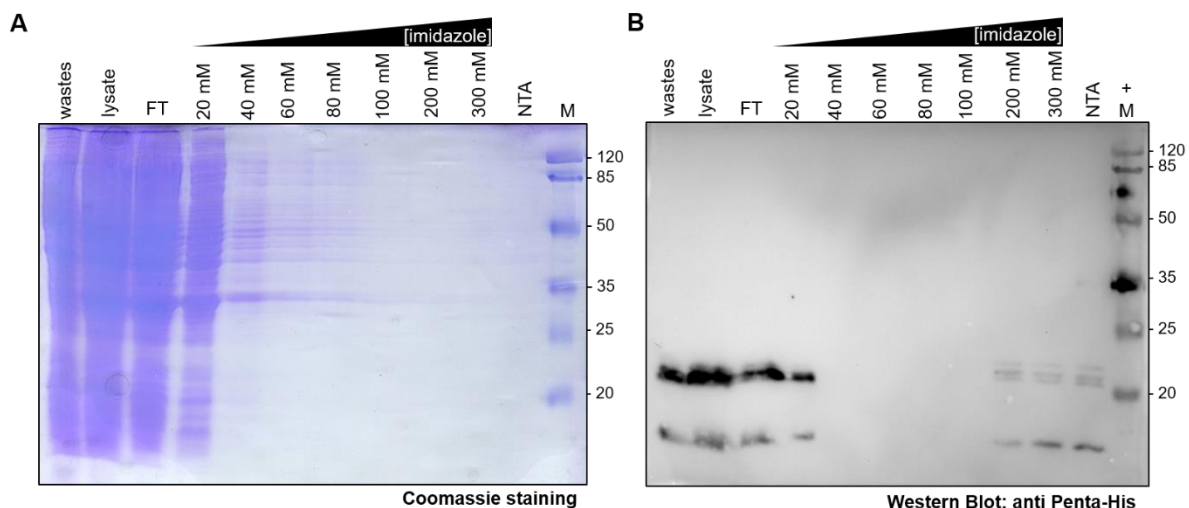


Figure 4. 55: (m)CAIV(p) expression test of pET21X transformed BL21(DE3) *E. coli*. SDS - PAGE of the cell lysis and IMAC purification visualized using Coomassie staining (A) or Western Blot anti Penta-His (B). The “wastes” and “lysate” fractions were the separated by centrifugation of the lysis crude extract. “FT” represents the flow through of the lysate through the Ni-NTA resin and “NTA” the resuspended resin. In the case of the Western Blot, a positive control (cell-free expressed PpFNT) was loaded on the same lane as the marker. Protein marker (M) was used to estimate the protein sizes (units are in kDa) and cell-free produced PpFNT was used as a Western Blot positive control (+).

This expression test was repeated including protease inhibitors (1× Complete EDTA-free, Roche) in the buffers, increasing the signal collection time and the contrast during the Western Blot revealing. Faint signals corresponding to the soluble CAIV were observed in the 200 mM imidazole elution fraction and the resuspended NTA resin (about 33 kDa).

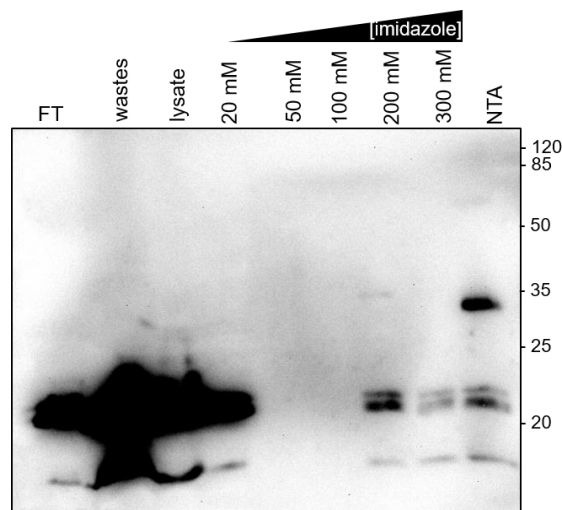


Figure 4. 56: (m)CAIV(p) expression test of pET21X transformed BL21(DE3) *E. coli*. SDS-PAGE of the cell lysis and IMAC purification visualized using Western Blot (anti Penta-His). The “wastes” and “lysate” fractions were the separated by centrifugation of the lysis crude extract. “FT” represents the flow through of the lysate through the Ni-NTA resin and “NTA” the resuspended resin. Protein marker (M) was used to estimate the protein sizes (units are in kDa).

This means that the protein of interest was expressed albeit at low expression levels. Unfortunately, it did not appear to elute as expected during IMAC. Besides, the main signals observed in the previous Western blots show the expression of Histidine rich proteins or protein fragments bearing the C-terminal His₁₀ tag. The fragments could not be attributed to proteolytic products, as they could be observed in the experiments containing protease inhibitor (Figure 4.56). These signals may be caused by the incorrect expression of the protein sequence, generating fragments of the expected soluble CAIV.

Using the pET21X plasmid showed little success. It was decided to attempt the expression of soluble CAIV in BL21(DE3) *E. coli* using the cell-free expression plasmid pIVEX 2.3w (m)CAIV(p) oHA developed in parallel. As its coding frame is also controlled by a T7 promoter that would be recognised by the IPTG inducible expression system of BL21 (DE3) *E. coli*.

Surprisingly, precultures of pIVEX oHA transformed BL21 (DE3) *E. coli* incubated at 37°C and 220 rpm took significantly more time to grow to apparent saturation (two days instead of overnight). After diluting these precultures to 0.2 to 0.15 in fresh culture media, a heavy lysogenic activity was observed. A few tests confirmed that this lysis was not caused by phage contamination. It had been reported that pIVEX plasmids were not best suited for expression in living organisms [215], which suggested that this lysis could have been caused by expression leaks or by the expression of toxic protein.

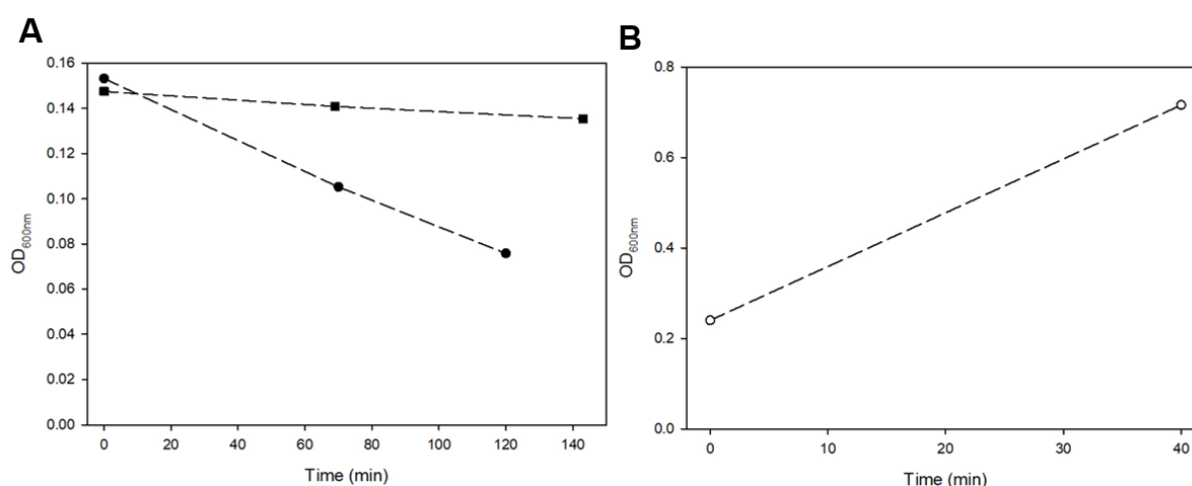


Figure 4. 57: pIVEX transformed BL21(DE3) *E. coli* cultures growing at 37°C in LB Amp. (A) Culture started from a preculture grown for two days at 37°C (black), cultures grown at 37°C (black circles) or 29°C (black squares). (B) Culture started from a preculture grown overnight at 20°C, grown at 37°C (white circles).

As displayed in Figure 4.57 A, the growth temperature of the culture appeared to play a significant role in the lytic activity. By decreasing the growth temperature to 29°C, lysis was almost stalled (black squares). After other tests, it was observed that growing the precultures at 20°C allowed for the inoculations of cultures that grew well at 37°C (Figure 4.57 B), thus allowing for the induction of the protein expression by IPTG.

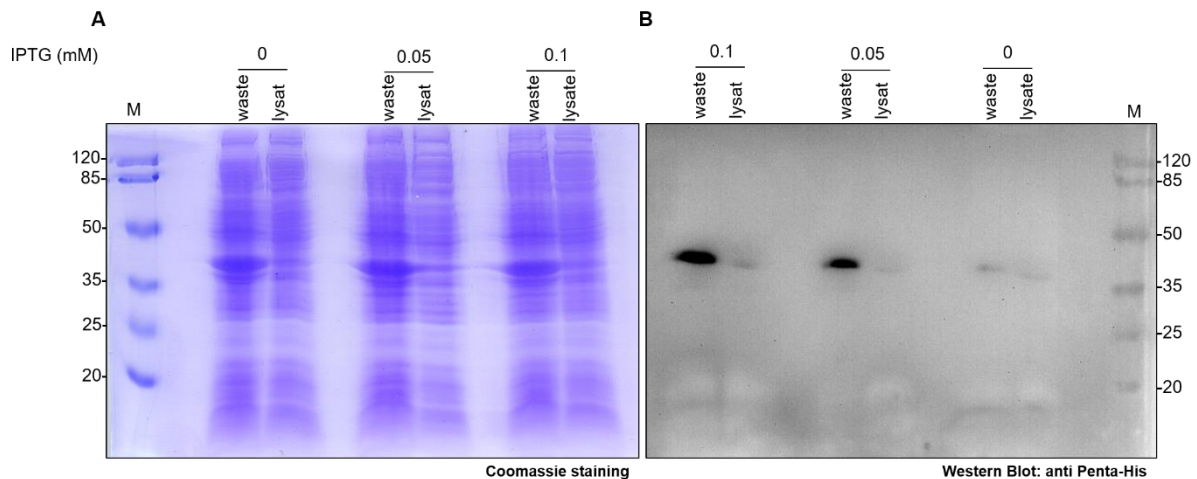


Figure 4. 58: (m)CAIV(p) expression test of pIVEX oHA transformed BL21(DE3) *E. coli*. SDS-PAGE of the cell lysis samples, visualized using Coomassie staining (A) or Western Blot anti Penta-His (B). The “wastes” and “lysate” fractions were the separated by centrifugation of the lysis crude extract (10 min, 12 000 rcf, 4°C). Protein marker (M) was used to estimate the protein sizes (units are in kDa).

A faint ECL signal was observed in the lysis fractions of the cell cultures whose expression was not induced (Figure 4.58 B, 0 mM IPTG). This confirms that in the absence of the LacI repressor in the pIVEX vector, some expression leaks were to be expected. More importantly, the addition of IPTG leads to the overexpression of a protein whose detected molecular weight fit that of the soluble CAIV (between 50 and 35 kDa), similarly to what was observed in the Figures 4.51 to 4.53. Some of these signals could be observed in the lysate, but unfortunately, the greater concentration of the overexpressed proteins appeared to have remained in the cell waste pellet.

The low concentrations of IPTG used were the results of dilutions errors, but they were enough to determine that the protein of interest could be expressed in BL21(DE3) *E. coli* transformed with pIVEX oHA.

Idrees *et al.* [172] reported that their expression of CAVA yielded a low yield of soluble proteins. The majority of the expressed proteins had formed inclusion bodies, aggregates of partially folded proteins.

Recovering soluble proteins from inclusion bodies requires washing the inclusion bodies from contaminants, resuspending the proteins in denaturing conditions then purifying them. The protocol was adapted from Idrees *et al.* [172], following information and adjustments based on the methods described by Palmer and Wingfield [216]. The cell cultures were pelleted (20 min, 4500 g, 4°C) and the pellets resuspended in lysis buffer (50 mM Tris-HCl pH=8, 500 mM NaCl, 5% glycerol, 5 mM β -mercaptoethanol, 1 \times protease inhibitor, 0.1 mg/mL lysozymes and 1% Triton X-100). After incubating at room temperature and gentle agitation (tilt shaking) for 20 min to let the lysozymes break the cell walls, the bacteria suspension was lysed by 5 cycles of French Press until the viscous and turbid suspension became translucent and fluid. The soluble proteins were separated from the cellular wastes and the inclusion bodies (IB) by centrifuging for 1 h at 15 000 g, 4°C. This is lower than the 22 000 g recommended by Palmer and Wingfield [216] but it was the maximal speed achievable by the Heraeus Multifuge. The recovered supernatant, containing the soluble CAIV, was further purified by using an adapted IMAC protocol. The pellets, containing cellular wastes and IBs, were resuspended in washing buffer solutions (50 mM Tris-HCl pH=8, 5 mM β -mercaptoethanol, 1% Triton X-100), with 8 to 10 mL of buffer per mg of pellet (as adapted from Palmer and Wingfield) then pelleted again (30 min at 15 000 g, 4°C). This process was repeated for three times to wash away the contaminant proteins and other membranes. The supernatant containing such contaminants were collected on the side. Finally, the washed pellet was suspended one last time in washing buffer solution without Triton using a homogenizer. It was pelleted as described above and frozen at -80°C until further uses. The next day, the IB pellet was thawed and resuspended in extraction buffer solution (50 mM Tris pH=8, 300 mM NaCl, 1% N-lauroylsarcosine) and incubated for 30 min a room temperature with a gentle agitation (tilt shaking) to solubilize the IB proteins. Finally, the detergent-solubilized proteins were separated from the debris by centrifugation (30 min at 15 000 g, 4°C).

Purification of CAIV from Inclusion Bodies

1 L of BL21 (DE3) culture was prepared as previously described. The different protein samples were diluted 3:4 in 4 \times SDS buffer and incubated 5 min at 95 °C before loading them on SDS-PAGE gels (12.5%), revealed by Coomassie staining or Western blot.

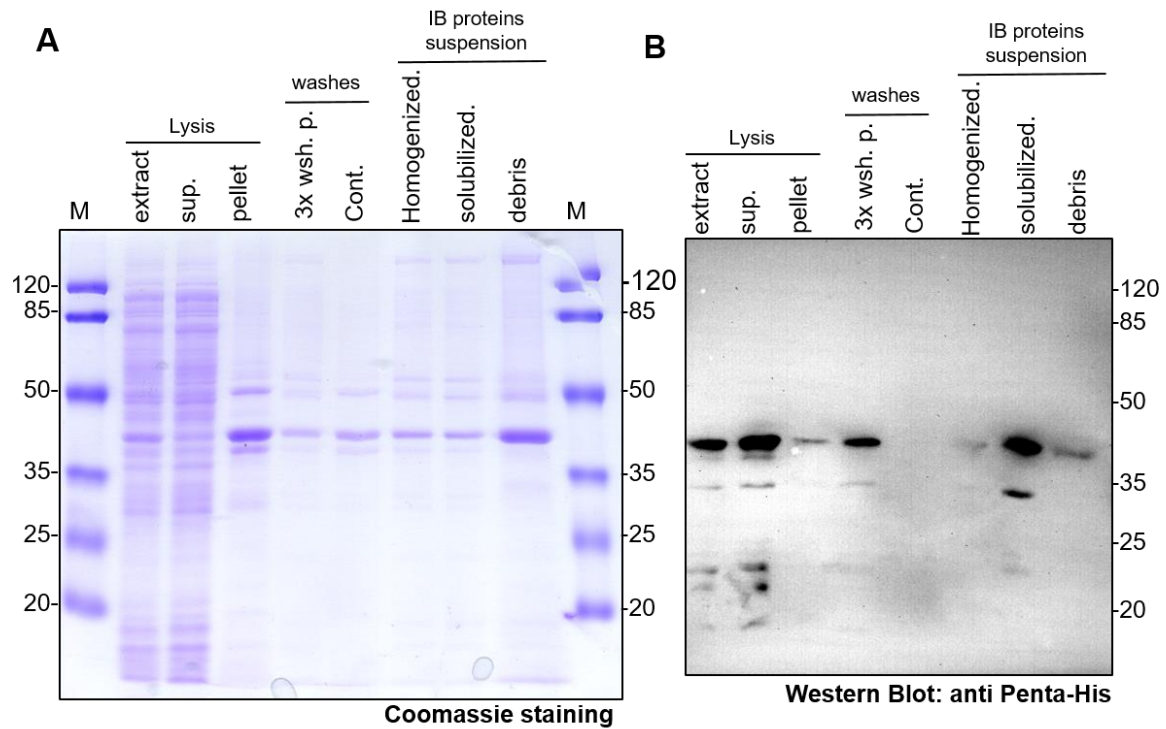


Figure 4.59: (m)CAIV(p) inclusion bodies extraction. SDS-PAGE samples visualized using Coomassie staining (**A**) or Western Blot (anti Penta-His) (**B**). The lysis crude extract (“extract”) was separated by centrifugation between the supernatant (“sup.”) and the pellet containing the IBs and contaminant proteins. The thrice -washed pellet is labeled “3× wsh. p.” and the contaminant proteins removed are “Cont.” The finally homogenized pellet (“Homogenized”) was pelleted again, then incubated in extraction buffer which was separated by centrifugation between the solubilized protein (“solubilized.”) and the pellet (“debris”). Each lane was loaded with 5 μ g or 10 μ g of total protein (for the Coomassie staining or Western Blot respectively) except the “pellet”, which were loaded with 2.5 μ g due to a calculation error. Protein marker (M) was used to estimate the protein sizes (units are in kDa).

It is not exactly clear if the largest band observed in the Coomassie stained gel and in the western blot (halfway between the 50 and 35 kDa) is the expected CAIV. By referring to the previous gels of cell-free expressed CAIV (Figure 4.51), we could have expected the CAIV to appear just above the 35 kDa marker. Interestingly, these potential contaminant bands were all present in the Coomassie stained gel, except in the Western Blot lane corresponding to the contaminant proteins washed away (“Cont.”).

At this stage, the proteins solubilized from the IBs did not contain pure CAIV(p), albeit appearing to be the fraction containing the highest concentration of soluble CAIV(p).

These detergent-solubilized were then purified using a modified IMAC protocol. 250 μ L of Ni-NTA resin were equilibrated in 20 volumes of equilibration buffer (50 mM Tris pH=8, 50 mM NaCl, 1% N-lauroylsarcosine) washed in 10 resin volumes of washing buffer (50 mM Tris

pH=8, 50 mM NaCl, 1% N-lauroylsarcosine, 20 mM imidazole) and eluted three times with 3 resin volumes of IMAC elution buffers (containing 100, 200 and 300 mM imidazole).

Despite the Bradford assay not being appropriate to measure the concentrations of CAIV, it was used to estimate the total protein concentration to perform an SDS-PAGE to visualize the protein composition in each of the fractions.

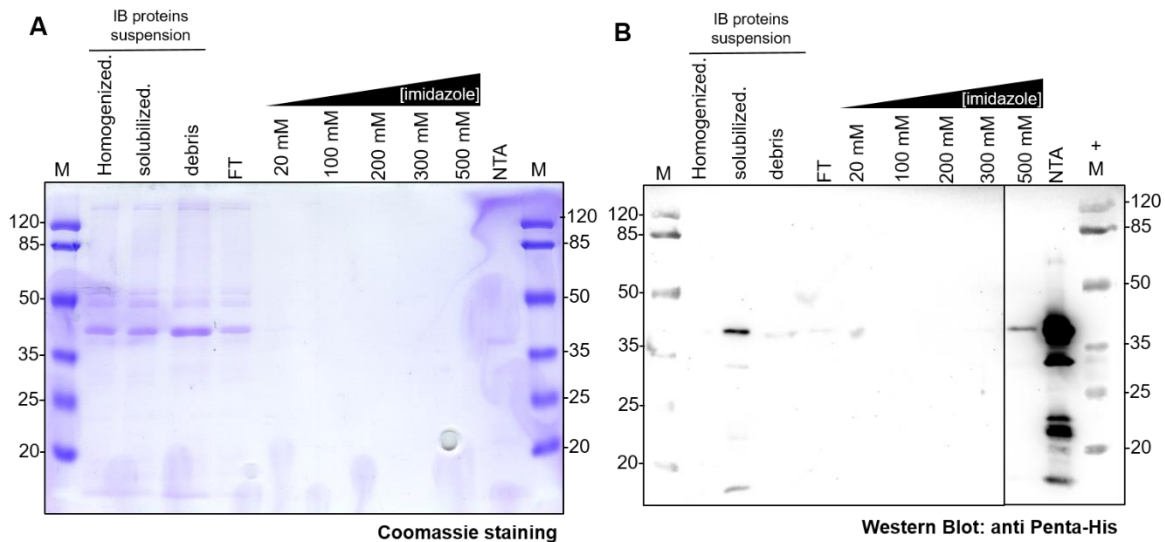


Figure 4. 60: (m)CAIV(p) inclusion bodies IMAC purification. SDS-PAGE different samples visualized using Coomassie staining (A) or Western Blot anti Penta-His (the fractions “500 mM” to “NTA” were displayed with a lower contrast to avoid saturation) (B). The gels represent the fraction from the IB protein resuspension described above, then the IMAC fractions: the flow-through (“FT”), the elution with increasing concentrations of imidazole, then the resuspended NTA resin (“NTA”). Each lane was loaded with 10 μg of total protein except the “pellet”, which got loaded with 2.5 μg because of a calculation error. Protein marker (M) was used to estimate the protein sizes (units are in kDa), and in the case of the Western Bot, 2.5 μg of cell-free expressed PpFNT was loaded on the same lane as a positive control.

It appeared that the IB solubilized proteins could not be efficiently purified, as they appeared to remain trapped in the NTA resin. Palmer and Wingfield [216] warn that detergent such as sarcosine may decrease the efficiency of nickel binding, yet such detergent were the most efficient at reconstituting soluble CAVA from IBs described by Idrees *et al.* [172].

The next step would have been the critical process of refolding the protein, typically by using dialysis to reduce the concentration of detergent gradually. After this process, it would have been necessary to ensure that the soluble CAIV purified out of inclusion bodies were functional or at least properly folded before its interaction with the yeast expressed Basigin could be measured. As such purification process appeared tedious and did not yield the expected protein

concentrations, it was dismissed as a method to produce and purify high quantities of soluble CAIV.

Purification of the soluble proteins

Some soluble (m)CAIV(p) was expressed alongside the inclusion bodies as can be observed in Figure 4.59 B, in the PAGE lane containing the lysis supernatant (“sup.”).

The proteins could be purified using an adapted IMAC protocol. 250 μ L of Ni-NTA resin were equilibrated in 50 mM Tris-HCl pH=8, 500 mM NaCl, 5% glycerol 5 mM β -mercaptoethanol, washed in 10 resin volumes of the same solution containing low concentrations of imidazole (20 or 60 mM), then eluted with 3 resin volumes of solution containing 300 mM imidazole.

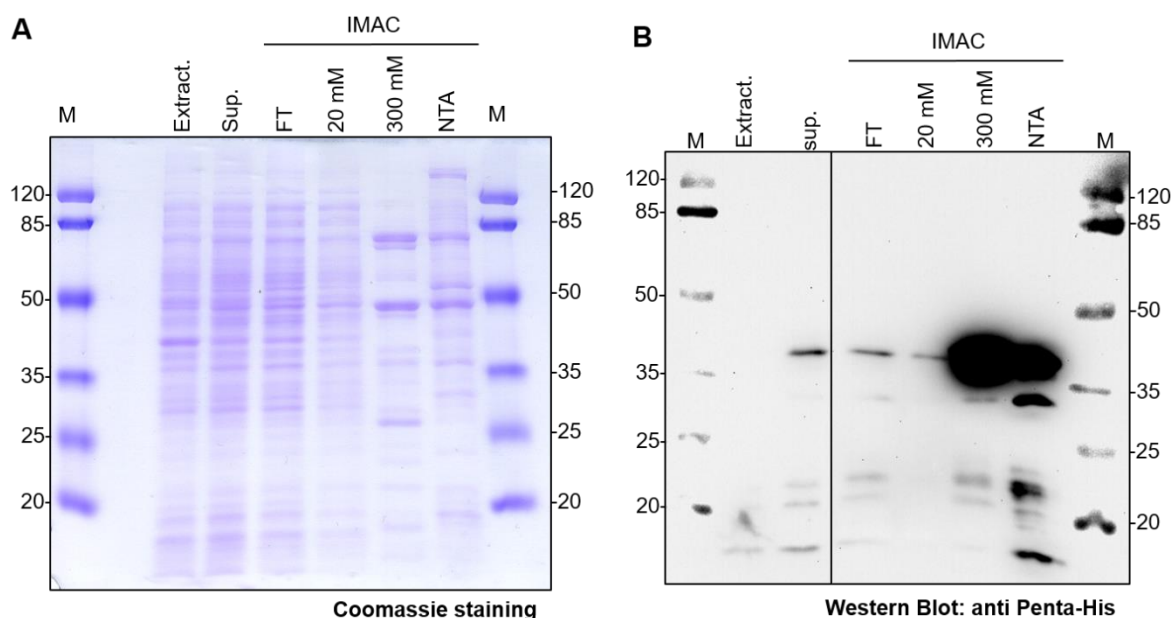


Figure 4. 61: Soluble (m)CAIV(p) IMAC purification. SDS-PAGE different samples visualized using Coomassie staining (A) or Western Blot anti Penta-His (B). The gels represent the fraction from the Lysis crude extract (“Extract.”) and the soluble protein supernatant (“sup.”) separated by centrifugation, then the IMAC fractions: the flow-through (“FT”), washing (“20mM”) and elution (“300 mM”) with imidazole, then the resuspended NTA resin (“NTA”). Each lane was loaded with 10 μ g of total protein. Protein marker (M) was used to estimate the protein sizes (units are in kDa).

The IMAC purification of soluble CAIV did not yield pure protein. At least three major contaminant proteins could be observed in the 300 mM imidazole elution fraction of Figure 4.61 A, weighing about 27, 50 and 80 kDa. Despite the high signal intensity detected in the

Western Blot, only a faint protein band could be detected at the level corresponding to the CAIV molecular weight.

As previously described, estimating the concentration of CAIV remained a challenge. The BCA assay was used as an alternative method to determine protein concentrations without relying on the Coomassie staining of the proteins. A calibration curve was prepared by precipitating known concentrations of BSA, as previously described (3.2.1.). 50 μ L of 300 mM elution fraction were precipitated then resuspended in either 1 mL or 0.5 mL of ddH₂O to determine the protein concentration.

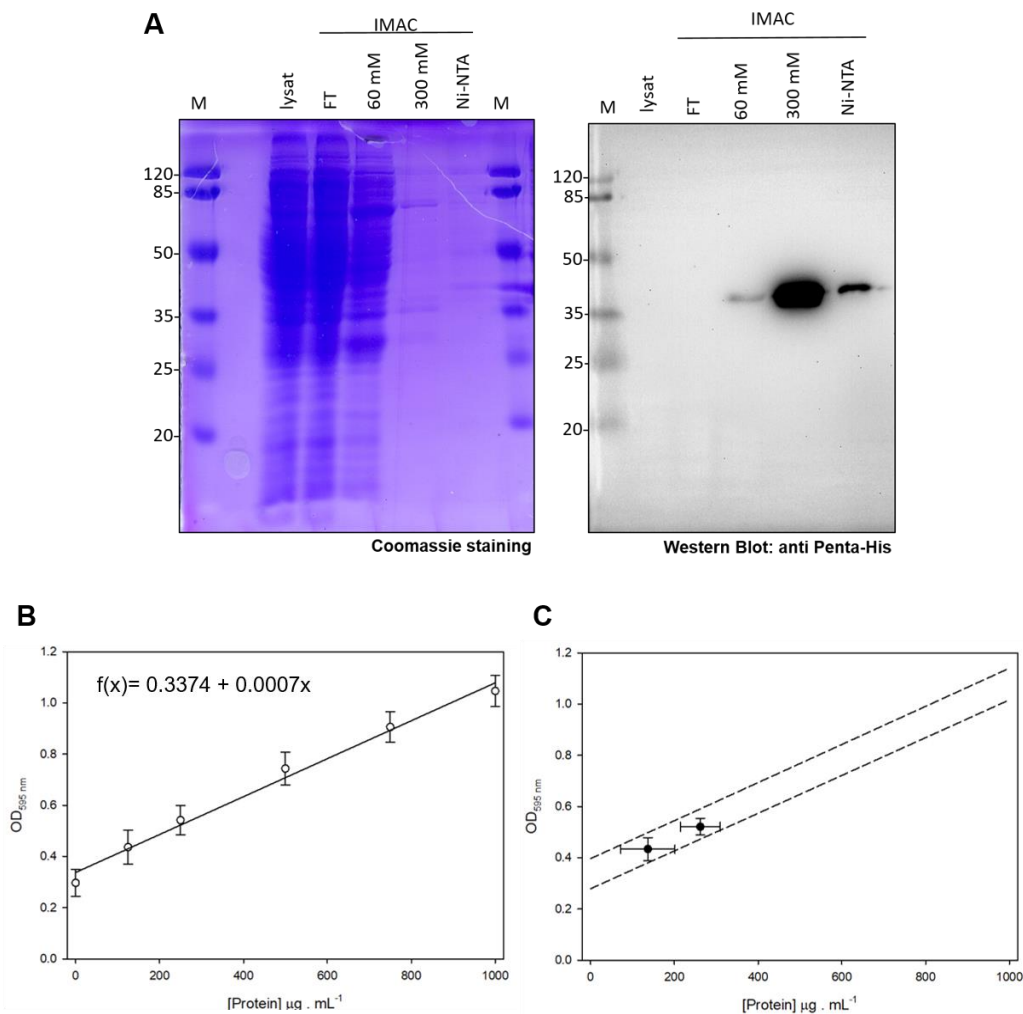


Figure 4.62: IMAC purification of soluble CAIV and BCA assay determination of the protein concentration. SDS-PAGE of the CAIV IMAC, visualized with Coomassie staining and Western Blot (anti Penta-His). Protein marker (M) was used to estimate the protein sizes (units are in kDa) (A). BCA calibration curve prepared with BSA (B) was used to estimate the CAIV concentrations in the 300 mM imidazole elution fraction based on the OD_{595 nm} of two dilutions (C). Error bars represent SEM (technical triplicates).

A calibration curve is created by fitting a polynomial curve through the points generated by measuring the $OD_{595\text{ nm}}$ of different known concentrations of BSA (Figure 4.62 B). It was used to determine the formula necessary to calculate the concentration of the CAIV samples based on their $OD_{595\text{ nm}}$ values (Figure 4.62 C), according to the following calculations:

$$f(x) = 0.3374 \times 0.0007x \quad (23)$$

$$OD_{595\text{ nm}} = 0.3374 \times (0.0007 \times [Protein]_{\mu\text{g.mL}^{-1}}) \quad (24)$$

$$[Protein]_{\mu\text{g.mL}^{-1}} = \frac{OD_{595\text{ nm}} - 0.3374}{0.0007} \quad (25)$$

Based on these calculations, it was estimated that the CAIV samples had a concentration of $134 (\pm 62) \mu\text{g/mL}$. The total protein yield of this purification was $201(\pm 93) \mu\text{g}$. As observed in Figure 4.61 A, the total protein concentration in the 300 mM elution fraction was relatively low, and did not contain pure CAIV.

Possible interaction with the yeasts cell walls

One crucial parameter that had not been considered in designing this experiment relying on the interaction between the yeast expressed Basigin - MCT1 fusion constructs and soluble CAIV was the thickness of the yeast cell wall.

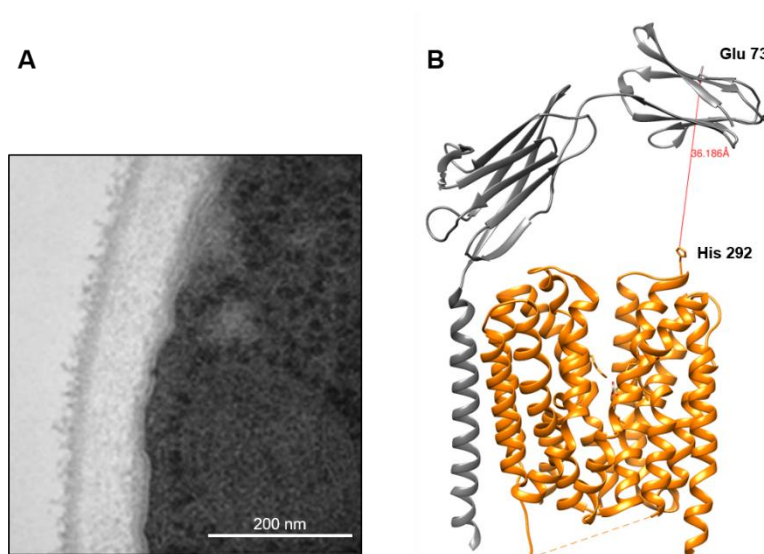


Figure 4. 63: (A) Transmission electron microscopy image of the *S. saccharomyces* cell wall. Adapted from Bzducha-Wróbel *et al.* [217]; (B) Visualisation of the distance between the Basigin Glu73 and the MCT1 His292. Based on PDB# 6LZ0 [104], using Chimera 1.14.

The *S. saccharomyces* cell wall was reported to have a thickness of hundreds of nanometers [217], [218] (Figure 4.63 A). The distance between the MCT1 transport path (represented by the His292), located at the level of the yeast plasma membrane and the Basigin Ig - C2 Glu73 (supposedly involved in the binding of CAIV [131]), was measured to be 36.186 Å using the Chimera 1.14 software (Figure 4.63 B). This corresponds to no more than 3.62 nm. This means that simply mixing yeasts expressing the Basigin - MCT1 fusion construct and soluble CAIV would never lead to the formation of a complex, as they would be separated by the width of the cell wall.

To ensure that the surface Basigins expressed by the yeasts are exposed to the solvent, available to bind to the eventual soluble CAIV, it would be necessary to ensure that the cell wall does not cause any interference. Such cell walls were digested by zymolase to form protoplasts, according to 3.5.6 and stored overnight in protoplast storage buffer (2.9.6).

After the final resuspension in a minimal volume, the resulting protoplast preparations resulted in concentrations of around $OD_{600\text{ nm}} = 17.67 \pm 0.5$, which is quite inferior to that of the $OD_{600\text{ nm}} = 50 \pm 5$ typically used for radiolabeled substrate transport assay (3.6.). To compare these data with the transport activity measured in yeasts, the transported concentration of lactate was normalized to the suspension $OD_{600\text{ nm}}$.

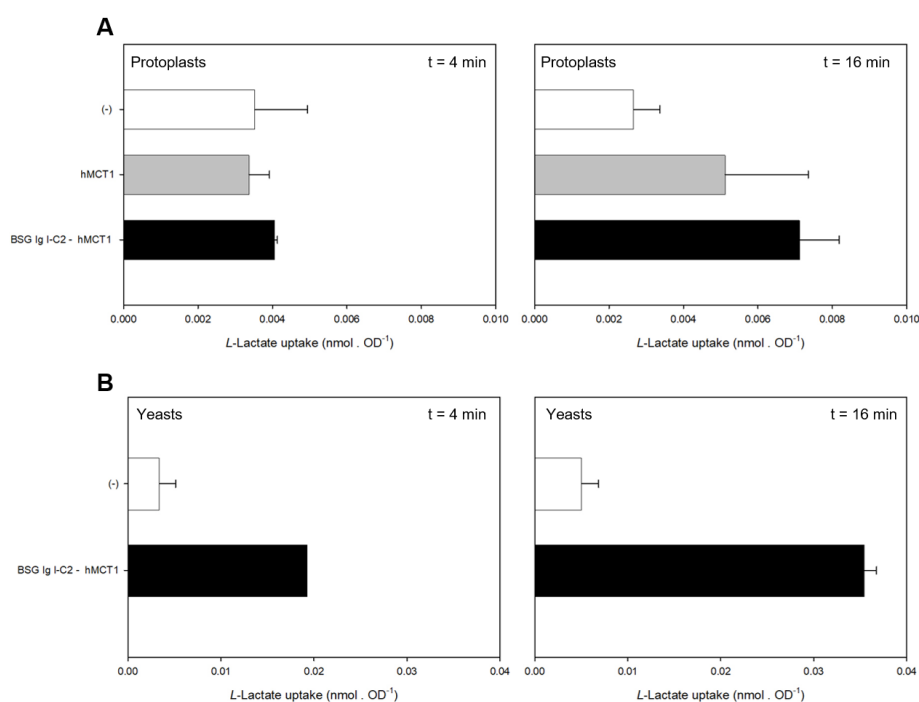


Figure 4. 64: Comparison of the L-Lactate uptake of the protoplasts (A) and yeasts (B) over 4 or 16 min. Radiolabeled lactate uptake assay, 1 mM L-Lactate. Measured in 10 mM MOPS pH=7.2, 1.2 M saccharose, 50 mM NaCl and CaCl₂ pH=7.2 (protoplasts) or in 50 mM Tris/HEPES pH=6.8 (yeasts). Error bars represent SEM (experimental duplicates).

The yeast protoplasts showed some uptake activity, as the amount of transported lactate significantly increased between 4 and 16 min of transports. Unfortunately, the transport of substrate measured in protoplasts was too weak to yield a good signal-to-noise ratio. Even after 16 min of transport, the background signal (-) represented between half and one third of the transport signal (Figure 4.64 A). The differences of measured substrate uptake between the control and the yeast expressing MCT1 or BSG IgI-C2 – MCT1 were not statistically significant (Student's t-test, two-tailed p-value = 0.404 and 0.0738 respectively). As a means of comparison, Figure 4.64 B shows the lactate uptake of yeasts expressing similar proteins. There, the difference between the background and the signal was significant (Student's t-test, two-tailed p-value < 0.005 after 16 min) and appeared about five times greater than the signal measured in protoplasts.

Some of this difference can be explained by the pH difference (7.2 and 6.8) that slightly decreases the concentration of substrate available for transport by protoplasts. Regardless, the low transport values make it impossible to accurately measure the substrate transport in protoplasts.

Measuring the transport functionality in protoplasts does not seem feasible, not without thoroughly adapting the assay to ensure a satisfying signal-to-noise ratio.

4.4. Investigating the influence of terminal tags on transporters functionality

4.4.1. Verifying the effect of terminal tags on MCT1 transport.

Noor *et al.* [143] reported that the presence of a 6 Histidine epitope in the C-terminal end of rat MCT4 facilitated transport activity by a nearly of 2 despite similar expression levels. This increase was as significant than the one caused by the co-expression with CAII, a proton antenna known for shuttling protons from the bulk cytosol to the MCT4 transport path, facilitating the efflux of substrate [122], [134], [135], [138], [142]. Furthermore, this increase could be cancelled by the addition of antibodies targeting the epitope. These findings suggest that the His-rich epitope would act as a putative proton collecting antenna and improve the monocarboxylate efflux through MCT4. As our experimental model used yeast expressing

MCT1 flanked by terminal tags, including a C-terminal His₁₀ tag, it was relevant to verify whether these tags affected the substrate transport, especially since it was intended to investigate proton antenna effects in further experiments.

The protein construct most used in our experiments are MCT1, expressed with an N-terminal HA tag and a C-terminal His₁₀ tag (separated from the protein coding sequence by a Factor Xa. Protease cleavage site), using the pDRTXa plasmid. Such proteins will be referred to as HA-MCT1-His. A plasmid expressing the MCT1 with only a C-terminal His-tag (and factor Xa cleavage site) was generated by digesting the pDRTXa_MCT1 with the restriction enzymes XbaI and SpeI (thus removing the sequence encoding the HA tag) and ligating the two compatible ends together. Such proteins will be referred to as MCT1-His. The pDR plasmid had been generated to allow the expression of untagged proteins in yeast. The DNA sequence encoding for the N-terminal HA tag and the MCT1 inserted in pDRT plasmids and the resulting protein labeled as HA-MCT1. As no primary antibodies were specifically raised against MCT1, the protein needed to be expressed with at least one HA or His terminal tag to detect its expression using Western Blots.

The generated plasmids were used to transform Δ jen1 Δ ady2 yeasts (3.5.2) to measure the transport of radiolabeled substrate over time (3.6.). Part of the cultures used for the radiolabeled substrate assay were lysed using glass beads to recover their microsomal fractions (3.5.4). Their protein contents were visualised by SDS-PAGE, followed by Western Blots.

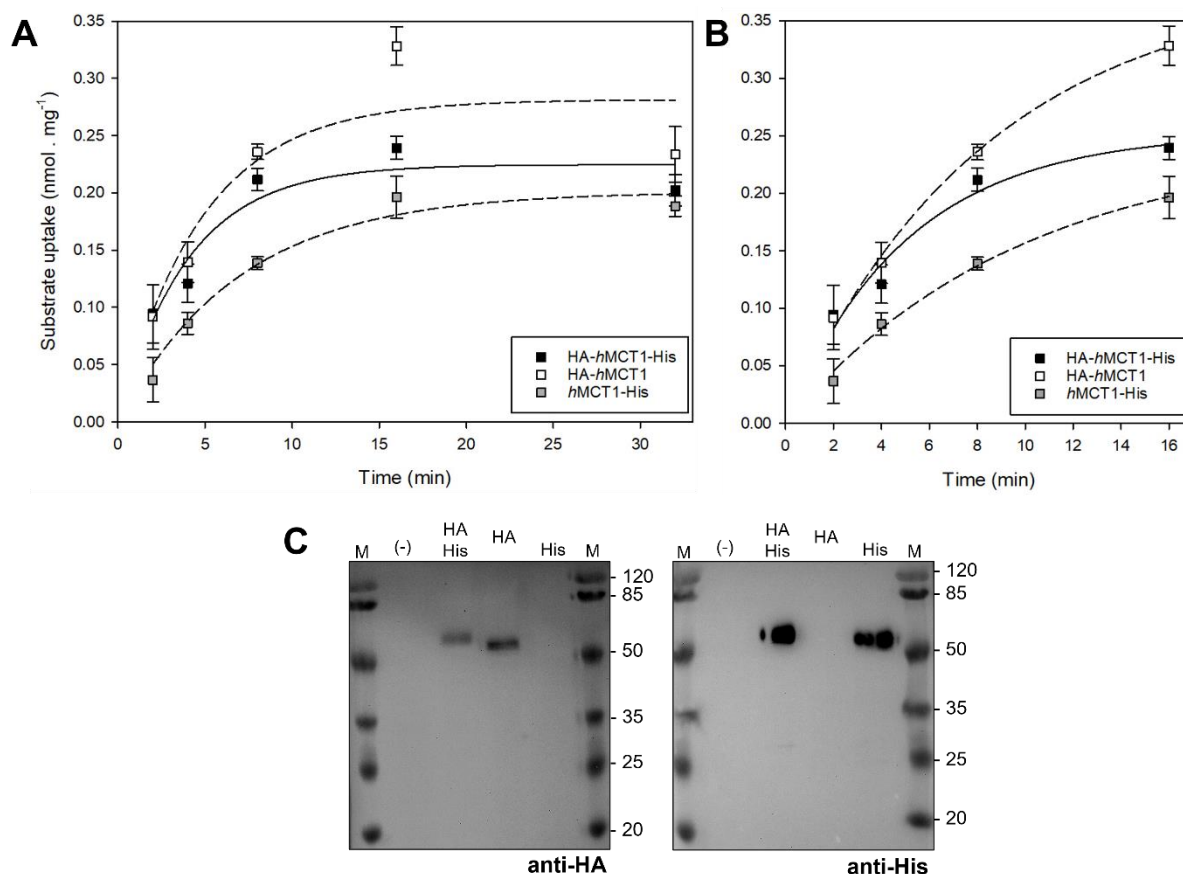


Figure 4. 65: Radiolabeled substrate uptake of the MCT1 constructs with different tags over time, measured in 50 mM Tris/HEPES pH=6.8, 1 mM L-lactate. Background subtracted. Error bars represent SEM of experimental triplicates. Background subtracted. The transport curves were fitted either between 2 and 32 min (A) or 2 and 16 min (B). The protein expressions were estimated based on a Western Blot (C) containing 10 μ g of total membrane proteins in each well. Protein marker (M) was used to estimate the protein sizes (units are in kDa).

The uptake measurements after 32 min were unexpected. An expected transport would have led to uptake values equal or greater than those measured earlier (8 or 16 min). Measuring lower values could be explained by a decrease of yeast fitness over the longer experimental time. Including these points in the calculation of the transport curve (Figure 4.65 A) would skew the uptake capacity plateau towards lower values. At the risk of extrapolating outside of the measured range, the transport was also fitted (as exponential rises to a maximum) excluding this last point at 32 min of transport. The resulting equations were used to determine the transport capacity and their implications are discussed later (5.4.1).

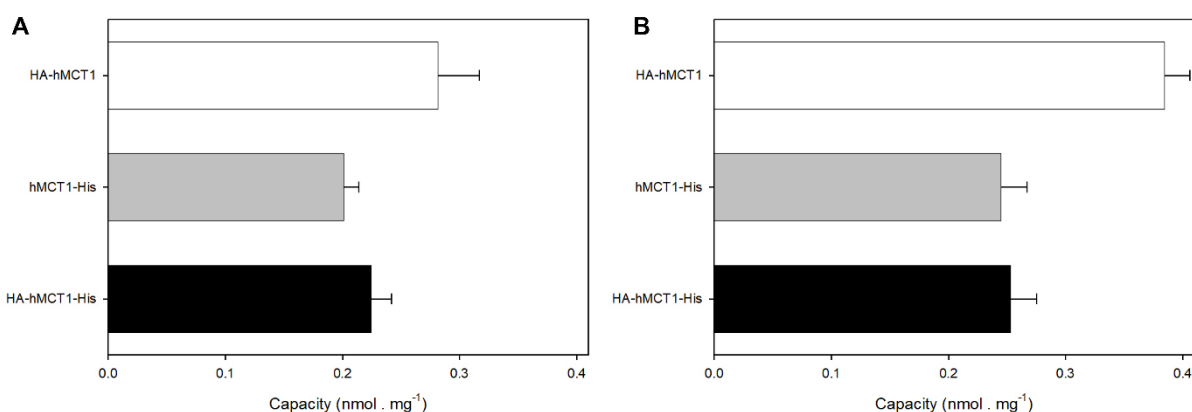


Figure 4. 66: Transport capacity at equilibrium of the MCT constructs with different tags. Calculated from the transport fitting curves of Figure 4.65 including (A) or excluding (B) the measures at 32 min. Errors represent the standard error (SEM) of the calculated fitting curves.

The transport capacities calculated from the curves including the transport at 32 min show no statistically significant differences (Student's t-tests, p -value > 0.05), despite the HA-MCT1 capacity appearing slightly higher than the rest (Figure 4:66 A). However, when the fitting curves equations were calculated based on the more accurate transport data (from 2 to 16 min), the capacities of the proteins containing an His-tag appear similar (Student t-test, p -value=0.809) and showed a statistically significant increase in the capacity of HA-MCT1 at transport equilibrium (Student t-test, p -value <0.05).

4.4.2. Investigating the potential effect of the terminal tags on PfFNT transport.

As previously described (4.2.1, Figure 4.26, Table 4.1), it was relevant to test the PfFNT activity in the absence of artificial tags to avoid any experimental interferences. Previous to this work, most yeast expressed transporters were encoded in the pDRTXa plasmids, carrying both the N-terminal HA-tag and the C-terminal His-tag (HA-PfFNT-His). It was important to investigate whether these artificial tags impacted the behavior of the transporter proteins. The pDR plasmid was used to express PfFNT without artificial tags (PfFNT) or linked to a single N-terminal HA tag (HA-PfFNT).

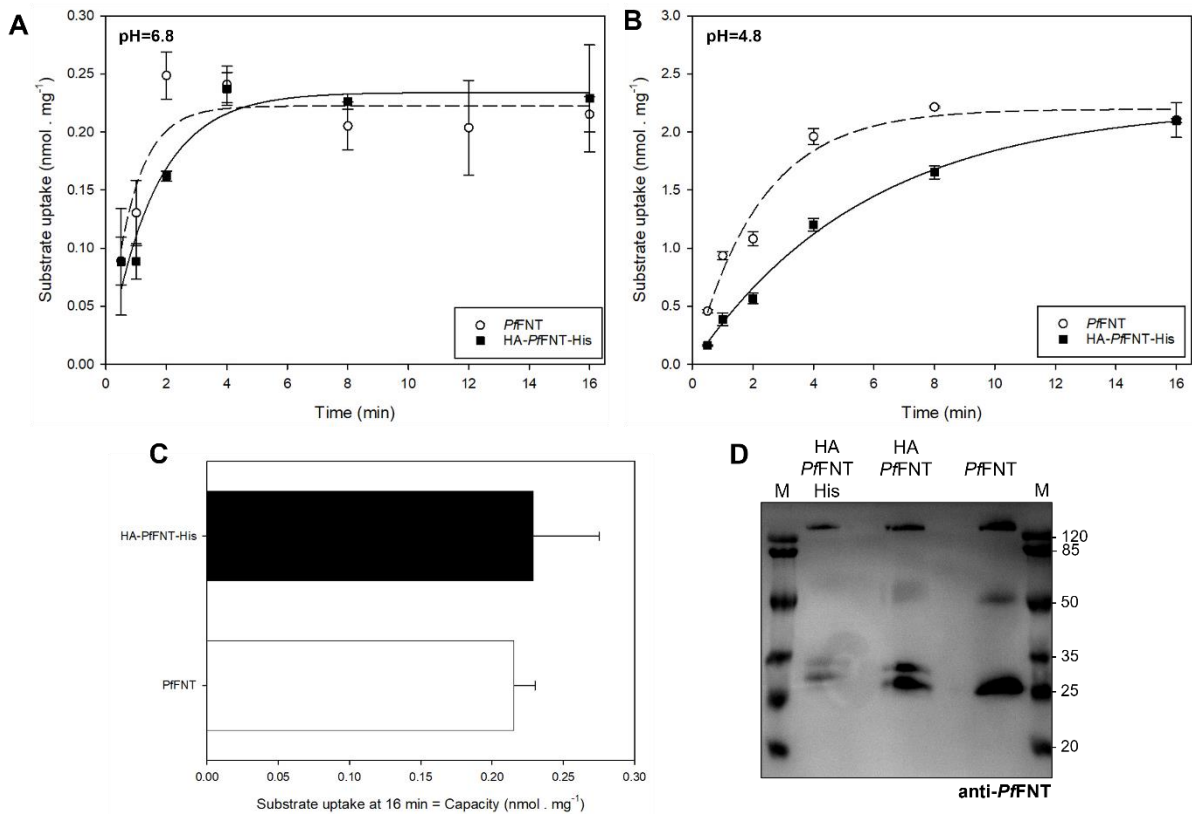


Figure 4.67: Substrate uptake of untagged (white circles) and HA/His₁₀-tagged (black squares) PfFNT expressing yeasts measured over time in 50 mM Tris/HEPES pH=6.8 (A and C) or 50 mM Tris/MES pH=4.8 (B). 1 mM L-Lactate. Background subtracted. Error bars represent SEM of experimental duplicates (HA-PfFNT-His, PfFNT pH=4.8) or biological triplicates with experimental triplicates (PfFNT pH=6.8). The protein expressions were estimated based on a Western Blot (D) containing 10 μ g of transformed yeast membrane proteins in each well. Protein marker (M) was used to estimate the protein sizes (units are in kDa).

The addition of N-terminal HA tag and C-terminal His₁₀-tags to the PfFNT sequence did not appear to have an impact on the protein influx. The substrate uptake over time measured with both constructs could be fitted with exponential rises to a maximum (single, two parameters). The untagged PfFNT (white circles) appeared to transport faster, especially at lower pH (Figure 4.67 B), but it could be explained by the much higher expression level (Figure 4.67 D). At a pH of 6.8, both curves appeared to reach a similar plateau after about 8 min of transport. The substrate uptake after 16 min of transports was used to represent the proteins capacities upon reaching equilibrium, as described in Figure 4.67 C. The difference between the capacities at pH=6.8 was not statistically significant (Welch's t-test: two-tailed p=0.816).

As further investigations of the protein C-terminal effect on transport warranted to use an N-terminal HA tag, HA-PfFNT was used as the basis of comparison from this point onward. It is also worth noting that between the sets of experiments displayed in Figure 4.67 and

Figure 4.68, some changes were made to the experimental set-up that made the comparison of older and newer data less accurate. Noticeably; the substrate uptake plateau measured for the HA-PfFNT-His construct did not reach exactly the same value between Figure 4.67 A and Figure 4.68 A.

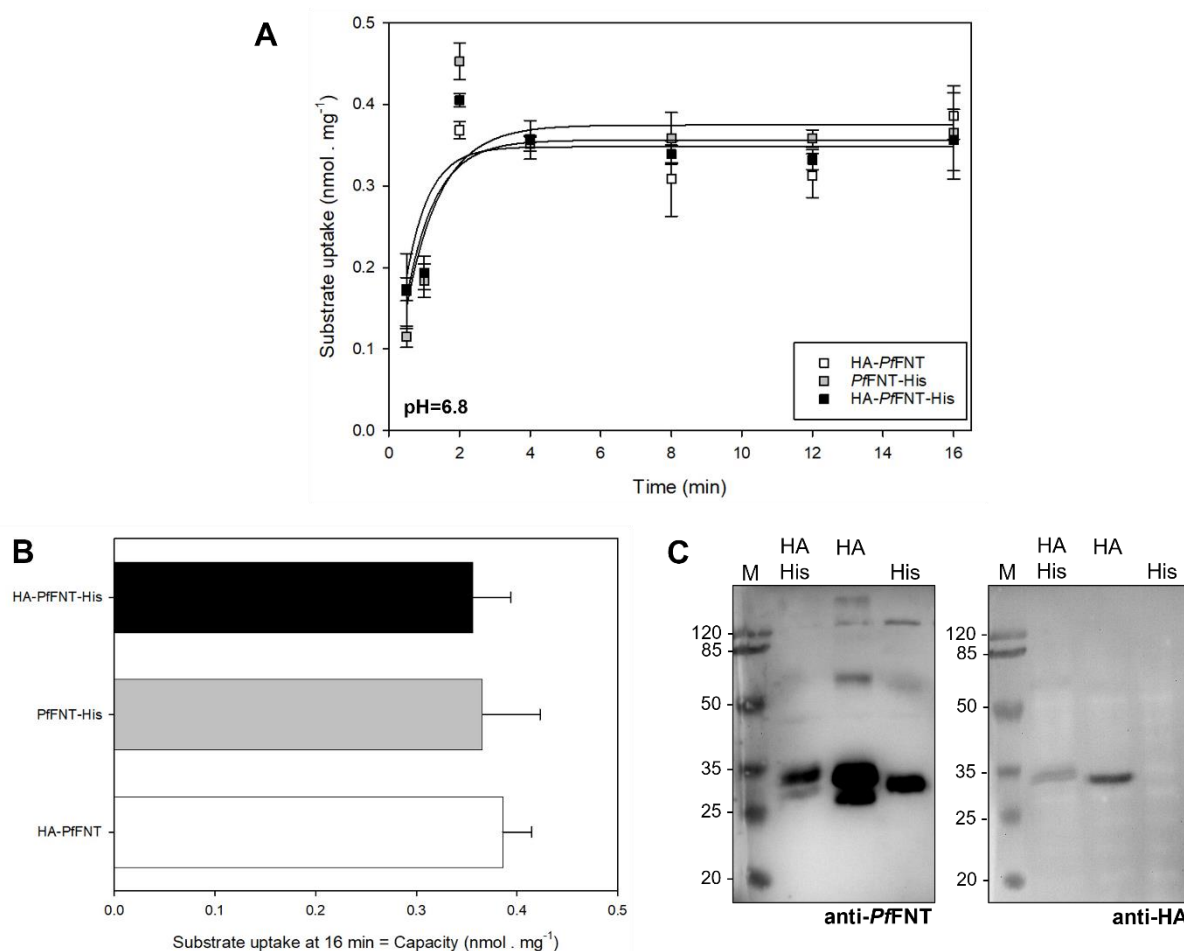
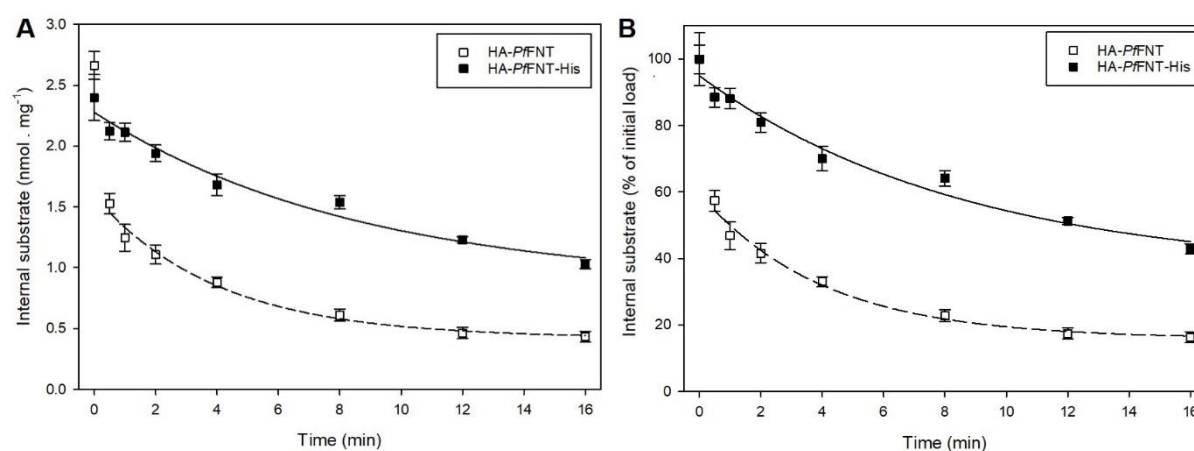


Figure 4. 68: Substrate uptake of HA (white squares), His (grey squares) and HA/His₁₀-tagged (black squares) PfFNT expressing yeasts measured over time in 50 mM Tris/HEPES pH=6.8 (A and B). 1 mM L-Lactate. Background subtracted. Error bars represent SEM of experimental duplicates. The protein expressions were estimated based on a Western Blot (C) containing 10 μ g of membrane proteins in each well. Protein marker (M) was used to estimate the protein sizes (units are in kDa).

The substrate uptake assay over time were fitted as exponential rises to a maximum (single, 2 parameters). Despite unequal protein expression levels (Figure 4.75 C), the differently tagged proteins showed equivalent rates and influx capacities at equilibrium (Figure 4.45 A). The uptake at 16 min, having reached the transport equilibrium, was used to compare the capacities (Figure 4.75 B) and showed no statistically significant differences (Student's t-test, p-values>0.05).

As the terminal extremities of the PfFNT proteins are located in the cytosolic side of the yeast [58], it was relevant to also measure how the presence of tags (especially the suspected His - tag) would impact substrate efflux.



: Substrate efflux of HA (white squares) and HA/His₁₀ (black squares) tagged PfFNT expressing yeasts. Measured over time in 50 mM Tris/HEPES pH=6.8. The cells were loaded for 8 min in 1 mM L-Lactate, 50 mM Tris/MES pH=4.8. Background subtracted. Error bars represent SEM of biological duplicates and experimental duplicates.

The efflux curves were fitted as exponential decays (Single, 3 parameters) but the first point of the HA-PfFNT had to be excluded from the fit to yield an equation that matched the rest of the curve. Despite equivalent uptake rate and capacities (Figure 4.68 A and B), Figure 4.69 B shows that the HA-PfFNT and the HA-PfFNT-His constructs efflux transport did not display the same behavior. After a somewhat equivalent initial substrate loading at pH=4.8 (Figure 4.76 A, 0 min), the efflux rate of HA-PfFNT appeared much faster than that of HA - PfFNT - His. Additionally, HA - PfFNT would eventually reach a much lesser internal substrate concentration at transport equilibrium (shortly after 16 min, deduced from the fitted curves). However, the pertinence of the efflux assays is questionable and discussed later (5.4.3.).

The pH-rate dependency of the PfFNT expressed with different terminal tags was also measured (Figure 4.70).

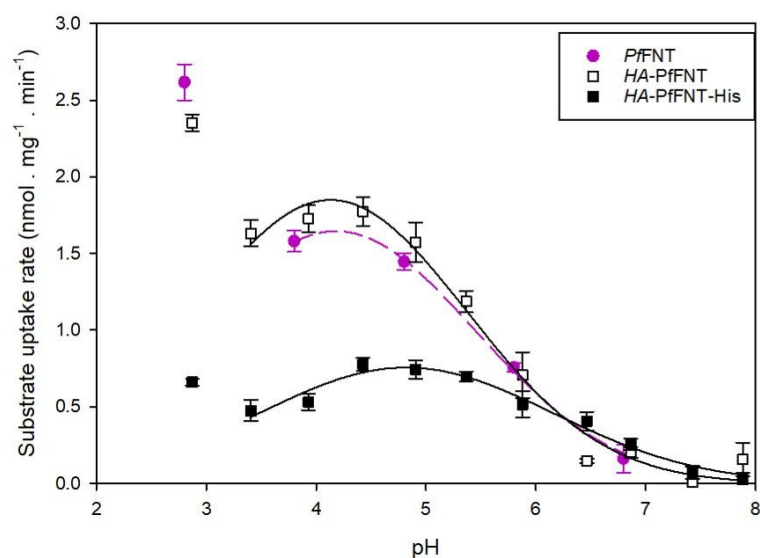


Figure 4. 69: Substrate uptake rates of untagged (magenta circles), HA (white squares) and HA and His₁₀ (black squares) tagged PfFNT expressing yeasts, measured at different extracellular pH. Measured over 30 seconds in 1 mM L-Lactate. Background subtracted. Error bars represent SEM of 2 to 4 (PfFNT), 2 (HA-PfFNT) and 3 (HA-PfFNT-His) biological replicates, each with experimental duplicates.

These rates over pH measurements were fitted as peaks (Gaussian, 3 parameters), excluding the data point at pH=2.8. Despite unequal expression rates (Figure 4.68 C), the pH dependency of the untagged and HA-tagged proteins appeared equivalent. The rates of HA and His₁₀-tagged proteins were much lower, which could be a result of the lower expression level (Figure 4.68 C). Interestingly, the presence of a C-terminal His₁₀-tag appeared to have shifted the highest value of the peak toward higher pH. In untagged and HA-tagged proteins, the highest peak value is observed around pH=4.2, whereas that of the HA and His-tagged PfFNT was around 4.8. This maximal transport rate at pH=4.8 matches the maximum previously reported in some studies of tagged PfFNT [57], [60], while the value of 4.2 was also observed for the same construct [51]. However, the observed behavior of the protein transport rate at low pH (pH<3.8) does not entirely match the previous studies [51], [57], [60] but are in agreement with the observations of Figure 4.35. These implications will be discussed further (5.4.2.3.).

5. DISCUSSION

5.1. Contributing to the determination of PfFNT structures

5.1.1. Formation of PfFNT nanodiscs

The high concentration of contaminants after the MSP protein purification was partially caused by an aged Ni-NTA resin that interacted with *E.coli* proteins (Figure 4.1, 4.2, 4.4 A) [220], [221]. The IEX purification proved an efficient method to separate these contaminants according to other properties than their binding to nickel ions (Figure 4.4 C and D). Pooling the least contaminated fractions and using size exclusion chromatography finally yielded satisfyingly pure MSP protein.

Despite the availability of MSP proteins, the main issue of nanodisc reconstitution was the PfFNT not forming pentamers in the lipid bilayers. Therefore, other methods were investigated to resolve the structure of the PfFNT using Cryo-EM, notably the simple suspension of pentamers in detergent micelles. This work then focused on assisting C. Hansen in the production of properly folded, properly assembled (and therefore functional) PfFNT mutant pentamers.

5.1.2. Cell-free expression of PfFNT

5.1.2.1. Production of N-term Strep II tagged PfFNT

Sanger DNA sequencing had proven that the insertion of the N-terminal Strep II tag coding sequence upstream the PfFNT encoding DNA in the expression plasmids had been successful. This coding sequence had properly been produced by the cell-free expression system, as proteins of the expected molecular weight and fused to functional GFP could be purified using IMAC (Figure 4.6). Moreover, SDS-PAGE revealed that these proteins carried both the C - terminal His-tag (Figure 4.8 A and B) and the N-terminal Strep II tag (Figure 4.8 C).

In Figure 4.7, it was observed that most of the proteins of interest simply eluted through the resin, without interacting with the bound streptavidin. Why would the streptavidin purification of these expressed proteins fail?

Several hypotheses could have explained this result. The experiment may have contained mistakes in its execution or in the buffer composition, but repeating it with different buffer preparations yielded the same result. It was therefore concluded that the tagged proteins could simply not interact with the resin-bound streptavidin. This could have been caused by a degraded resin, but repeating the purification with a regenerated resin yielded the same result. The last hypothesis was that the N-terminal Strep-tag was not accessible.

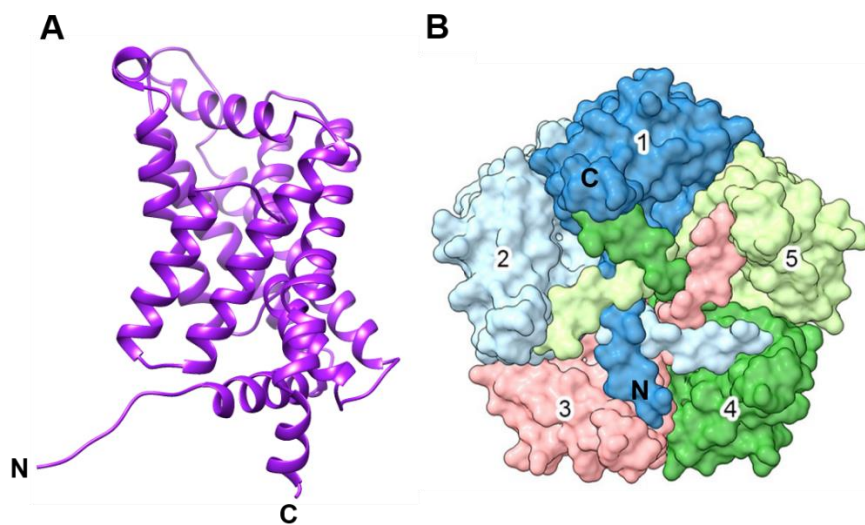


Figure 5. 1: (A) Structural representation of the PfFNT monomer: Side view, N and C termini labeled as such (PDB# 6VQQ, Chain A [52]). (B) Structural representation of the PfFNT pentamer, facing the cytosolic side (PDB# 7E26 [53]), adapted from Peng *et al.* [53]. N and C termini of the subunit 1 (dark blue) are labeled as such.

At the time, the structure of wild-type PfFNT had just been resolved (PDB# 6VQQ [52]). Half a year later, the same team published an even more accurate structure (PDB# 7E26 [53]). These structures (Figure 5.1) showed that the PfFNT N-termini are involved in the assembly of the pentamers, each N-terminal tail weaving itself with the others and interacting with the opposite parts of the complexes. This went a long way in explaining why this N-terminal Strep-tag was not accessible for Strep-Tactin[®] purification. The authors of these studies had expressed their PfFNT proteins fused to a Twin Strep tag, located in the C-terminal end.

As C. Hansen investigated alternatives to the assembly of PfFNT pentamers in MSP nanodiscs, the purification of Strep II tagged proteins were no longer considered a priority. Later,

M. Möller successfully purified Strep-tagged PffNT by expressing the protein with a C-terminal Strep II tag, separated from the protein termini by a flexible linker that allowed for the tag-streptavidin interaction. This confirmed that the single Strep II tag at the PffNT N-terminal end was not accessible.

5.1.2.2. Production of C-term His-tagged PffNT

The reliable expression of His₁₀-tagged PffNT using pIVEX2.3w in cell-free protein synthesis system has proven to be a very efficient method to express it in a large scale [58], [183], [184]. The subsequent IMAC purification appeared to yield satisfying yields of purified PffNT. As bands corresponding to the expected product molecular weights could be observed in the Coomassie stained SDS-PAGE gels, it was reasonable to assume that the PffNT peptide sequence was well expressed using the cell-free system (4.1.2.). Detecting the C-terminal tag His₁₀-tag at the expected molecular weight in the Western Blots was also an indication that the full length of the coding sequence was expressed.

However, neither of these observations on SDS-PAGEs were indications that the properly expressed peptide chains folded into their relevant 3D structures, which are required for function.

SDS-PAGE of cell-free, IMAC purified PffNT showed protein bands that would correspond to the molecular weights of PffNT dimers or trimers when incubated 1 h at 37°C (low denaturation). This means that the proteins were able to assemble into multimers. The proportions of these multimers decreased when incubation at 60°C for 10 to 20 min (higher denaturation). Observing multimeric protein quaternary structures was encouraging, but it is no predictor of the PffNT structural assembly into pentamers, let alone of functional monocarboxylates transport.

Attempts were made to observe the multimerization state of the cell-free expressed and IMAC purified PffNT based on the methods for native PAGE described by Schägger *et al.* [222]–[224]. However, it did not yield satisfying results and was not investigated further.

Mutants PffNT expressed with C-terminal GFP were shipped to Intana Bioscience GmbH (Martinsried, Germany) in order for I. Jakóbowska to measure the interaction of the protein to fluorescently labeled inhibitors, using fluorescence cross correlation spectroscopy. Her results

showed that the provided proteins displayed an extremely low (if not insignificant) level of complex formation with the inhibitors, which suggested that they were not properly folded. It was later observed that these cell-free expressed PffNT aggregated while being transported in a sealed polystyrene box in the presence of a -20°C cooling pack. The cell-free expressed PffNT could not remain solubilized upon freezing in 150 mM NaCl, 20 mM Tris pH=8, 0.05% Brij78.

5.1.3. PffNT reconstitution in proteoliposomes

A cause of further concerns were the measures of proteoliposome reconstituted proteins using stopped-flow spectroscopy. In the past, these cell-free expressed FNT had already been reconstituted in liposomes and appeared to display monocarboxylate transport activities [58], [183]. After some initial difficulties to reproduce these methods, reconstitution of the protein in liposome was seemingly achieved.

Figures 4.9 and 4.10 are representative of PffNT being reconstituted in liposomes (Figure 4.9 B and 4.10 B) and the transport activity (Figure 4.9 A and 4.10 A) of format. However, these transport activities could not be inhibited by the addition of 5 μ M BH296 inhibitor, which represents about 50 times the IC₅₀ measured in yeasts (Figure 4.10). What could be the cause of this format transport if it could not be blocked by the addition of PffNT inhibitor? Could it simply be that the experimental conditions did not properly allow for the inhibitor to be effective? Adding inhibitors directly in the extrusion buffer appeared to cancel the transport functionality (Figure 4.11), suggesting it had been the case.

Pyranine loaded liposomes never reconstituted any proteins, as represented by the data displayed in Figure 4.14. Moreover, after ongoing the reconstitution protocol or after the addition of gramicidin, a steady increase of the liposome internal fluorescence (corresponding to an increase of the pH) was measured (Figures 4.14 and 4.15).

It had already been reported that the presence of ion gradient (potassium and phosphate) could induce an internal alkalization of pH-probe loaded liposome, even in the absence of ionophores [225]. Moreover, calcium cations were also reported to cross lipid membranes unassisted, through transient pores[226], [227]. In this work, the lipid bilayer might have been permeable for sodium ions and protons. Since our experimental assay used sodium formate salt as a source of soluble substrate (formate), perhaps the 50 mM sodium gradient lead to some

exchanges between the intravesicular protons and the extravesicular sodium ions, in an attempt to maintain the overall electrostatic charge.

Figure 4.14 shows that the internal pyranine loaded in the liposomes was sensitive to the changes of intravesicular pH, which was an encouraging development. Unfortunately, observing these changes of fluorescence before the addition of transporters or ionophores means either that the liposomes membranes were permeable to proton exchange or that a significant number of probes remained bound to the extravesicular surface. Preparing proton-tight liposomes membranes is an arduous task, but not an impossible one [228], [229]. Although pH - sensitive liposomes would be a great tool to measure the functionality of PfFNT, this work did not produce a satisfying method to prepare them.

5.1.4. HEK cells expression.

5.1.4.1. Expression and extraction of PfFNT mutants

As cell-free expressed PfFNT pentamers could not be observed in detergent micelles or nanodiscs using electron microscopy, it became necessary to investigate alternative methods of expressions. Since the PfFNT mutants could be expressed, extracted and measured in complexes with dye-bound inhibitors in HEK cells by I. Jakóbowska [67], it was decided to use the same expression system for the generation of stable cell lines.

This work was successful in generating stable cell lines capable of producing the PfFNT mutants G107S, G21E and V196L. Such proteins were tagged with a C-terminal His₁₀-tag. The transformed and selected cell lines expressed the mutant PfFNT two to three weeks after the transformation. As transient transfection typically wears off after a week, it can be concluded that the cells selected had the PfFNT coding sequences stably integrated into their genome. These cell lines were stored in liquid nitrogen for further uses.

C. Hansen experimented with extraction techniques, and has already succeeded in extracting the expressed cells in 1.5% DDM, then purifying them using IMAC. At the time of writing, the usual yield of 0.25 g of HEK cells, harvested at confluence, yielded a final mass of 100 to 200 µg of extracted proteins of interest.

It would be ideal to functionally characterize the HEK 293 cells expressed PffNT proteins before concluding that this work was a complete success. Nevertheless, it is now an established alternative to the cell-free and yeast expression of proteins.

5.1.4.2. Pertinence of the Metformin/AZD3965 selection

This work intended to use selective growth condition of 40 mM Metformin and 0.1 mM AZD3965 to select the HEK cells capable of expressing functional PffNT, thus being able to survive the intracellular lactate accumulation.

However, it was observed that the difference between the PffNT expression levels before and after two to three weeks of selection were sometimes not so significant in some cases (Figures 4.19-21).

The AZD3965 does not inhibit the activity of MCT4 [104], one of the members of the SLC16 family that is usually expressed in glycolytic cells [230]. It happens to be expressed in kidney cells [69], [231]. The HEK293 T-REx cell line used in this work is a highly modified cell line based on kidney cells. They can be considered tumorigenic and display a high genome instability and chaotic gene expression [232]. It is reasonable to assume that the cultures of HEK cells were capable of expressing MCT4, especially during the selective pressure applied by the Metformin/AZD3965 selection process.

Overall, it is unclear if the selection process significantly increased the quantity (or quality) of the HEK cell expressed PffNT. However, the cell lines produced by this selection continued to produce the mutants PffNT, which remains a success.

5.1.4.3. Antibodies non-specific interactions.

The first Western Blots done to determine the expression levels of PffNT mutants expressed by the HEK cells were revealed with primary rabbit antibodies against the PffNT C-terminal extremity, then secondary goat anti-rabbit, HRP-conjugated antibodies. Figure 4.18 showed signals that corresponded specifically to PffNT multimers, suggesting that the HEK 293 cells transformed at Intana Bioscience GmbH were capable to express the PffNT mutants and that

these antibodies were specific. A signal corresponding to the PffNT pentamers is observed above the 120 kDa molecular weights, while the monomers appear between 35 and 25 kDa.

It was therefore concerning that the extracts from HEK 293 cells grown in Kiel displayed many more signals when using the same antibodies, visible in Figures 4.19 to 21. The presence of such contaminants in the HEK 293 cells extract produced in Kiel and their absence in the extracts produced at Intana Bioscience GmbH could be attributed to undetected differences in the culture methods and media. It was also feared that after cultivating the cells using an older stock of blasticidin, the plasmid responsible for the repression of the PffNT gene could have been lost, thus allowing the expression leak of fragmented PffNT sequences. However, a brief test of the blasticidin efficiency suggested that all the stocks used in cultures were capable of maintaining selective conditions. This, however, may explain why the expression of the PffNT G21E mutant also appeared to be expressed in the absence of induction by tetracycline (Figure 4.20 D).

The most important contaminant protein would be the band detected at 20 kDa, which are present in all lanes of the Western Blots, except in the detergent-solubilized lane. An even smaller band, weighing under 20 kDa could only be detected in the lysis wastes. A fainter signal could be observed between the 50 and 35 kDa weights. Lastly, a sharp signal could be observed just under 85 kDa, but this protein appears entirely soluble, as it is only found in the lysate, and the soluble fraction after ultracentrifugation.

These protein bands were not detected in the Western Blots using mouse anti Penta-His and rabbit anti-mouse HRP-conjugated antibodies (beside faint signals under the 20 kDa weights), suggesting that they are not PffNT multimers, aggregates or digestion products. Moreover, these contaminants were observed independently from the protein production induction by the addition of tetracycline.

Why and how would these other proteins be detected in the first place? The most reasonable explanation would be that they are off-targets recognised by the antibodies used during the Western Blot. To check if these antibodies could have recognised endogenous HEK cells proteins, a protein BLAST search of PffNT and of the anti PffNT C-terminus antibody epitope (NND AQMKSLSIERLM) against the human proteome was done (*homo sapiens*, taxid 9606). No match could be found with the default parameters, nor with a reduced detection threshold (down to 2 amino acids to initiate alignment). Perhaps it was the polyclonal goat anti-rabbit secondary antibodies that recognised non-specific targets.

5.2. Investigating the PffNT C-terminus

5.2.1. The role of Tyr285 and Glu289

The Tyr285 and Glu289 of the PffNT C-terminal end did not seem important for the lactate substrate influx activity at physiological pH. Peng *et al.* [53] had hypothesised that these residues played a key role in stabilising the PffNT N-termini. However, mutating Tyr285 to Trp and Glu289 to Gln did not affect the transport capacity of the proteins (Figures 4.33 and 4.34) at relatively neutral pH (pH=6.8). The stabilisation of the N and C-terminal ends do not seem to rely entirely on these residues.

5.2.2. Explaining the previous observations of termini deletion affecting capacity

It appears that the decreased transport capacity at low pH measured by A. Jansen in N-terminal and C-terminal truncated PffNT ($\Delta 1-18_ \Delta 299$, Figure 4.25) were not caused by a truncation of the proteins C-terminus ($\Delta 299$), but rather by the deletion of the first 18 amino acids of the N-terminus. Indeed, Figure 4.29. shows that the deletion of the last 10 amino acids ($\Delta 299$) had no significant effect on the protein transport functionality compared to the wild type. It is worth noting that Lü *et al.* reported, based on the observations of the crystal structure of *Salmonella typhimurium* FocA at pH=4.0, that the N-terminal helix was observed in the way of the transport path, suggesting a pH gating mechanism (at low pH) [233]. This would be consistent with other reports of EcFocA transport being gated by the termini [195]. However, this hypothesis was mainly based on the observation of the crystal structure and was not backed by further experiments [234]. It may have been that the crystal packing of the protein had perturbed the proper conformation of the N-terminal helix. Moreover, the structure of PffNT observed by Lyu *et al.* [52] and Peng *et al.* [53] shows that the PffNT differs from the EcFocA structure, notably by its longer N-terminal helix, followed by an N-terminal chain, tightly stabilized by interactions with its C-terminus (Figure 5.1 B) and the other monomers, suggesting a static state of the N-terminal helix in the wild type protein. Therefore, the decreased of capacity observed in the $\Delta 1-18_ \Delta 299$ at low pHs were likely the result of the N-terminal helix gating the transport path, after the amino acids stabilizing the N-termini were removed.

5.2.3. C-terminal deletion increases transport capacity, but only in acidic pH

Truncating the entire C-terminal end ($\Delta 282$) did not seem to significantly affect PfFNT lactate transport at physiological pH. If the initial experiments showed slower influx and efflux rates (Figure 4.30), it was most likely only because the untagged PfFNT $\Delta 282$ was significantly less expressed. Once expressed to a detectable level after the addition of an N-terminal HA-tag, the PfFNT $\Delta 282$ truncation did not appear to affect the substrate influx at pH=6.8 (Figure 4.34 A), pH-rate dependency (Figure 4.35) or the efflux (Figure 4.36).

These C-terminal deletion did not seem to affect the efflux of substrate either, but the pertinence of the radiolabeled substrate efflux assay can be questioned and is discussed later (5.4.3.).

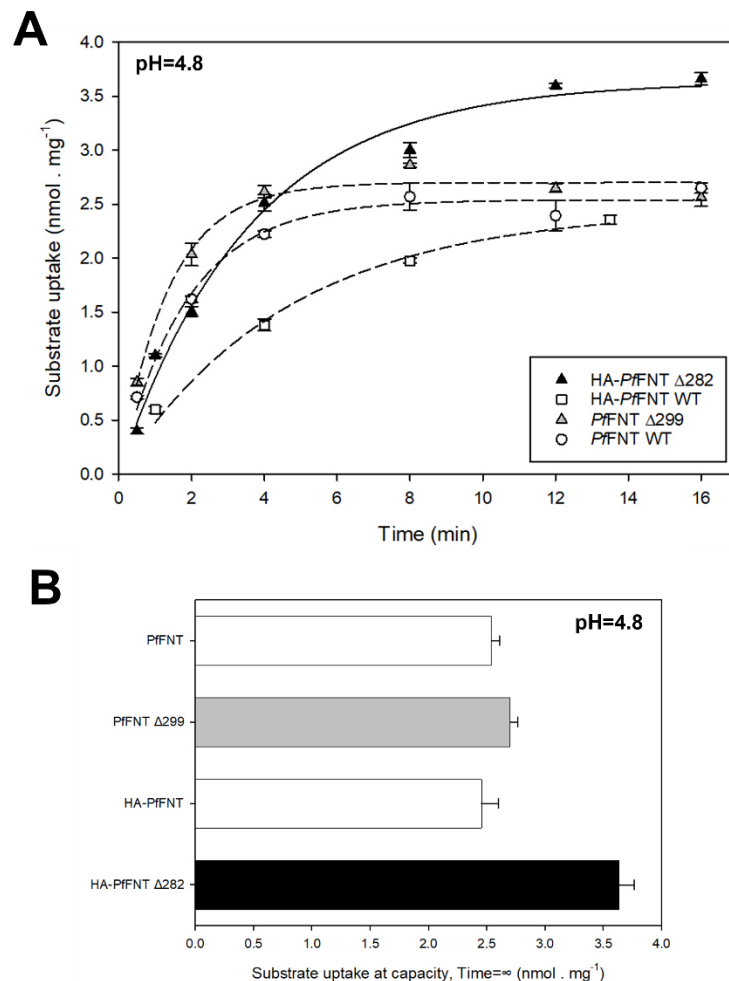


Figure 5. 2: Radiolabeled substrate uptake of the different PfFNT constructs over time (**A**) and at equilibrium (**B**), measured in 50 mM Tris/HEPES pH=4.8, 1 mM L-lactate. Background subtracted. Error bars represent SEM of experimental duplicates. Background subtracted. This figure was generated based on the curves of Figure 4.29 B and 4.34 B.

However, such C-terminal deletion appeared to have an effect on the transport capacity measured in an external pH of 4.8 (Figure 4.34 B and 5.2). It could be observed that the transport capacity approximately reached the same equilibrium between the different constructs, except when fully deleting the C-terminus ($\Delta 282$). In that case, the capacity at transport equilibrium was significantly higher (Student's t-test, $p < 0.026$). Partial deletion of the C-terminus ($\Delta 299$) did not appear to cause such an effect, and no deletion appeared to affect the pH-rate dependency of the protein (Figure 4.29 C and 4.35). The capacity at transport equilibrium was shifted at higher extracellular pH, probably because in these conditions, with higher concentration of substrate, modulations of the transport become more obvious.

Why would transport be higher when the protein is missing a piece? Perhaps the C-terminus, most specifically the 282 to 298 amino acids, are responsible for the generation of a substrate rich microdomain on the cytosolic side of the transporter. Thus, its removal would actually improve substrate influx, as the substrate transported from the extracellular volume could diffuse more readily in the cytosol.

It would still remain unclear if this is caused by an accumulation of protons (potentially caused by the Glu283, 289, 306, Asp294 or the phosphate groups of Ser302 and 304) or lactate (potentially caused by Arg290, 293, 308, Lys292 and 301) (Figure 5.3). Point mutations inverting or neutralizing these residues charges could help identify the nature of this effect. Ideally, replicating this experiment would be necessary to validate the relevance of this effect, as the observation of the HA-PfFNT $\Delta 282$ transport curve at pH=4.8 was measured with a single yeast culture (Figures 4.34 and 5.2).

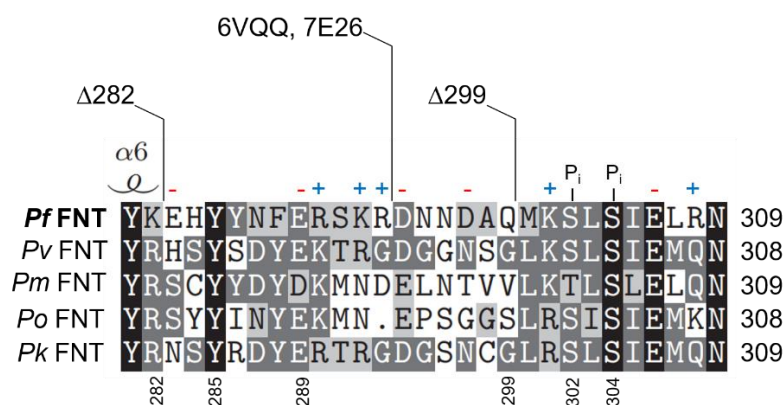


Figure 5. 3: Multiple sequence alignment of the *Plasmodium falciparum* (*Pf*), *vivax* (*Pv*), *malariae* (*Pm*), *ovale* (*Po*) and *knowlesi* (*Pk*) FNT C-termini. Adapted from Walloch *et al.* 2021 [54]. Net charges of the amino acids residues have been marked in red (negative) and blue (positive). Phosphorylated serines are marked with P_i. The positions of the truncations have been labeled as $\Delta 282$ and $\Delta 299$. The numbered amino acids positions correspond to the sequence of PfFNT.

5.3. MCT1 proton antennas

5.3.1. Effects of the Basigin chaperone on transport

5.3.1.1. Intracellular pH of Basigin -MCT1 expressing yeasts

The results of the intracellular pH evolution of carboxyfluorecine-loaded, Basigin-MCT1 expressing yeasts after the addition of 1 mM substrate are displayed in the Figure 4.37. Overall, it shows that the intracellular pH of the carboxyfluorecine-loaded dye remained consistent during the 32 min of assay time. Their overall intracellular pH appeared around 6.3 to 6.5, which is slightly more acidic than the external buffer in which they were kept (pH=6.8).

This experiment had a few drawbacks, notably the long dye loading process. The experimental time between harvesting from the culture and the measure was of 24 to 27 h for the pH-sensitive probe fluorescence assay, while the yeasts harvested for radiolabeled substrate assay are typically measured within 1 to 2 h after harvesting. Nonetheless, the probe loaded yeasts were still alive after the 24 to 27 h period, as they were able to grow on SD AWLH agar plates after the experiment.

Ideally, it would have been relevant to use some of these probes loaded yeasts to perform a radiolabeled substrate assay, to verify that their expressed transporters remained active after the loading time. Moreover, a better adjustment of the parameters of the fluorimeter (most notably by opening the fluorimeter slits) would have yielded measures with less noise.

The slightly acidic intracellular pH measured (approximately 6.3 on average) may have resulted from the longer experimental time compared to the somewhat direct measurement of transport using the radiolabeled substrate assay. These findings are in line with the yeast intracellular pH values reported in the literature [235], [236]. However, the main finding of this experiment was that this intracellular pH remained stable during the 32 min of assay time.

5.3.1.2. pH transport rate dependency of the Basigin – MCT1 fusion constructs

The pH-rate dependency of Basigin – MCT1 lactate transport was measured and compared to the observations of K. Geistlinger [105], [180]. These results were displayed in Figures 4.39 to 4.41.

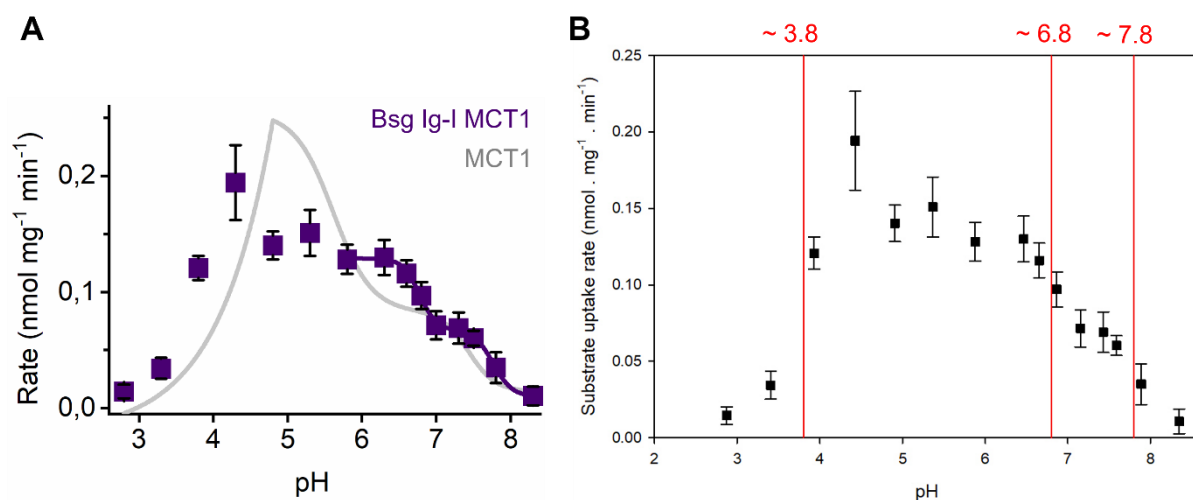


Figure 5. 4: pH transport rate dependency of Basigin IgI - MCT1 fusion constructs (squares). (A) Representation overlaid with the MCT1 pH rate dependency curve measured by K. Geistlinger (adapted from her doctoral thesis [180]). (B) Visible breakout points in the curves were highlighted in red. Measured over 2 min in 1 mM L-Lactate. Background subtracted. Error bars represent SEM of 4 biological replicates.

K. Geistlinger had measured that the breakout points of the MCT1 pH rate dependency corresponded to pH values of 4 ± 0.02 , 5.65 ± 0.05 and 7.43 ± 0.07 [105], [180]. In the presence of the Basigin IgI domain, the corresponding points were found at approximate pH values of 3.8, 6.8 and 7.8 (Figure 5.4). The double sigmoidal curve of the Basigin IgI-MCT1 complex was shifted toward basic pH compared to that of the MCT1. This effect is explained by the presence of the negatively charged patch of amino acids in the surface of the IgI domain. As described by A - L. Köpnick [114], [115], this patch acts as a proton collecting antenna, generating close to the transport path a microdomain where the proton concentration is greater than in the bulk external buffer. Therefore, as the Basigin IgI negatively charged patch is present, the transport rate increase associated with greater concentration of protons will occur at higher pH than the one occurring with the MCT1 alone.

5.3.2. Effects of the Embigin chaperone on transport

A-L. Köpnick and K. Geistlinger have identified that the patches of electrostatically charged residues at the surface of the Basigin IgI domain were responsible for the transporter increase of lactate uptake capacity [114]. The residues of the positively charged patch, especially the Arg 201 and 203, closest from the transport path, are hypothesised to attract lactate anions. Inversely, the residues of the negatively charged patch are thought to act as a proton collecting antenna. By generating microenvironments of greater substrate concentration at the level of the transport path, the Basigin – MCT1 complex is capable of importing a greater concentration of lactate than the general concentration of the bulk would allow. Would the Embigin play a similar role if no such charged patches were observed?

Embigin is typically a chaperone of the MCT2 protein, which has been identified to be linked with lactate efflux out of glycolytic cells. Basigin and Embigin chaperones protein sequence appear to show some identities (Figure 4.42), but the charged amino acids of BSG had little to no similarities with EMB.

Since this protein has not yet been properly expressed in the yeast system used for radiolabeled substrate assay, it was not possible to measure if the co-expression with its chaperone extracellular domains would affect its transport capacity. Previous attempts were made to create a fusion construct of the Embigin with MCT1 in order to measure if the cytosolic Ig domains would also impact the transport capacity similarly to those of Basigin. Such fusion constructs were poorly expressed and their low level of transport activity made any analysis difficult [115]. The alternative method of expression employed in this work consisted in expressing chimeric proteins that would express the Embigin cytosolic domains fused to the Basigin transmembrane domain (itself fused to MCT1). However, these protein fusions appeared to be neither functional nor properly expressed (Figure 4.44).

5.3.3. Carbonic anhydrase

5.3.3.1. CAIV – Basigin - MCT1 fusion constructs

There was no guarantee that fusing the CAIV(p) C-terminus to the Basigin N-terminus would result in either of these protein domains folding correctly. Adding a flexible linker between the two domains was supposed to mitigate this concern. Moreover, if the positive effect of CAIV on transport relied on the proper docking of the CAIV onto the Basigin Ig C2, as described in Figure 4.50. The fusion construct would not be able to display this effect. Despite being expressed by the yeasts (Figure 4.46), the CAIV(p) – Basigin – MCT1 fusion constructs were not capable to transport lactate (Figures 4.47 to 4.49), which means that the expressed proteins were probably misfolded or were not properly addressed to the membrane.

5.3.3.2. Expression and purification of soluble CAIV

In human cells, the CAIV is bound to the membrane using a GPI anchor, a post-translational modification that is ubiquitous in eukaryotes [237]–[240]. *E. coli* are incapable of this post-translational modification, and the artificial addition of synthetic GPI anchor appeared to be a complex topic [240]. Whenever the CAIV would be expressed using BL21 (DE3) cultures or S30 extract (for cell-free expression), they would be expressed without GPI anchor. The only way they would interact with the Basigin – MCT1 fusion construct expressed at the surface of the yeast would be through the interaction described by Forero-Quintero *et al.* [131] (Figure 4.50).

Expressing soluble CAIV using *E. coli* was a good idea on paper, but it led to different issues and ultimately did not lead to a satisfying conclusion.

The IB expression and purification of CAIV from inclusion bodies was not pursued beyond the recovery and purification of proteins in N-lauroylsarcosine. The most critical part of such recovery process is the refolding of the denatured and detergent solubilized proteins, and as no efficient methods to assess the protein folding and functionality, it would not have been immediately possible to test and develop the right refolding method.

Setting up a carbonic anhydrase activity assay would have allowed to determine if the produced and purified proteins were correctly folded. But setting up such assay correctly would have required having some functional carbonic anhydrases as a positive control. In this “chicken or egg?” situation, neither method could be properly established. Buying purified carbonic anhydrase could be the next step to establish an activity assay.

If this project is to be further investigated, a promising alternative would be to attempt co-expression in the host. In yeasts systems, great care should be taken to ensure that the CAIV and the Basigins can interact properly despite interferences of the yeast cell wall. As yeasts are capable of adding GPI anchor to proteins [207], such co-production and interactions should be possible. HEK cells could also prove to be a suitable system for co-expression, but it would require careful consideration of the putative monocarboxylate transporters activity and of the potential expression of endogenous carbonic anhydrase.

5.4. Effects of terminal tags

The expression of the monocarboxylate transporters in yeast fused with N-terminal HA tag and C-terminal His-tag makes a lot of sense from an experimental point of view. These tags permitted to assess if the proteins are properly expressed in yeasts, using commonly available antibodies. If protein bands can be detected at the same size regardless of the antibody used, it meant that the protein was expressed from beginning to end without issue.

Histidine rich tags however, may not be as benign as the HA tags. The pK_a of histidines imidazole side chain is approximately 6. Below a pH of 6, the imidazole ring is bi-protonated and positively charged. Above, it is neutrally charged and capable of being protonated. At physiological pH, in the slightly acidic yeast cytosol or in proton-rich microenvironments, histidines are at the limits where they can act as a donor or an acceptor of protons.

The characterisation of the MCT1 transport done in our lab usually monitor the substrate influx (using the radiolabeled substrate assay), where the contribution of such proton antenna effect should be minimal. It could still shift the value of the transport equilibrium.

While investigating proton antenna, it was critical to assess the impact that the His terminal tags could have on the measure and if possible, remove any of its contribution to transport.

5.4.1. His₁₀ deletion appeared to increase MCT1 transport capacity

The substrate uptake of MCT1 carrying different terminal tags were measured (Figure 4.65). When the last point of measure is ignored, we observe a statistically significant difference between the capacities at transport equilibrium levels (Figure 4.65 B and 4.66 B). However, there are good reasons to exclude this point from the fitting curves, as the fitness of the yeast during the assay appeared to have significantly decreased over time.

It appeared that the presence of the C-terminal His-tag significantly decreased the substrate transport equilibrium (by a factor of about 0.65). Assuming the His-tag acts as a proton collecting antenna in the yeast cytosol, as previously reported [143], such difference could be explained by the MCT1 efflux functionality being improved by the increased availability of protons around the transport path.

A. Jansen had previously established that a substrate uptake signal of $0.23 \pm 0.03 \text{ nmol} \cdot \text{mg}^{-1}$ corresponded to 1 mM of substrate concentration [114], [151]. This value was compared to the transport equilibrium levels of the different MCT1 constructs (using the fitted curves of the 0.5 to 16 min measurements, Figure 4.65 B).

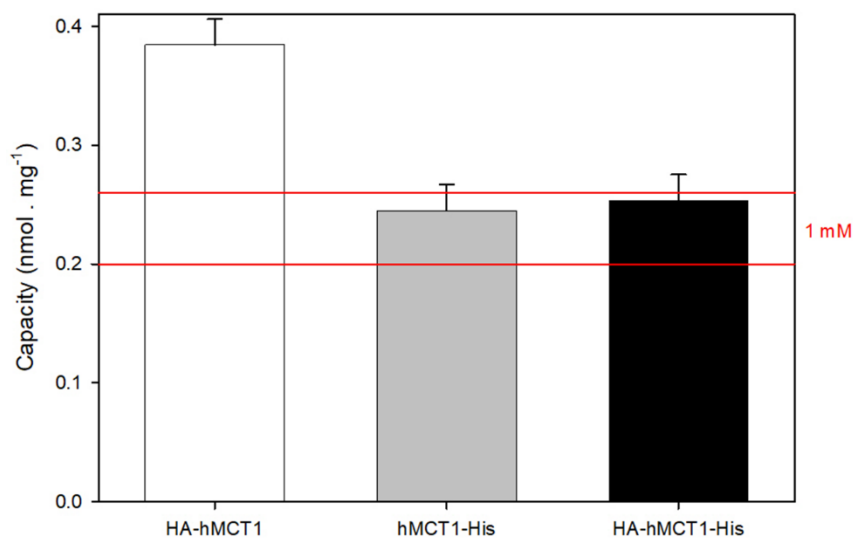


Figure 5. 5: Transport capacity at equilibrium of the MCT1 constructs with different tags. Determined from the fitted curves of the substrate uptake measured in 50 mM Tris/HEPES pH=6.8, 1 mM L-lactate. Error bars represent SEM of experimental triplicate. Background subtracted. The transport curves were fitted between 2 and 16 min. The red lines represent the range of values corresponding to an internal concentration of 1 mM substrate.

Despite different transport rates (Figure 4.65 A and B) caused by their differences in protein expression levels (Figure 4.65 C) the His-tagged proteins appeared to reach the same transport equilibrium. Coincidentally, it corresponds to internal substrate values of 1 mM, which suggests that these transporters reached a perfect equilibrium between the external and internal substrate concentrations. The MCT1 that did not include an His-tag appeared to have transported significantly more substrate than the other constructs. Moreover, it appeared to have transported substrate above the 1 mM external substrate concentration.

If this influx is representative of that of the protein without His₁₀-tag, it means that the presence of the C-terminal His-tag increased the efflux rate, probably by acting as a proton collecting antenna, accumulating substrate close to the transport site.

These measures and hypothesis are in line with the observations of Noor *et al.* [143]. However, it is important to note that these measures were done from a single yeast culture. Ideally, before validating this claim, it would be preferable to increase the amount of biological replicates. It would also have been ideal to plan other experiments to quantify this efflux rate and compare it to the influx. However, the yeast expressing MCT1 are poor candidates to be used in a lactate efflux assay (3.6.2). Since their uptake rate is slower (compared to the PffNT expressing yeasts), having a suitably long loading time to generate a good signal-to-noise ratio and sufficiently long efflux time to reach the transport equilibrium would require an experimental time from 30 min to more than an hour, which would significantly affect the fitness of the yeast and skew the resulting equilibrium state [115].

5.4.2. Effects of the terminal tags on PffNT transport

5.4.2.1. Alterations of the expression levels

The addition of terminal protein tags to the PffNT protein sequence definitely impacted the protein expression in yeast.

The greater levels of proteins expression were also observed (in Western Blots) for the proteins expressed without any terminal tags. The proteins expressed with a single tag had an intermediate level of expression. Those tagged with the N-terminal HA appeared to have a slightly greater expression than those tagged with a C-terminal His₁₀. Finally, the proteins with

both N and C-termini had the lowest expression level of all (excluding the deletion mutants). As such observations were made using the signal intensities observed in Western Blots, no accurate quantitative measures were made.

Moreover, as the expression plasmids included a start codon at the beginning of the N-terminal His-tag and another start codon at the beginning of the PfFNT coding sequence, the yeast ribosomes were able to read two coding frames. This led to the expression of both tagged and untagged proteins (Figure 5.6). If this double expression had to be avoided, the start codon situated between the HA tag and the PfFNT coding sequence should be mutated or better, deleted. For unexplained reason, the expression of MCT1 was not impacted by this same issue.

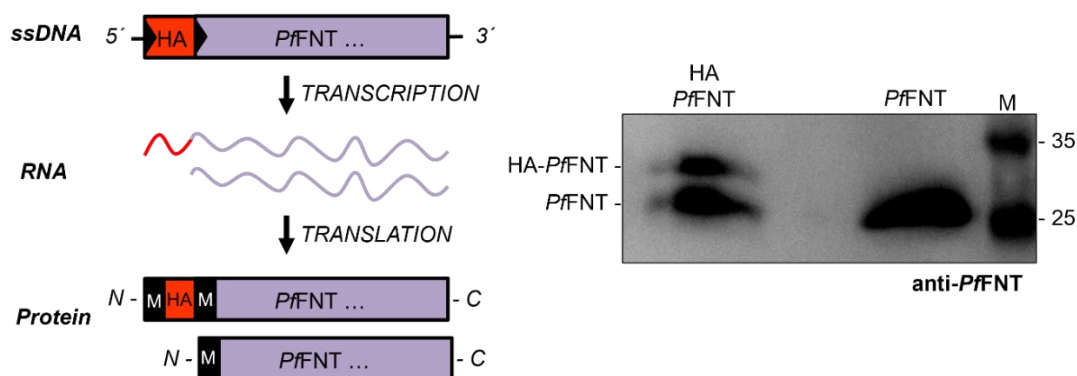


Figure 5. 6: Schematic representation of the double expression of PfFNT and HA-PfFNT caused by the presence of two start codons (black arrows) in the coding sequence (left), resulting in two different protein band visualised in Western blots (right).

5.4.2.2. Effect of the tags on transport.

It can be observed that the presence of terminal tags did not significantly impact the PfFNT substrate uptake rate (Figures 4.67 and 4.68) and transport equilibrium, as the transport curves appeared similar (Figure 4.67 A) despite disparate levels of expressions (Figure 4.67 C) and reached equivalent substrate transport equilibrium (Figure 4.67 B).

When comparing the pH-rate dependency of PfFNT \pm His₁₀ tag (Figure 4.70) it can be noticed that the Gaussian peak of the fitted curves are not centered in the same values. The protein expressed with a single HA tag had a maximal rate at a pH of about 4.2, whereas the HA and His-tagged protein show a maximal rate closer to a pH of 4.8.

Some differences can also be observed in the substrate effluxes. The two measured yeasts systems expressing HA-tagged PfFNT (\pm C-terminal His-tag) showed a similar initial uptake of radiolabeled substrate during the 8 min of loading at an external pH of 4.8. This can be observed in Figure 4.69 A, at $t=0$ min. This initial point is in accord to what was previously observed: the presence of an His-tag does not affect the lactate uptake. However, after measuring the radiolabeled lactate concentration still present in the yeasts after different efflux times, it appears that the internal substrate concentration decreased faster and to a lower level in the yeasts expressing the protein without His-tag. The most significant decrease occurred during the first 30 seconds of the transport. After this point, the decrease rate appears slower and somewhat equivalent to that of the His-tagged proteins. However, the pertinence of the radiolabeled substrate efflux assay is questioned later (5.4.3.).

5.4.2.3. PfFNT pH-rate dependency

The pH-rate dependency of PfFNT had already been measured. Wu *et al.* [51] showed that the rate of PfFNT had a sigmoidal increase to a maximum at $\text{pH}=3.8$ followed by a sharp rate decrease at lower pH. The peak of the resulting curve was centered around a pH of 4.2. Other measures [57], [60] showed the pH-rate dependency of PfFNT behaved as a Gaussian peak, centered on a pH of 4.8. These measures were showing that the PfFNT substrate transport was decreasing as the lactate concentration decreased ($\text{pK}_a=3.86$, equation 3). These previous studies had measured PfFNT expressed in the pDRTXa plasmid, flanked by N - terminal HA and C - terminal His₁₀ tags.

However, measuring the same parameter with yeasts expressing the untagged PfFNT consistently showed that no decrease of the rate was observed at low pH (Figure 4.70, purple curve). On the contrary, the protein transport rate appeared to continuously increase as the external pH got lower. At first, it was assumed that this behavior was the result of the absence of the terminal tags. However, repeating the experiment and producing the same type of curve (with a greater number of external pH conditions) using N - terminally tagged or C - terminally His-tagged proteins showed that these proteins transport rates behaved like a peak (centered around $\text{pH}\approx 4.2$), but that the transport rates increased again once the pH decreased further ($\text{pH}<3.8$) (Figure 4.70 black curves, Figure 4.35).

The difference in the curves levels can be explained by the different levels of expressions: as the pH-rate dependency was calculated using 30 seconds of transport, the initial transport rates depend on the number of proteins expressed by each cell. Western blots were used to determine qualitatively that the most expressed proteins were the untagged PffNT, followed closely by the HA tagged PffNT. The lowest level of expression was the HA and His-tagged PffNT (Figure 4.67 D and 4.68 C). PffNT pH-rate dependency of the same shapes were also measured for the proteins with deleted C - terminal (Figure 4.35).

Considering all these consistent measures, this work can affirm that the pH-transport rate dependency of the PffNT proteins is more than a Gaussian peak. Between alkaline conditions to pH of around 4.4, the transport rate of PffNT appeared to only increase as the pH of the external buffer increased. This increase followed the shape of a sigmoidal (or perhaps double sigmoidal, but the curve resolution is too low to determine it accurately). Past that point, as the pH increases further, the transport rate starts to decrease. Fitting Gaussian peaks to this side of the curves showed maximal rates at a pH of 4.2 for untagged PffNT and HA-PffNT (which is in line with the values of Wu *et al.* [51]) and closer to 4.8 for the HA-PffNT-His₁₀ (which is in line with the values measured by A. Jansen [57], [151] and M. Wiechert [60]). The reason for this shift is unexplained. It could be caused by the presence of the C-terminal His-tag, or by different handling of the yeast during the measures, affecting their fitness. Finally, after the pH of the external buffer decreased further (pH<3.8), the transport rate of the proteins appeared to increase again.

The differences between the pH-rate dependency curves measured previously [51], [57], [60], and in this work (Figures 4.35 and 4.70) may come from a different handling of the yeast suspension during the radiolabeled substrate assay. Previously, cultures of yeasts were harvested, washed in water then the 1× pH buffer, diluted to OD_{600nm}=50 in 1× pH buffer, then stored on ice before measures. In this work, the yeast cultures were handled as described (3.6.4.). This way, the time during which the yeasts are resuspended in buffer is minimized. In the case of low pH (pH<3.8), this step may have increased the survival of the yeast. Moreover, such method also minimizes the yeast suspension OD_{600nm} differences between the different pH points of the curve.

To visualize the evolution of the transport rate depending on pH and substrate concentrations, the pH-rate dependency curve of HA-PffNT-His₁₀ was plotted alongside the concentrations in protons, lactic acid and lactate present in the external buffer of the radiolabeled substrate uptake assays.

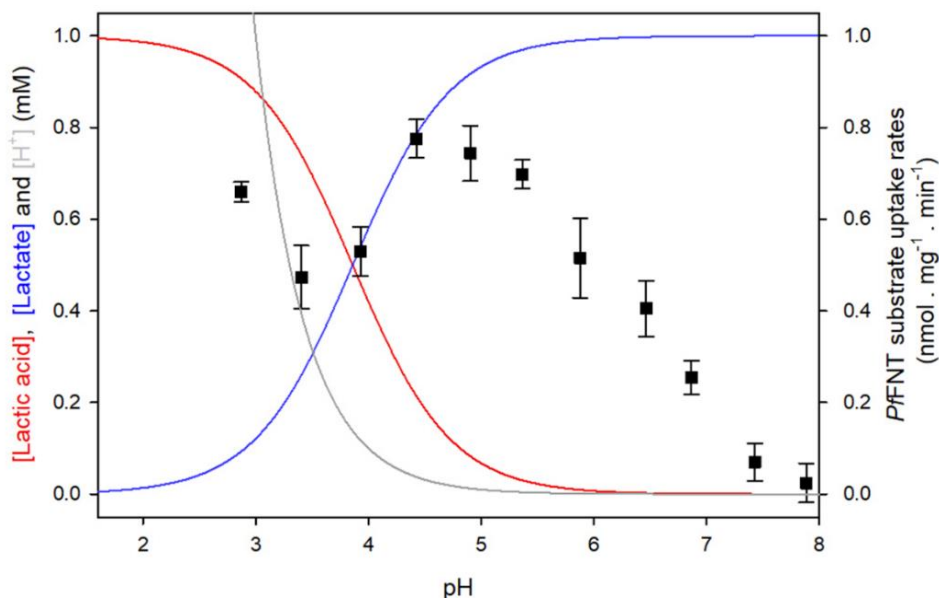


Figure 5. 7: pH-rate dependency curve of HA-PfFNT-His₁₀ (black squares), measured using the radiolabeled substrate assay. Measured over 30 seconds in 1 mM L-Lactate and different pH conditions. Expressed in $\text{nmol} \cdot \text{mg}^{-1} \cdot \text{min}^{-1}$. Background subtracted. Error bars represent SEM of biological triplicates and experimental duplicates. The colored curves represent the concentrations (mM) of protons (grey), lactate (blue) and lactic acid (red) in the extracellular buffer of the assay; expressed in mM.

The first thing to keep in mind when analyzing the Figure 5.7 is that the pH-rate dependency (squared points, right) and the substrates concentrations (curves, left) have different and incompatible scales. It nonetheless allows to observe that the protein transport rate initially decreases as the concentration of lactate decreases (at $\text{pH} < 4.4$), then increases as the proton concentration exponentially increases.

The previously observed peaks were explained by the lactate concentration decreasing in favor of that of lactic acid. The pK_a value at which 50% of the compound exists as lactic acid and 50% as lactate is around a pH of 3.86. As the decrease of the PfFNT substrate concentration is expected to lead to a decrease of the transport rate, and the present findings do not dispute this point.

The interesting aspect of this work's findings is the second increases of the transport rate, in acidic pH conditions in which the lactate concentration decreases and lactic acid concentration increases. This work proposes the hypothesis that PfFNT, that transports lactate and protons under physiological conditions, becomes capable of transporting lactic acid once the external buffer conditions become acidic enough. But what could be the cause of this shift in substrate selectivity?

This work proposes that the PffNT substrate selectivity, normally excluding lactic acid from the transport path is decreased, if not outright cancelled, upon either the accumulation of lactic acid (and the decrease of the usual lactate substrate) or the protonation of key amino acids in the transport path. This shift at $\text{pH} < 3.8$ does not match exactly the protonable amino acids pK_a (Table 5.1), but this may be caused by the lack of water molecules in the hydrophobic transport path, which would increase the local pH as a decrease in solvent accessibility. It would be difficult to estimate what the transport path actual pH would be.

Table 5. 1: pK_a of protonable amino acid side chains (at 25°C)

Amino acid	pK_a of the side chain
Aspartic acid (Asp, D)	3.9
Glutamic acid (Glu, E)	4.3
Histidine (His, H)	6
Arginine (Arg, R)	12.5
Lysine (Lys, K)	10.5

This lactic acid transport is observed at relatively high pH ($\text{pH} < 3.8$). The *Plasmodium* parasite cytosolic pH is reported to be neutral ($\text{pH} = 7.15 \pm 0.07$) [199], these conditions are well out of the physiological range. However, it may hold some relevance as understanding the cause of this effect could identify the amino acids involved in substrate selection and further improve our models of the PffNT transport.

Previous studies identified that the substrate selectivity in FNT occurs at the level of the transport path constriction [61], [241], [242]. These previous findings suggested that the substrates were selected by their negative charge, attracted to a binding site, and a proton-acceptor site for neutralization. For now, the protonation site of PffNT remains elusive [57].

PffNT Lys177 has already been identified to play a role in substrate selectivity [241]. This positively charged residue is one of the few in the hydrophobic vestibule (alongside Lys176) and are expected to attract the negatively charged lactate at the level of the transport path constriction. At the same constriction level stands Glu229, a residue who remains invariable across the five human-pathogenic species of *Plasmodium* [54] and other FNT such as *E. coli* FocA and NirC [241]. Moreover, another residue patch of two lysines in proximity to a negatively charged side chain can be found mirrored on the other side of the PffNT constriction: Lys35, Lys46 and Asp103. This group of residues is as highly conserved than the other.

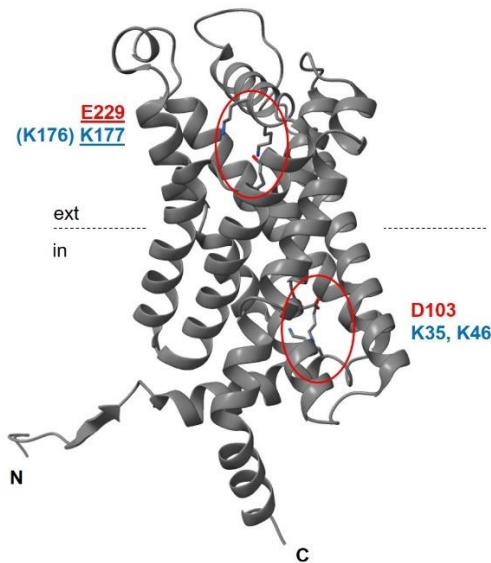


Figure 5. 8: Schematic representation of the PfFNT monomer (PDB#7E26, Chain A). Nitrogen atoms of the lysines are represented in blue, oxygen atoms of the carboxyl groups are represented in red. N and C termini are labeled as such. Assembled using ChimeraX 1.5.

Therefore, this work suggests that the Glu229 may act as the proton donor, harvesting proton from the bulk solution in close proximity to the lactate anions, thus facilitating the protonation of the substrate into lactic acid. The Asp103 may play a similar role during the efflux of lactate. Exposed to low pH, these residues may be protonated and become neutrally charged. No longer capable of protonating the lactate substrate, the PfFNT may eventually allow for the passage of lactic acid as its concentration keep increasing while the pH lowers.

Of course, this hypothesis needs to be experimentally tested: points mutations should be used to mutate Glu229 to Gln or Asp103 to Asn. Radiolabeled substrate uptake assay could be used to determine whenever these points mutation cancelled or impaired lactate influx or efflux.

5.4.3. Pertinence of the radiolabeled substrate efflux assay

In order to assess if intracellular tags or domains affected the transporters activity, the method of the radiolabeled uptake substrate assay had been adjusted to also measure substrate efflux out of the cells after initial loading. However, the experiments of this work suggest that the method used to that end may not have been pertinent.

The radiolabeled substrate uptake assays indirectly measure the efflux as well as the influx rates. Once the substrate influx reaches a plateau, the internal substrate concentration is supposedly maintained at equilibrium by the influx and efflux rate being equivalent, as described in the following equation:

$$k_{influx} = k_{efflux} \quad (38)$$

Where k represents the transport rates.

It had previously been calculated that the intracellular volumes of the yeast were approximately 33 fL [114] and that the yeast pellets contained about 8.6×10^6 cfu/mg [57]. This estimation of the intracellular volume was in line with other values reported in the literature [243]–[245]. It means that for the usual 5.6 mg of yeast pellet used in the radiolabeled substrate assay, the intracellular volume in the yeast is approximately 1.59 μ L. Applied to the context of the substrate efflux assay, this means that once the cells are pelleted after the initial load and the 1 mM lactate solution gets replaced by 100 μ L of buffer, the radiolabeled substrate concentration (transported inside the yeasts) is diluted by about 63. Under these conditions, if the efflux and influx rates were truly equivalent, one would expect the intracellular substrate concentration to decrease by a factor of 63, from 100% of the initial load (at transport equilibrium) to approximately 1.59%. However, most of the efflux curves measured can all be fitted to exponential decays reaching a plateau, decreasing their concentration by 30 to 60 % compared to the initial load. (Figures 4.31, 4.36 and 4.69)

If this experiment was to be considered representative of the transporter behavior, it would mean that the proteins have a lesser capacity for efflux than for influx. This appears inaccurate as MCT1 is known to be bidirectional and PfFNT is mainly involved in the export of the glycolysis metabolic wastes. Then why so much radiolabeled substrate remained inside the cells? K. Geistlinger *et al.* [246] observed that the AQP9 transported the neutrally charged lactic

acid and leads to an accumulation of radiolabeled substrate despite its theoretical role as an equilibrative transporter of neutral substrates. They proposed that the lactic acid dissociates in the intracellular space, buffered by an ion trap. As long as the internal pH of the yeast is greater than the lactic acid pK_a (3.86), the transported lactic acid will dissociate into lactate and proton. The efflux rate and capacity of yeast expressed MCT1 and PfFNT would therefore not only depend on the intracellular lactate concentration, but also the intracellular pH. Moreover, as the accumulation of lactate inside the cells during fermentation and an increase of the intracellular pH causes stress to the yeasts, they have evolved complex mechanisms intended to regulate these parameters [247], [248]. While our yeast strain cannot express the Jen1 and Axd2 genes, the main endogenous lactate transporters, other proteins and metabolic pathways are thought to be involved in the regulation of the lactate concentration [248].

The intracellular space of the yeast is a more complex system than the extracellular buffer, which means that using this efflux assay may not be the most accurate method to accurately measure the substrate efflux rates and capacities.

References

- [1] R. Chaudhry and M. Varacallo, *Biochemistry, Glycolysis*, StatPearls. Treasure Island (FL): StatPearls Publishing, 2023.
- [2] R. A. Robergs, F. Ghiasvand, and D. Parker. Biochemistry of exercise-induced metabolic acidosis. *Am. J. Physiol.-Regul. Integr. Comp. Physiol.*, vol. 287, no. 3, pp. R502–R516, Sep. 2004, doi: 10.1152/ajpregu.00114.2004.
- [3] B. Phipers and J. T. Pierce. Lactate physiology in health and disease. *Contin. Educ. Anaesth. Crit. Care Pain*, vol. 6, no. 3, pp. 128–132, Jun. 2006, doi: 10.1093/bjaceaccp/mkl018.
- [4] M. J. Rogatzki, B. S. Ferguson, M. L. Goodwin, and L. B. Gladden. Lactate is always the end product of glycolysis. *Front. Neurosci.*, vol. 9, Feb. 2015, doi: 10.3389/fnins.2015.00022.
- [5] M. S. Gomez *et al.* Substrate and cofactor specificity and selective inhibition of lactate dehydrogenase from the malarial parasite *P. falciparum*. *Mol. Biochem. Parasitol.*, vol. 90, no. 1, pp. 235–246, Dec. 1997, doi: 10.1016/S0166-6851(97)00140-0.
- [6] M. J. Lambeth and M. J. Kushmerick. A Computational Model for Glycogenolysis in Skeletal Muscle. *Ann. Biomed. Eng.*, vol. 30, no. 6, pp. 808–827, Jun. 2002, doi: 10.1114/1.1492813.
- [7] B. S. Ferguson, M. J. Rogatzki, M. L. Goodwin, D. A. Kane, Z. Rightmire, and L. B. Gladden. Lactate metabolism: historical context, prior misinterpretations, and current understanding. *Eur. J. Appl. Physiol.*, vol. 118, no. 4, pp. 691–728, Apr. 2018, doi: 10.1007/s00421-017-3795-6.
- [8] G. A. Brooks. The Science and Translation of Lactate Shuttle Theory. *Cell Metab.*, vol. 27, no. 4, pp. 757–785, Apr. 2018, doi: 10.1016/j.cmet.2018.03.008.
- [9] D. L. Vander Jagt, L. A. Hunsaker, N. M. Campos, and B. R. Baack. D-Lactate production in erythrocytes infected with *Plasmodium falciparum*. *Mol. Biochem. Parasitol.*, vol. 42, no. 2, pp. 277–284, Sep. 1990, doi: 10.1016/0166-6851(90)90171-H.
- [10] A. R. Fernie, F. Carrari, and L. J. Sweetlove. Respiratory metabolism: glycolysis, the TCA cycle and mitochondrial electron transport. *Curr. Opin. Plant Biol.*, vol. 7, no. 3, pp. 254–261, Jun. 2004, doi: 10.1016/j.pbi.2004.03.007.
- [11] M. Adeva-Andany *et al.* Comprehensive review on lactate metabolism in human health. *Mitochondrion*, vol. 17, pp. 76–100, Jul. 2014, doi: 10.1016/j.mito.2014.05.007.
- [12] C. F. Cori. The glucose-lactic acid cycle and gluconeogenesis. *Curr. Top. Cell. Regul.*, vol. 18, pp. 377–387, 1981.
- [13] G. A. Brooks. Lactate as a fulcrum of metabolism. *Redox Biol.*, vol. 35, p. 101454, Aug. 2020, doi: 10.1016/j.redox.2020.101454.
- [14] P. Makam and R. Matsa. “Big Three” Infectious Diseases: Tuberculosis, Malaria and HIV/AIDS. *Curr. Top. Med. Chem.*, vol. 21, no. 31, pp. 2779–2799, Dec. 2021, doi: 10.2174/1568026621666210916170417.
- [15] World Health Organization, *World malaria report 2022*. Geneva: World Health Organization, 2022. Accessed: May 11, 2023. [Online]. Available: <https://apps.who.int/iris/handle/10665/365169>
- [16] Q. Liu, W. Jing, L. Kang, J. Liu, and M. Liu. Trends of the global, regional and national incidence of malaria in 204 countries from 1990 to 2019 and implications for malaria prevention. *J. Travel Med.*, vol. 28, no. 5, p. taab046, Jul. 2021, doi: 10.1093/jtm/taab046.
- [17] R. Carter and K. N. Mendis. Evolutionary and Historical Aspects of the Burden of Malaria. *Clin. Microbiol. Rev.*, vol. 15, no. 4, pp. 564–594, Oct. 2002, doi: 10.1128/CMR.15.4.564-594.2002.

- [18] World Health Organization, *World malaria report 2017*. Geneva: World Health Organization, 2017. Accessed: May 11, 2023. [Online]. Available: <https://apps.who.int/iris/handle/10665/259492>
- [19] T. N. C. Wells, R. H. Van Huijsduijnen, and W. C. Van Voorhis. Malaria medicines: a glass half full?. *Nat. Rev. Drug Discov.*, vol. 14, no. 6, pp. 424–442, Jun. 2015, doi: 10.1038/nrd4573.
- [20] L. Cui, S. Mharakurwa, D. Ndiaye, P. K. Rathod, and P. J. Rosenthal. Antimalarial Drug Resistance: Literature Review and Activities and Findings of the ICEMR Network. *Am. J. Trop. Med. Hyg.*, vol. 93, no. 3_Suppl, pp. 57–68, Sep. 2015, doi: 10.4269/ajtmh.15-0007.
- [21] K. N. Suh. Malaria. *Can. Med. Assoc. J.*, vol. 170, no. 11, pp. 1693–1702, May 2004, doi: 10.1503/cmaj.1030418.
- [22] C. Crosnier *et al.* Basigin is a receptor essential for erythrocyte invasion by *Plasmodium falciparum*. *Nature*, vol. 480, no. 7378, pp. 534–537, Dec. 2011, doi: 10.1038/nature10606.
- [23] B. Cooke, R. Coppel, and M. Wahlgren. Falciparum Malaria: Sticking up, Standing out and Out-standing. *Parasitol. Today*, vol. 16, no. 10, pp. 416–420, Oct. 2000, doi: 10.1016/S0169-4758(00)01753-1.
- [24] N. J. White. Anaemia and malaria. *Malar. J.*, vol. 17, no. 1, p. 371, Dec. 2018, doi: 10.1186/s12936-018-2509-9.
- [25] C. Nerlich, N. H. Epalle, P. Seick, and E. Beitz. Discovery and Development of Inhibitors of the Plasmodial FNT-Type Lactate Transporter as Novel Antimalarials. *Pharmaceuticals*, vol. 14, no. 11, p. 1191, Nov. 2021, doi: 10.3390/ph1411191.
- [26] M. Kasahara and P. C. Hinkle. Reconstitution and purification of the D-glucose transporter from human erythrocytes. *J. Biol. Chem.*, vol. 252, no. 20, pp. 7384–7390, Oct. 1977.
- [27] M. Mehta, H. M. Sonawat, and S. Sharma. Malaria parasite-infected erythrocytes inhibit glucose utilization in uninfected red cells. *FEBS Lett.*, vol. 579, no. 27, pp. 6151–6158, Nov. 2005, doi: 10.1016/j.febslet.2005.09.088.
- [28] S. A. Desai, D. J. Krogstad, and E. W. McCleskey. A nutrient-permeable channel on the intraerythrocytic malaria parasite. *Nature*, vol. 362, no. 6421, pp. 643–646, Apr. 1993, doi: 10.1038/362643a0.
- [29] J. M. Matz, J. R. Beck, and M. J. Blackman. The parasitophorous vacuole of the blood-stage malaria parasite. *Nat. Rev. Microbiol.*, vol. 18, no. 7, pp. 379–391, Jul. 2020, doi: 10.1038/s41579-019-0321-3.
- [30] C. J. Woodrow, J. I. Penny, and S. Krishna. Intraerythrocytic *Plasmodium falciparum* Expresses a High Affinity Facilitative Hexose Transporter. *J. Biol. Chem.*, vol. 274, no. 11, pp. 7272–7277, Mar. 1999, doi: 10.1074/jbc.274.11.7272.
- [31] D. Ortiz *et al.* Identification of Selective Inhibitors of the *Plasmodium falciparum* Hexose Transporter PfHT by Screening Focused Libraries of Anti-Malarial Compounds. *PLOS ONE*, vol. 10, no. 4, p. e0123598, Apr. 2015, doi: 10.1371/journal.pone.0123598.
- [32] S. Krishna, C. J. Woodrow, R. J. S. Burchmore, K. J. Saliba, and K. Kirk. Hexose Transport in Asexual Stages of *Plasmodium falciparum* and Kinetoplastidae. *Parasitol. Today*, vol. 16, no. 12, pp. 516–521, Dec. 2000, doi: 10.1016/S0169-4758(00)01762-2.
- [33] M. Torrentino-Madamet, J. Desplans, C. Travaille, Y. Jammes, and D. Parzy. Microaerophilic Respiratory Metabolism of *Plasmodium falciparum* Mitochondrion as a Drug Target. *Curr. Mol. Med.*, vol. 10, no. 1, pp. 29–46, Feb. 2010, doi: 10.2174/156652410791065390.
- [34] B. J. Foth, L. M. Stimmler, E. Handman, B. S. Crabb, A. N. Hodder, and G. I. McFadden. The malaria parasite *Plasmodium falciparum* has only one pyruvate dehydrogenase complex, which is located in the apicoplast: The single, plastidic PDH of *Plasmodium falciparum*. *Mol. Microbiol.*, vol. 55, no. 1, pp. 39–53, Nov. 2004, doi: 10.1111/j.1365-2958.2004.04407.x.

- [35] Y. Pei *et al.* *Plasmodium* pyruvate dehydrogenase activity is only essential for the parasite's progression from liver infection to blood infection. *Mol. Microbiol.*, vol. 75, no. 4, pp. 957–971, Feb. 2010, doi: 10.1111/j.1365-2958.2009.07034.x.
- [36] H. Ke *et al.* Genetic Investigation of Tricarboxylic Acid Metabolism during the *Plasmodium falciparum* Life Cycle. *Cell Rep.*, vol. 11, no. 1, pp. 164–174, Apr. 2015, doi: 10.1016/j.celrep.2015.03.011.
- [37] A. B. Vaidya and M. W. Mather. Mitochondrial Evolution and Functions in Malaria Parasites. *Annu. Rev. Microbiol.*, vol. 63, no. 1, pp. 249–267, Oct. 2009, doi: 10.1146/annurev.micro.091208.073424.
- [38] G. G. Van Dooren, L. M. Stimmler, and G. I. McFadden. Metabolic maps and functions of the *Plasmodium* mitochondrion. *FEMS Microbiol. Rev.*, vol. 30, no. 4, pp. 596–630, Jul. 2006, doi: 10.1111/j.1574-6976.2006.00027.x.
- [39] L. W. Scheibel and W. K. Pflaum. Carbohydrate metabolism in *Plasmodium knowlesi*. *Comp. Biochem. Physiol.*, vol. 37, no. 4, pp. 543–553, Dec. 1970, doi: 10.1016/0010-406X(70)90099-X.
- [40] R. W. McKee, R. A. Ormsbee, C. B. Anfinsen, Q. M. Geiman, and E. G. Ball. Studies on malarial parasites: VI. The chemistry and metabolism of normal and parasitized (*P.knowlesi*) monkey blood. *J. Exp. Med.*, vol. 84, no. 6, pp. 569–582, Dec. 1946, doi: 10.1084/jem.84.6.569.
- [41] J. I. MacRae *et al.* Mitochondrial metabolism of sexual and asexual blood stages of the malaria parasite *Plasmodium falciparum*. *BMC Biol.*, vol. 11, no. 1, p. 67, Dec. 2013, doi: 10.1186/1741-7007-11-67.
- [42] H. Ginsburg. Abundant proton pumping in *Plasmodium*, but why?. *Trends Parasitol.*, vol. 18, no. 11, pp. 483–486, Nov. 2002, doi: 10.1016/S1471-4922(02)02350-4.
- [43] H. Ginsburg, M. Krugliak, O. Eidelman, and Z. Ioav Cabantchik. New permeability pathways induced in membranes of *Plasmodium falciparum* infected erythrocytes. *Mol. Biochem. Parasitol.*, vol. 8, no. 2, pp. 177–190, Jun. 1983, doi: 10.1016/0166-6851(83)90008-7.
- [44] P. Wilairatana, W. Mala, M. Kotepui, and K. U. Kotepui. Alteration of Blood Lactate Levels in Severe Falciparum Malaria: A Systematic Review and Meta-Analysis. *Biology*, vol. 10, no. 11, p. 1085, Oct. 2021, doi: 10.3390/biology10111085.
- [45] E. F. Roth, C. Raventos-Suarez, M. Perkins, and R. L. Nagel. Glutathione stability and oxidative stress in *P. falciparum* infection in vitro: Responses of normal and G6PD deficient cells. *Biochem. Biophys. Res. Commun.*, vol. 109, no. 2, pp. 355–362, Nov. 1982, doi: 10.1016/0006-291X(82)91728-4.
- [46] E. F. Roth, M. C. Calvin, I. Max-Audit, J. Rosa, and R. Rosa. The enzymes of the glycolytic pathway in erythrocytes infected with *Plasmodium falciparum* malaria parasites. *Blood*, vol. 72, no. 6, pp. 1922–1925, Dec. 1988.
- [47] J. Kanaani and H. Ginsburg. Transport of lactate in *Plasmodium falciparum*-infected human erythrocytes. *J. Cell. Physiol.*, vol. 149, no. 3, pp. 469–476, Dec. 1991, doi: 10.1002/jcp.1041490316.
- [48] S. L. Cranmer, A. R. Conant, W. E. Gutteridge, and A. P. Halestrap. Characterization of the Enhanced Transport of L- and D-Lactate into Human Red Blood Cells Infected with *Plasmodium falciparum* Suggests the Presence of a Novel Saturable Lactate Proton Cotransporter. *J. Biol. Chem.*, vol. 270, no. 25, pp. 15045–15052, Jun. 1995, doi: 10.1074/jbc.270.25.15045.
- [49] J. L. Elliott, K. J. Saliba, and K. Kirk. Transport of lactate and pyruvate in the intraerythrocytic malaria parasite, *Plasmodium falciparum*. *Biochem. J.*, vol. 355, no. 3, pp. 733–739, May 2001, doi: 10.1042/bj3550733.

- [50] R. V. Marchetti, A. M. Lehane, S. H. Shafik, M. Winterberg, R. E. Martin, and K. Kirk. A lactate and formate transporter in the intraerythrocytic malaria parasite, *Plasmodium falciparum*. *Nat. Commun.*, vol. 6, no. 1, p. 6721, Mar. 2015, doi: 10.1038/ncomms7721.
- [51] B. Wu *et al.* Identity of a *Plasmodium* lactate/H⁺ symporter structurally unrelated to human transporters. *Nat. Commun.*, vol. 6, no. 1, p. 6284, Feb. 2015, doi: 10.1038/ncomms7284.
- [52] M. Lyu, C. Su, J. W. Kazura, and E. W. Yu. Structural basis of transport and inhibition of the *Plasmodium falciparum* transporter PffNT. *EMBO Rep.*, vol. 22, no. 12, Dec. 2021, doi: 10.15252/embr.202153596.
- [53] X. Peng *et al.* Structural characterization of the *Plasmodium falciparum* lactate transporter PffNT alone and in complex with antimalarial compound MMV007839 reveals its inhibition mechanism. *PLOS Biol.*, vol. 19, no. 9, p. e3001386, Sep. 2021, doi: 10.1371/journal.pbio.3001386.
- [54] P. Walloch, C. Hansen, T. Priegann, D. Schade, and E. Beitz. Pentafluoro-3-hydroxypent-2-en-1-ones Potently Inhibit FNT-Type Lactate Transporters from all Five Human-Pathogenic *Plasmodium* Species. *ChemMedChem*, vol. 16, no. 8, pp. 1283–1289, Apr. 2021, doi: 10.1002/cmdc.202000952.
- [55] W. Lü, J. Du, N. J. Schwarzer, T. Wacker, S. L. A. Andrade, and O. Einsle. The formate/nitrite transporter family of anion channels. *bchm*, vol. 394, no. 6, pp. 715–727, Jun. 2013, doi: 10.1515/hsz-2012-0339.
- [56] Y. Wang *et al.* Structure of the formate transporter FocA reveals a pentameric aquaporin-like channel. *Nature*, vol. 462, no. 7272, pp. 467–472, Nov. 2009, doi: 10.1038/nature08610.
- [57] A. Bader and E. Beitz. Transmembrane Facilitation of Lactate/H⁺ Instead of Lactic Acid Is Not a Question of Semantics but of Cell Viability. *Membranes*, vol. 10, no. 9, p. 236, Sep. 2020, doi: 10.3390/membranes10090236.
- [58] F. Helmstetter, P. Arnold, B. Höger, L. M. Petersen, and E. Beitz. Formate–nitrite transporters carrying nonprotonatable amide amino acids instead of a central histidine maintain pH-dependent transport. *J. Biol. Chem.*, vol. 294, no. 2, pp. 623–631, Jan. 2019, doi: 10.1074/jbc.RA118.006340.
- [59] M. Wiechert and E. Beitz. Formate–nitrite transporters: Monoacids ride the dielectric slide. *Channels*, vol. 11, no. 5, pp. 365–367, Sep. 2017, doi: 10.1080/19336950.2017.1329999.
- [60] M. Wiechert and E. Beitz. Mechanism of formate–nitrite transporters by dielectric shift of substrate acidity. *EMBO J.*, vol. 36, no. 7, pp. 949–958, Apr. 2017, doi: 10.15252/embj.201695776.
- [61] J. D. R. Schmidt and E. Beitz. Mutational widening of constrictions in a formate–nitrite/H⁺ transporter enables aquaporin-like water permeability and proton conductance. *J. Biol. Chem.*, vol. 298, no. 1, p. 101513, Jan. 2022, doi: 10.1016/j.jbc.2021.101513.
- [62] N. H. Epalle and E. Beitz. Local Attraction of Substrates and Co-Substrates Enhances Weak Acid and Base Transmembrane Transport. *Biomolecules*, vol. 12, no. 12, p. 1794, Nov. 2022, doi: 10.3390/biom12121794.
- [63] T. Spangenberg, J. N. Burrows, P. Kowalczyk, S. McDonald, T. N. C. Wells, and P. Willis. The Open Access Malaria Box: A Drug Discovery Catalyst for Neglected Diseases. *PLoS ONE*, vol. 8, no. 6, p. e62906, Jun. 2013, doi: 10.1371/journal.pone.0062906.
- [64] A. Gollmack *et al.* Substrate-analogous inhibitors exert antimalarial action by targeting the *Plasmodium* lactate transporter PffNT at nanomolar scale. *PLOS Pathog.*, vol. 13, no. 2, p. e1006172, Feb. 2017, doi: 10.1371/journal.ppat.1006172.
- [65] S. V. Hapuarachchi *et al.* The Malaria Parasite’s Lactate Transporter PffNT Is the Target of Antiplasmodial Compounds Identified in Whole Cell Phenotypic Screens. *PLOS Pathog.*, vol. 13, no. 2, p. e1006180, Feb. 2017, doi: 10.1371/journal.ppat.1006180.

- [66] P. Walloch, B. Henke, S. Häuer, B. Bergmann, T. Spielmann, and E. Beitz. Introduction of Scaffold Nitrogen Atoms Renders Inhibitors of the Malarial L -Lactate Transporter, PfFNT, Effective against the Gly107Ser Resistance Mutation. *J. Med. Chem.*, vol. 63, no. 17, pp. 9731–9741, Sep. 2020, doi: 10.1021/acs.jmedchem.0c00852.
- [67] I. Jakóbowska *et al.* Fluorescence Cross-Correlation Spectroscopy Yields True Affinity and Binding Kinetics of *Plasmodium* Lactate Transport Inhibitors. *Pharmaceuticals*, vol. 14, no. 8, p. 757, Aug. 2021, doi: 10.3390/ph14080757.
- [68] A. P. Halestrap and D. Meredith. The SLC16 gene family—from monocarboxylate transporters (MCTs) to aromatic amino acid transporters and beyond. *Pflugers Arch. Eur. J. Physiol.*, vol. 447, no. 5, pp. 619–628, Feb. 2004, doi: 10.1007/s00424-003-1067-2.
- [69] M. A. Felmler, R. S. Jones, V. Rodriguez-Cruz, K. E. Follman, and M. E. Morris. Monocarboxylate Transporters (SLC16): Function, Regulation, and Role in Health and Disease. *Pharmacol. Rev.*, vol. 72, no. 2, pp. 466–485, Apr. 2020, doi: 10.1124/pr.119.018762.
- [70] A. P. Halestrap. Monocarboxylic Acid Transport. in *Comprehensive Physiology*, R. Terjung, Ed., 1st ed. Wiley, 2013, pp. 1611–1643. doi: 10.1002/cphy.c130008.
- [71] S. Bröer, H.-P. Schneider, A. Bröer, B. Rahman, B. Hamprecht, and J. W. Deitmer. Characterization of the monocarboxylate transporter 1 expressed in *Xenopus laevis* oocytes by changes in cytosolic pH. *Biochem. J.*, vol. 333, no. 1, pp. 167–174, Jul. 1998, doi: 10.1042/bj3330167.
- [72] S. Bröer *et al.* Comparison of Lactate Transport in Astroglial Cells and Monocarboxylate Transporter 1 (MCT 1) Expressing *Xenopus laevis* Oocytes. *J. Biol. Chem.*, vol. 272, no. 48, pp. 30096–30102, Nov. 1997, doi: 10.1074/jbc.272.48.30096.
- [73] C. K. Garcia, M. S. Brown, R. K. Pathak, and J. L. Goldstein. cDNA Cloning of MCT2, a Second Monocarboxylate Transporter Expressed in Different Cells than MCT1. *J. Biol. Chem.*, vol. 270, no. 4, pp. 1843–1849, Jan. 1995, doi: 10.1074/jbc.270.4.1843.
- [74] S. Bröer, A. Bröer, H.-P. Schneider, C. Stegen, A. P. Halestrap, and J. W. Deitmer. Characterization of the high-affinity monocarboxylate transporter MCT2 in *Xenopus laevis* oocytes. *Biochem. J.*, vol. 341, no. 3, pp. 529–535, Aug. 1999, doi: 10.1042/bj3410529.
- [75] E. F. Grollman, N. J. Philp, P. McPhie, R. D. Ward, and B. Sauer. Determination of Transport Kinetics of Chick MCT3 Monocarboxylate Transporter from Retinal Pigment Epithelium by Expression in Genetically Modified Yeast. *Biochemistry*, vol. 39, no. 31, pp. 9351–9357, Aug. 2000, doi: 10.1021/bi000464+.
- [76] K. S. Dimmer, B. Friedrich, F. Lang, J. W. Deitmer, and S. Bröer. The low-affinity monocarboxylate transporter MCT4 is adapted to the export of lactate in highly glycolytic cells. *Biochem. J.*, vol. 350 Pt 1, no. Pt 1, pp. 219–227, Aug. 2000.
- [77] A. P. Halestrap. The monocarboxylate transporter family—Structure and functional characterization. *IUBMB Life*, vol. 64, no. 1, pp. 1–9, Jan. 2012, doi: 10.1002/iub.573.
- [78] A. P. Halestrap and N. T. Price. The proton-linked monocarboxylate transporter (MCT) family: structure, function and regulation. *Biochem. J.*, vol. 343 Pt 2, no. Pt 2, pp. 281–299, Oct. 1999.
- [79] A. P. Halestrap. The SLC16 gene family – Structure, role and regulation in health and disease. *Mol. Aspects Med.*, vol. 34, no. 2–3, pp. 337–349, Apr. 2013, doi: 10.1016/j.mam.2012.05.003.
- [80] L. Pellerin and P. J. Magistretti. Glutamate uptake into astrocytes stimulates aerobic glycolysis: a mechanism coupling neuronal activity to glucose utilization.. *Proc. Natl. Acad. Sci.*, vol. 91, no. 22, pp. 10625–10629, Oct. 1994, doi: 10.1073/pnas.91.22.10625.
- [81] P. G. Bittar, Y. Charnay, L. Pellerin, C. Bouras, and P. J. Magistretti. Selective Distribution of Lactate Dehydrogenase Isoenzymes in Neurons and Astrocytes of Human Brain. *J. Cereb. Blood Flow Metab.*, vol. 16, no. 6, pp. 1079–1089, Nov. 1996, doi: 10.1097/00004647-199611000-00001.

- [82] L. Pellerin and P. J. Magistretti. Food for Thought: Challenging the Dogmas. *J. Cereb. Blood Flow Metab.*, vol. 23, no. 11, pp. 1282–1286, Nov. 2003, doi: 10.1097/01.WCB.0000096064.12129.3D.
- [83] A.-K. Bouzier-Sore, M. Merle, P. J. Magistretti, and L. Pellerin. Feeding active neurons: (re)emergence of a nursing role for astrocytes. *J. Physiol.-Paris*, vol. 96, no. 3–4, pp. 273–282, May 2002, doi: 10.1016/S0928-4257(02)00016-5.
- [84] A.-K. Bouzier-Sore, P. Voisin, V. Bouchaud, E. Bezancon, J.-M. Franconi, and L. Pellerin. Competition between glucose and lactate as oxidative energy substrates in both neurons and astrocytes: a comparative NMR study. *Eur. J. Neurosci.*, vol. 24, no. 6, pp. 1687–1694, Sep. 2006, doi: 10.1111/j.1460-9568.2006.05056.x.
- [85] L. K. Bak and A. B. Walls. CrossTalk opposing view: lack of evidence supporting an astrocyte-to-neuron lactate shuttle coupling neuronal activity to glucose utilisation in the brain: CrossTalk. *J. Physiol.*, vol. 596, no. 3, pp. 351–353, Feb. 2018, doi: 10.1113/JP274945.
- [86] D. Roosterman, G. S. Cottrell, 1 Ruhr Universität Bochum, LWL-Hospital of Psychiatry, Bochum, Germany, and 2 School of Pharmacy, University of Reading, Reading, RG6 6AP, UK. Astrocytes and neurons communicate via a monocarboxylic acid shuttle. *AIMS Neurosci.*, vol. 7, no. 2, pp. 94–106, 2020, doi: 10.3934/Neuroscience.2020007.
- [87] L. F. Barros, I. Ruminot, A. San Martín, R. Lerchundi, I. Fernández-Moncada, and F. Baeza-Lehnert. Aerobic Glycolysis in the Brain: Warburg and Crabtree Contra Pasteur. *Neurochem. Res.*, vol. 46, no. 1, pp. 15–22, Jan. 2021, doi: 10.1007/s11064-020-02964-w.
- [88] C. V. Dang and G. L. Semenza. Oncogenic alterations of metabolism. *Trends Biochem. Sci.*, vol. 24, no. 2, pp. 68–72, Feb. 1999, doi: 10.1016/S0968-0004(98)01344-9.
- [89] O. Warburg. The Metabolism of Carcinoma Cells. *J. Cancer Res.*, vol. 9, no. 1, pp. 148–163, Mar. 1925, doi: 10.1158/jcr.1925.148.
- [90] O. Warburg, F. Wind, and E. Negelein. The metabolism of tumors in the body. *J. Gen. Physiol.*, vol. 8, no. 6, pp. 519–530, Mar. 1927, doi: 10.1085/jgp.8.6.519.
- [91] K. G. De La Cruz-López, L. J. Castro-Muñoz, D. O. Reyes-Hernández, A. García-Carrancá, and J. Manzo-Merino. Lactate in the Regulation of Tumor Microenvironment and Therapeutic Approaches. *Front. Oncol.*, vol. 9, p. 1143, Nov. 2019, doi: 10.3389/fonc.2019.01143.
- [92] S. Y. C. Choi, C. C. Collins, P. W. Gout, and Y. Wang. Cancer-generated lactic acid: a regulatory, immunosuppressive metabolite?. *J. Pathol.*, vol. 230, no. 4, pp. 350–355, Aug. 2013, doi: 10.1002/path.4218.
- [93] P. Sonveaux *et al.* Targeting the Lactate Transporter MCT1 in Endothelial Cells Inhibits Lactate-Induced HIF-1 Activation and Tumor Angiogenesis. *PLoS ONE*, vol. 7, no. 3, p. e33418, Mar. 2012, doi: 10.1371/journal.pone.0033418.
- [94] P. Sonveaux *et al.* Targeting lactate-fueled respiration selectively kills hypoxic tumor cells in mice. *J. Clin. Invest.*, p. JCI36843, Nov. 2008, doi: 10.1172/JCI36843.
- [95] S. Hui *et al.* Glucose feeds the TCA cycle via circulating lactate. *Nature*, vol. 551, no. 7678, pp. 115–118, Nov. 2017, doi: 10.1038/nature24057.
- [96] S. Pavlides *et al.* The reverse Warburg effect: Aerobic glycolysis in cancer associated fibroblasts and the tumor stroma. *Cell Cycle*, vol. 8, no. 23, pp. 3984–4001, Dec. 2009, doi: 10.4161/cc.8.23.10238.
- [97] S. Benny, R. Mishra, M. K. Manojkumar, and T. P. Aneesh. From Warburg effect to Reverse Warburg effect; the new horizons of anti-cancer therapy. *Med. Hypotheses*, vol. 144, p. 110216, Nov. 2020, doi: 10.1016/j.mehy.2020.110216.
- [98] G. A. Brooks. Cell-cell and intracellular lactate shuttles: Lactate: Darth Vader or Jedi Knight of exercise physiology?. *J. Physiol.*, vol. 587, no. 23, pp. 5591–5600, Dec. 2009, doi: 10.1113/jphysiol.2009.178350.

- [99] T. Hashimoto, R. Hussien, and G. A. Brooks. Colocalization of MCT1, CD147, and LDH in mitochondrial inner membrane of L6 muscle cells: evidence of a mitochondrial lactate oxidation complex. *Am. J. Physiol.-Endocrinol. Metab.*, vol. 290, no. 6, pp. E1237–E1244, Jun. 2006, doi: 10.1152/ajpendo.00594.2005.
- [100] G. A. Brooks, M. A. Brown, C. E. Butz, J. P. Sicurello, and H. Dubouchaud. Cardiac and skeletal muscle mitochondria have a monocarboxylate transporter MCT1. *J. Appl. Physiol.*, vol. 87, no. 5, pp. 1713–1718, Nov. 1999, doi: 10.1152/jappl.1999.87.5.1713.
- [101] Y.-J. Chen *et al.* Lactate metabolism is associated with mammalian mitochondria. *Nat. Chem. Biol.*, vol. 12, no. 11, pp. 937–943, Nov. 2016, doi: 10.1038/nchembio.2172.
- [102] K. Sahlin, M. Fernström, M. Svensson, and M. Tonkonogi. No evidence of an intracellular lactate shuttle in rat skeletal muscle. *J. Physiol.*, vol. 541, no. 2, pp. 569–574, Jun. 2002, doi: 10.1113/jphysiol.2002.016683.
- [103] P. D. Bosshart, D. Kalbermatter, S. Bonetti, and D. Fotiadis. Mechanistic basis of L-lactate transport in the SLC16 solute carrier family. *Nat. Commun.*, vol. 10, no. 1, p. 2649, Jun. 2019, doi: 10.1038/s41467-019-10566-6.
- [104] N. Wang *et al.* Structural basis of human monocarboxylate transporter 1 inhibition by anti-cancer drug candidates. *Cell*, vol. 184, no. 2, pp. 370–383.e13, Jan. 2021, doi: 10.1016/j.cell.2020.11.043.
- [105] K. Geistlinger, J. D. R. Schmidt, and E. Beitz. Human monocarboxylate transporters accept and relay protons via the bound substrate for selectivity and activity at physiological pH. *PNAS Nexus*, vol. 2, no. 2, p. pgad007, Feb. 2023, doi: 10.1093/pnasnexus/pgad007.
- [106] P. Kirk, M. C. Wilson, C. Heddle, M. H. Brown, A. N. Barclay, and A. P. Halestrap. CD147 is tightly associated with lactate transporters MCT1 and MCT4 and facilitates their cell surface expression. *EMBO J.*, vol. 19, no. 15, pp. 3896–3904, Aug. 2000, doi: 10.1093/emboj/19.15.3896.
- [107] M. C. Wilson, D. Meredith, J. E. M. Fox, C. Manoharan, A. J. Davies, and A. P. Halestrap. Basigin (CD147) Is the Target for Organomercurial Inhibition of Monocarboxylate Transporter Isoforms 1 and 4. *J. Biol. Chem.*, vol. 280, no. 29, pp. 27213–27221, Jul. 2005, doi: 10.1074/jbc.M411950200.
- [108] C. Biswas *et al.* The human tumor cell-derived collagenase stimulatory factor (renamed EMMPRIN) is a member of the immunoglobulin superfamily. *Cancer Res.*, vol. 55, no. 2, pp. 434–439, Jan. 1995.
- [109] R.-P. Huang, M. Ozawa, K. Kadomatsu, and T. Muramatsu. Embigin, a Member of the Immunoglobulin Superfamily Expressed in Embryonic Cells, Enhances Cell-Substratum Adhesion. *Dev. Biol.*, vol. 155, no. 2, pp. 307–314, Feb. 1993, doi: 10.1006/dbio.1993.1030.
- [110] R. C. Poole and A. P. Halestrap. Interaction of the Erythrocyte Lactate Transporter (Monocarboxylate Transporter 1) with an Integral 70-kDa Membrane Glycoprotein of the Immunoglobulin Superfamily. *J. Biol. Chem.*, vol. 272, no. 23, pp. 14624–14628, Jun. 1997, doi: 10.1074/jbc.272.23.14624.
- [111] A. A. Deora, N. Philp, J. Hu, D. Bok, and E. Rodriguez-Boulan. Mechanisms regulating tissue-specific polarity of monocarboxylate transporters and their chaperone CD147 in kidney and retinal epithelia. *Proc. Natl. Acad. Sci.*, vol. 102, no. 45, pp. 16245–16250, Nov. 2005, doi: 10.1073/pnas.0504419102.
- [112] M. J. Ovens, C. Manoharan, M. C. Wilson, C. M. Murray, and A. P. Halestrap. The inhibition of monocarboxylate transporter 2 (MCT2) by AR-C155858 is modulated by the associated ancillary protein. *Biochem. J.*, vol. 431, no. 2, pp. 217–225, Oct. 2010, doi: 10.1042/BJ20100890.
- [113] C. Manoharan *et al.* The role of charged residues in the transmembrane helices of monocarboxylate transporter 1 and its ancillary protein Basigin in determining plasma

- membrane expression and catalytic activity. *Mol. Membr. Biol.*, vol. 23, no. 6, pp. 486–498, Jan. 2006, doi: 10.1080/09687860600841967.
- [114] A.-L. Köpnick, A. Jansen, K. Geistlinger, N. H. Epalle, and E. Beitz. Basigin drives intracellular accumulation of l-lactate by harvesting protons and substrate anions. *PLOS ONE*, vol. 16, no. 3, p. e0249110, Mar. 2021, doi: 10.1371/journal.pone.0249110.
- [115] A.-L. Köpnick. Fusion of human monocarboxylate transporter 1 with Basigin and expression in *S. cerevisiae*: Is Basigin more than a chaperone?. 2021. [Online]. Available: https://macau.uni-kiel.de/receive/macau_mods_00001362
- [116] C. Martínez. General requirement for harvesting antennae at Ca²⁺ and H⁺ channels and transporters. *Front. Neuroenergetics*, 2010, doi: 10.3389/fnene.2010.00027.
- [117] M. J. Ovens, A. J. Davies, M. C. Wilson, C. M. Murray, and A. P. Halestrap. AR-C155858 is a potent inhibitor of monocarboxylate transporters MCT1 and MCT2 that binds to an intracellular site involving transmembrane helices 7–10. *Biochem. J.*, vol. 425, no. 3, pp. 523–530, Feb. 2010, doi: 10.1042/BJ20091515.
- [118] L. F. Barros and C. Martínez. An Enquiry into Metabolite Domains. *Biophys. J.*, vol. 92, no. 11, pp. 3878–3884, Jun. 2007, doi: 10.1529/biophysj.106.100925.
- [119] V. Sacks, Y. Marantz, A. Aagaard, S. Checover, E. Nachliel, and M. Gutman. The dynamic feature of the proton collecting antenna of a protein surface. *Biochim. Biophys. Acta BBA - Bioenerg.*, vol. 1365, no. 1–2, pp. 232–240, Jun. 1998, doi: 10.1016/S0005-2728(98)00073-5.
- [120] A. Shinobu, G. J. Palm, A. J. Schierbeek, and N. Agmon. Visualizing Proton Antenna in a High-Resolution Green Fluorescent Protein Structure. *J. Am. Chem. Soc.*, vol. 132, no. 32, pp. 11093–11102, Aug. 2010, doi: 10.1021/ja1010652.
- [121] A.-N. Bondar. Proton-Binding Motifs of Membrane-Bound Proteins: From Bacteriorhodopsin to Spike Protein S. *Front. Chem.*, vol. 9, p. 685761, May 2021, doi: 10.3389/fchem.2021.685761.
- [122] A. Shinobu and N. Agmon. Mapping Proton Wires in Proteins: Carbonic Anhydrase and GFP Chromophore Biosynthesis. *J. Phys. Chem. A*, vol. 113, no. 26, pp. 7253–7266, Jul. 2009, doi: 10.1021/jp8102047.
- [123] A. Shinobu and N. Agmon. Proton Wire Dynamics in the Green Fluorescent Protein. *J. Chem. Theory Comput.*, vol. 13, no. 1, pp. 353–369, Jan. 2017, doi: 10.1021/acs.jctc.6b00939.
- [124] A.-N. Bondar. Graphs of Hydrogen-Bond Networks to Dissect Protein Conformational Dynamics. *J. Phys. Chem. B*, vol. 126, no. 22, pp. 3973–3984, Jun. 2022, doi: 10.1021/acs.jpcc.2c00200.
- [125] J. Heberle, J. Riesle, G. Thiedemann, D. Oesterheld, and N. A. Dencher. Proton migration along the membrane surface and retarded surface to bulk transfer. *Nature*, vol. 370, no. 6488, pp. 379–382, Aug. 1994, doi: 10.1038/370379a0.
- [126] M. Brändén, T. Sandén, P. Brzezinski, and J. Widengren. Localized proton microcircuits at the biological membrane–water interface. *Proc. Natl. Acad. Sci.*, vol. 103, no. 52, pp. 19766–19770, Dec. 2006, doi: 10.1073/pnas.0605909103.
- [127] M. Gutman and E. Nachliel. Time-resolved dynamics of proton transfer in proteinous systems. *Annu. Rev. Phys. Chem.*, vol. 48, no. 1, pp. 329–356, Oct. 1997, doi: 10.1146/annurev.physchem.48.1.329.
- [128] M. G. Wolf, H. Grubmüller, and G. Groenhof. Anomalous Surface Diffusion of Protons on Lipid Membranes. *Biophys. J.*, vol. 107, no. 1, pp. 76–87, Jul. 2014, doi: 10.1016/j.bpj.2014.04.062.
- [129] E. Flenner, J. Das, M. C. Rheinstädter, and I. Kosztin. Subdiffusion and lateral diffusion coefficient of lipid atoms and molecules in phospholipid bilayers. *Phys. Rev. E*, vol. 79, no. 1, p. 011907, Jan. 2009, doi: 10.1103/PhysRevE.79.011907.

- [130] L. Xu, L. N. Öjemyr, J. Bergstrand, P. Brzezinski, and J. Widengren. Protonation Dynamics on Lipid Nanodiscs: Influence of the Membrane Surface Area and External Buffers. *Biophys. J.*, vol. 110, no. 9, pp. 1993–2003, May 2016, doi: 10.1016/j.bpj.2016.03.035.
- [131] L. S. Forero-Quintero *et al.* Membrane-anchored carbonic anhydrase IV interacts with monocarboxylate transporters via their chaperones CD147 and GP70. *J. Biol. Chem.*, vol. 294, no. 2, pp. 593–607, Jan. 2019, doi: 10.1074/jbc.RA118.005536.
- [132] S. Jamali *et al.* Hypoxia-induced carbonic anhydrase IX facilitates lactate flux in human breast cancer cells by non-catalytic function. *Sci. Rep.*, vol. 5, no. 1, p. 13605, Sep. 2015, doi: 10.1038/srep13605.
- [133] M. Klier, C. Schüler, A. P. Halestrap, W. S. Sly, J. W. Deitmer, and H. M. Becker. Transport Activity of the High-affinity Monocarboxylate Transporter MCT2 Is Enhanced by Extracellular Carbonic Anhydrase IV but Not by Intracellular Carbonic Anhydrase II. *J. Biol. Chem.*, vol. 286, no. 31, pp. 27781–27791, Aug. 2011, doi: 10.1074/jbc.M111.255331.
- [134] M. H. Stridh *et al.* Lactate flux in astrocytes is enhanced by a non-catalytic action of carbonic anhydrase II: CAII enhances lactate transport in astrocytes. *J. Physiol.*, vol. 590, no. 10, pp. 2333–2351, May 2012, doi: 10.1113/jphysiol.2011.220152.
- [135] S. I. Noor *et al.* Analysis of the Binding Moiety Mediating the Interaction between Monocarboxylate Transporters and Carbonic Anhydrase II. *J. Biol. Chem.*, vol. 290, no. 7, pp. 4476–4486, Feb. 2015, doi: 10.1074/jbc.M114.624577.
- [136] M. Klier, F. T. Andes, J. W. Deitmer, and H. M. Becker. Intracellular and Extracellular Carbonic Anhydrases Cooperate Non-enzymatically to Enhance Activity of Monocarboxylate Transporters. *J. Biol. Chem.*, vol. 289, no. 5, pp. 2765–2775, Jan. 2014, doi: 10.1074/jbc.M113.537043.
- [137] S. Ames, S. Pastorekova, and H. M. Becker. The proteoglycan-like domain of carbonic anhydrase IX mediates non-catalytic facilitation of lactate transport in cancer cells. *Oncotarget*, vol. 9, no. 46, pp. 27940–27957, Jun. 2018, doi: 10.18632/oncotarget.25371.
- [138] S. I. Noor, S. Jamali, S. Ames, S. Langer, J. W. Deitmer, and H. M. Becker. A surface proton antenna in carbonic anhydrase II supports lactate transport in cancer cells. *eLife*, vol. 7, p. e35176, May 2018, doi: 10.7554/eLife.35176.
- [139] J. W. Deitmer and H. M. Becker. Transport metabolons with carbonic anhydrases. *Front. Physiol.*, vol. 4, 2013, doi: 10.3389/fphys.2013.00291.
- [140] H. M. Becker and J. W. Deitmer. Transport Metabolons and Acid/Base Balance in Tumor Cells. *Cancers*, vol. 12, no. 4, p. 899, Apr. 2020, doi: 10.3390/cancers12040899.
- [141] H. M. Becker and J. W. Deitmer. Proton Transport in Cancer Cells: The Role of Carbonic Anhydrases. *Int. J. Mol. Sci.*, vol. 22, no. 6, p. 3171, Mar. 2021, doi: 10.3390/ijms22063171.
- [142] H. M. Becker and J. W. Deitmer. Nonenzymatic Proton Handling by Carbonic Anhydrase II during H⁺-Lactate Cotransport via Monocarboxylate Transporter 1. *J. Biol. Chem.*, vol. 283, no. 31, pp. 21655–21667, Aug. 2008, doi: 10.1074/jbc.M802134200.
- [143] S. I. Noor, J. Pouyssegur, J. W. Deitmer, and H. M. Becker. Integration of a “proton antenna” facilitates transport activity of the monocarboxylate transporter MCT4. *FEBS J.*, vol. 284, no. 1, pp. 149–162, Jan. 2017, doi: 10.1111/febs.13964.
- [144] S. Bock. Zellfreie Synthese von schwer herstellbaren Proteinen. 2014. [Online]. Available: https://macau.uni-kiel.de/receive/diss_mods_00014298
- [145] T. H. Bayburt, Y. V. Grinkova, and S. G. Sligar. Self-Assembly of Discoidal Phospholipid Bilayer Nanoparticles with Membrane Scaffold Proteins. *Nano Lett.*, vol. 2, no. 8, pp. 853–856, Aug. 2002, doi: 10.1021/nl025623k.

- [146] A. Meyer, S. Eskandari, S. Grallath, and D. Rentsch. AtGAT1, a High Affinity Transporter for γ -Aminobutyric Acid in *Arabidopsis thaliana*. *J. Biol. Chem.*, vol. 281, no. 11, pp. 7197–7204, Mar. 2006, doi: 10.1074/jbc.M510766200.
- [147] D. Wipf, M. Benjdia, E. Rikirsch, S. Zimmermann, M. Tegeder, and W. B. Frommer. An expression cDNA library for suppression cloning in yeast mutants, complementation of a yeast *his4* mutant, and EST analysis from the symbiotic basidiomycete *Hebeloma cylindrosporum*. *Genome*, vol. 46, no. 2, pp. 177–181, Apr. 2003, doi: 10.1139/g02-121.
- [148] D. Rentsch, M. Laloi, I. Rouhara, E. Schmelzer, S. Delrot, and W. B. Frommer. *NTR1* encodes a high affinity oligopeptide transporter in *Arabidopsis*. *FEBS Lett.*, vol. 370, no. 3, pp. 264–268, Aug. 1995, doi: 10.1016/0014-5793(95)00853-2.
- [149] A. Müller-Lucks. Optimierung der zellfreien Proteinsynthese durch Etablierung einer schnellen in-situ Faltungskontrolle mittels GFP-Fusion.. 2012. [Online]. Available: https://macau.uni-kiel.de/receive/diss_mods_00010216
- [150] J. Holm-Bertelsen. Expressionssysteme zur Gewinnung von rekombinantem PffNT zur Reinigung, Funktionsuntersuchung & Kristallisation. 2016. [Online]. Available: https://macau.uni-kiel.de/receive/diss_mods_00019128
- [151] A. Jansen. Formiat-Nitrit-Transporter Formiat-Nitrit-Transporter. Eine einfache Einordnung als Kanäle oder Transporter?. 2022. [Online]. Available: https://macau.uni-kiel.de/receive/macau_mods_00002875
- [152] M. Meselson and R. Yuan. DNA Restriction Enzyme from *E. coli*. *Nature*, vol. 217, no. 5134, pp. 1110–1114, Mar. 1968, doi: 10.1038/2171110a0.
- [153] F. William Studier, A. H. Rosenberg, J. J. Dunn, and J. W. Dubendorff. Use of T7 RNA polymerase to direct expression of cloned genes. in *Methods in Enzymology*, Elsevier, 1990, pp. 60–89. doi: 10.1016/0076-6879(90)85008-C.
- [154] A. Pacheco *et al.* Lactic acid production in *Saccharomyces cerevisiae* is modulated by expression of the monocarboxylate transporters Jen1 and Ady2. *FEMS Yeast Res.*, vol. 12, no. 3, pp. 375–381, May 2012, doi: 10.1111/j.1567-1364.2012.00790.x.
- [155] M. Casal, S. Paiva, R. P. Andrade, C. Gancedo, and C. Leão. The Lactate-Proton Symport of *Saccharomyces cerevisiae* Is Encoded by *JEN1*. *J. Bacteriol.*, vol. 181, no. 8, pp. 2620–2623, Apr. 1999, doi: 10.1128/JB.181.8.2620-2623.1999.
- [156] I. Soares-Silva, S. Paiva, G. Djalinas, and M. Casal. The conserved sequence NXX[S/T]HX[S/T]QDXXXT of the lactate/pyruvate:H⁺ symporter subfamily defines the function of the substrate translocation pathway. *Mol. Membr. Biol.*, vol. 24, no. 5–6, pp. 464–474, Jan. 2007, doi: 10.1080/09687680701342669.
- [157] F. Helmstetter. Untersuchung der Abhängigkeit der Funktionalität von Formiat-Nitrit Transportern vom zentralen Histidin. 2019. [Online]. Available: https://macau.uni-kiel.de/receive/diss_mods_00024919
- [158] T. D. Goddard *et al.* UCSF ChimeraX: Meeting modern challenges in visualization and analysis: UCSF ChimeraX Visualization System. *Protein Sci.*, vol. 27, no. 1, pp. 14–25, Jan. 2018, doi: 10.1002/pro.3235.
- [159] E. F. Pettersen *et al.* UCSF CHIMERAX: Structure visualization for researchers, educators, and developers. *Protein Sci.*, vol. 30, no. 1, pp. 70–82, Jan. 2021, doi: 10.1002/pro.3943.
- [160] E. Jurrus *et al.* Improvements to the APBS biomolecular solvation software suite. *Protein Sci.*, vol. 27, no. 1, pp. 112–128, Jan. 2018, doi: 10.1002/pro.3280.
- [161] N. Rego and D. Koes. 3Dmol.js: molecular visualization with WebGL. *Bioinformatics*, vol. 31, no. 8, pp. 1322–1324, Apr. 2015, doi: 10.1093/bioinformatics/btu829.
- [162] W. A. Kibbe. OligoCalc: an online oligonucleotide properties calculator. *Nucleic Acids Res.*, vol. 35, no. Web Server, pp. W43–W46, May 2007, doi: 10.1093/nar/gkm234.

- [163] P. Stothard. The Sequence Manipulation Suite: JavaScript Programs for Analyzing and Formatting Protein and DNA Sequences. *BioTechniques*, vol. 28, no. 6, pp. 1102–1104, Jun. 2000, doi: 10.2144/00286ir01.
- [164] E. Gasteiger *et al.* Protein Identification and Analysis Tools on the ExPASy Server. in *The Proteomics Protocols Handbook*, J. M. Walker, Ed., Totowa, NJ: Humana Press, 2005, pp. 571–607. doi: 10.1385/1-59259-890-0:571.
- [165] J. Jumper *et al.* Highly accurate protein structure prediction with AlphaFold. *Nature*, vol. 596, no. 7873, pp. 583–589, Aug. 2021, doi: 10.1038/s41586-021-03819-2.
- [166] K. Tunyasuvunakool *et al.* Highly accurate protein structure prediction for the human proteome. *Nature*, vol. 596, no. 7873, pp. 590–596, Aug. 2021, doi: 10.1038/s41586-021-03828-1.
- [167] F. Madeira *et al.* Search and sequence analysis tools services from EMBL-EBI in 2022. *Nucleic Acids Res.*, vol. 50, no. W1, pp. W276–W279, Jul. 2022, doi: 10.1093/nar/gkac240.
- [168] J. Marmur and P. Doty. Determination of the base composition of deoxyribonucleic acid from its thermal denaturation temperature. *J. Mol. Biol.*, vol. 5, no. 1, pp. 109–118, Jul. 1962, doi: 10.1016/S0022-2836(62)80066-7.
- [169] R. B. Wallace, J. Shaffer, R. F. Murphy, J. Bonner, T. Hirose, and K. Itakura. Hybridization of synthetic oligodeoxyribonucleotides to $\Phi_x 174$ DNA: the effect of single base pair mismatch. *Nucleic Acids Res.*, vol. 6, no. 11, pp. 3543–3558, 1979, doi: 10.1093/nar/6.11.3543.
- [170] S. N. Cohen, A. C. Y. Chang, and L. Hsu. Nonchromosomal Antibiotic Resistance in Bacteria: Genetic Transformation of *Escherichia coli* by R-Factor DNA. *Proc. Natl. Acad. Sci.*, vol. 69, no. 8, pp. 2110–2114, Aug. 1972, doi: 10.1073/pnas.69.8.2110.
- [171] M. M. Bradford. A rapid and sensitive method for the quantitation of microgram quantities of protein utilizing the principle of protein-dye binding. *Anal. Biochem.*, vol. 72, no. 1–2, pp. 248–254, May 1976, doi: 10.1016/0003-2697(76)90527-3.
- [172] D. Idrees *et al.* Cloning, expression, purification and characterization of human mitochondrial carbonic anhydrase VA. *3 Biotech*, vol. 6, no. 1, p. 16, Jun. 2016, doi: 10.1007/s13205-015-0334-1.
- [173] R.-B. Rues, A. Gräwe, E. Henrich, and F. Bernhard. Membrane Protein Production in *E. coli* Lysates in Presence of Preassembled Nanodiscs. in *Heterologous Gene Expression in E.coli*, N. A. Burgess-Brown, Ed., in *Methods in Molecular Biology*, vol. 1586. New York, NY: Springer New York, 2017, pp. 291–312. doi: 10.1007/978-1-4939-6887-9_19.
- [174] T. Lodi, F. Fontanesi, and B. Guiard. Co-ordinate regulation of lactate metabolism genes in yeast: the role of the lactate permease gene JEN1. *Mol. Genet. Genomics*, vol. 266, no. 5, pp. 838–847, Jan. 2002, doi: 10.1007/s00438-001-0604-y.
- [175] R. Daniel Gietz and R. A. Woods. Transformation of yeast by lithium acetate/single-stranded carrier DNA/polyethylene glycol method. in *Methods in Enzymology*, Elsevier, 2002, pp. 87–96. doi: 10.1016/S0076-6879(02)50957-5.
- [176] B. Wu. Oligomerization of Ammonium Transporter LeAMT1;1 and Its Interactions with Other Proteins. 2004. [Online]. Available: <https://publikationen.uni-tuebingen.de/xmlui/bitstream/handle/10900/48581/pdf/thesis.pdf?sequence=1&isAllowed=y>
- [177] D. Bracey, C. D. Holyoak, G. Nebe-von Caron, and P. J. Coote. Determination of the intracellular pH (pHi) of growing cells of *Saccharomyces cerevisiae*: the effect of reduced-expression of the membrane H⁺-ATPase. *J. Microbiol. Methods*, vol. 31, no. 3, pp. 113–125, Jan. 1998, doi: 10.1016/S0167-7012(97)00095-X.
- [178] J. Rambow. Characterization of PfFNT – a lactate transporter in *Plasmodium falciparum*. 2015. [Online]. Available: https://macau.uni-kiel.de/servlets/MCRFileNodeServlet/dissertation_derivate_00005974/Rambow_-_Dissertation_final_1.1.pdf

- [179] A. Gollmack. Entdeckung von Inhibitoren des Lactat-Transporters aus dem Malaria-Erreger *Plasmodium falciparum*. 2017. [Online]. Available: https://macau.uni-kiel.de/receive/diss_mods_00022480
- [180] K. Geistlinger. Der Protonentransport über den humanen Monocarboxylattransporter 1 wird durch das anionische Substrat vermittelt. 2022. [Online]. Available: https://macau.uni-kiel.de/receive/macau_mods_00003282
- [181] D. Schwarz *et al.* Preparative scale expression of membrane proteins in *Escherichia coli*-based continuous exchange cell-free systems. *Nat. Protoc.*, vol. 2, no. 11, pp. 2945–2957, Nov. 2007, doi: 10.1038/nprot.2007.426.
- [182] D. Schwarz *et al.* Preparative scale cell-free expression systems: New tools for the large scale preparation of integral membrane proteins for functional and structural studies. *Methods*, vol. 41, no. 4, pp. 355–369, Apr. 2007, doi: 10.1016/j.ymeth.2006.07.001.
- [183] J. Holm-Bertelsen, S. Bock, F. Helmstetter, and E. Beitz. High-level cell-free production of the malarial lactate transporter PfFNT as a basis for crystallization trials and directional transport studies. *Protein Expr. Purif.*, vol. 126, pp. 109–114, Oct. 2016, doi: 10.1016/j.pep.2016.06.008.
- [184] P. Hajek, A. Bader, F. Helmstetter, B. Henke, P. Arnold, and E. Beitz. Cell-Free and Yeast-Based Production of the Malarial Lactate Transporter, PfFNT, Delivers Comparable Yield and Protein Quality. *Front. Pharmacol.*, vol. 10, p. 375, Apr. 2019, doi: 10.3389/fphar.2019.00375.
- [185] I. Jakóbowska. Development of novel antimalarials targeting the plasmodial lactate transporter (PfFNT) through a fluorescence-cross correlation spectroscopy-based approach and functional assay. 2023.
- [186] D. Benjamin *et al.* Dual Inhibition of the Lactate Transporters MCT1 and MCT4 Is Synthetic Lethal with Metformin due to NAD⁺ Depletion in Cancer Cells. *Cell Rep.*, vol. 25, no. 11, pp. 3047–3058.e4, Dec. 2018, doi: 10.1016/j.celrep.2018.11.043.
- [187] K. A. Giuliano and R. J. Gillies. Determination of intracellular pH of BALBc-3T3 cells using the fluorescence of pyranine. *Anal. Biochem.*, vol. 167, no. 2, pp. 362–371, Dec. 1987, doi: 10.1016/0003-2697(87)90178-3.
- [188] N. R. Clement and J. M. Gould. Pyranine (8-hydroxy-1,3,6-pyrenetrisulfonate) as a probe of internal aqueous hydrogen ion concentration in phospholipid vesicles. *Biochemistry*, vol. 20, no. 6, pp. 1534–1538, Mar. 1981, doi: 10.1021/bi00509a019.
- [189] K. Kano and J. H. Fendler. Pyranine as a sensitive pH probe for liposome interiors and surfaces. pH gradients across phospholipid vesicles. *Biochim. Biophys. Acta BBA - Biomembr.*, vol. 509, no. 2, pp. 289–299, May 1978, doi: 10.1016/0005-2736(78)90048-2.
- [190] M. J. Borgnia and P. Agre. Reconstitution and functional comparison of purified GlpF and AqpZ, the glycerol and water channels from *Escherichia coli*. *Proc. Natl. Acad. Sci.*, vol. 98, no. 5, pp. 2888–2893, Feb. 2001, doi: 10.1073/pnas.051628098.
- [191] D. A. Doyle and B. A. Wallace. Crystal structure of the Gramicidin/Potassium thiocyanate complex. *J. Mol. Biol.*, vol. 266, no. 5, pp. 963–977, Mar. 1997, doi: 10.1006/jmbi.1996.0837.
- [192] M. Poxleitner, J. Seitz-Beywl, and K. Heinzinger. Ion Transport through Gramicidin A. Water Structure and Functionality. *Z. Für Naturforschung C*, vol. 48, no. 7–8, pp. 654–665, Aug. 1993, doi: 10.1515/znc-1993-7-820.
- [193] R. A. Noble *et al.* Inhibition of monocarboxyate transporter 1 by AZD3965 as a novel therapeutic approach for diffuse large B-cell lymphoma and Burkitt lymphoma. *Haematologica*, vol. 102, no. 7, pp. 1247–1257, Jul. 2017, doi: 10.3324/haematol.2016.163030.
- [194] D. Hunger, M. Röcker, D. Falke, H. Lilie, and R. G. Sawers. The C-terminal Six Amino Acids of the FNT Channel FocA Are Required for Formate Translocation But Not

- Homopentamer Integrity. *Front. Microbiol.*, vol. 8, p. 1616, Aug. 2017, doi: 10.3389/fmicb.2017.01616.
- [195] M. Kammel, D. Hunger, and R. G. Sawers. The soluble cytoplasmic N-terminal domain of the FocA channel gates bidirectional formate translocation. *Mol. Microbiol.*, vol. 115, no. 4, pp. 758–773, Apr. 2021, doi: 10.1111/mmi.14641.
- [196] M. Kammel, C. Pinske, and R. G. Sawers. FocA and its central role in fine-tuning pH homeostasis of enterobacterial formate metabolism. *Microbiology*, vol. 168, no. 10, Oct. 2022, doi: 10.1099/mic.0.001253.
- [197] F. Sievers and D. G. Higgins. Clustal Omega, Accurate Alignment of Very Large Numbers of Sequences. in *Multiple Sequence Alignment Methods*, D. J. Russell, Ed., in *Methods in Molecular Biology*, vol. 1079. Totowa, NJ: Humana Press, 2014, pp. 105–116. doi: 10.1007/978-1-62703-646-7_6.
- [198] C. Aurrecochea *et al.* PlasmoDB: a functional genomic database for malaria parasites. *Nucleic Acids Res.*, vol. 37, no. Database, pp. D539–D543, Jan. 2009, doi: 10.1093/nar/gkn814.
- [199] Y. Kuhn, P. Rohrbach, and M. Lanzer. Quantitative pH measurements in *Plasmodium falciparum*-infected erythrocytes using pHluorin. *Cell. Microbiol.*, vol. 9, no. 4, pp. 1004–1013, Apr. 2007, doi: 10.1111/j.1462-5822.2006.00847.x.
- [200] R. Hayward, K. J. Saliba, and K. Kirk. The pH of the digestive vacuole of *Plasmodium falciparum* is not associated with chloroquine resistance. *J. Cell Sci.*, vol. 119, no. 6, pp. 1016–1025, Mar. 2006, doi: 10.1242/jcs.02795.
- [201] M. D. Jensen, M. Conley, and L. D. Helstowski. Culture of *Plasmodium falciparum*: the role of pH, glucose, and lactate. *J. Parasitol.*, vol. 69, no. 6, pp. 1060–1067, Dec. 1983.
- [202] E. Hopkins, T. Sanvictores, and S. Sharma. Physiology, Acid Base Balance. in *StatPearls*, Treasure Island (FL): StatPearls Publishing, 2023. Accessed: May 12, 2023. [Online]. Available: <http://www.ncbi.nlm.nih.gov/books/NBK507807/>
- [203] A. Yamaguchi, Y. Futagi, M. Kobayashi, K. Narumi, A. Furugen, and K. Iseki. Extracellular lysine 38 plays a crucial role in pH-dependent transport via human monocarboxylate transporter 1. *Biochim. Biophys. Acta BBA - Biomembr.*, vol. 1862, no. 2, p. 183068, Feb. 2020, doi: 10.1016/j.bbamem.2019.183068.
- [204] Y. Futagi, S. Sasaki, M. Kobayashi, K. Narumi, A. Furugen, and K. Iseki. The flexible cytoplasmic loop 3 contributes to the substrate affinity of human monocarboxylate transporters. *Biochim. Biophys. Acta BBA - Biomembr.*, vol. 1859, no. 10, pp. 1790–1795, Oct. 2017, doi: 10.1016/j.bbamem.2017.05.014.
- [205] T. Stams, S. K. Nair, T. Okuyama, A. Waheed, W. S. Sly, and D. W. Christianson. Crystal structure of the secretory form of membrane-associated human carbonic anhydrase IV at 2.8-Å resolution. *Proc. Natl. Acad. Sci.*, vol. 93, no. 24, pp. 13589–13594, Nov. 1996, doi: 10.1073/pnas.93.24.13589.
- [206] T. Okuyama, A. Waheed, W. Kusumoto, X. L. Zhu, and W. S. Sly. Carbonic anhydrase IV: Role of removal of C-terminal domain in glycosylphosphatidylinositol anchoring and realization of enzyme activity. *Arch. Biochem. Biophys.*, vol. 320, no. 2, pp. 315–322, Jul. 1995, doi: 10.1016/0003-9861(95)90015-2.
- [207] M. Pittet and A. Conzelmann. Biosynthesis and function of GPI proteins in the yeast *Saccharomyces cerevisiae*. *Biochim. Biophys. Acta BBA - Mol. Cell Biol. Lipids*, vol. 1771, no. 3, pp. 405–420, Mar. 2007, doi: 10.1016/j.bbalip.2006.05.015.
- [208] W. Vernier *et al.* Thioether benzenesulfonamide inhibitors of carbonic anhydrases II and IV: Structure-based drug design, synthesis, and biological evaluation. *Bioorg. Med. Chem.*, vol. 18, no. 9, pp. 3307–3319, May 2010, doi: 10.1016/j.bmc.2010.03.014.
- [209] C. A. Challener. Fusion Proteins Pose Manufacturability Challenges. *BioPharm Int.*, vol. 30, no. 5, pp. 30–37, 37, May 2017.

- [210] S. R. Schmidt. Fusion Protein Technologies for Biopharmaceuticals: Applications and Challenges PART I INTRODUCTION. 2013, doi: 10.13140/2.1.4445.5366.
- [211] X. Chen, J. L. Zaro, and W.-C. Shen. Fusion protein linkers: Property, design and functionality. *Adv. Drug Deliv. Rev.*, vol. 65, no. 10, pp. 1357–1369, Oct. 2013, doi: 10.1016/j.addr.2012.09.039.
- [212] X.-L. Yu *et al.* Crystal Structure of HAb18G/CD147. *J. Biol. Chem.*, vol. 283, no. 26, pp. 18056–18065, Jun. 2008, doi: 10.1074/jbc.M802694200.
- [213] A. Mickevičiūtė *et al.* Intrinsic thermodynamics of high affinity inhibitor binding to recombinant human carbonic anhydrase IV. *Eur. Biophys. J.*, vol. 47, no. 3, pp. 271–290, Apr. 2018, doi: 10.1007/s00249-017-1256-0.
- [214] C. Temperini, A. Scozzafava, D. Vullo, and C. T. Supuran. Carbonic Anhydrase Activators. Activation of Isozymes I, II, IV, VA, VII, and XIV with L- and D-Histidine and Crystallographic Analysis of Their Adducts with Isoform II: Engineering Proton-Transfer Processes within the Active Site of an Enzyme. *Chem. - Eur. J.*, vol. 12, no. 27, pp. 7057–7066, Sep. 2006, doi: 10.1002/chem.200600159.
- [215] J. Rogé and J.-M. Betton. Use of pIVEX plasmids for protein overproduction in *Escherichia coli*. *Microb. Cell Factories*, vol. 4, no. 1, p. 18, Dec. 2005, doi: 10.1186/1475-2859-4-18.
- [216] I. Palmer and P. T. Wingfield. Preparation and Extraction of Insoluble (Inclusion-Body) Proteins from *Escherichia coli*. *Curr. Protoc. Protein Sci.*, vol. 38, no. 1, Nov. 2004, doi: 10.1002/0471140864.ps0603s38.
- [217] A. Bzducha-Wróbel, St. Błażej, and K. Tkacz. Cell wall structure of selected yeast species as a factor of magnesium binding ability. *Eur. Food Res. Technol.*, vol. 235, no. 2, pp. 355–366, Aug. 2012, doi: 10.1007/s00217-012-1761-4.
- [218] V. Dupres, Y. F. Dufrière, and J. J. Heinisch. Measuring Cell Wall Thickness in Living Yeast Cells Using Single Molecular Rulers. *ACS Nano*, vol. 4, no. 9, pp. 5498–5504, Sep. 2010, doi: 10.1021/nn101598v.
- [219] L. M. Petersen. Arzneimittelresistenz-assoziierte, protozoische Membranproteine: Untersuchungen zur Struktur und Inhibitorfindung des plasmodialen Chloroquin-Resistenz-Transporters sowie zum Pentamidin-Aufnahmemechanismus über das trypanosomale Aquaglyceroporin 2.. 2021. [Online]. Available: https://macau.uni-kiel.de/receive/macau_mods_00001401
- [220] V. M. Bolanos-Garcia and O. R. Davies. Structural analysis and classification of native proteins from *E. coli* commonly co-purified by immobilised metal affinity chromatography. *Biochim. Biophys. Acta BBA - Gen. Subj.*, vol. 1760, no. 9, pp. 1304–1313, Sep. 2006, doi: 10.1016/j.bbagen.2006.03.027.
- [221] P. Bartlow *et al.* Identification of native *Escherichia coli* BL21 (DE3) proteins that bind to immobilized metal affinity chromatography under high imidazole conditions and use of 2D-DIGE to evaluate contamination pools with respect to recombinant protein expression level. *Protein Expr. Purif.*, vol. 78, no. 2, pp. 216–224, Aug. 2011, doi: 10.1016/j.pep.2011.04.021.
- [222] H. Schägger and G. Von Jagow. Blue native electrophoresis for isolation of membrane protein complexes in enzymatically active form. *Anal. Biochem.*, vol. 199, no. 2, pp. 223–231, Dec. 1991, doi: 10.1016/0003-2697(91)90094-A.
- [223] H. Schagger, W. A. Cramer, and G. Vonjagow. Analysis of Molecular Masses and Oligomeric States of Protein Complexes by Blue Native Electrophoresis and Isolation of Membrane Protein Complexes by Two-Dimensional Native Electrophoresis. *Anal. Biochem.*, vol. 217, no. 2, pp. 220–230, Mar. 1994, doi: 10.1006/abio.1994.1112.
- [224] H. Schägger. Tricine-SDS-PAGE. *Nat. Protoc.*, vol. 1, no. 1, pp. 16–22, Jun. 2006, doi: 10.1038/nprot.2006.4.

- [225] C. E. Cooper, J. M. Wrigglesworth, and P. Nicholls. The mechanism of potassium movement across the liposomal membrane. *Biochem. Biophys. Res. Commun.*, vol. 173, no. 3, pp. 1008–1012, Dec. 1990, doi: 10.1016/S0006-291X(05)80886-1.
- [226] D. Roesel, M. Eremchev, C. S. Poojari, J. S. Hub, and S. Roke. Ion-Induced Transient Potential Fluctuations Facilitate Pore Formation and Cation Transport through Lipid Membranes. *J. Am. Chem. Soc.*, vol. 144, no. 51, pp. 23352–23357, Dec. 2022, doi: 10.1021/jacs.2c08543.
- [227] M. Eremchev, D. Roesel, C. S. Poojari, A. Roux, J. S. Hub, and S. Roke. Passive transport of Ca²⁺ ions through lipid bilayers imaged by widefield second harmonic microscopy. *Biophys. J.*, vol. 122, no. 4, pp. 624–631, Feb. 2023, doi: 10.1016/j.bpj.2023.01.018.
- [228] H. Komatsu and P. L.-G. Chong. Low Permeability of Liposomal Membranes Composed of Bipolar Tetraether Lipids from Thermoacidophilic Archaeobacterium *Sulfolobus acidocaldarius*. *Biochemistry*, vol. 37, no. 1, pp. 107–115, Jan. 1998, doi: 10.1021/bi972163e.
- [229] K. G. Hugentobler *et al.* Lipid Composition Affects the Efficiency in the Functional Reconstitution of the Cytochrome c Oxidase. *Int. J. Mol. Sci.*, vol. 21, no. 19, p. 6981, Sep. 2020, doi: 10.3390/ijms21196981.
- [230] A. P. Halestrap and M. C. Wilson. The monocarboxylate transporter family—Role and regulation. *IUBMB Life*, vol. 64, no. 2, pp. 109–119, Feb. 2012, doi: 10.1002/iub.572.
- [231] M. E. Morris and M. A. Felmlee. Overview of the Proton-coupled MCT (SLC16A) Family of Transporters: Characterization, Function and Role in the Transport of the Drug of Abuse γ -Hydroxybutyric Acid. *AAPS J.*, vol. 10, no. 2, p. 311, Jun. 2008, doi: 10.1208/s12248-008-9035-6.
- [232] A. A. Stepanenko and V. V. Dmitrenko. HEK293 in cell biology and cancer research: phenotype, karyotype, tumorigenicity, and stress-induced genome-phenotype evolution. *Gene*, vol. 569, no. 2, pp. 182–190, Sep. 2015, doi: 10.1016/j.gene.2015.05.065.
- [233] W. Lü, J. Du, T. Wacker, E. Gerbig-Smentek, S. L. A. Andrade, and O. Einsle. pH-Dependent Gating in a FocA Formate Channel. *Science*, vol. 332, no. 6027, pp. 352–354, Apr. 2011, doi: 10.1126/science.1199098.
- [234] A. B. Waight, J. Love, and D.-N. Wang. Structure and mechanism of a pentameric formate channel. *Nat. Struct. Mol. Biol.*, vol. 17, no. 1, pp. 31–37, Jan. 2010, doi: 10.1038/nsmb.1740.
- [235] M. Valli, M. Sauer, P. Branduardi, N. Borth, D. Porro, and D. Mattanovich. Intracellular pH Distribution in *Saccharomyces cerevisiae* Cell Populations, Analyzed by Flow Cytometry. *Appl. Environ. Microbiol.*, vol. 71, no. 3, pp. 1515–1521, Mar. 2005, doi: 10.1128/AEM.71.3.1515-1521.2005.
- [236] K. Van Eunen *et al.* Measuring enzyme activities under standardized in vivo-like conditions for systems biology: Standardized enzyme assays for systems biology. *FEBS J.*, vol. 277, no. 3, pp. 749–760, Feb. 2010, doi: 10.1111/j.1742-4658.2009.07524.x.
- [237] M. A. J. Ferguson, S. W. Homans, R. A. Dwek, and T. W. Rademacher. Glycosyl-Phosphatidylinositol Moiety That Anchors *Trypanosoma brucei* Variant Surface Glycoprotein to the Membrane. *Science*, vol. 239, no. 4841, pp. 753–759, Feb. 1988, doi: 10.1126/science.3340856.
- [238] M. A. J. Ferguson and A. F. Williams. Cell-surface anchoring of proteins via glycosyl-phosphatidylinositol structures. *Annu. Rev. Biochem.*, vol. 57, no. 1, pp. 285–320, Jun. 1988, doi: 10.1146/annurev.bi.57.070188.001441.
- [239] P. T. Englund. The structure and biosynthesis of glycosyl phosphatidylinositol protein anchors. *Annu. Rev. Biochem.*, vol. 62, no. 1, pp. 121–138, Jun. 1993, doi: 10.1146/annurev.bi.62.070193.001005.

- [240] Z. Guo. Synthetic Studies of Glycosylphosphatidylinositol (GPI) Anchors and GPI-Anchored Peptides, Glycopeptides, and Proteins. *Curr. Org. Synth.*, vol. 10, no. 3, pp. 366–383, May 2013, doi: 10.2174/1570179411310030003.
- [241] M. Wiechert, H. Erler, A. Gollmack, and E. Beitz. A widened substrate selectivity filter of eukaryotic formate-nitrite transporters enables high-level lactate conductance. *FEBS J.*, vol. 284, no. 16, pp. 2663–2673, Aug. 2017, doi: 10.1111/febs.14117.
- [242] J. D. R. Schmidt. Wasser- und Protonenausschluss in Formiat-Nitrit-Transportern. 2022. [Online]. Available: https://macau.uni-kiel.de/receive/macau_mods_00003103
- [243] R. K. Mortimer. Radiobiological and genetic studies on a polyploid series (haploid to hexaploid) of *Saccharomyces cerevisiae*. *Radiat. Res.*, vol. 9, no. 3, pp. 312–326, Sep. 1958.
- [244] M. Uchida *et al.* Quantitative analysis of yeast internal architecture using soft X-ray tomography. *Yeast*, vol. 28, no. 3, pp. 227–236, Mar. 2011, doi: 10.1002/yea.1834.
- [245] S. Abuhattum *et al.* Intracellular Mass Density Increase Is Accompanying but Not Sufficient for Stiffening and Growth Arrest of Yeast Cells. *Front. Phys.*, vol. 6, p. 131, Nov. 2018, doi: 10.3389/fphy.2018.00131.
- [246] K. Geistlinger, J. D. R. Schmidt, and E. Beitz. Lactic Acid Permeability of Aquaporin-9 Enables Cytoplasmic Lactate Accumulation via an Ion Trap. *Life*, vol. 12, no. 1, p. 120, Jan. 2022, doi: 10.3390/life12010120.
- [247] R. Orij, S. Brul, and G. J. Smits. Intracellular pH is a tightly controlled signal in yeast. *Biochim. Biophys. Acta BBA - Gen. Subj.*, vol. 1810, no. 10, pp. 933–944, Oct. 2011, doi: 10.1016/j.bbagen.2011.03.011.
- [248] A. Peetermans, M. R. Foulquié-Moreno, and J. M. Thevelein. Mechanisms underlying lactic acid tolerance and its influence on lactic acid production in *Saccharomyces cerevisiae*. *Microb. Cell*, vol. 8, no. 6, pp. 111–130, Jun. 2021, doi: 10.15698/mic2021.06.751.

SUPPLEMENTARY MATERIALS

Supp. 1: DNA and protein sequences

The characters of the coding sequences (DNA) represent nucleotides, those of the protein sequences represents amino acids. The underlined characters represent parts of the sequences subject to deletion or omission from the coding frame. The bold or colored characters represent codons and amino acids subjects to mutation.

Supp. 1.1. MSP1E3D1 membrane scaffold protein.

>MSP1E3D1 coding sequence (DNA)

```
ATGagcaccttttagcaaaactgCGTgaacagctgggcccggTgaccaggaatTTTgggataa
cctggaaaaagaaaccgaaggcctgCGTcaggaaatgagcaaagatctggaagaggtgaaag
cgaaagtgcagccgtatctggatgacTTTCAGAAAAAATGGCAGGAAGAGATGGAACGTAT
CGTCAGAAAGTGGAAACCGCTGCGTGCAGGAACTGCAGGAAGGCGCGCTCAGAAACTGCATGA
ACTGCAGGAAAAACTGAGCCCGCTGGGCGAAGAGATGCGTGATCGTGCGCGTGCATGTGG
ATGCGCTGCGTACCCATctggCGccgtatctggatgacTTTCAGAAAAAATGGCAGGAAGAG
ATGGAACGTATCGTCAGAAAGTGGAAACCGCTGCGTGCAGGAACTGCAGGAAGGCGCGCTCA
GAAACTGCATGAACTGCAGGAAAAACTGAGCCCGCTGGGCGAAGAGATGCGTGATCGTGCGC
GTGCGCATGTGGATGCGTACCCATctggCGCCGTATAGCGATGAACTGCGTCAGCGT
CTGGCGGCCCGTCTGGAAGCGCTGAAAGAAAACGGCGGTGCGCGTCTGGCGGAATATCATGC
GAAAGCGACCGAACATCTGAGCACCCCTGAGCGAAAAAGCGAAACCGGCGCTGGAAGATCTGC
GTCAGGGCCTGCTGCCGGTGCTGGAAAGCTTTAAAGTGAGCTTTCTGAGCGCGCTGGAAGAG
TATACCAAAAAACTGAACACCCAG
```

>MSP1E3D1 protein sequence

```
MSTFSKLREQLGPVTQEFWDNLEKETEGLRQEMSKDLEEVKAKVQPYLDDFQKKWQEEMEL - 60
YRQKVEPLRAELQEGARQKLHELQEKLSPLGEEMRDRARAHVDALRTHLAPYLDDFQKKW - 120
QEEMELYRQKVEPLRAELQEGARQKLHELQEKLSPLGEEMRDRARAHVDALRTHLAPYSD - 180
ELRQRLAARLEALKENGGARLAEYHAKATEHLSTLSEKAKPALEDLRQGLLPVLESFKVS - 240
FLSALEEYTKKLNTQ - 255
```

Supp. 1.2. PfFNT.

>PfFNT (Wild Type) coding sequence (DNA)

ATGCCTCCCAACAACCTCGAAATATGTTCTTGACCCTGTTTCTATCAAAAGCGTGTGCGGAGG
GGAAGAAAGCTATATCCGTTGTGTTGAGTATGGCAAGAAGAAAGCCCATTACAGTAATCTGA
ATCTTTTAGCCAAAGCTATTCTGGCAGGGATGTTTCGTAGGCCTGTGTGCACATGCGTCAGGA
ATCGCGGGTGGGTTGTTCTACTACCACAAACTGCGTGAGATTGTTGGAGCGTCTATGAGTGT
CTTTGTGTACGGCTTTACATTTCCGATAGCATTCATGTGCATCATCTGTACCGGTTCCGGATT
TGTTTACC**GGTA**AATACACTAGCGGTCACAATGGCACTGTACGAAAAGAAAGTTAAACTTTTA
GACTATCTCCGGGTTATGACCATCTCGTTATTTGGGAACTATGTCGGTGCAGTCTCATTTCG
TTTCTTTGTGTCTACTTGTCTGGGTGCTTTCACTAACGTGCATGCTGTGGAAAAGAATCATT
TcTTtCAGTTTCTGAATGATATCGCAGAGAAGAAAGTTCACCATACATTTGTGGAATGCGTT
AGCTTAGCCGTGGGTTGTAACATATTT**GTA**TGCTTGGCGGTGTATTTTCGTGCTGACTCTCAA
AGATGGGGCTGGgTATGTATTTTCTGTGTTCTTTGCAGTTTATGCCTTTGCGATTGCCGGCT
ATGAGCATATCATAGCCAACATCTATACCCTGAATATAGCCCTGATGGTGAATACGAAGATT
ACGGTGTATCAGGCCTATATTA AAAACCTGCTGCCGACACTGTTGGGCAACTACATTGCGGG
tGCGATTGTCCTGGGACTGCCGCTGTATTTCAATTTACAAAGAACACT**ACT**TACAACCTT**GAAC**
GCAGTAAACGCGACAACAATGATGCGCAAATGAAATCCCTGAGCATTGAACTGCGCAAC

>PfFNT (Wild Type) Protein sequence

MPPNNSKYVLDPVSIKSVCG**GEES**YIRCVEYGKKKAHYSNLNLLAKAILAGMFVGLCAHA - 60
SGIAGGLFYHKLREIVGASMSVFVYGFTFPPIAFMCI ICTGSDLFT**GNT**LAVTMALYEKK - 120
VKLLDYLRVMTISLFGNYVGAVSFAFFVSYLSGAF TNVHAVEKNHFFQFLNDIAEKKVHH - 180
TFVECVSLAVGCNIF**V**CLAVYFVLT LKDGAGYVFSVFFAVYAF AIAGYEH I ANIYTLNI - 240
ALMVNTKITVYQAYIKNLLPTLLGN IAGAIVLGLPLYFIYKEH**Y**YN**FERS**KRDNNDAQM - 300
KSLSIELRN - 309

Production of the Y285F and E289Q PfFNT mutant.

The Y285F mutation was done by a Site-directed mutagenesis using the primers SDM_PfFNT-Y285F_s and SDM_PfFNT-Y285_as. The plasmid pDRTXa PfFNT was used as a template. The E289Q mutation was done in the same way, using the primers SDM_PfFNT-E289Q_s and SDM_PfFNT-E289_as (Table 2.3). Sanger sequencing was carried out with the primers PMA5 and ADH3 (Table 2.1) to validate the efficiency for the mutation and the absence of significant undesired mutations. Once the correct sequences were identified they inserted in and pDR vectors. The double mutant (Y285F E289Q) was generated by performing a Site-directed mutagenesis using pDR HA PfFNT Y285F as PCR template, with the primers SDM_PfFNT-E289Q_s and SDM_PfFNT-E289_as.

Supp. 1.3. hMCT1

>MCT1 (Wild Type) coding sequence

ATGCCACCAGCAGTTGGAGGTCCAGTTGGATACACCCCCCAGATGGAGGCTGGGGCTGGGC
AGTGGTAATTGGAGCTTTCATTTCCATCGGCTTCTCTTATGCATTTCCC**AA**AATCAATTACTG
TCTTCTTCAAAGAGATTGAAGGTATATTCATGCCACCACCAGCGAAGTGTCATGGATATCC
TCCATAATGTTGGCTGTCATGTATGGTGGAGGTCCTATCAGCAGTATCCTGGTGAATAAATA
TGGAAGTCGTATAGTCATGATTGTTGGTGGCTGCTTGTGAGGCTGTGGCTTGATTGCAGCTT
CTTTCTGTAACACCGTACAGCAACTATACGTCTGTATTGGAGTCATTGGAGGCTCTGGGCTT
GCCTTCAACTTGAATCCAGCTCTGACCATGATTGGCAAGTATTTCTACAAGAGGCGACCATT
GGCCAACGGACTGGCCATGGCAGGCAGCCCTGTGTTCCCTCTGTACTCTGGCCCCCTCAATC
AGGTTTTCTTCGGTATCTTTGGATGGAGAGGAAGCTTCTAATTCTTGGGGGCTTGCTACTA
AACTGCTGTGTTGCTGGAGCCCTCATGCGACCAATCGGGCCCAAGCCAACCAAGGCAGGGAA
AGATAAGTCTAAAGCATCCCTTGAGAAAGCTGGAAAATCTGGTGTGAAAAAAGATCTGCATG
ATGCAAATACAGATCTTATTGGAAGACACCCTAAACAAGAGAAACGATCAGTCTTCCAAACA
ATTAATCAGTTCCTGGACTTAACCCTATTCACCCACAGAGGCTTTTTGCTATAACCTCTCTGG
AAATGTGATCATGTTTTTTGGACTCTTTGCACCTTTGGTGTCTTCTTAGTAGTTATGGGAAGA
GTCAGCATTATTCTAGTGAGAAGTCTGCCTTCCTTCTTTCCATTCTGGCTTTTGTGACATG
GTAGCCCGACCATCTATGGGACTTGTAGCCAACACAAAGCCAATAAGACCTCGAATTCAGTA
TTTTCTTTGCGGCTTCCGTTGTTGCAAATGGAGTGTGTCATATGCTAGCACCTTTATCCACTA
CCTATGTTGGATTCTGTGTCTATGCGGGATTCTTTGGATTTGCCTTCGGGTGGCTCAGCTCC
GTATTGTTTGAAACATTGATGGACCTTGTGGACCCCAGAGGTTCTCCAGCGCTGTGGGATT
GGTGACCATTGTGGAATGCTGTCCTGTCCTCCTGGGGCCACCCTTTTAGGTTCGGCTCAATG
ACATGTATGGAGACTACAAATACATACTGGGCATGTGGCGTCGTCCTAATTATTTTCAGGT
ATCTATCTCTTCATTGGCATGGGCATCAATTATCGACTTTTGGCAAAGAAGCAAGCAAA
CGAGCAGAAAAAGGAAAGTAAAGAGGAAGAGACCAGTATAGATGTTGCTGGGAAGCCAAATG
AAGTTACCAAAGCAGCAGAATCTCCGGACCAGAAAGACACAGATGGAGGGCCCAAGGAGGAG
GAAAGTCCAGTC

>MCT1 (Wild Type) protein sequence

MPPAVGGPVGYTPPDGGWGWAVVIGAFISIGFSYAF**PK**SITVFFKEIEGIFHATTSEVSW - 60
ISSIMLAVMYGGGPISSILVNKYGSRIVMIVGGCLSGCLIAASFCNTVQQLYVCIGVIG - 120
GLGLAFNLPALTMIGKYFYKRRPLANGLAMAGSPVFLCTLAPLNQVFFGIFGWRGSFLI - 180
LGGLLLNCCVAGALMRPIGPKPTKAGKDKSKASLEKAGKSGVKKDLHDANTDLIGRHPKQ - 240
EKRSVFQTIHQFLDLTLFTHRGFLLYLSGNVIMFFGLFAPLVFLSSYGKSQHYSEKSAF - 300
LLSILAFVDMVARPSMGLVANTKPIRPRIQYFFAASVVANGVCHMLAPLSTTYVGFVYA - 360
GFFGFAGVWLVFETLMDLVGPQRFSSAVGLVTIVECCPVLLGPPLLGRNDMYGDYK - 420
YTYWACGVVLIISGIYLFIMGINYRLLAKEQKANEQKESKEEETSIDVAGKPNEVTKA - 380
AESPQKDTDGGPKKEEESPV - 500

Supp. 1.4. Basigin, hMCT1 chaperone.

>h Basigin Isoform 2 (Wild Type) coding sequence (DNA)

ATGGCGGCTGCGCTGTTTCGTGCTGCTGGGATTCGCGCTGCTGGGCACCCACGGAGCCTCCGG
GGCTGCCGGCACAGTCTTCACTACCGTAGAAGACCTTGGCTCCAAGATACTCCTCACCTGCT
CCTTGAATGACAGCGCCACAGAGGTCACAGGGCACCGCTGGCTGAAGGGGGGCGTGGTGTCTG
AAGGAGGACGCGCTGCCCGGCCAGAAAACGGAGTTCAAGGTGGACTCCGACGACCAGTGGGG
AGAGTACTCCTGCGTCTTCCCTCCCCGAGCCCATGGGCACGGCCAACATCCAGCTCCACGGGC
CTCCCAGAGTGAAGGCTGTGAAGTTCGTCA GAA CACATCAAC GAGGGGGAGACGGCCATGCTG
GTCTGCAAGTCAGAGTCCGTGCCACCTGTCACTGACTGGGCCTGGTACAAGATCACTGACTC
TGAGGACAAGGCCCTCATGAACGGCTCCGAGAGCAGGTTCTTCGTGAGTTCCTCGCAGGGCC
GGTCA GAGCTACACATT GAGAACCTGAACATGGAGGCCGACCCCGGCCAGTACCGGTGCAAC
GGCACCAGCTCCAAGGGCTCCGACCAGGCCATCATCACGCTCCGCGTGCGCAGCCACCTGGC
CGCCCTCTGGCCCTTCCCTGGGCATCGTGGCTGAGGTGCTGGTGCTGGTCACCATCATCTTCA
TCTACGAGAAGCGCCGGAAGCCCGAGGACGTCCTGGATGATGACGACGCCGGCTCTGCACCC
CTGAAGAGCAGCGGGCAGCACCAGAATGACAAAGGCAAGAACGTCCGCCAGAGGAACCTCTTC
C

>h Basigin Isoform 2 (Wild Type) protein sequence

MAAALFVLLGFALLGTHGASGAAGTVFTTVEDLGSKILLTCSLNSATEVTGHRWLKGGV - 60
VLKEDALPGQKTEFKVSDSQWGEYSCVFLPEPMGTANIQLHGPPRVKAVKSSEHINEGE - 120
TAMLVCKSESVPPVTDWAWYKIDTSEDKALMNGSESRRFFVSSSQGRSELHIENLNMEADP - 180
GQYRCNGTSSKGSQAIITLRVRSHLAALWPFLGIVA EVLVLTIIIFIYEKRRKPEDVLD - 240
DDDAGSAPLKSSGQHQNDRKGNVRQRNSS - 269

>h Basigin IgI-C2 (Δ 139) protein sequence

MGTVFTTVEDLGSKILLTCSLNSATEVTGHRWLKGGVVLKEDALPGQKTEFKVSDSQW - 60
GEYSCVFLPEPMGTANIQLHGPPRVKAVKSSEHINEGETAMLVCKSESVPPVTDWAWYKI - 120
TSEDKALMNGSESRRFFVSSSQGRSELHIENLNMEADPGQYRCNGTSSKGSQAIITLRV - 180
RSHLAALWPFLGIVA EVLVLTIIIFIYEKRRKPEDVLD DDDAGSAPLKSSGQHQNDRKGN - 240
VRQRNSS - 247

>h Basigin IgI (Δ 220) protein sequence

MPRVKAVKSSEHINEGETAMLVCKSESVPPVTDWAWYKIDTSEDKALMNGSESRRFFVSSSQ - 60
GRSELHIENLNMEADPGQYRCNGTSSKGSQAIITLRVRSHLAALWPFLGIVA EVLVLTII - 120
IFIYEKRRKPEDVLD DDDAGSAPLKSSGQHQNDRKGNVRQRNSS - 164

>h *Basigin* ΔIg (Δ308) protein sequence

MSDQAIITLVRSHLAALWPFLLGIVA EVLVLVTIIIFIYEKRRKPEDVLD DDDAGSAPLKS - 60
SGQHQN DKGNVRQRNSS - 78

Supp. 1.5. Embigin, hMCT1 chaperone

>h *Embigin* (Wild Type) coding sequence (DNA)

ATGCGCGCCCTCCCCGGCCTGCTGGAGGCCAGGGCGCGTACGCCCCGGCTGCTCCTCCTCCA
GTGCCTTCTCGCTGCCGCGCGCCCAAGCTCGGCGGACGGCAGTGCCCCAGATTCGCCTTTTA
CAAGTCCACCTCTCAGAGAAGAAATAATGGCAAATAACTTTTCCTTGGAGAGTCATAACATA
TCACTGACTGAACATTCTAGTATGCCAGTAGAAAAAATATCACTTTAGAAAGGCCTTCTAA
TGTAATCTCACATGCCAGTTCACAACATCTGGGGATTTGAATGCAGTAAATGTGACTTGGA
AAAAAGATGGTGAACAACCTTGAGAATAATTATCTTGTGTCAGTGCAACAGGAAGCACCTTGTAT
ACCCAATACAGGTTCCACCATCATTAATAGCAAACAAATGGGAAGTTATTCTTGTTCCTTTTCG
AGAGGAAAAGGAACAAAGGGGAACATTTAATTTCAAAGTCCCTGAACTTCATGGGAAAAACA
AGCCATTGATCTCTTACGTAGGGGATTCTACTGTCTTGACATGTAAATGTCAAATTTGTTTT
CCTTTAAATTTGGACCTGGTACAGTAGTAATGGGAGTGTAAGGTTCCCTGTTGGTGTTCAAAT
GAATAAATATGTGATCAATGGAACATATGCTAACGAAACAAAGCTGAAGATAACACAACCTTT
TGGAGGAAGATGGGGAATCTTACTGGTGCCGTGCACTATTCCAATTAGGCGAGAGTGAAGAA
CACATTGAGCTTGTGGTGTGAGCTATTTGGTGCCCTCAAACCATTTCTTGTAAATAGTGGC
TGAGGTGATTCTTTTAGTGGCCACCATTCTGCTTTGTGAAAAGTACACACAAAAGAAAAAGA
AGCACTCAGATGAGGGGAAAGAATTTGAGCAGATTGAACAGCTGAAATCAGATGATAGCAAT
GGTATAGAAAATAATGTCCCCAGGCATAGAAAAAATGAGTCTCTGGGCCAG

>h *Embigin* (Wild Type) protein sequence

MRALPGLLEARARTPRLLLLQCLLAAARPSSADGSAPDSPFTSPPLREEIMANNFSLESH - 60
NISL TEHSSMPVEKNITLERPSNVNLT CQFTTSGDLNAVNV TWKKDGEQLENNYLVSATG - 120
STLYTQYRFTI INSKQMGSYSCFFREEKEQRGTFNFKVPELHGKNKPLISYVGDSTVLTC - 180
KCQNC FPLNWTWYSSNGSVKVPVGVQM NKYVINGTYANETKLKITQLLEEDGESYWCRAL - 240
FQLGESEEHIELVVL SYLVLPLKPFLVIVAEVILLVATILLCEKYTQKKKKHSDEGKEFEQ - 300
IEQLKSDDSNGIENNVPRHRKNESLGQ - 327

>h *Embigin* Ig V1-2 protein sequence

MPVEKNITLERPSNVNLT CQFTTSGDLNAVNV TWKKDGEQLENNYLVSATGSTLYTQYRF - 60
TI INSKQMGSYSCFFREEKEQRGTFNFKVPELHGKNKPLISYVGDSTVLTKCKQNC FPLN - 120
WTWYSSNGSVKVPVGVQM NKYVINGTYANETKLKITQLLEEDGESYWCRALFQLGESEEH - 180
IELVVL SYLVLPLKPFLVIVAEVILLVATILLCEKYTQKKKKHSDEGKEFEQIEQLKSDDSN - 240
NGIENNVPRHRKNESLGQ - 257

>h Embigin Ig V2 protein sequence

MPELHGKNKPLISYVGDSTVLTCKCQNCFPLNWTWYSSNGSVKVPVGVQMNKYVINGTYA - 60
NETKLIKITQLLEEDGESYWCRALFQLGESEEHIELVVLSYLVPLKPFVLVIVAEVILLVAT - 120
ILLCEKYTQKKKKHSDEGKEFEQIEQLKSDDSNGIENNVP~~RR~~RKNESLGQ - 170

Expressing EMB Ig-BSG TM-hMCT1 using pDRTXa

The Basigin transmembrane domain coding sequence was amplified flanked by the restriction sites SpeI-SacI in one side and BamHI-PstI in the other using PCR (3.1.2.), using the SpeI-SacI-BSGd308_PCR_s and hBSG_BamHI_PstI_as primers (2.3.4.). The extracted insert was inserted in dephosphorylated (3.1.6) pDRTXa_LK_MCT1 using the SpeI and PstI enzymes. Then, the Embigin Ig domains were amplified by PCR, flanked by the restriction enzyme sites SpeI and SacI, using the primers described in Table 2.4. The extracted inserts were inserted in the dephosphorylated plasmid using the SpeI and SacI restriction enzymes. Sanger sequencing was done to ensure that the PCR steps did not insert unwanted mutations, using the PMA5 and ADH3 primers (2.3.1.).

Table Supp. 1: Primers used for inserting the Embigin domains upstream of the Basigin transmembrane sequence (2.3.4.)

Primer s	Primer as
SpeI-M-EMBvar1deltaTM_PCR_s	
SpeI-EMB_IgV1-2_deltaTM_PCR_s	EMBdeltaTM-SacI_PCR_as
SpeI-M-EMB_IgV2_deltaTM_PCR_s	

Supp. 1.6. Carbonic anhydrase IV

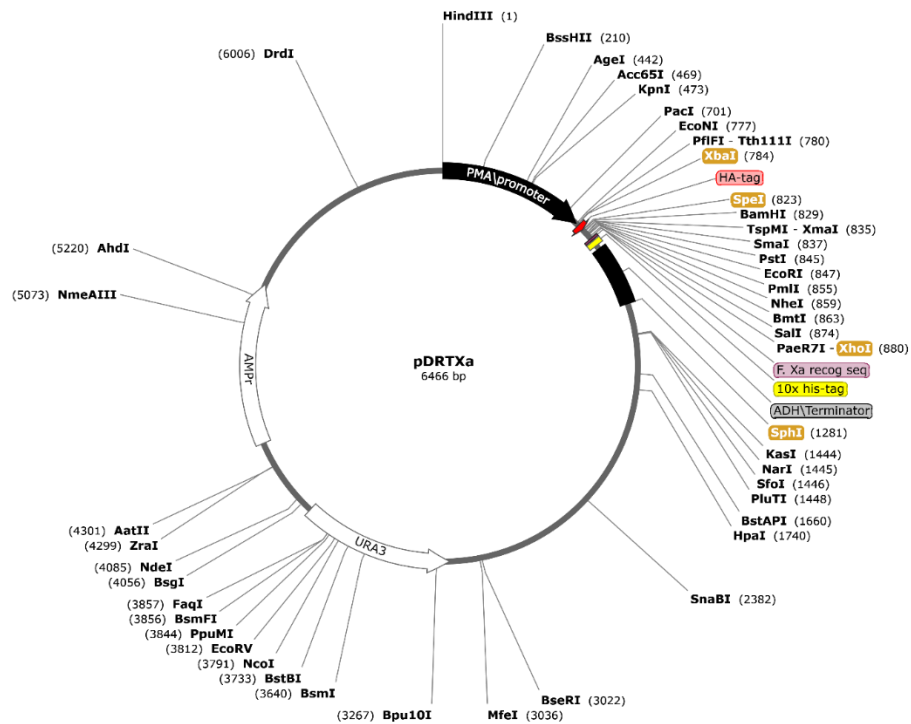
>h Carbonic anhydrase 4 coding sequence (DNA)

ATGCGGATGCTGCTGGCGCTCCTGGCCCTCTCCGCGGCGGGCCATCGGCCAGTGCAGAGTC
ACACTGGTGCTACGAGGTTCAAGCCGAGTCCCTCCAAC TACCCCTGCTTGGTGCCAGTCAAGT
GGGGTGGAAACTGCCAGAAGGACCGCCAGTCCCCATCAACATCGTCACCACCAAGGCAAAG
GTGGACAAAAAACTGGGACGCTTCTTCTTCTCTGGCTACGATAAGAAGCAAACGTGGACTGT
CCAAAATAACGGGCACTCAGTGATGATGTTGCTGGAGAACAAGGCCAGCATTTCTGGAGGAG
GACTGCCTGCCCCATAACCAGGCCAAACAGTTGCACCTGCACTGGTCCGACTTGCCATATAAG
GGCTCGGAGCACAGCCTCGATGGGGAGCACTTTGCCATGGAGATGCACATAGTACATGAGAA
AGAGAAGGGGACATCGAGGAATGTGAAAGAGGGCCCAGGACCCTGAAGACGAAATTGCGGTGC
TGGCCTTTCTGGTGGAGGCTGGAACCCAGGTGAACGAGGGCTTCCAGCCACTGGTGGAGGCA
CTGTCTAATATCCCCAAACCTGAGATGAGCACTACGATGGCAGAGAGCAGCCTGTTGGACCT
GCTCCCCAAGGAGGAGAACTGAGGCACTACTTCCGCTACCTGGGCTCACTCACCACACCGA
CCTGCGATGAGAAGGTCTGCTGGACTGTGTTCCGGGAGCCATT CAGCTTCACAGAGAACAG
ATCCTGGCATTCTCTCAGAAGCTGTACTACGACAAGGAACAGACAGTGAGCATGAAGGACAA
TGTCAGGCCCCCTGCAGCAGCTGGGGCAGCGCACGGTGATAAAGTCCGGGGCCCCGGGTCCGC
CGCTGCCCTGGGCCCTGCCTGCCCTGCTGGGCCCCATGCTGGCCTGCCTGCTGGCCGGCTTC
CTGCGA

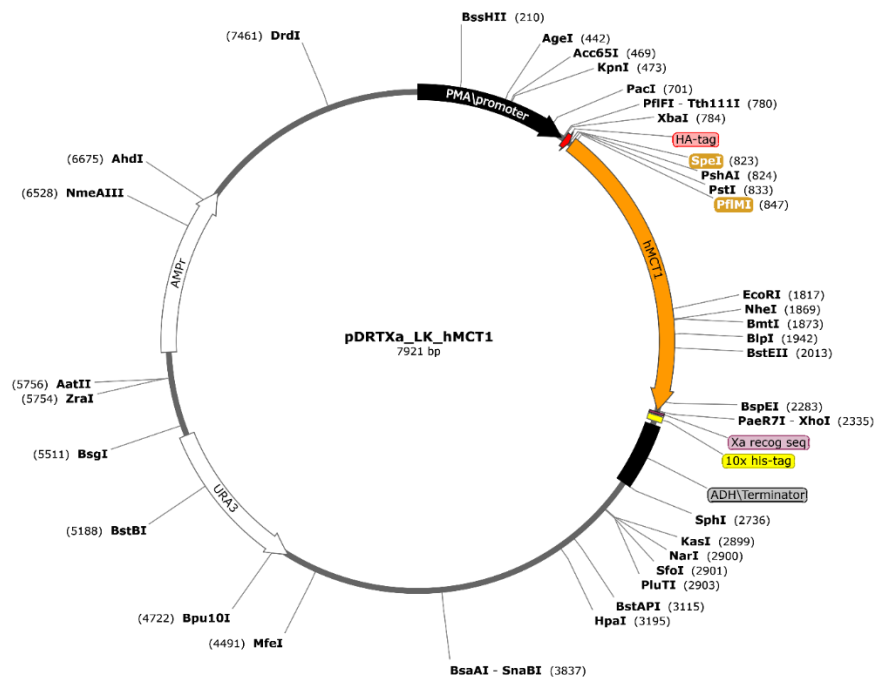
>h Carbonic anhydrase 4 protein sequence

MRMLLALLALSARPSASAESHWCYEVQAESSNYPLVPVKWGGNCQKDRQSPINIVTTK - 60
AKVDKKLGRFFFSGYDKKQTTWTVQNNGHSVMMLLENKASISGGGLPAPYQAKQLHLHWS - 120
LPYKGSEHSLDGEHFAMEMHIVHEKEKGTSRNVKEAQDPED EIAVLAFLEAGTQVNEGF - 180
QPLVEALSNI PKPEMSTTMAESSLLDLLPKEEKLRHYFRYLGSLTTPCDEKVVWTVFRE - 240
PIQLHREQILAFS QKLYYDKEQTVSMKDNVRPLQQLGQRTVIKSGAPGRPLPWALPALLG - 300
PMLACLLAGFLR - 312

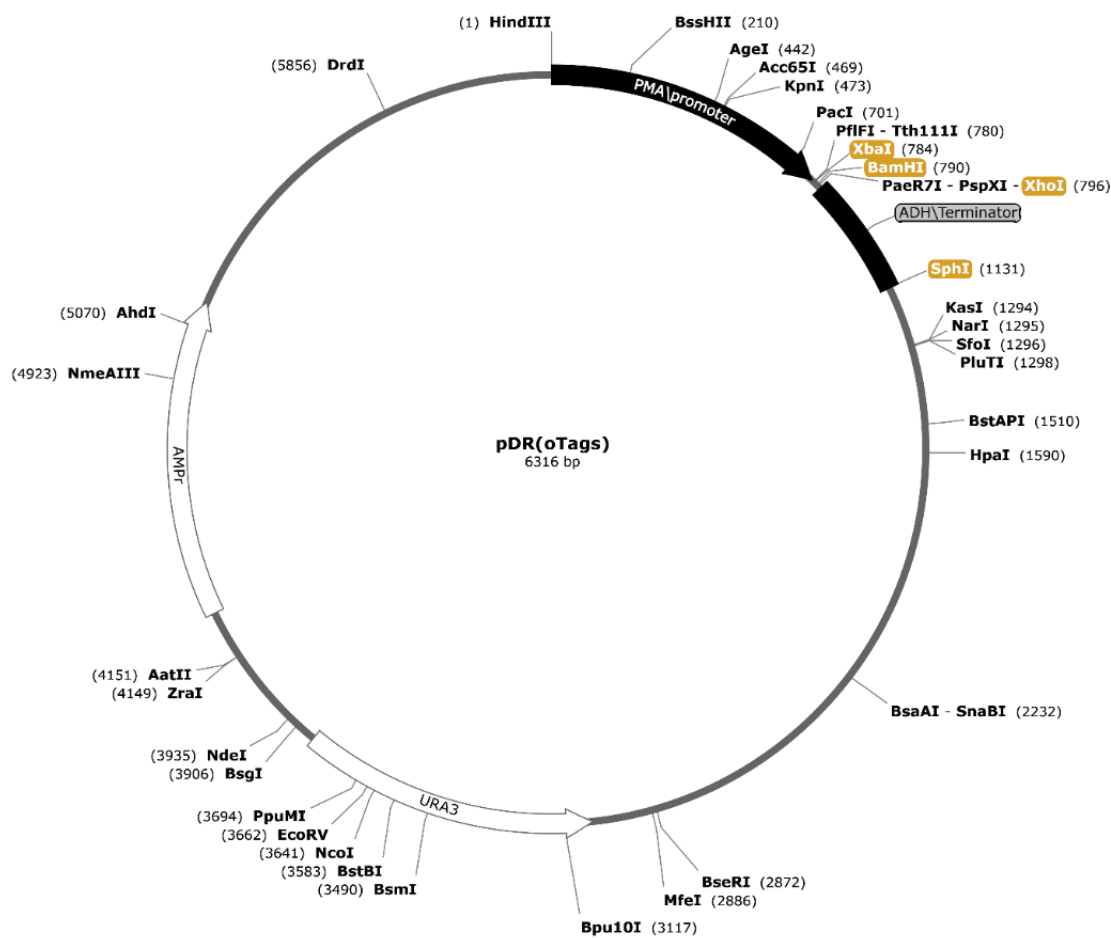
Supp. 2: Plasmids maps



Supp 2.1: Vector map of the pDRTXa plasmid, generated using SnapGene® Viewer. The most relevant restriction sites for cloning are highlighted (gold).

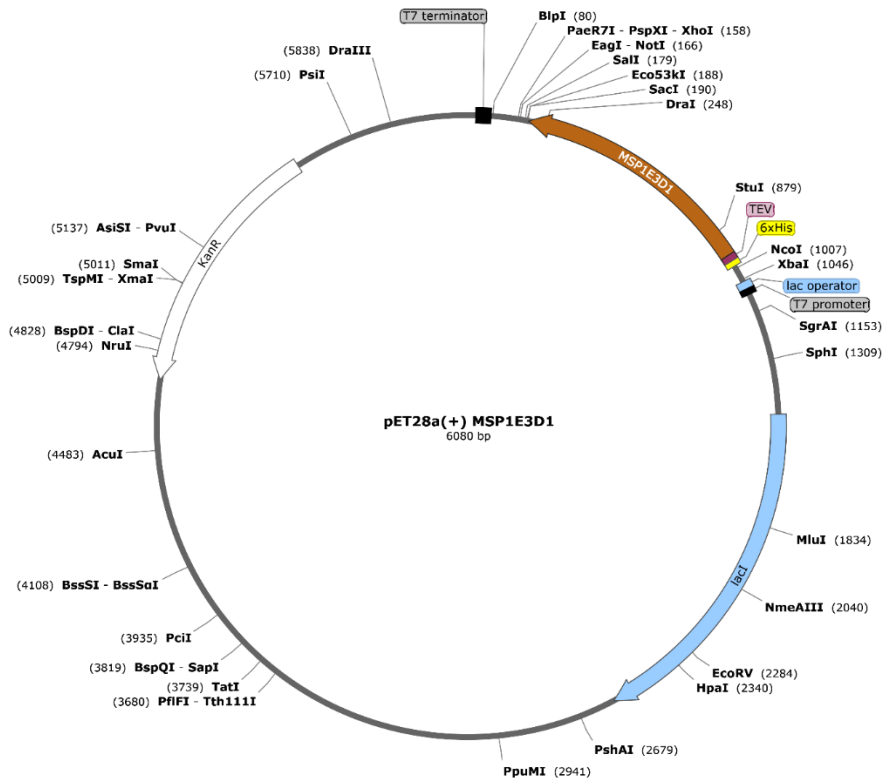


Supp 2.2: Vector map of the pDRTXa_LK_MCT1 plasmid, generated using SnapGene® Viewer. The most relevant restriction sites for cloning are highlighted (gold).

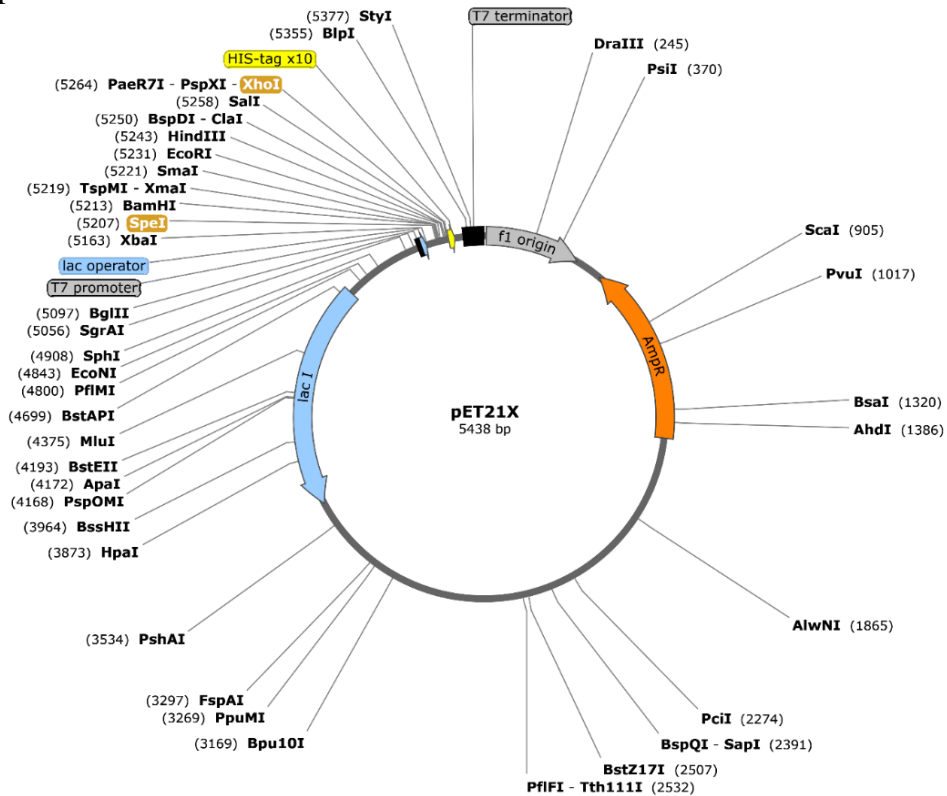


Supp 2.3: Vector map of the pDR(oTags) plasmid, generated using SnapGene® Viewer. The most relevant restriction sites for cloning are highlighted (gold).

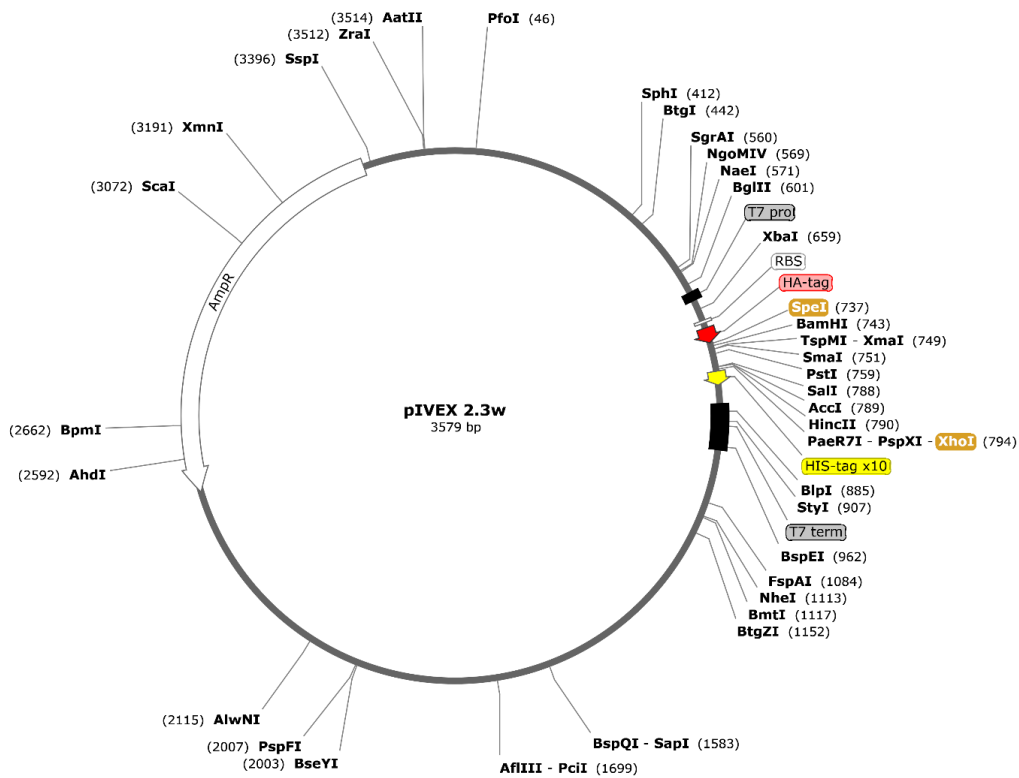
In order to remove the N-terminal HA tag and the C-terminal Factor Xa cleavage site and His₁₀-tag expressed in pDRTXa, the plasmid pDR was generated. First, PCR was used to amplify the ADH terminator with the primers PCR_pDRTXaDtag_s and PCR_pDRTXaDtag_as (Table 2.4). The overhang of the PCR_pDRTXaDtag_s primer adds before the ADH terminator a new MCS sequence composed of a XbaI site, an extra BamHI site and a XhoI site followed by a stop codon. Both the PCR product and the pDRTXa plasmid were digested with the restriction enzymes XbaI and SphI, and they were ligated together to replace the entire HA and multiple cloning site sequence. The new plasmid was sequenced using the Seq_fullADHterm_rev primer to ensure a correct insertion and no unwanted mutations).



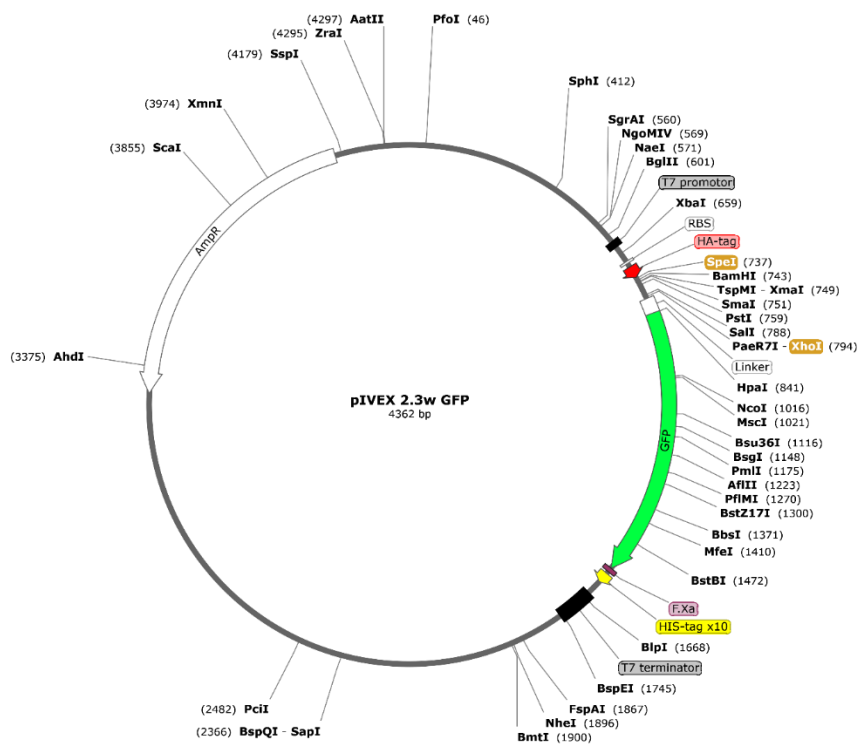
Supp 2.4: Vector map of the pET28a(+) plasmid containing the MSP1E3D1 gene, generated using SnapGene® Viewer.



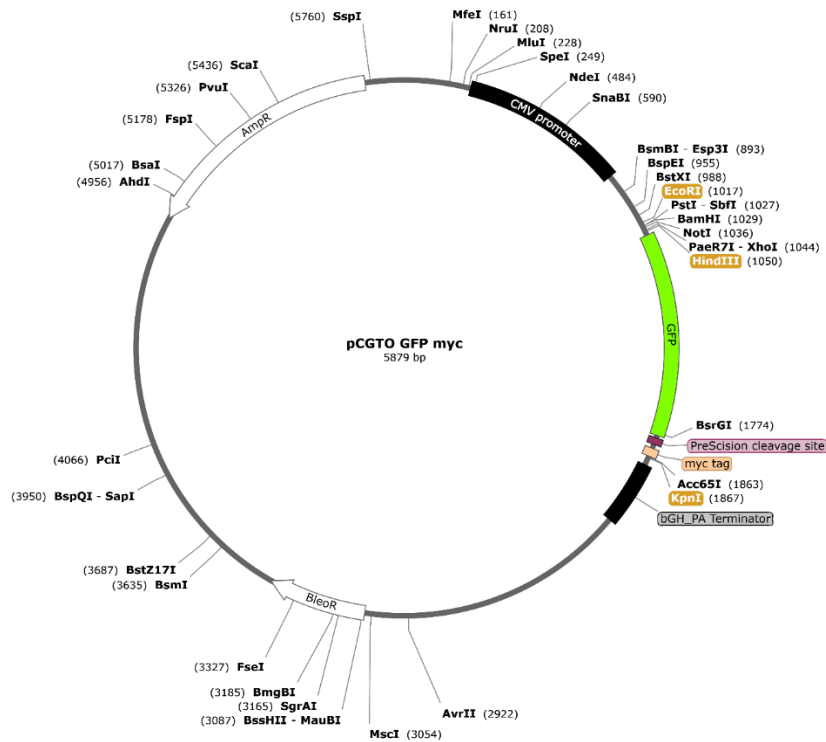
Supp 2.5: Vector map of the pET21X plasmid, generated using SnapGene® Viewer. The most relevant restriction sites for cloning are highlighted (gold).



Supp 2.6: Vector map of the pIVEX 2.3w plasmid, generated using SnapGene® Viewer. The most relevant restriction sites for cloning are highlighted (gold).



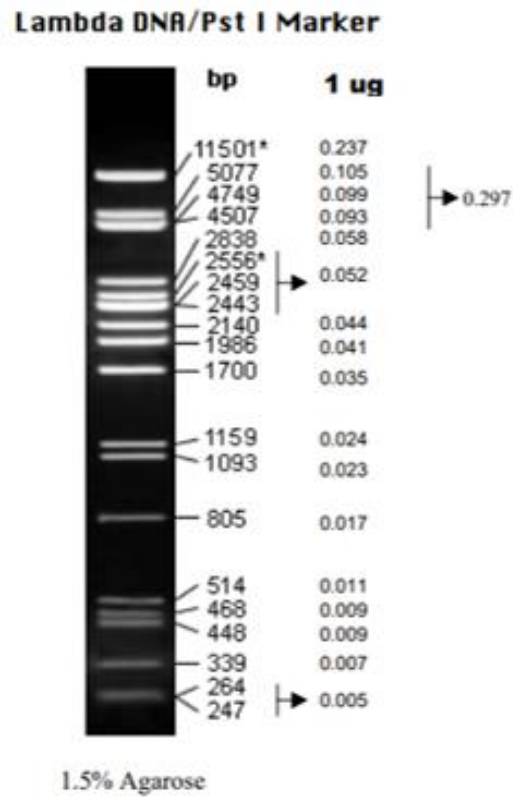
Supp 2.7: DNA sequence of the pIVEX 2.3w GFP plasmid between the promoter and terminator, generated using SnapGene® Viewer. The most relevant restriction sites for cloning are highlighted (gold).



Supp 2.8: DNA sequence of the pCGTO GFP myc plasmid between the promoter and terminator, generated using SnapGene® Viewer. The most relevant restriction sites for cloning are highlighted (gold).

Supp. 3: Lamda DNA/PstI Marker

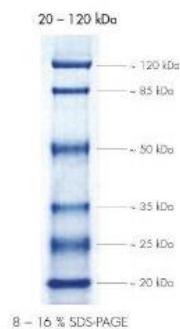
Used to estimate the sizes of the DNA fragment during Agarose gel electrophoresis (3.1.4.).



The cohesive ends of the 12 nt cos site of bacteriophage lambda from fragments of 11501 bp and 2556 bp (indicated) may anneal and form an additional band at 14057 bp. These fragments can be separated by heating at 65°C for 5min and then cooling on ice for 3min.

Supp. 4: preqGOLD Marker III (VWR)

Used to estimate the protein sizes in SDS-PAGE (3.2.4.)

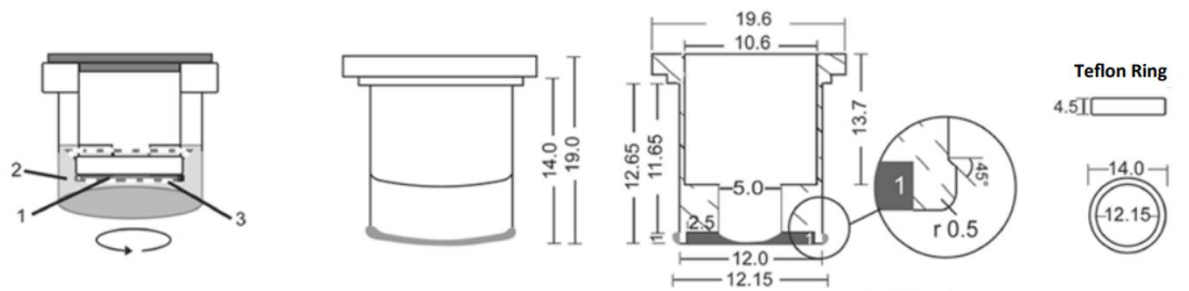


Supp. 5: Cell-free expression system: reaction chambers

Technical drawings adapted from the figures of S. Bock's doctoral thesis [180].

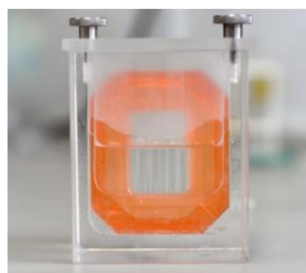
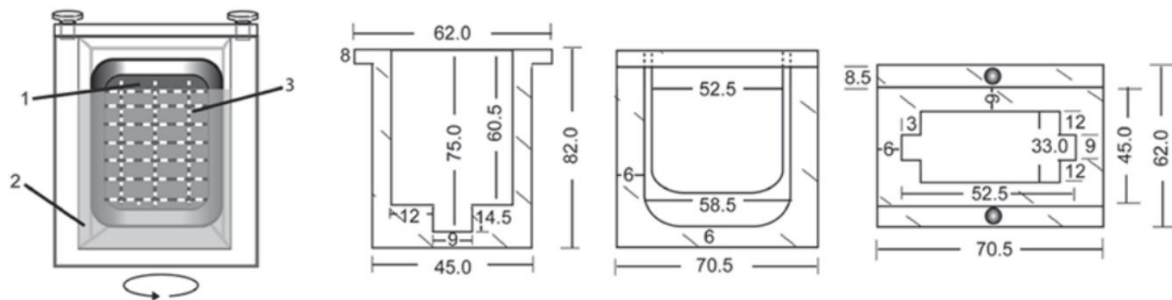
Unites are in mm.

Analytic chamber (70 μ L of reaction volume): Placed in a 12-well plate.



(1) Reaction mix, (2) Feeding mix and (3) dialysis membrane (14 kDa MWCO)

Preparative chamber (1 mL of reaction volume):



(1) Reaction mix inside the Slide-A-Lyzer™ Dialysis Cassette, (2) Feeding mix and (3) membrane of the Slide-A-Lyzer™ Dialysis Cassette (10 kDa MWCO)

Eidesstattliche Erklärung

Hiermit erkläre ich eidesstattlich, dass ich die vorliegende Arbeit, abgesehen von der Beratung durch den Betreuer, nach Inhalt und Form selbst und selbstständig angefertigt habe und keine weiteren Quellen und Hilfsmittel als die angegebenen verwendet habe. Diese Arbeit hat weder ganz noch in Teilen im Rahmen eines Prüfungsverfahrens vorgelegen, und wurde an anderer Stelle weder veröffentlicht noch zur Veröffentlichung eingereicht. Ich habe / werde die Zulassung zur Promotion nicht mit demselben Thema zeitgleich an einer anderen Fakultät im In- oder Ausland beantragt / beantragen. Ich habe noch an keiner anderen Hochschule oder an keiner anderen Fakultät dieser Hochschule ein Promotionsvorhaben endgültig nicht bestanden, und mir wurde noch kein akademischer Grad entzogen.

Die Arbeit ist gemäß den Regeln zur guten wissenschaftlichen Praxis der Deutschen Forschungsgemeinschaft angefertigt worden

Declaration

I hereby declare under oath that, apart from the advice of my supervisor, I have prepared this thesis independently in terms of content and form and have not used any sources or aids other than those indicated. This thesis has not been submitted in whole or in part of an examination procedure and has not been published or submitted for publication elsewhere. I have not / will not apply for admission to doctoral studies with the same subject at the same time at another faculty in Germany or abroad. I have not failed a doctoral project at any other higher education institution, and no academic degree has ever been withdrawn from me.

The thesis has been prepared in accordance with the rules of good scientific practice of the German Research Foundation (Deutschen Forschungsgemeinschaft).

Translated from German with www.DeepL.com/Translator (free version)

This research was funded by the European Union's Horizon 2020 research and innovation program under the Marie Skłodowska Curie Grant 860592.

Parts of this work has already been published in the following publications:

Köpnick, A.-L., Jansen, A., Geistlinger, K., Epalle, N. H. and Beitz, E. (2021) Basigin drives intracellular accumulation of L -lactate by harvesting protons and substrate anions. *PLoS One* **16**, e0249110. doi: 10.1371/journal.pone.0249110.

Jakóbowska, I., Becker, F., Minguzzi, S., Hansen, K., Henke, B., Epalle, N. H., Beitz, E. and Hannus, S. (2021) Fluorescence Cross-Correlation Spectroscopy Yields True Affinity and Binding Kinetics of *Plasmodium* Lactate Transport Inhibitors. *Pharmaceuticals (Basel)* **14**. doi: 10.3390/ph14080757.

Nerlich, C., Epalle, N. H., Seick, P. and Beitz, E. (2021) Discovery and Development of Inhibitors of the Plasmodial FNT-Type Lactate Transporter as Novel Antimalarials. *Pharmaceuticals (Basel)* **14**. doi: 10.3390/ph14111191.

Epalle, N. H. and Beitz, E. (2022) Local Attraction of Substrates and Co-Substrates Enhances Weak Acid and Base Transmembrane Transport. *Biomolecules* **12**. doi:10.3390/biom12121794.

Curriculum Vitae

Personal data

Name	Nathan Hugo Epalle
Date of birth	21 June 1996
Place of birth	Romans-sur-Isère, France
Nationality	French

Scholarity

2008-2011	Diplôme national du Brevet	Collège E.J. Lapassat, Romans-sur-Isère.
2011-2014	Baccalauréat Scientifique	Lycée Albert Triboulet, Romans-sur-Isère.
2014-2017	License: Life Sciences (6 semesters)	Université J. Fourier, Grenoble
2016-2017	Erasmus exchange	University of York, York
2018	Master I: Molecular and Cellular biology (2 semesters)	Université Grenoble Alpes, Grenoble
2019	Master II: Integrative Structural Biology (2 semesters)	

Acknowledgements

I cannot stress enough how grateful I am for my working group and fellow doctoral students.

I want to thank my supervisor, Eric Beitz, for his kindness and patience. Thank you for giving me this opportunity to work here on such interesting subjects.

Many thanks to Anna Meier, Lea Petersen, Philip Walloch, Annika Jansen, Anna-Lena Köpnick, Jana Schmidt, Katharina Geistlinger, Bastian Höger, Christian Hansen, Moira Möller, Cornelius Nerlich, Timo Beyer, Marc Scherwing, Katrin Jeuken, Maike Menzel, Sebastian Buss, Philip Seick, Solveig Feddersen, Gregor Ott, Jesko Caliebe, Robin Hertel, Olatomide Fadare, Oluwatobi Olakojo, Larissa Einfeldt, Maria Sklomeit, Susan Häuer, Anna Fuchs and Björn Henke. Thank you for our talks, the bigs and the smalls, for your help and assistance, your ideas, your feedback, your teachings. My work would have been impossible without you. Most of all, thank you for your friendship.

To the students I supervised, Yasmin, Marvin, Malissa, 'Jay', 'Jinny' and 'Mimii'; I hope that I was able to show you some fun and interesting things. Thank you for your attention and your enthusiastic participation. And thank you to Prof. Dawid Krenc for sending his student to us.

I would like to thank the entire Pharmazeutisches Institute for creating such a great work environment. Thanks to Till Priegann for his advices on HEK cell cultures and Daniel Riege, for sharing his protocol and material for the BCA. Thanks to Dirk Böhme and Kalle Bock, for always finding a solution to our technical problems. Thank you Volkmar Kelppa for the fantastic IT assistance.

Thank you to Prof. Lorenzen, for sharing her time and expertise to help me with my circular dichroism experiments.

Thank you Mrs. Isolda Ritter and Dr. Nancy Schmidt for helping me find my bearings in Kiel.

The team at Intana Bioscience GmbH welcomed me in their company during my secondment. Thanks to Iga Jakóbowka, Franck Becker, Stefan Hannus, Kerrin Hansen, Stefano Minguzzi

and Maria for teaching me how to cultivate HEK cells. And thank you Norbert for welcoming me in Martinsried. Also, thanks to Frank and Stephan for organising the Industry Workshop.

Prof. Peter Pohl welcomed me in his lab for my second secondment. Thanks to him and all of his team, to Stefania Brescia and Nikolaus Goessweiner for helping me with my work.

Great thanks go to all the actors responsible for the PROTON ITN, for giving us students the opportunity to do our research. Many thanks to Denis Knyazev, our ever-patient coordinator.

I also would like to thank all my fellow PROTON students, for being such fantastic people to be around. Thank you, Abhinav Insan, Alejandro Martinez Leon, Anna Maznichenko, Bhav Kapur, Bingxin Chu, Flore Kersten, Giorgia Roticiani, Honey Jain, Iga Jakóbowska, Isabel Králová, Iuliana-Marilena Andrei, Mateu Montserrat, Paras Wanjari, Satyaranjan Biswal, Seonwoo Lee and Stefania Brescia. I wish we had more opportunities to see each other, but it was really inspiring to meet you all.

Many thanks to all my former professors and mentors. Without them I never would have gone anywhere in Science. Thank you Prof. Michael Plevin; Dr. Andréa Dessen, Dr. Carlos Contreras-Martel and Alexandre Martins; Dr. Cécile Breyton and Dr. Elisabetta Boeri Erba. Thank you, Prof. Corrine Mercier, for inspiring me to help against pathogens, parasites and especially, *Plasmodium*.

Thanks to the “Bio Int” crew. It’s thanks to you guys that I persevered in Research.

Un grand merci à ma famille et à mes amis. Pour tout.

...and thank you, for reading this far.